Magnetic Excitations in Iron-based Superconductors

I n a u g u r a l - D i s s e r t a t i o n

zur

Erlangung des Doktorgrades

der Mathematisch-Naturwissenschaftlichen Fakultät

der Universität zu Köln

vorgelegt von

Florian Tim Waßer
aus Solingen

Köln, 2018

Berichterstatter:	Prof. Dr. Markus Braden Prof. Dr. Thomas Lorenz
Vorsitzender der Prüfungskommission:	Prof. Dr. Simon Trebst
Tag der mündlichen Prüfung:	16. Okt. 2018

Contents

Page

1 Iron-based Superconductors **1**
- 1.1 Crystal and Magnetic Structure . . . 1
- 1.2 Nematicity in Iron-based Superconductors . . . 4
- 1.3 Superconductivity and Spin Resonance Mode in FeSCs . . . 7

2 Spin Reorientation Transitions and Magnetic Excitations in $Ba_{1-x}Na_xFe_2As_2$ **11**
- 2.1 Spin Reorientation Transitions . . . 12
  - 2.1.1 Section Introduction . . . 14
  - 2.1.2 Temperature Dependence of Elastic Bragg Scattering . . . 16
  - 2.1.3 Suppression of Magnetic Intensity Below T_c . . . 20
  - 2.1.4 Polarisation Analysis . . . 22
  - 2.1.5 Profile Analysis of Magnetic Bragg Reflection . . . 24
  - 2.1.6 Temperature Dependence of the Orthorhombic Distortion in $Ba_{0.65}Na_{0.35}Fe_2As_2$ . . . 26
  - 2.1.7 Section Summary . . . 27
- 2.2 Magnetic Excitations in $Ba_{1-x}Na_xFe_2As_2$ . . . 29
  - 2.2.1 Section Introduction . . . 29
  - 2.2.2 Results and Analysis . . . 30
  - 2.2.3 Section Summary . . . 47
- 2.3 Discussion . . . 51
- 2.4 Methods . . . 55
  - 2.4.1 M: Spin Reorientation Transitions . . . 56
  - 2.4.2 M: Magnetic Excitations in $Ba_{1-x}Na_xFe_2As_2$ . . . 57
    - 2.4.2.1 Data Treatment Na25 . . . 58
    - 2.4.2.2 Data Treatment Na31 . . . 58
    - 2.4.2.3 Data Treatment Na35b . . . 58
    - 2.4.2.4 Data Treatment Na39 . . . 58
    - 2.4.2.5 Data Treatment Na40 . . . 59

3 Magnetic Excitations in $Ba(Fe_{1-x}Co_x)_2As_2$ **61**
- 3.1 Introduction . . . 62

3.2 Anisotropic Magnetic Excitations in Underdoped $Ba(Fe_{1-x}Co_x)_2As_2$ . . . 64
3.3 Spin Resonance Mode in $Ba(Fe_{0.94}Co_{0.06})_2As_2$ . . . 71
3.4 Summary and Discussion . . . 77
3.5 Methods . . . 80

4 Incommensurate to Commensurate Magnetic Excitations in $LiFe_{1-x}Co_xAs$ 81
4.1 Introduction . . . 81
4.2 Magnetic Excitations in $LiFe_{0.82}Co_{0.18}As$ . . . 85
4.3 Discussion . . . 89
4.4 Methods . . . 90

5 The Quest for the Resonance Mode in $NdFeAsO_{1-x}F_x$ 93
5.1 Introduction . . . 93
5.2 Results . . . 94
5.3 Summary and Discussion . . . 100
5.4 Methods . . . 101

6 Methods: Neutron Scattering 103
6.1 Basics . . . 103
6.2 Triple Axis Spectrometer . . . 104
6.3 Time-of-Flight Spectrometer, IN4 . . . 108
6.4 Absolute Unit Calculation . . . 108
6.5 Polarisation Analysis . . . 112

Appendix 117
A.1 Spin Reorientation transitions . . . 117
A.2 Magnetic Excitations in $Ba_{1-x}Na_xFe_2As_2$ . . . 118
A.3 Spin Excitations in Na25 and Na31 . . . 123
A.4 Magnetic Excitations in $Ba(Fe_{1-x}Co_x)_2As_2$ . . . 126
A.5 Incommensurate to Commensurate Magnetic Excitations in $LiFe_{0.95}Co_{0.05}As$ . . . 128
A.6 List of Samples . . . 130

List of Figures 132

List of Tables 133

Bibliography 158

Danksagung 159

Abstract **161**

Kurzzusammenfassung **163**

Teilpublikationen **165**

Erklärung **166**

Definitions

Acronyms and Initials

AE	alkaline earth metal (2^{nd} main group)
AFM	antiferromagnet, -ic, -ism,(s)
AIST	National Institute of Advanced Industrial Science and Technology
AM	alkaline metal (1^{st} main group)
ARPES	angle resolved photo emission spectroscopy
BaCo45	$Ba(Fe_{0.955}Co_{0.045})_2As_2$
BaCo60	$Ba(Fe_{0.94}Co_{0.06})_2As_2$
BZ	Brillouin zone
C_2	two-fold rotation symmetry
C_4	four-fold rotation symmetry
c-AFM	AFM with moments along the *c*-axis
CF	crystal field
CH	chalcogenides
CuSC	cuprate superconductors
DFT	density functional theory
EDX	energy dispersive X-ray spectroscopy
FeSC	iron-based superconductor
FL	Fermi liquid
FR	flipping ratio
FS	Fermi surface
f.u.	formula unit
gdos	generalised (phonon) density of states
HFSC	heavy fermion superconductor
IFW	Leibnitz Institut für Festkörper- und Werkstoffforschung
	Leibnitz Institute for Solid State and Materials Research
ILL	Institute Laue - Langevin
INS	inelastic neutron scattering
IR	infrared
LAMP	large array manipulation program
LDA	local density approximation
LiCo05	$LiFe_{0.95}Co_{0.05}As$
LiCo18	$LiFe_{0.82}Co_{0.18}As$
LLB	Laboratoire Léon Brillouin

MEC	magneto-elastic coupling
Na25	$Ba_{0.75}Na_{0.25}Fe_2As_2$
Na31	$Ba_{0.69}Na_{0.31}Fe_2As_2$
Na35a	$Ba_{0.65}Na_{0.35}Fe_2As_2$
Na35b	$Ba_{0.65}Na_{0.35}Fe_2As_2$
Na39	$Ba_{0.61}Na_{0.39}Fe_2As_2$
Na40	$Ba_{0.6}Na_{0.4}Fe_2As_2$
NdF13	$NdFeAsO_{0.87}F_{0.13}$
NFL	non-Fermi liquid
NMR	nuclear magnetic resonance
NSF	non-spin flip
OrgSC	organic superconductors
ORT	orthorhombic
PDF	pair distribution function
pINS	polarised inelastic neutron scattering
PM	paramagnet, -ic, -ism,(s)
QCP	quantum critical point
QPI	quasi-particle interference
RE	rare earth (element)
RG	renormalisation group
rlu	reciprocal lattice unit
SC	superconduct -or, -ivity, -ive, -ing
SF	spin flip
SOC	spin-orbit coupling
SQUID	superconducting quantum interference device
SRM	spin resonance mode
TAS	triple axis spectrometer
TET	tetragonal
TOF	time-of-flight
WDX	wave-length dispersive X-ray spectroscopy
XRD	X-ray diffraction

Mathematical Symbols

a	lattice constant
b	lattice constant
b^{scat}	(nuclear) scattering length
$\boldsymbol{B}$	magnetic field
B_w	bandwidth of resonance mode
c	velocity of light, lattice constant
$\delta(...)$	delta-function

$\delta_{\alpha\beta}$	Kronecker delta
$\boldsymbol{\Delta}$	four-dimensional difference vector in $(\boldsymbol{Q}, E)$-space
e	elementary charge
E	transferred energy from the scattered neutron to the sample
$\|f\rangle$	final state
$f(\boldsymbol{Q})$	magnetic form factor
F_{coh}	BCS coherence factor
g	Landé factor
$g(\boldsymbol{Q})$	geometry factor
γ	$(= -1.913)$ gyromagnetic ratio of the neutron
$\|i\rangle$	initial state
$\hat{I}$	unit matrix
$I\,(\boldsymbol{Q}, E)$	neutron intensity at $(\boldsymbol{Q}, E)$
k_f	final neutron momentum
k_i	initial neutron momentum
m	mass
M	total mass
m_e	mass of electronic
m_n	mass of neutron
$\boldsymbol{M}(\boldsymbol{Q}, E)$	resolution matrix
$\boldsymbol{\mu}$	magnetic moment
μ	absolute value of magnetic moment
$\boldsymbol{\mu}_e$	magnetic moment of electron
$\boldsymbol{\mu}_n$	magnetic moment of neutron
$n(E)$	Bose population factor (at fixed temperature)
N	number of unit cells
p	$(= (\gamma r_0/2)^2 = 2.695\,\mathrm{fm})$ scattering "length" ... for a single magnetic moment of $1\,\mu_\mathrm{B}$
$\boldsymbol{p}$	momentum of electron
P	neutron polarisation vector
Π	total neutron beam polarisation
Φ_{scale}	scaling factor for absolute unit calculation
$\boldsymbol{Q}$	scattering vector
Q	absolute value of $\boldsymbol{Q}$
$\mathfrak{R}$	Gaußian approximation of TAS resolution
r_0	$(= e^2/m_e c^2)$ classical electron radius
$\frac{d^2\sigma}{d\Omega dE}$	double differential cross section
T_{mod}	temperature of neutron moderator
U	neutron interaction potential
$\hat{U}$	interaction matrix
V	volume of unit cell

W	L bandwidth of the spin resonance mode
$\boldsymbol{\xi}$	phonon polarisation vector
$\chi'(\boldsymbol{Q}, E)$	real part of dynamic susceptibility
$\chi''(\boldsymbol{Q}, E)$	imaginary part of dynamic susceptibility
$\chi_0(\boldsymbol{Q}, E)$	bare spin susceptibility
$\chi(\boldsymbol{Q}, E)$	spin susceptibility

1 Iron-based Superconductors

Contents

1.1 Crystal and Magnetic Structure 1
1.2 Nematicity in Iron-based Superconductors 4
1.3 Superconductivity and Spin Resonance Mode in FeSCs . . . 7

1.1 Crystal and Magnetic Structure

Iron-based superconductors (FeSCs) are a fertile ground to study the interplay between structure, magnetism and superconductivity in a novel class of materials. Correspondingly, this is the fourth big material class, next to the cuprate (CuSCs) [1–4], heavy fermion (HFSCs) [5–8] and organic superconductors (OrgSC) [9–11], where the mediation of superconductivity is not based on phonons [12]. In order to cultivate that ground many new materials, since their initial discovery [13, 14] in 2006 respectively 2008, were synthesised. Chemically, the common building blocks are always FePn[1] or FeCH[2] layers which are more or less separated by an additional spacer layer, c.f. Fig.: 1.1. According to their stoichiometry four main material classes are formed; the *1111* REFePnO[3] [15–18], the *122* AEFe$_2$As$_2$[4] [19–23], the *111* AMFeAs[5] [24–27] and the *11* FeCH [28, 29]. In this thesis compounds belonging to three of these four classes are investigated, in particular $Ba_{1-x}Na_xFe_2As_2$ in Chap. 2 and $Ba(Fe_{1-x}Co_x)_2As_2$ in Chap. 3 of the *122*s, LiFeAs in Chap. 4 of the *111*s and $NdFeAsO_{1-x}F_x$ in Chap. 5 of the *1111*s.
Superconductivity in FeSCs can be induced by adding or removing charges via doping [19,22,23,30–32], by isovalent substitution [33–35] or by applying external pressure [36–38]. Thereby, the orthorhombic and antiferromagnetic (o-AFM) phase becomes suppressed while the tetragonal paramagnetic (t-PM) one is restored. However, there is a regime in the phase diagram, called orthorhombic superconducting (o-SC), where it microscopically coexists with AFM order [39–43], c.f. the schematic phase diagram for charge doping in Fig.: 1.2. In that context the highest

[1] Pn = pnictogen e.g. P or As
[2] CH = chalcogenide e.g. S, Se, Te
[3] RE = rare earth e.g. La, Nd, Sm, Gd
[4] AE = alkaline earth metal e.g. Ba, Sr, Ca
[5] AM = alkali metal e.g. Li, Na

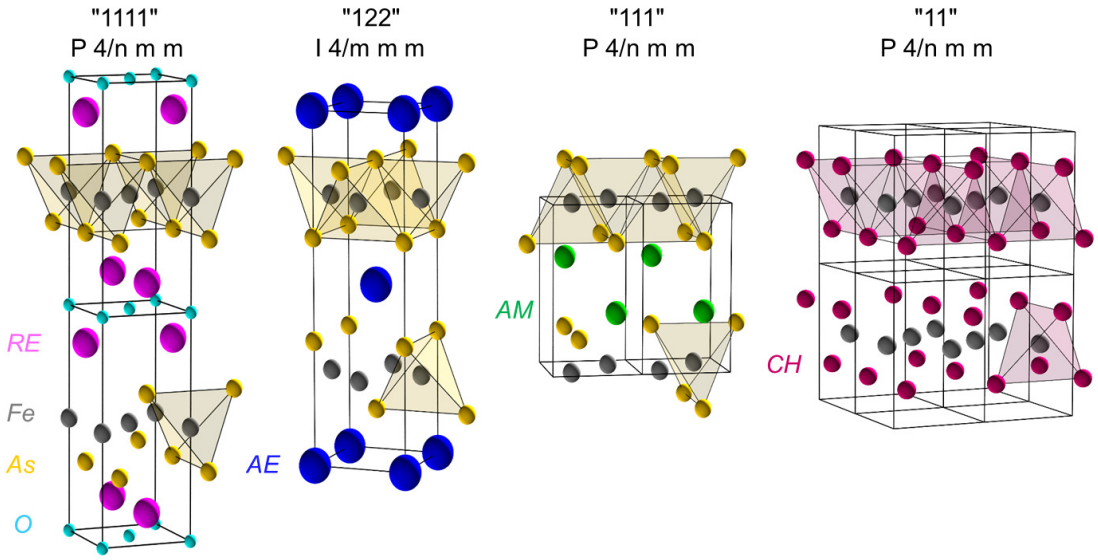

Figure 1.1: Room temperature crystal structures of FeSC families. The commonality of FeSCs are the edge-sharing FeAs-tetrahedrons, which are separated by a spacer-layer or by no spacer-layer at all, as in iron-chalcogenides (CH = Se, Te). From left to right the spacer-layer thickness decreases and is either composed of a rare earth (RE = La, Ce, Pr, Nd), an alkaline earth (AE = Ba, Sr, Ca), or an alkaline metal (AM = Na, Li).

T_c values are found close to the end-point of the o-AFM phase [19, 22, 23, 30–32], where the $FeAs_4$ tetrahedra are most regular [30, 51, 52], and the three t_{2g} orbitals (d_{xy}, d_{zy}, d_{xz}) are most degenerate due to the crystal field.
Furthermore, this observation inspired two different explanations for the pairing mechanism, whereas the first is based on spin fluctuations [53–64] and the second on phonon assisted orbital fluctuations [65–70]. This underlines the triangular relation between structure, magnetism and superconductivity, which are manifestations of the same mechanism in the spin-driven nematic scenario c.f. Sec. 1.2. Additionally, details of the SC pairing mechanism are outlined in Sec. 1.3.
In the o-AFM phase, magnetic moments of $\sim 1\ \mu_B$[6] point along the a axis and are ferromagnetically aligned along b and antiferromagnetical along c and a [26, 72, 73], c.f. Fig.: 1.2 for a sketch. Consequently, magnetic Bragg peaks in neutron scattering are observed at $\boldsymbol{Q} = (1,0,L)_{ort} = (0.5,0.5,L)_{tet}$ in the orthorhombic or tetragonal notation, which both will by employed in this thesis. Iron-based superconductors are layered magnets, due to their order, and the fact that they mechanically cleave easily along the c axis.

[6] c.f. Lumsden *et al.* [71] and references therein

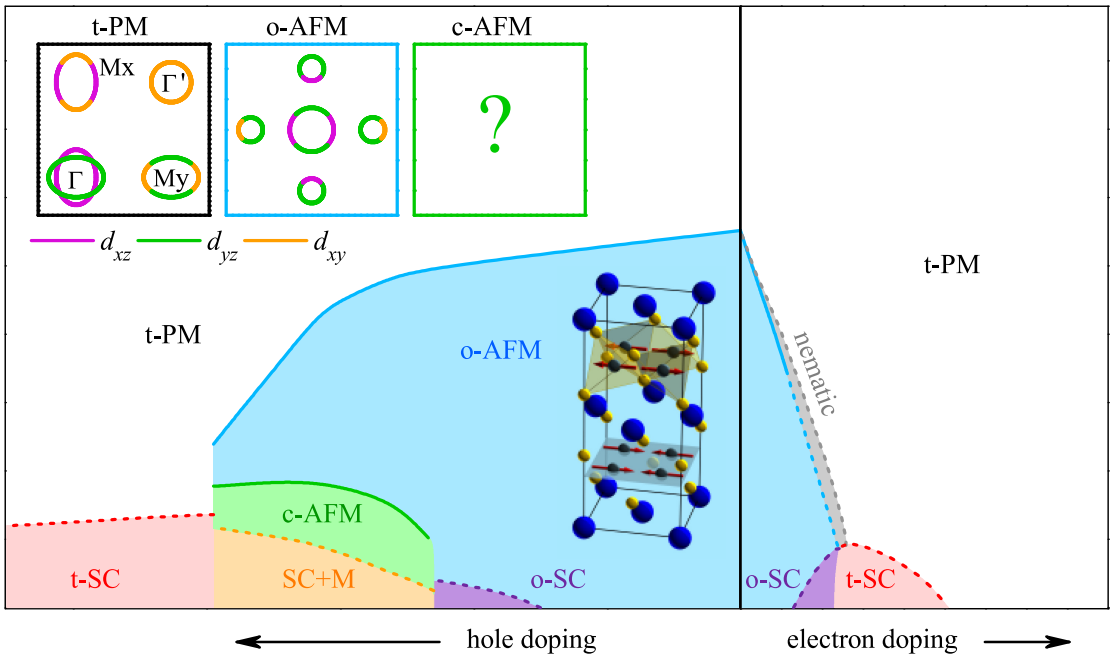

Figure 1.2: Generic phase diagrams of FeSCs. Solid lines denote first order phase transitions and dotted lines second order. Note that according to Kim *et al.* [44] the nature of T_N changes from first to second order in $Ba(Fe_{1-x}Co_x)_2As_2$. The phase diagram is based on various reports in the literature [31, 45–47] and the Fermi surfaces are reproduced from Ref. [48–50].

Moreover, in the phase diagram, the T_N transition line is coupled closely to the T_s one, signalling the orthorhombic distortion due to strong magneto-elastic coupling (MEC) [74]. With increasing hole doping both transition temperatures are always identical, first order in nature and never split [30, 46, 75]. On the opposite, with increasing electron doping, the T_N-T_s transition-lines are still coupled, but begin to split and thus give place to the so-called nematic phase, which is described in more detail in Sec. 1.2. Furthermore, the T_N transition character changes from first to second order before SC emerges [44]. In any case, for underdoped FeSCs superconductivity develops from an orthorhombic and antiferromagnetically ordered state. This means that the SC gap opens on an already reconstructed and partially gapped Fermi surface with an orbital polarisation [48–50, 76, 77]. The orbital polarisation arises below T_s, as the degeneracy of the d_{zy} and d_{xz} orbitals is lifted by the orthorhombic distortion [49]. A sketch of the FS in the t-PM and o-AFM phase is given in the inset of Fig.: 1.2. Once more, this highlights the intimate relation between lattice structure, magnetic order and superconductivity. In particular, this indicates that a complete description of the SC state needs to take

the details of an orbital-dependent band structure into account. The consequences when superconductivity emerges in the presence of strong AFM gaps are explored in Sec. 3.2.

Another aspect was highlighted by polarised inelastic neutron (pINS) scattering, where an intriguing spin-space-anisotropy was found, which indicates the importance of spin-orbit coupling (SOC). Although FeSCs are layered magnets the magnetic anisotropy gap for out-of-FeAs-layer excitations is smaller than the one for in-layer excitations [78–80]. In a recent theoretical calculation including the effect of SOC the gap anisotropy could be reproduced [81]. Moreover, the c polarised low-energy excitations can condense via a spin reorientation for at the AE-site hole doped 122s, while the associated c-AFM phase occupies a small fraction in the o-AFM dome in the corresponding phase diagram [45–47, 82–84]. This spin reorientation, where magnetic moments realign from their in FeAs-layer alignment towards the c axis via a first order phase transition, documents the role of SOC, again. Consequently, the transition will reconstruct the reconstructed Fermi surface and thus forms a new basis from which superconductivity emerges ultimately. Notably, hole-doping at the Fe-site in the *122* family also yields to a magnetic order with moments pointing along the c axis, but superconductivity is not induced [85–89]. However, the spin reorientation transition does not inflict a major penalty on the T_c values. This transition and the associated implications for superconductivity are explored in more detail in Chap. 2.

1.2 Nematicity in Iron-based Superconductors

The crystal and magnetic structure of FeSCs, i.e. the t-PM, o-AFM or c-AFM phase, form the basis from which superconductivity emerges, eventually, and as a consequence, understanding of these normal state properties is paramount to comprehend the SC one. From the advent of FeSC, a strong coupling between magnetic order and orthorhombic lattice distortion is observed, as the associated (T_s,T_N) transition lines follow each other in the ($T - x$) phase diagram, c.f. Fig.: 1.2. Thereby, early theoretical works proposed that the orthorhombic phase is not driven by the lattice degrees of freedom, i.e. phonons, but by electronic ones [90, 91]. In this context, large anisotropies along the two directions of the FeAs-layers were observed experimentally, e.g. in resistivity measurements in $Ba(Fe_{1-x}Co_x)_2As_2$, where it reaches a factor of two [92–94], in ARPES measurements d_{zy}/d_{xz} orbitals split at temperature far above T_s [49], susceptibility [95] and magnetic torque measurements [96] and in polarised inelastic neutron scattering (pINS) where the magnetic signal in the spin flip (SF) channels y and z split at $70\,\mathrm{K} > T_S = 33\,\mathrm{K}$ in $Ba(Fe_{0.952}Ni_{0.048})_2As_2$ [97]. Note that the orthorhombic distortion causes real crystals to form twin domains, whereas the

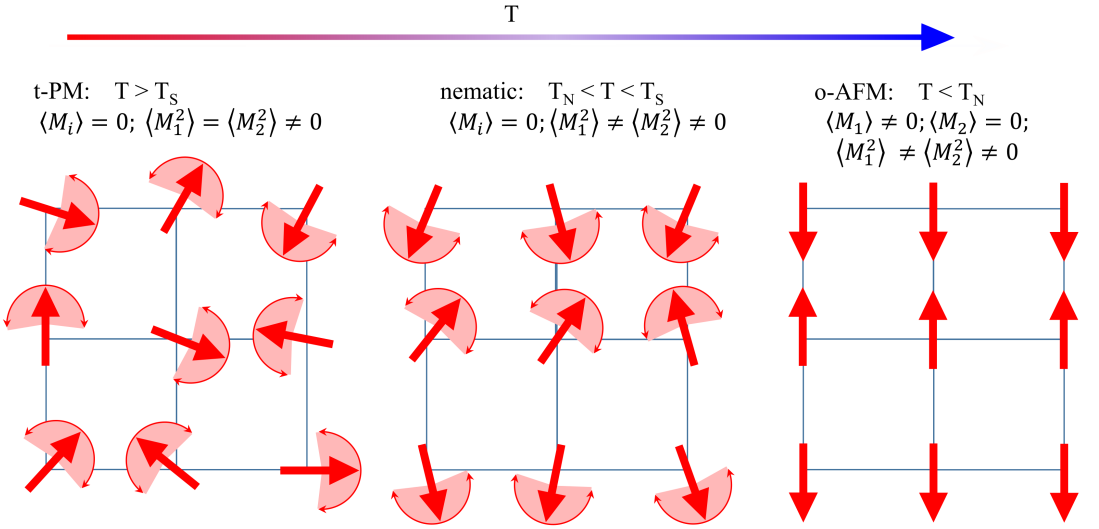

Figure 1.3: Schematic sketch of the spin-nematic and magnetic transition. The rotational symmetry of the lattice and the time-reversal symmetry can be broken in two consecutive steps. First, only the C_4 lattice symmetry is broken, no static magnetic order develops $\langle M_i \rangle = 0$, but directed spin-fluctuations are formed $\langle M_1^2 \rangle \neq \langle M_2^2 \rangle \neq 0$. Second, static magnetic order sets in and time-reversal symmetry is broken, $\langle M_1 \rangle \neq 0$, $\langle M_2 \rangle = 0$ and $\langle M_1^2 \rangle \neq \langle M_2^2 \rangle \neq 0$. This picture is reproduced from Fernandes *et al.* [99].

above listed experiments were predominantly conducted on detwinned samples realised by applying a small pressure, a few MPa, along one axis. Nonetheless, an orthorhombic distortion, where the corresponding a and b lattice constants deviate by just $\sim 0.5\,\%$ from each other, can hardly explain the observed anisotropies, in particular their doping dependence, as e.g. the resistivity anisotropy in $Ba(Fe_{1-x}Co_x)_2As_2$ is largest at $x \sim 4.5\,\%$ Co doping and not at $0\,\%$, where the orthorhombic distortion is largest [92, 98].
The observed anisotropies are associated to an (electronic) order parameter, which breaks the rotational symmetry, but preserves the time-reversal symmetry [91, 99]. By construction, this order parameter is similar to the one in liquid crystals, when rod-like molecules all point in one direction, and is hence termed by analogy as *nematic* [91]. Since the orthorhombic distortion in FeSCs force the order parameter to point in one direction, a or b, it becomes Ising-like and associated phase is thus called *Ising-nematic order* [91, 99].
Theoretical calculations emphasise that the origin of the nematic phase and the SC pairing symmetry are consequences of the same scenario [91]. This implies that a detailed knowledge of the normal state properties has direct consequences

on the superconducting one. However, the nematic transition can be driven by two electronic degrees of freedom, either charge/orbital or spin fluctuations. As a consequence, the charge/orbital scenario provides an SC state whose gap function preserve its sign on the hole and electron Fermi surface pockets, i.e. a s^{++}-wave, while the magnetic scenario induces a sign change of the gap on the corresponding pockets and thus yields a $s^{\pm}$-wave, c.f. next section for the SC pairing symmetry. Although, both electronic degrees of freedom are strongly coupled to each other, meaning the divergence of one susceptibility causes the other's also diverge, i.e. magnetic order triggers orbital order and vice versa, a recent renormalisation group (RG) analysis could demonstrate that nematic order is caused by spin fluctuations [53].

In the following, the interplay between nematic and magnetic order is elucidated. The o-AFM phase is doubly degenerate as spins can order in parallel stripes along the b axis, yielding a propagation vector $\boldsymbol{Q}_1 = (\pi, 0)$, or in parallel stripes along the a axis with $\boldsymbol{Q}_2 = (0, \pi)$. Correspondingly, the magnetic orders are labelled as $\langle M_1 \rangle$ and $\langle M_2 \rangle$, and either breaks the time-reversal symmetry and the rotational one of the lattice below T_N. However, (spin) fluctuations, labelled as $\langle M_i^2 \rangle$, can separate both symmetry-breaks such that the rotational C_4 lattice symmetry is broken to C_2 at a higher temperature, than the time-reversal symmetry. Accordingly, as stated above, the nematic phase is characterised by broken C_4 lattice symmetry due to directed spin fluctuations $\langle M_1^2 \rangle \neq \langle M_2^2 \rangle \neq 0$, while no static order is developed $\langle M_i \rangle = 0$, yet. Moreover, at a lower temperature static magnetic order sets in, e.g. $\langle M_1 \rangle \neq 0$ and $\langle M_2 \rangle = 0$. The split transitions from the t-PM phase via the nematic one to the o-AFM state are summariesed in Fig.: 1.3.

Due to its direct connection to SC, nematicity in FeSCs is a hotly debated topic [98–102], while the most recent discussions are focussed on FeSe [28, 29, 103–108]. This compound displays the largest nematic region in FeSCs is observed so far, as there is a structural phase transition at $\sim 90\,\mathrm{K}$ but no static magnetic order is realised down to lowest temperatures, while SC emerges at $\sim 8\,\mathrm{K}$. Additionally, electronic nematicity is proposed to be realised in CuSCs [109] and HFSCs [110], as well, hence it seems to be a more general property of high-temperature superconductors [111]. In this context a nematic SC state was recently discovered in the topological superconductor $Cu_xBi_2Se_3$ [112].

1.3 Superconductivity and Spin Resonance Mode in FeSCs

Superconductivity is one of the most mesmerising phenomena in solids. In this phase, electrons bind to Cooper pairs, and within BCS-theory this binding is based on an attractive interaction, which is mediated by an exchange boson [113]. In the early days before the advent of heavy fermion (HFSCs) and cuprate superconductors (CuSCs) this exchange boson is a phonon, which naturally provides an easy explanation for the isotope effect $\left(T_c \sim m^{-\frac{1}{2}}\right)$. Moreover, BCS theory as an electron-phonon weak-coupling approach yielded two fundamental equations to calculate the critical temperature T_c and the corresponding energy gap Δ_{SC}, which can be interpreted as the Cooper pair's binding energy

$$k_{\mathrm{B}} T_c = 1.13 \hbar \omega_D \cdot \exp\left(-\frac{1}{\lambda}\right), \tag{1.1}$$

$$2\Delta_{SC} = 3.52 k_{\mathrm{B}} T_c. \tag{1.2}$$

ω_D is the Debye frequency and λ the electron-phonon coupling parameter. By this reason the T_c value of today's record holder H_3S with $T_c(200\,\mathrm{GPa}) \sim 200\,\mathrm{K}$ can easily be understood [114].
On the other hand and today not fully resolved is the emergence of superconductivity in HFSCs, CuSCs, OrgSCs and FeSCs [3,11,60,115,116] where the interaction is mediated without phonons [117, 118]. In particular it was theoretically shown by density-functional perturbation theory that λ in $LaFeAsO_{1-x}F_x$ is 5-6 times too small to account for the observed T_c values [12]. Moreover, the change in magnetic exchange energy between the normal (NS) and the superconducting (SC) state in the CuSC compound $YBa_2Cu_3O_{6.95}$ and the HFSC compound $CeCu_2Si_2$ is respectively 15 or 20 times larger than the corresponding SC condensation energy [119,120]. Consequently, this observation supports the argument that superconductivity is driven by (residual) spin-spin interactions [5–7]. In view of BCS theory the associated exchange-boson to mediate the electron-electron interaction will be called paramagnon [121]; whereas in recent literature the rather unspecific term spin fluctuation is mostly propagated. The importance of paramagnos is demonstrated by time-of-flight (TOF) and resonant inelastic X-ray scattering (RIXS) experiments, where their dispersions and spectral weights in the nonmagnetic and doped compounds resemble those of magnons in the corresponding host compounds [4, 122–124]. This observation connects the FeSCs to the CuSCs and possibly to the HFSCs [125] as well. Furthermore, investigation of the spin excitation spectra in the NS and SC state can provide information on the pairing mechanism. Although, the pairing symmetry in CuSCs is $d_{x^2-y^2}$ [126, 127], in FeSCs it is broadly agreed on $s^{\pm}$ [55–59, 128] and is still unsettled in HFSCs [115, 129]; all these compounds share another experimental feature - the spin

resonance mode [120, 130–135].

The spin resonance mode (SRM) is characterised by a divergence in the imaginary part of the dynamical susceptibility, which is observable in INS. Theoretically within an random-phase approximation (RPA) the dynamical spin susceptibility is given by

$$\chi\left(\boldsymbol{Q}, E\right) = \left[\hat{I} - \hat{U}\chi_0\left(\boldsymbol{Q}, E\right)\right]^{-1} \chi_0\left(\boldsymbol{Q}, E\right), \tag{1.3}$$

with unit and interaction[7] matrices $\hat{I}$ and $\hat{U}$ respectively and the bare spin susceptibility $\chi_0\left(\boldsymbol{Q}, E\right)$ [8,56,57,59,116,118]. The emergence of a resonance (divergence) in this term is related to the BCS coherence factor for flipping the spin of a quasiparticle scattered from $\boldsymbol{k}$ to $\boldsymbol{k}+\boldsymbol{Q}$ which is given by

$$F_{coh} = \frac{1}{2}\left(1 - \frac{\Delta\left(\boldsymbol{k}\right)\Delta\left(\boldsymbol{k}+\boldsymbol{Q}\right)}{E\left(\boldsymbol{k}\right)E\left(\boldsymbol{k}+\boldsymbol{Q}\right)}\right) \tag{1.4}$$

on which $\chi_0\left(\boldsymbol{Q}, E\right)$ depends. Thereby, $E(\boldsymbol{k}) = \sqrt{\varepsilon^2(\boldsymbol{k}) + \Delta^2\left(\boldsymbol{k}\right)}$ is the SC quasiparticle energy, $\varepsilon(\boldsymbol{k})$ denotes the quasiparticle dispersion and $\Delta\left(\boldsymbol{k}\right)$ is the SC gap function. If the gap function possesses the same sign at $\Delta(\boldsymbol{k})$ and $\Delta(\boldsymbol{k}+\boldsymbol{Q})$ the coherence factor vanishes and causes a smooth increase of the magnetic response above the threshold value $\Omega_c = \min\left(|\Delta(\boldsymbol{k})| + |\Delta(\boldsymbol{k}+\boldsymbol{Q})|\right)$, i.e. there is no resonance while a shift and accumulation of spectral weight could experimentally still be observable. On the other hand if $\mathrm{sgn}\left(\Delta(\boldsymbol{k})\right) = -\mathrm{sgn}\left(\Delta(\boldsymbol{k}+\boldsymbol{Q})\right)$ there is a divergence in $\chi''(\boldsymbol{Q}, E)$ and the corresponding resonance peak is to be found at E_{SRM}, pushed below Ω_c by an amount which scales with $\hat{U}$ [116]. Consequently, the SRM is deeply related to the pairing symmetry and its exploration provides vital information on the corresponding mechanism. While the *d*-wave gap symmetry in CuSCs [9,127,136] and HFSCs [8,120,137] naturally displays the required sign change for the SRM to appear, the situation is more challenging in FeSCs, due to their multi-band and -orbital Fermi surface. Phase-sensitive measurements showed that the gap symmetry in FeSCs is a *s*-wave [128,138–140], which can only be reconciled with the SRM when the gap function changes its sign on distinct pockets of the Fermi surface connected by $\boldsymbol{Q}$. Accordingly, the SC gap symmetry is called $s^{\pm}$. At the Fermi surface of FeSCs the hole pockets located at the $\boldsymbol{\Gamma}$-point and the electron pockets at the $\boldsymbol{M}$-point fulfil that condition [77, 141–145], c.f. Fig.: 1.4 (a).
Although this points to the potential importance of nesting, and indeed in the parent compounds AFM order is observed at $\boldsymbol{Q}$, magnetic moments are neither fully itinerant nor local, but instead, a hybrid picture holds, c.f. Ref. [146] Chap. 10

[7] note that the interaction leading to $s^{\pm}$ superconductivity is repulsive, while the one leading to s^{++} superconductivity is attractive

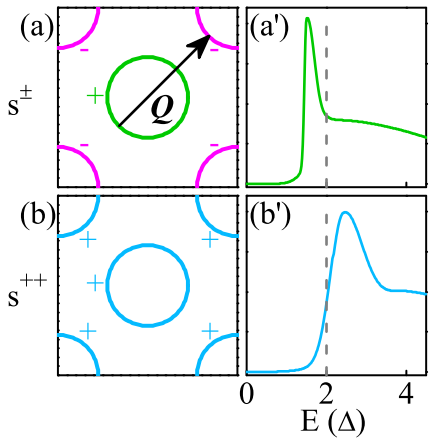

Figure 1.4:
Pairing symmetry and spin resonance mode. **(a)** Typical FS in FeSCs when Δ_{SC} changes sign, $s^{\pm}$-wave. **(a')** corresponding SRM peaking below $2\Delta_{SC}$. **(b)** same as in (a) for s^{++}-wave. **(b')** corresponding SRM peaking above $2\Delta_{SC}$. This sketch is based various reports in the literature [57,66]

and references therein. Moreover, the nesting condition is not crucial for superconductivity to emerge as one of the electron bands e.g. sinks below the Fermi surface in $Ba_{0.1}K_{0.9}Fe_2As_2$ ($T_c \sim 9\,\mathrm{K}$) [147], is badly nested in LiFeAs [148] ($T_c \sim 18\,\mathrm{K}$) or is even absent in $K_{0.8}Fe_{1.7}Se_2$ ($T_c \sim 30\,\mathrm{K}$) [149]. Although there is a broad consensus that superconductivity is driven by paramagnons [53–64] an alternative model based on para-orbitons[8] is proposed [65–70]. In this model, there is no sign change on the hole and electron pockets of the Fermi surface and the corresponding SC gap symmetry is labelled as s^{++}, c.f. Fig.: 1.4 (b). Consequently, there is no divergence in $\chi''(\boldsymbol{Q}, E)$ and thus no SRM in the INS spectra. However, a resonance-like mode can be mimicked as the spectral weight of low-energy excitations is shifted and accumulated above $2\Delta_{SC}$. Therefore, the SRM can function as means to distinguish between both pairing symmetries, i.e. in particular $E_{res} < 2\Delta \Rightarrow s^{\pm}$ indicates $s^{\pm}$ pairing symmetry, while the opposite case $E_{res} > 2\Delta$ points towards s^{++} symmetry, c.f. Fig.: 1.4 (a'), (b').
Recently Korshunov *et al.* [58] elaborated this condition in the case of two unequal SC gaps and attached an extensive list of compounds found in the literature. In short, the overwhelming majority of all listed compounds adhere to this condition and corroborate the $s^{\pm}$ pairing symmetry mediated by paramagnons. Therefore, the SRM includes information on which low-energy paramagnons (spin-fluctuations) can contribute to the pairing, especially when superconductivity emerges from an antiferromagnetically ordered state like in underdoped $Ba(Fe_{1-x}Co_x)_2As_2$, c.f. Chap. 3. Additionally, it also contains information on the paramagnon's polarisation, in particular, when the ordered moments, and thus in a naive picture, the associated fluctuations concomitantly rotate from an alignment within the FeAs-layers to a perpendicular one, as it is the case in $Ba_{1-x}Na_xFe_2As_2$, c.f. Chap. 2. Since the SRM is based on the quasiparticle scattering processes at the Fermi surface, which is predominantly composed of the

[8] in view of BCS theory the para-orbiton is the associated boson to phonon assisted charge fluctuations in the t_{2g} and d_{z^2} orbital occupation to mediate SC

three t_{2g} (d_{xy}, d_{xz} and d_{zy}) orbitals [49, 50, 76, 150], it also retains information on the orbital dependence of the pairing mechanism itself. Notably an orbital and band selective pairing mechanism [151] is proposed to explain the split or double SRM in several FeSCs [61, 152–155]. Thereby the part at low energies is anisotropic in spin space while the one at higher energies is still isotropic [152,153,155], which already indicates the relevance of spin-orbit coupling (SOC). However, the energy at which the isotropic part of the SRM peaks scales with the corresponding T_c like in CuSCs [152, 156–158] yielding

$$\frac{E_{res}}{k_\mathrm{B} T_c} \approx \begin{cases} 5.3 & \text{for CuSCs,} \\ 4.3 & \text{for FeSCs.} \end{cases} \tag{1.5}$$

Until today there is still no overall theory on superconductivity in FeSCs, which includes SOC, orbital selectivity, considers MEC effects, states how SC can emerge from an AFM ordered state, and what happened when the underlying magnetic ordering direction is changed. Accordingly, the study of magnetic excitations, in particular, the SRM continues to contribute vital information to aid our understanding of superconductivity.

2 Spin Reorientation Transitions and Magnetic Excitations in $Ba_{1-x}Na_xFe_2As_2$

Abstract
In iron-based superconductors the lattice degrees of freedom, magnetic order and superconductivity are strongly coupled. This particular interplay is investigated by X-ray, elastic and inelastic neutron scattering in $Ba_{1-x}Na_xFe_2As_2$. Over a broad doping range $0.25 \leq x \leq 0.39$ the magnetic moments undergo a second transition and realign themselves from the ab plane along the c axis, before any magnetic order terminates at $0.4 \leq x$. The spin reorientation documents the importance of spin-orbit coupling in theses materials and defines an altered magnetic ground state from which superconductivity eventually emerges. The intuitive picture of concomitantly rotated low-energy spin fluctuations (paramagnons) to mediate superconductivity is not confirmed as these are equally polarised as in the electron doped compound without a spin reorientation. Consequently, low-energy spin fluctuations are decoupled from the underlying static order which puts further constrains on a band and orbital selective pairing mechanism. Another experimental fingerprint of the superconducting pairing mechanism is the spin resonance mode. In $Ba_{1-x}Na_xFe_2As_2$ this mode is split and, as shown by absolute unit calculation, the intensity of the low-energy part is the recaptured amount of the suppressed static magnetic moment below T_c. This provides a simple explanation of the recently observed double spin resonance modes in various compounds and should be reconsidered in the band and orbital selective pairing mechanism.

Contents

2.1 Spin Reorientation Transitions **12**
2.1.1 Section Introduction 14
2.1.2 Temperature Dependence of Elastic Bragg Scattering . 16
2.1.3 Suppression of Magnetic Intensity Below T_c 20
2.1.4 Polarisation Analysis 22
2.1.5 Profile Analysis of Magnetic Bragg Reflection 24
2.1.6 Temperature Dependence of the Orthorhombic Distortion in $Ba_{0.65}Na_{0.35}Fe_2As_2$ 26
2.1.7 Section Summary 27
2.2 Magnetic Excitations in $Ba_{1-x}Na_xFe_2As_2$ **29**
2.2.1 Section Introduction 29
2.2.2 Results and Analysis 30
2.2.3 Section Summary 47
2.3 Discussion **51**
2.4 Methods **55**
2.4.1 M: Spin Reorientation Transitions 56
2.4.2 M: Magnetic Excitations in $Ba_{1-x}Na_xFe_2As_2$ 57

2.1 Spin Reorientation Transitions

Info

The data presented in this section are already published in Waßer *et al.*., physica status solidi (b), **254**, 1600181 (2017) [159] and partially in Waßer *et al.*., Phys. Rev B, **91**, 060505(R) (2015) [82]. This section is based on these publications.

Section Abstract

Hole doping on the alkaline earth metal side in *122* iron-based superconductors induces a second magnetic phase within but at the end of the o-AFM dome. In this phase, the moments are rotated from their previous alignment within the FeAs-layers towards the c, and thus perpendicular to the layers concomitantly with a reversion of the orthorhombic distortion. Accordingly, this novel magnetic phase is labelled as c-AFM and the properties of a prototypical compound $Ba_{1-x}Na_xFe_2As_2$ with $25\,\% \leq x \leq 40\,\%$ are presented. Increasing the Na doping from 25 % to 39 % reduces T_N from 120 K to 61 K, while the transition temperature for the c-AFM phase T_{reo} remains rather stable between 35 K and 46 K, while any magnetic order vanishes abruptly at $x = 40\,\%$. The second magnetic transition is exclusively attributed to the reorientation and first order in nature, while it is only complete at $x \sim 35\,\%$. Moreover, in the superconducting and AFM coexistence phase, the ordered magnetic moment's suppression increases with T_c. In particular, when both magnetic configurations coexist the c-AFM alignment is stronger suppressed than the o-AFM one, indicating that the former is less compatible with superconductivity than the latter.

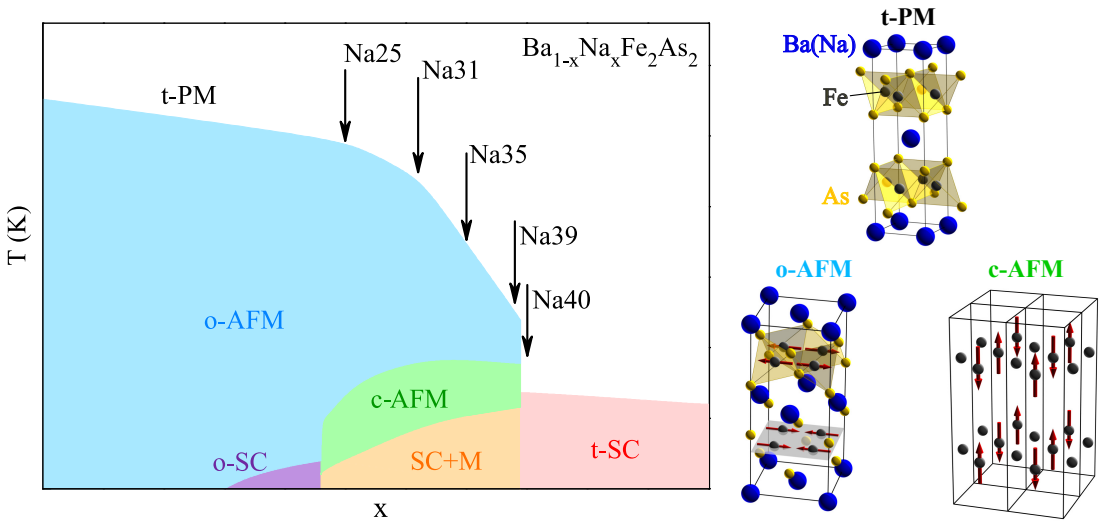

Figure 2.1: Schematic phase diagram of $Ba_{1-x}Na_xFe_2As_2$. $Ba_{1-x}Na_xFe_2As_2$ hosts at least six different phases like *tetragonal paramagnetic* (t-PM), *orthorhombic antiferromagnetic* (o-AFM), *orthorhombic antiferromagnetic and superconducting* (o-SC), a spin reoriented phase with moments along the *c* axis (c-AFM), c-AFM with superconductivity (SC+M) and a purely superconducting tetragonal phase (t-SC). The corresponding crystal and magnetic structure for the t-PM, o-AFM and c-AFM are shown on the right-hand side.

2.1.1 Section Introduction

Doping holes on the *AE* (Alkaline Earth metal) in $AEFe_2As_2$ stabilises a peculiar second magnetic phase within the o-AFM dome [45, 46, 83]. It emerges at intermediate doping levels and is a phase, where the moments reorient from their alignment within the FeAs-layers towards a perpendicular orientation [82]. Consequently this magnetic phase is labelled c-AFM and a schematic phase diagram of $Ba_{1-x}Na_xFe_2As_2$ and the corresponding crystal/magnetic structures are presented in Fig.: 2.1. The spin reorientation is in line with the low-T AFM gap anisotropy of the host compound $BaFe_2As_2$. There pINS experiments showed that it is easier to rotate the spins out of the FeAs-layers than within, counter-intuitive to a layered magnet [78]. A similar spin space anisotropy is reported for the *111* system NaFeAs [80,160], however a spin reorientation has not been observed since it is impossible to hole-dope this system on the Na-site, most likely. In the *1111* FeSC compounds the spin space anisotropy is uncharted territory as it is a chemical non-bested challenge to synthesise large single crystals. However, spin space anisotropy indicates the importance of spin-orbit coupling (SOC) as it is the natural origin to pin magnetic moments along certain crystallographic axes, i.e. here along $[1,1,0]_{\text{tet}}$ (tetragonal notation) or equivalent along $[1,0,0]_{\text{ort}}$ (orthorhombic

notation). A recent theoretical study explores the influence of SOC on the magnetic anisotropy and can reproduce the experimental observations albeit neglected magneto-elastic coupling (MEC) [81].
Due to strong MEC, the spin reorientation leads to a reduction of the orthorhombic phase with C_2 symmetry and thus to a recovery of the tetragonal phase with C_4 symmetry. Since the reorientation can be viewed as a spin-flop, it is necessarily a first-order transition, which allows phase coexistence of both magnetic orders. An early study on $Ba_{1-x}Na_xFe_2As_2$ reported the recovery of C_4 symmetry coexisting with a doping dependent orthorhombic C_2 fraction, reaching up to 40 % [45]. In the related compound $Ba_{1-x}K_xFe_2As_2$, thermal expansion measurements observed a full recovery of C_4 symmetry in the c-AFM[1] phase [46], in contrast to X-ray and neutron diffraction studies on polycrystalline samples where a phase fraction of only $\sim 10\,\%$ is reported [84]. Note, the c-AFM phase in $Ba_{1-x}K_xFe_2As_2$ occupies a much smaller volume in the phase diagram than in $Ba_{1-x}Na_xFe_2As_2$, but it can be expanded under hydrostatic pressure [161, 162]. In a simple hard-ball model of atoms, the smaller ionic radius of Na in comparison to K induces chemical, equivalent to external, pressure and thus enlarges the c-AFM phase.

Single- vs. Double-Q Structure
Although, neutron scattering can unambiguously determine the spin reorientation it cannot distinguish between a single- and a double-$\mathbf{Q}$ structure. In the former, moments simply rotate out of the FeAs-layers, but the overall lattice symmetry is still orthorhombic; while in the latter a superposition of the two ordering vectors $(\pi, 0)$ (horizontal AFM stripes) and $(0, \pi)$ (vertical AFM stripes) is observed, which results in tetragonal lattice symmetry with half of the Fe-sites carrying a doubled magnetic moment while the rest is non-magnetic. The double-$\mathbf{Q}$ structure is compatible with the thermal expansion measurements [46] and has been confirmed by infra-red spectroscopy [163, 164], muon spin rotation [164, 165] and Mößbauer spectroscopy [166]. However, a recent pair distribution function (PDF) analysis indicated that the short-range local symmetry around 20 Å ~ 5 lattice constants, is still orthorhombic while on larger length scales the system is tetragonal [167]. To reconcile this observation with the highly local results from Mößbauer [166] the authors concluded that the orthorhombic regions in the c-AFM phase are fluctuating on time-scales between 10^{-7}s to 10^{-13}s [167]. Since Mößbauer can sense phenomena on time-scales up 10^{-7} s, the overall magnetic/lattice structure appears to be double-$\boldsymbol{Q}$/tetragonal in this technique. On the other side, the deviation from the data for the tetragonal model is only slightly larger than for the orthorhombic one and a phase coexistence of c-AFM and o-AFM regions is

[1] due to their macroscopic measurement the authors labelled this phase C_4 phase, contrary to the notation here. Moreover, the label C_4 for this phase is more widespread than c-AFM in the literature.

not discussed [167]. Here, by using large single crystals of $Ba_{1-x}Na_xFe_2As_2$, it will be shown that the spin reorientation is only complete in the middle of the c-AFM dome and that otherwise a mixture of c-AFM and o-AFM can be found, as consequence of the first order phase transition.

2.1.2 Temperature Dependence of Elastic Bragg Scattering

The structural and magnetic transition temperatures, T_s, T_N and T_{reo}, can be easily identified by neutron scattering. Therefore, the intensity at fixed $\boldsymbol{Q}$-positions was traced as a function of temperature. In particular, since the orthorhombic distortion is expected to be small in the doping range $25\,\% \leq x$, the tetragonal notation is employed meaning the magnetic Bragg peaks are found at (half-integer, half-integer, odd integer) as HKL values. $Ba_{1-x}Na_xFe_2As_2$ samples are referred according to their EDX-determined Na composition, e.g. $Ba_{0.61}Na_{0.39}Fe_2As_2$ is Na39. Figure 2.2 summarises the data at the nuclear Bragg peaks for Na25, Na31, Na35a, Na39 and Na40 in (a)-(e), respectively, while the data for the magnetic Bragg peaks are shown in (a')-(e'). Furthermore, the extracted transition temperatures are listed in Tab.: 2.1. Note that there are two 35 % Na-doped samples labelled as Na35a and Na35b, while the former is used exclusively in this section, the latter is employed for the inelastic studies in Sec. 2.2 due to its bigger mass. Although they should be stoichiometrically identical within EDX error, Na35b displays a slightly higher T_N of 79 K than Na35a as can be seen in Fig.: 2.14(e). However, the (normalised) temperature vs. intensity curves of the $(0.5, 0.5, 1)$ magnetic Bragg peaks fall on top of each other at $T \gtrsim 60\,\mathrm{K}$ and display an identical T_{reo} as well as the intensity suppression below T_c. Since the slope of the T_N-transition line in this region of the phase diagram is steep, c.f. Fig.: 2.1 and Ref. [45], even a very small variation of x will cause this shift of T_N but will leave T_{reo} and T_c unaffected, as the corresponding slopes of the transition lines are gradual to flat. A comparison of the temperature dependence for both samples is given in Fig.: A.1.1 of the appendix.
Identically to $Ba_{1-x}K_xFe_2As_2$ the T_s-T_N-transition line does not split with doping throughout the phase diagram and is always first order in nature [30, 46, 47, 75]. Even small orthorhombic distortions have a strong impact on the nuclear Bragg peaks, as the resulting (twin) domain formation drastically reduces extinction and multiple scattering events. Therefore, the structural transition at T_s can be easily observed as an intensity increase for all studied samples, except for Na40 which shows no structural/magnetic transition down to 3 K[2]. When the system enters the c-AFM phase the magnetic moments rotate out of the FeAs-layers [82] reducing the orthorhombic splitting and hence recovering the extinction and multiple scat-

[2]most likely there is no magnetic order below that temperature, as it would realise a very rare scenario: magnetic order develops deep in the superconducting phase.

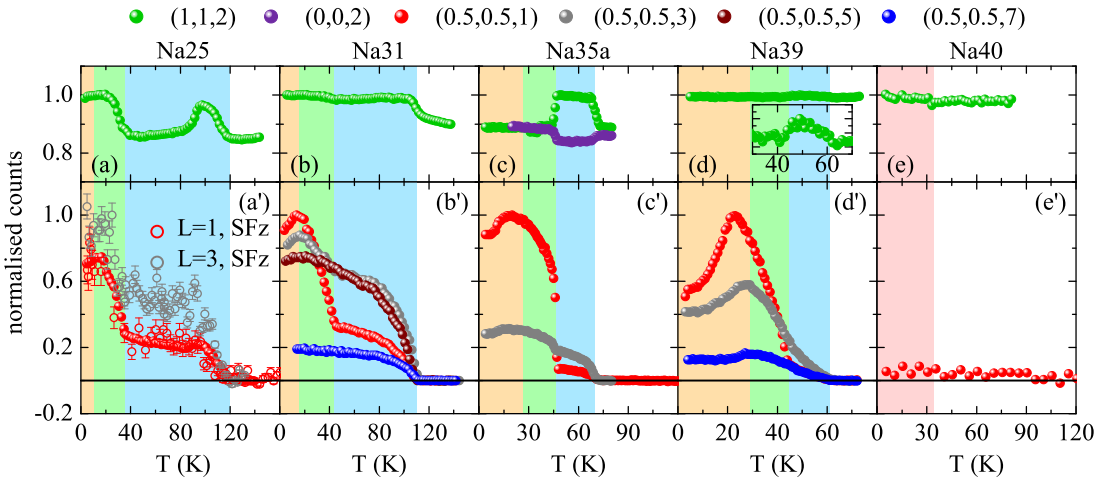

Figure 2.2: Temperature dependence of the nuclear and magnetic Bragg peaks in $Ba_{1-x}Na_xFe_2As_2$. In order to define the two magnetic transition temperatures the nuclear **(a)-(e)** and magnetic **(a')-(e')** Bragg peak intensities were scanned, respectively for Na25, Na31, Na35a, Na39 and Na40. Open symbols in (a') result from a polarised neutron scattering at 4F1 spectrometer and are rescaled. In particular, the spin reorientation transition in Na25 and Na31 is incomplete as the intensity at L = 3 is stronger or only slightly weaker than at L = 1. The coloured areas correspond to the phases defined in Fig.: 2.1 and the presented data are published in [159].

tering events, which ultimately lead to an intensity decrease of the nuclear Bragg peaks. By this reason the nuclear Bragg peak intensity for Na35a and Na39 drops

Table 2.1: Transition temperatures of the $Ba_{1-x}Na_xFe_2As_2$ samples. The structural and magnetic transitions temperatures rely on the data from Fig.: 2.2, while T_c results from magnetisation measurements conducted at the IFW.

Name	x_{EDX} (%)	T_s (K)	T_{reo} (K)	T_c (K)
Na25	25	120	35	10
Na31	31	110	43	$\sim$ 15
Na35a	35	70	46	26
Na35b	35	79	46	26
Na39	39	61	44.5	29
Na40	40	–	–	34

to the continuously extrapolated[3] values of the t-PM phase. For Na25 and Na31 the temperature dependence is a bit more complicated, as the intensity originates from a composite effect of the orthorhombic splitting. On the one hand side, the intensity increases below T_s due to the formation of orthorhombic domains; on the other hand, with decreasing temperature the orthorhombic splitting increases, the fixed $\boldsymbol{Q}$-position is not the centre anymore, and intensity decreases. Clearly, the latter effect overcompensates the former in Na25. When Na25 and Na31 enter the c-AFM phase, the orthorhombicity is reduced due to the spin reorientation, and the peak intensity increases again. This can be reconciled with the behaviour of Na35a and Na39 by looking at the magnetic Bragg peak intensity of Na25/Na31. In Na25 the intensity at $(0.5, 0.5, 3)$ is always higher than at $(0.5, 0.5, 1)$, which clearly demonstrates that the spin reorientation is only realised in a small fraction of the sample. Therefore, the intensity reduction of the orthorhombic splitting is compensated by reducing the orthorhombicity itself, while a residual fraction remains and thus prevents the recovery of extinction and multiple scattering events. Ultimately this is the reason for an intensity increase instead of a decrease at T_{reo}. In Na31 the situation is similar. Here the $(0.5, 0.5, 1)$ magnetic Bragg peak is only marginally more intense than $(0.5, 0.5, 3)$, which demonstrates an incomplete spin reorientation, although the c-AFM volume fraction is larger than in Na25. A complete spin reorientation would render $(0.5, 0.5, 1) \sim 2.7$ times more intense than the $(0.5, 0.5, 3)$. However, the most progressed spin reorientation is observed in Na35a, where only a small fraction of 13 % of the o-AFM phase remains [82]. Measuring the temperature dependence of the magnetic Bragg peaks by neutron scattering cannot resolve the issue whether there is a phase separation of o-AFM and c-AFM or the magnetic moments rotate by an arbitrary angle towards the c direction. The latter scenario seems unlikely as a mixture o-AFM and c-AFM phases were directly observed in powder experiments [45, 84] and by symmetry considerations[4]. A magnetic configuration where the rotated moments point at an intermediate direction corresponds to a lower symmetry as in either the c-AFM and o-AFM phases. Moreover, in $Ba_{1-x}K_xFe_2As_2$ the spin reorientation induces an elongation of the FeAs-tetrahedra [46] similar to a martensitic transition[5]. Again this fact highlights the strength of MEC and is further the natural explanation of the c-AFM and o-AFM phase separation. In a local picture, the FeAs-tetrahedra elongation causes a shear force on the Fe-Fe-planes, which will stabilise the o-AFM phase. This is evidenced by strain experiments on $BaFe_2As_2$ where T_s shifts to higher temperatures [168]. Therefore, this picture helps to understand why the spin reorientation is only complete in the middle of the c-AFM dome, where the

[3] constant extrapolation at $(1, 1, 2)$ and linear at $(0, 0, 2)$

[4] the phase with moments along the c axis cannot be a subgroup of a phase where the moments are aligned within the plane

[5] first order structural transition. Most famous example is the transition in Fe from non-magnetic fcc to magnetic bcc.

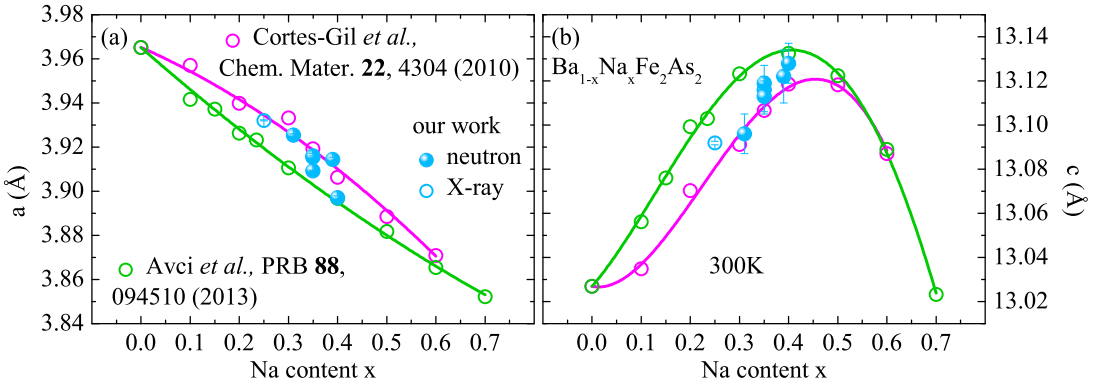

Figure 2.3: Lattice constants of the $Ba_{1-x}Na_xFe_2As_2$ samples investigated in this thesis. Room temperature lattice constants a and c obtained by neutron or X-ray scattering in comparison to the values reported by Avci *et al.* [75] and Cortes-Gil *et al.* [169], in **(a)** and **(b)** respectively. Lines are polynomial fits and serve as guides for the eye, while the data is published in [159].

difference in free energy to the o-AFM phase is largest and hence phase coexistence is suppressed, supposedly. Starting from low Na-doping levels the o-AFM phase is the magnetic ground state and is slowly excelled by the c-AFM phase with increasing Na doping; however, it is stabilised by the induced strain as long as the difference in free energy between both phases is not yet large enough. Towards optimal doping, the free energy gain of magnetic order is reduced, generally. Moreover, the absence of a subgroup relation imposes the spin reorientation to be a first order phase transition, allowing phase coexistence of both magnetic alignments.

Comparison to other Phase diagrams

Today there are three phase diagrams of $Ba_{1-x}Na_xFe_2As_2$ published by three different experimental groups. In an early work, Cortes-Gil *et al.* set-up a rather rough phase diagram based on powder samples without the c-AFM phase [169]; Avci *et al.* refined the phase diagram also by studying powder samples [75], and most recently Wang *et al.* published the most detailed phase diagram with nine different phases based on small single-crystals [47]. The phase diagrams of Avci *et al.* [75] and Wang *et al.* [47] agree in the low doping regime but deviate slightly for higher doping as the magnetic phase is more extended in the work of Wang than in the one of Avci. The c-AFM phase in both cases ends at $x \sim 30\,\%$ while the corresponding phase boundary towards high doping levels coincide with the boundary of the o-AFM phase in Avci *et al.* [45], those transition lines are split in

Wang *et al.*, and the o-AFM phase ends at $x \sim 37.5\,\%$ [47]. Wang *et al.* labelled the reappearing o-AFM phase C_2', however, their many phases cannot be reproduced with the samples used in this thesis. Instead, both magnetic phases are observed up to the critical concentration $39\,\% < x < 40\,\%$ where magnetic order terminates in general. Entering the c-AFM is conceived by crossing a first-order phase transition line, which allows o-AFM/c-AFM phase coexistence below T_{reo}. Moreover, the system rapidly fluctuates between the orthorhombic domains, and the corresponding very small lattice distortion in the slightly underdoped regime could provide an explanation why the reorientation transition could be missed, despite the relatively high resolution of capacitative dilatometry. Additionally, the phase mixture of o-AFM and c-AFM can explain why the overall sample seems to be in C_2' state.
The observed magnetic behaviour resembles the phase diagram of Avci *et al.*, but shifted by $x \sim 10\,\%$, which is also confirmed by comparing the lattice constants at room-temperature of their work [75] with the data from Cortes-Gil *et al.* [169] and the results within this thesis, c.f. Fig.: 2.3. Although Na is highly volatile and the synthesis of comparable large single crystal is chemically challenging, a $10\,\%$ shift of the Na concentration will be clearly resolvable by energy dispersive X-ray (EDX) analysis. The corresponding EDX analysis yielded deviations of $\Delta x \leq 0.01$ [32], which documents the high quality of the samples. Moreover, the magnetic transitions are all sharp[6], and thus a broad distribution of Na over the sample can be excluded. However, a comparison of the various studies is facilitated by looking at the a and c lattice constants in Fig.: 2.3.

2.1.3 Suppression of Magnetic Intensity Below T_c

Below T_c SC and AFM order compete for the same electronic states, which eventually leads to a suppression of the ordered magnetic moment. Consequently, strong MEC reduces the orthorhombic splitting as a feedback effect [31]. When the system undergoes the spin reorientation the T_c values drop by a few Kelvin [46, 47], indicating that the c-AFM phase is less compatible with SC than the o-AFM one. The SC+M phase is investigated further by normalising the magnetic Bragg peak intensity temperature-dependence from Fig.: 2.2 on their corresponding maximum, c.f. Fig.: 2.4. Thereby, a uniform intensity reduction of $\sim 9\,\%$ below T_c in Na35a can be observed, meaning that o-AFM and c-AFM are suppressed equally. Moreover, the intensities at $(0.5, 0.5, 1)$ and $(0.5, 0.5, 3)$ coincide up to T_{reo}, but at elevated temperatures, this simple scaling cannot hold due to the change of the geometric projection of scattering vector $\boldsymbol{Q}$ and magnetic moment $\boldsymbol{\mu}$. However, the fact that both magnetic Bragg peaks scale that perfectly below T_{reo} documents that a single magnetic phase must be realised, in particular, the spin reorienta-

[6] compare with $Sr_{1-x}Na_xFe_2As_2$ powder samples in Taddei *et al.* [83]

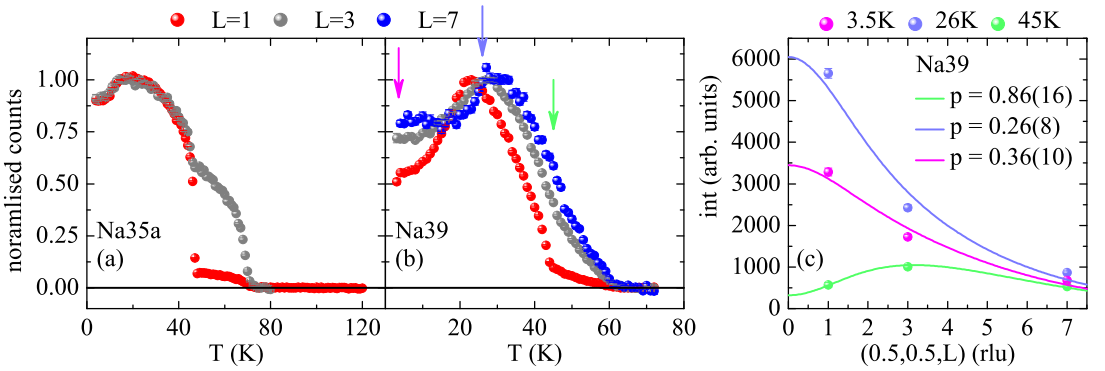

Figure 2.4: Suppression of magnetic Bragg peak intensity in SC state. (a)(b) normalised magnetic Bragg peak intensities at $(0.5, 0.5, 1)$ and $(0.5, 0.5, 3)$ for Na35a, and additionally $(0.5, 0.5, 7)$ for Na39. For Na35a the magnetic moment is uniformly suppressed, while for Na39 the suppression is non-uniform and stronger for the c-AFM phase than for the o-AFM. **(c)** Fit of the L dependence in Na39 according to Eq.: (2.1) in the o-AFM phase at 45 K, in the c-AFM +M phase lightly below T_c at 26 K and deep in the SC phase at 3.5 K. The extracted polarisations document that the c-AFM phase competes stronger with SC than the o-AFM. The data points are published in [159].

tion is complete. The absence of this simple scaling behaviour in Na31 evidences an incomplete spin reorientation and highlights the phase mixture of c-AFM and o-AFM caused by the first order phase transition.
In Na39 the normalised magnetic Bragg peak intensity also does not follow this simple scaling relation, hence documenting an incomplete spin reorientation close to optimal doping. The puzzling observation that the maximum intensity at $(0.5, 0.5, 1)$ is reached at a lower temperature than at $(0.5, 0.5, 3)$ is not an experimental artefact of too rapid cooling and bad thermal coupling, rather it is an intrinsic effect as it has been observed on a different spectrometer with a stabilised temperature. An initial explanation could be that the c-AFM and o-AFM phases display intrinsically different T_c values, which would be in stark contrast to the SQUID measurement, where only one SC transition is observed. Alternatively, the c oriented magnetic moment still increases below T_c, before SC suppresses the magnetic phase. Another fact is the non-uniform reduction in the SC state; while the magnetic Bragg peak at $(0.5, 0.5, 1)$ is reduced by almost 50 % the one at $(0.5, 0.5, 3)$ is reduced by ~ 30 % and the one at $(0.5, 0.5, 7)$ by just ~ 20 %. This non-equal reduction points to a different compatibility of magnetic orders with SC, as the c-AFM phase competes stronger than the o-AFM one. Particularly, the $(0.5, 0.5, 1)$ magnetic Bragg peak is most sensitive for the c-AFM phase, while

the $(0.5, 0.5, 7)$ magnetic Bragg peak is the one for the o-AFM phase. Furthermore, the fraction of c-AFM and o-AFM phases can be extracted by fitting the L dependence with

$$I = S \cdot f^2(\boldsymbol{Q}) \cdot \left((1-p) \cdot \cos^2(\alpha) + p \cdot \sin^2(\alpha)\right), \tag{2.1}$$

where S is a scaling factor, $f(\boldsymbol{Q})$ the Fe^{2+} magnetic form factor, α is the angle between the $[1, 1, 0]$, i.e. o-AFM, ordering direction and scattering vector $\boldsymbol{Q}$ while p denotes the o-AFM fraction. The data points in Fig.: 2.4(c) are corrected for their corresponding Lorentz-factor[7] and at 45 K this fit yields $p = 0.86(16)$ meaning that within error the moments are aligned in the FeAs-layers as it is expected. At 26 K this fit states that the c-AFM phase is realised in three-quarter and the o-AFM phase in one quarter of the sample; documenting again that the spin reorientation is not complete. Since the intensity suppression below T_c is non-uniform the (relative) fraction of the o-AFM phase is increased to 36 %, documenting again it is more compatible with SC than the c-AFM phase, in agreement with [46,47,83]. The same conclusion also holds for Na31 where the incomplete spin reorientation generates a c-AFM/o-AFM phase mixture, whereas the c-AFM phase competes stronger with SC as the $(0.5, 0.5, 1)$ magnetic Bragg peak is the most affected, again.

2.1.4 Polarisation Analysis

The rapid intensity decline with increasing L in Fig.: 2.4 proved a sizable c component of the magnetic moment. However, this analysis also incorporates, if there is, any b[8] component, which drives the value of p towards 0.5 obfuscating the polarisation in the *ac*-plane. Avci *et al.* [45] also observed the spin reorientation but initially misinterpreted it as the condensation of two nematic order parameters leading to a hedgehog-like alignment of the magnetic moments within the FeAs-layers, c.f. Fig.: 2.5(d"). Theoretically, the third option of a magnetic order could be realised below T_{reo} where the moments are arranged in a loop-like fashion [170]. In order to explore the spin reorientation further a polarisation analysis for the $(0.5, 0.5, 1)$ magnetic Bragg peak in Na25 was conducted. The results are identical to the observation in Na35a [82] where the moments reorient in the *ac*-plane exclusively. In Figure 2.5 the frame of reference is shown, while a more detailed explanation is given in the methods section 6.5. This is summarised as: the spin flip (SF) $\boldsymbol{x}$ channel measures the sum of SF $\boldsymbol{y}$ and $\boldsymbol{z}$ and is thus sensitive to components along a, b and c, while SFz is only sensitive for the a and c component and SFy for the b component exclusively. Note: the spin-flip channel only measures the component perpendicular to scattering vector $\boldsymbol{Q}$ and polarisation $\boldsymbol{P}$, while

[7] $= 1/\sin(2\Theta)$ and describes how the Bragg peak is rotated through the Ewald sphere

[8] b is parallel to $[0, 1, 0]_{\text{ort}} = [1, \overline{1}, 0]_{\text{tet}}$

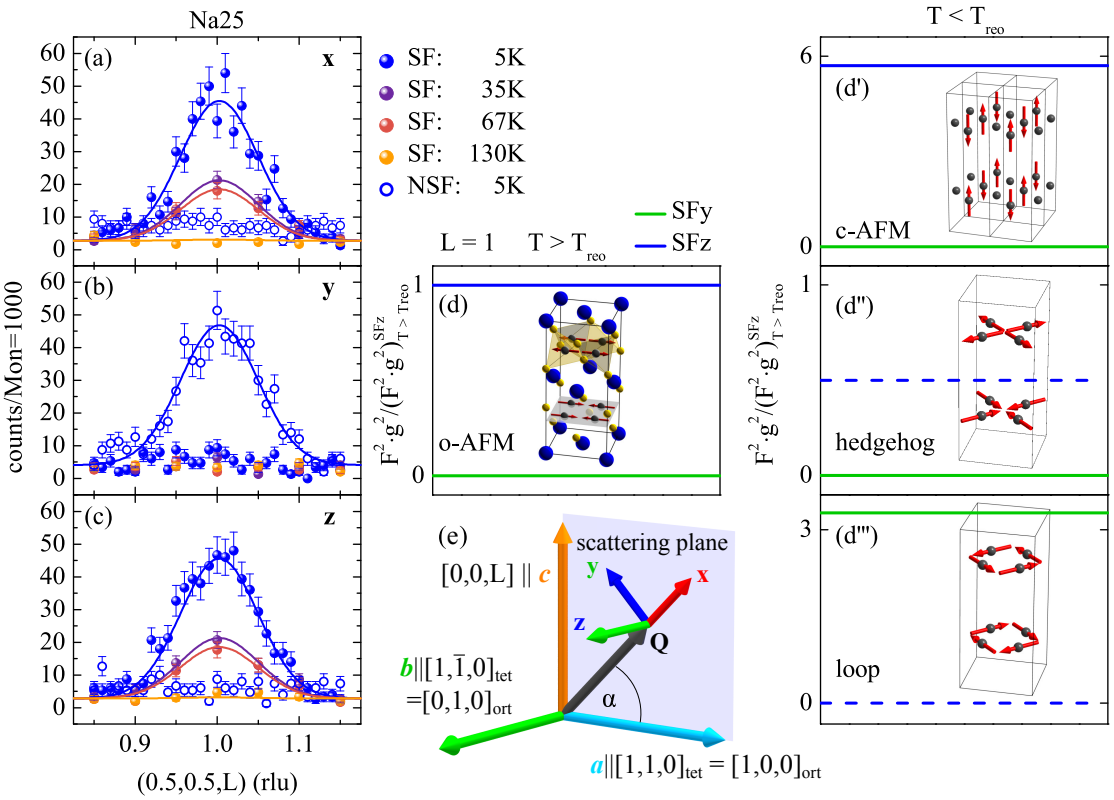

Figure 2.5: Polarisation analysis of the magnetic signal in Na25. Magnetic Bragg peak intensity at L = 1 for various temperatures in the three spin flip (SF) channels x, y and z in **(a)-(c)** respectively. **(d)** At $T > T_{reo}$ in the o-AFM phase magnetic intensity, i.e. the (squared) product of magnetic structure and geometry factor is exclusively in SFz. Below T_{reo} three different magnetic structures are possible. **(d′)** In the c-AFM configuration the geometry factor boots the SFz intensity at L = 1, while SFy remains zero. **(d″)** For the hedgehog configuration SFy remains also zero but the SFz intensity is reduced, while in **(d‴)** the loop alignment yields a non-zero SFy and a vanishing SFz. Both cases are incompatible with the data in (b). **(e)** Frame of reference for the polarisation analysis, same as in Fig.: 6.2. The data points are published in [159].

the non-spin flip (NSF) channel measures the component perpendicular to $\boldsymbol{Q}$ and parallel to $\boldsymbol{P}$.
Down to lowest temperature the SFy channel exhibits only background, while the entire signal can be found in the SFz channel. Therefore, the spins realign in the ac plane exclusively and in total agreement with the observation in Na35a [82]. The missing signal in the SFy channel is consequently found in the NSFy channel,

and the data at 5 K in SFx, SFz and NSFy are fitted globally by a Gaußian. For the other temperatures, the same fitting procedure was conducted for SFx and SFz. Moreover, Fig.: 2.4(d)-(d‴) shows the calculated (squared) magnetic structure factors multiplied by their geometric projection at L = 1 for the SFy and SFz channels, normalised on their values in the o-AFM phase for the c-AFM (d′), the hedgehog (d″) and the loop (d‴) alignment. Only the c-AFM phase can explain the intensity gain at L = 1 below T_{reo}, while SFy remains zero. In the hedgehog arrangement, the SFy channel is also zero, but the intensity at SFz drops to 50 % when a mono-domain sample is assumed. However, the o-AFM phase transition at T_N will cause the development of orthorhombic twins from which one twin will not contribute to the measured scattering intensity, but whose contribution, yielding a factor two, is captured below T_{reo}. Therefore, the hedgehog configuration will have only a marginal effect on the scattering intensity which is incompatible with the data in Fig.: 2.2. On the other hand, a hedgehog magnetic structure is proposed to be realised in electron-doped (Co,Ni) $CaKFe_4As_4$ [171] based on symmetry analysis and NMR data and was later confirmed by neutron scattering [172].
The proposed loop-like magnetic structure would yield an intensity shift from SFz to SFy, but since SFy is always zero and SFz is always finite this structure can clearly be excluded. Concluding, the experimental data is only consistent with the c-AFM phase, whose first-order phase transition generates a c-AFM/o-AFM phase mixture.

2.1.5 Profile Analysis of Magnetic Bragg Reflection

An incommensuration of the magnetic structure has been reported for (Co,Ni) doped Ba122 in a small vicinity of the phase diagram below the critical concentration x_c at which the magnetic dome ends [173–175]. Moreover, the incommensurate order evolves along the b, $(1, \bar{1}, 0)$, i.e. transversal[9] direction and thus reflecting the incommensurate magnetic excitations at high doping levels [160]. On the other hand, for hole-overdoped samples like $Ba_{1-x}K_xFe_2As_2$, a longitudinal incommensuration is observed for higher doping levels [176–178]. However, Wang *et al.* observed a change in the curvature of the o-AFM transition line in the phase diagrams of $Ba_{1-x}Na_xFe_2As_2$ and $Ba_{1-x}K_xFe_2As_2$ and proposed that at this point an incommensurate order like in the electron-doped compounds will develop [47]. Additionally, an incommensurate phase has also been discussed in a theoretical work [179]. Therefore, the magnetic Bragg-peak's width in Na35a was checked on 3T1 spectrometer, via rocking scans over $(0.5, 0.5, 1)$ and $(0.5, 0.5, 3)$ at 50 K above T_{reo} and at 3 K below T_c, c.f. Fig.: 2.6. The first scan is rather a $(0, 0, L)$ scan while the second covers a sizeable $(h, h, 0)$ component as well. A very good

[9] with respect to the o-AFM ordering direction

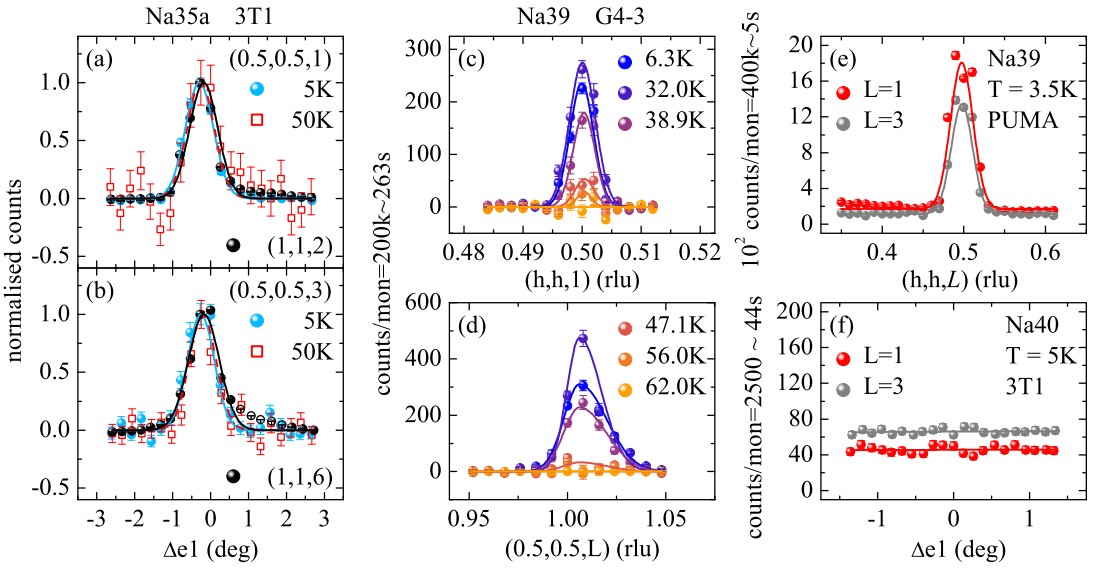

Figure 2.6: Line-shape of the magnetic Bragg peaks in Na35a, Na39 and Na40. **(a) (b)** Rocking scans over the magnetic Bragg peaks at L = 1 and L = 3 at 5 K and 50 K respectively. the instrumental resolution of 3T1 diffractometer is estimated by the width of the nuclear Bragg peaks at $(1, 1, 2)$ and $(1\ 1\ 6)$, which is equal to the magnetic ones and thus no indication on an potential incommensurate ordering is given. **(c) (d)** Scans along the $(h, h, 0)$ and $(0, 0, L)$ direction at various temperatures at the high resolution G4-3 cold TAS for the $(0.5, 0.5, 1)$ magnetic Bragg peak in Na39 displays only commensurate scattering as well; in agreement with the scans at the thermal TAS PUMA in **(e).** **(f)** For Na40 there is no magnetic order present. The data points are published in [159].

estimation of the instrumental resolution can be obtained by conducting rocking scans over nuclear Bragg peaks, here $(1, 1, 2)$ and $(1, 1, 6)$, whose width is only resolution limited. Comparing these scans with the magnetic ones at $(0.5, 0.5, 1)$ and $(0.5, 0.5, 3)$, shows that a potential incommensuration of the magnetic order cannot be resolved within the instrumental resolution, c.f. Fig.: 2.6(a)(b), respectively.

Inspired by the electron-doped counterparts the incommensuration is increasing towards x_c; giving thus reason to conduct $(h, h, 0)$ and $(0, 0, L)$ scans in Na39 at PUMA and G4-3 spectrometer, c.f. Fig.: 2.6(c)-(e). The G4-3 spectrometer was operated with $10'$ collimators, which provided a very high resolution. Thereby, peak widths of $\mathrm{FWHM}_{ab} \sim 0.006\,\text{Å}^{-1}$ and $\mathrm{FWHM}_{c} \sim 0.052\,\text{Å}^{-1}$ were obtained

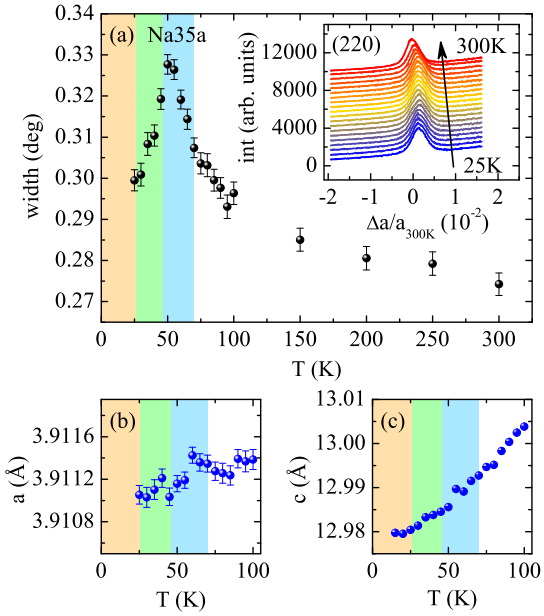

Figure 2.7:
Orthorhombicity in Na35a. **(a)** Temperature dependence of the $(2, 2, 0)$ Bragg-peak width indicating the orthorhombic distortion. The reduction below T_{reo} shows that the C_4 symmetry is the c-AFM phase is going to be restored. In the inset the $(2, 2, 0)$ peak obtained by X-ray diffraction with D5000 diffractometer is displayed. For reasons of clarity each scan is given an offset. **(b)(c)** display the temperature dependence of the a and c lattice constant respectively. The data points are published in [159].

based on Gaußian or asymmetric[10] Gaußian fits in Fig.: 2.6(c)(d), respectively. For (Co,Ni) doped $BaFe_2As_2$ an incommensuration $\delta_{ab} = 0.023\,\text{Å}^{-1}$ was reported [173, 174], which should be clearly resolvable. This is not the case. If there is any incommensuration of the static magnetic signal, it is smaller than the reported FWHM values here. In this context, an incommensurate magnetic ordering in $Sr_{1-x}Na_xFe_2As_2$ could also not be resolved within the experimental resolution, as reported in the literature [83].
Finally, in Na40 no magnetic ordering can be observed down to 5 K, c.f. Fig.: 2.6(f).

2.1.6 Temperature Dependence of the Orthorhombic Distortion in $Ba_{0.65}Na_{0.35}Fe_2As_2$

The iron-iron distance will be affected by the spin reorientation transition due to strong magnetoelastic coupling. In macroscopic measurements like capacitative dilatometry [46, 47] the recovery of C_4 symmetry is observed, while microscopic techniques, like neutron scattering and X-ray/neutron PDF analysis either found a c-AFM/ o-AFM phase mixture [45] or rapidly oscillating orthorhombic domains, whose time-average mimic C_4 symmetry [167]. However, the signature of the spin reorientation will be visible in the line-shape of a X-ray experiment. Therefore, the temperature dependence of the $(2, 2, 0)$ Bragg-peak width is measured by the custom-designed D5000 diffractometer in Bragg-Brentano geometry at Cologne University. X-rays are generated by Cr-tube with $\lambda = 2.289\,760\,\text{Å}$, in order to

[10] the asymmetry results from the analyser crystal and is an experimental artefact

facilitate a higher resolution compared to a Cu-tube. Figure 2.7(a) displays the obtained $(2, 2, 0)$ peak width by Gaußian fitting, while the inset shows the corresponding raw data. There is a remarkable peak-broadening already in the temperature regime between T_s and 300 K, which must be attributed to orthorhombic precursor correlations [73, 180]. Furthermore, the peak strongly broadens at T_s when the orthorhombic order sets in. Below T_{reo} the width decreases again due to the spin reorientation and the associated strong MEC. At 25 K the peak is as broad as at 80 K in the t-PM phase but significantly broader than at room temperature. Since the recorded peaks contain the time-average value of the local structure, no conclusion about rapidly fluctuating orthorhombic domains can be drawn, but the restored peak width is in agreement with the neutron scattering data [82] that only a marginal o-AFM fraction remains in the c-AFM phase. An increasing orthorhombicity from room temperature, i.e. far above T_s, down to T_s can be interpreted as the impact of nematic fluctuations or as a local strain effect [180].
The temperature dependence of the a and c lattice constant is respectively depicted in Fig.: 2.7(b)(c). Despite the relatively high resolution, jumps of the lattice constants at T_s or T_{reo} are not resolvable. Nonetheless, anomalies in the order of 2×10^{-5} relative units have been reported by capacitative dilatometry in (K,Na) doped Ba122 [46, 47]. In particular, there is an elongation at T_{reo} of the c lattice constant [46], which documents the strong MEC in these materials and is consistent with the spin reorientation where the moments align along this axis.

2.1.7 Section Summary

In the studied $Ba_{1-x}Na_xFe_2As_2$ compounds a spin reorientation transition is found at $T_{reo} < T_N$ in the broad range of $0.25 \leq x \leq 0.39$, while any magnetic order is abruptly suppressed at $x = 0.40$. The magnetic moments realign themselves from the FeAs-layers in the ab-plane along the c axis exclusively, and thus hedgehog or loop-like orders can be excluded. Moreover, the reorientation transition temperature T_{reo} itself is rather stable throughout the studied doping regime, ranging between 35 K and 46 K, whereas T_N is strongly reduced from 120 K to 61 K. Presumably, the saving in free energy associated with the c-AFM phase is increasing with doping, while simultaneously the total saving in free energy by magnetic ordering is reduced. Consequently, this explains a decreasing o-AFM and a stable c-AFM transition line, which points to a large volume in configuration space being available for spin fluctuation, and thus for strong paramagnons in order to promote superconductivity.
Furthermore, the spin reorientation is a first-order transition and only complete around $x \sim 0.35$ in the sense that otherwise a mesoscopic c-AFM/ o-AFM phase mixture is observed. When the spins realign, the c lattice parameter discontinuously enlarges due to strong magneto-elastic coupling, hence generating a strain in

the sample which stabilises the o-AFM phase similar to a martensitic transition. Therefore, the magnetic phase mixture must be considered as an intrinsic property of $Ba_{1-x}Na_xFe_2As_2$ as well as in at the *AE*-site hole doped *122* FeSCs in general. Beyond that, the spin reorientation highlights the importance of SOC combined with some lifting of orbital degeneracy in these materials, and in extension in all FeSCs. Additionally, the spin reorientation follows the spin-space anisotropy of $BaFe_2As_2$, as a is the ordering direction and c the one in which the moments can be rotated easiest.
Moreover, the prodigious interplay between SC and AFM order is highlighted towards the end-point of AFM order as the $(0.5, 0.5, 1)$ magnetic Bragg peak intensity is reduced by $\sim 50\,\%$ below T_c. This suppression is not uniform, and c-AFM order competes more severe with SC than o-AFM order does. An enhanced compatibility of an in-FeAs-layer anisotropy is observed another time in $6\,\%$ doped $Ba(Fe_{1-x}Co_x)_2As_2$, c.f. Chap. 3, where low-energy spin excitations are suppressed below T_c along the b direction, although the lattice remains tetragonal.

2.2 Magnetic Excitations in $Ba_{1-x}Na_xFe_2As_2$

Section Abstract
The mediation of superconductivity in iron-based superconductors based on spin fluctuations, or paramagnons, is nowadays broadly accepted. In this regard, the polarisation of these low-energy fluctuations may play a crucial role and is expected to be coupled to the underlying magnetic order. $Ba_{1-x}Na_xFe_2As_2$ in the regime of $0.25 \leq x \leq 0.39$ undergoes two successive magnetic phase transitions, whereas the second transition is a spin reorientation which rotates the ordered moments from the *ab* plane towards the *c* axis. Consequently, superconductivity emerges from a different magnetic state, is mediated by differently polarised low-energy paramagnons as these intuitively follow the rotation of the static moments. Inelastic neutron scattering experiments were performed to investigate the impact of the spin reorientation on the low-energy excitation spectra and its polarisation. For $x = 0.25$ and 0.31, the spin reorientation affects the normal state response only slightly before faint resonance modes emerge in the superconducting state. At $x \geq 0.35$ it becomes apparent that the spin resonance mode in the superconducting state consists of two contributions peaking at E_{SRM-1} and E_{SRM-2}; but while the intensity of SRM-1 strongly increases towards and vanishes beyond the magnetic end-point at = 0.40 in the phase diagram, it increases continuously for SRM-2. Moreover, by absolute unit calculation, it can be shown that the intensity of SRM-1 originates from the suppressed ordered magnetic moment and is the most intense resonance mode observed until today for $x = 0.39$. Furthermore, the polarisation analysis of SRM-1 shows that it is predominately polarised along *c* and partially along *a* which is identical to the electron-doped counterparts where there is no spin reorientation. Therefore the spin reorientation does not change the polarisation of the paramagnons, and the mediation of superconductivity is decoupled from the underlying magnetic order.

2.2.1 Section Introduction

Iron-based superconductors display an intricate interplay between the lattice structure, orbital degrees of freedom, magnetic order and superconductivity [91, 116, 181]. This is best exemplified in the electronic phase diagram of $Ba(Fe_{1-x}Co_x)_2As_2$, c.f. Fig.: 1.2, where there is a regime of microscopic phase coexisting magnetic and superconducting order [39–43]. Moreover, orthorhombic lattice distortion and magnetic order are strongly coupled and become both reverted when the latter competes with SC for the same electronic states [31,182]. In that particular regime of the phase diagram, SC emerges from a state where the orthorhombic distortion reconstructs and orbitally polarises the Fermi surface while magnetic order gaps parts of it [48–50, 76, 183]. Consequently, the spin resonance mode (SRM) as the fingerprint of the SC pairing mechanism will be affected thereof. Especially, when

the magnetic gap is larger than twice the SC one, as it is the case for the longitudinal gap in $Ba(Fe_{0.955}Co_{0.045})_2As_2$ (BaCo45), the associated SRM appears only in the two remaining transversal directions and thus anisotropic, Ref. [153] and Chap. 3. This means that longitudinal low-energy spin fluctuation cannot contribute to the pairing, which may explain the lower T_c values on the underdoped site of the phase diagram. Furthermore, the two transversal contributions peak at different energies, whereby the mode polarised along b peaks at a higher energy than the one polarised along c, which is perpendicular to the FeAs-layers [153]. In this context, c polarised low-energy excitations were reported for many FeSCs like $NaFe_{1-x}Co_xAs$ [184], FeSe [185] and overdoped $Ba_{1-x}K_xFe_2As_2$ [186, 187], hence indicating their importance for SC to be realised. Since the SC pairing interaction is mediated by paramagnons, these should be coupled to the magnetic ordering direction, in a naive view.
The emergence of superconductivity in hole underdoped[11] compounds of the *122* family puts this simple view to a test as it is formed from the o-AFM as well as the c-AFM phase. Tracing the SC dome from its onset in the o-AFM phase toward optimal doping, T_c monotonically increases except for a marginal discontinuous reduction at the border which delineates the o-SC from the SC+M phase [46, 47]. Moreover, the T_c values in these compounds even exceed those in the electron doped counterparts [31, 35, 46, 47, 83, 188]. For example in Na35 where the spin reorientation is (almost) complete the corresponding T_c value is higher than in $Ba(Fe_{0.94}Co_{0.06})_2As_2$ (BaCo60) which is optimally Co-doped. Apparently, the spin reorientation associated with a reconstruction of the reconstructed Fermi surface while gapping further, additional or new parts of it, does not impede the emergence of SC. Additionally, the (possible) change of the low-energy paramagnon's polarisation mediates the pairing interaction equally well if not better. As a consequence, the SRM must also change its polarisation, and since it is the fingerprint of the pairing mechanism, the associated inter and intra-orbital scattering rates would be altered as well. Inelastic neutron scattering studies on $Ba_{1-x}Na_xFe_2As_2$, covering a broad doping range from $0.25 \leq x \leq 0.40$, were conducted to probe the impact of the spin reorientation on the excitation spectra.

2.2.2 Results and Analysis

Magnetic excitations in $Ba_{1-x}Na_xFe_2As_2$ are investigated by several E-scans, which are shown first. Additionally, $\boldsymbol{Q}$-scans were performed as a consistency check and to explore the corresponding (h,h)-width. In the second step, the L dispersion of the SRM is traced, as E_{SRM} at odd L peaks at a lower energy as the one at even L. Third, the polarisation of the SRMs at 4 meV and 10 meV in Na39 are probed by means of pINS. Fourth, the presented spectra at fixed temperatures are connected

[11] at the AE site

by tracing the temperature evolution of excitations at specific energies. Finally, all obtained information is summarised in a phenomenological model which allows comparing the gained spectral weight in the SC state to the intensity loss of the static, ordered magnetic moment.

The spin excitation spectra for Na35b, Na39 and Na40 were examined by INS in all phases given by the corresponding phase diagram in Fig.: 2.1. For consistency two symmetry equivalent positions $\boldsymbol{Q}_{AFM,1} = (0.5, 0.5, 1)$ and $\boldsymbol{Q}_{AFM,3} = (0.5, 0.5, 3)$ were probed by a series of E-scans in the SC state and at least once in the NS. In order to facilitate a direct comparison of the scattering intensities these were transformed to an absolute scale by normalising on phonon[12] scattering which, however, still contains the instrumental resolution and the geometry factor $g(\boldsymbol{Q})$. The normalisation process itself was conducted by Reslib, a Matlab routine, which estimates the instrumental resolution within the Cooper-Nathans approximation [189–191]. Moreover, it convolutes the resolution with a model for $\chi''(\boldsymbol{Q}, E)$ and fits it to the observed intensities, for details see Sec. 6.4. Furthermore, the background was estimated appropriately away from $\boldsymbol{Q}_{AFM}$, subtracted from the spectra which were subsequently corrected for the Bose factor and higher order contaminations in the monitor. Eventually, the results are depicted in Fig.: 2.8. The spectra in the superconducting state at L = 1 and 3 for Na35b, Na39 and Na40 are shown in Fig.: 2.8 (a)-(f). Remarkably, the SRM is split into two parts, one peaking at $E_{SRM-1} \approx 4\,\text{meV}$ the other at $E_{SRM-2} \approx 10\,\text{meV}$. Although the doping range is quite narrow $0.35 \leq x \leq 0.4$ SRM-1 displays a dramatic evolution; starting from a notable feature in Na35b over to the dominating one in Na39 and finishing as a less significant shoulder in Na40. Keeping the phase diagram in mind, the intensity of this mode massively increases towards the magnetic end-point and thus displays an intimate relation to static AFM order. The shape of the SRM in Na39 resembles the one in $NaFe_{0.985}Co_{0.015}As$ [192] since both display an intensity ratio between SRM-1 and SRM-2 of 2:1. However, the doping evolution of SRM-1 in $NaFe_{0.985}Co_{0.015}As$ is in opposition to the one in $Ba_{1-x}Na_xFe_2As_2$ as its intensity is continuously suppressed and vanishes when static AFM order terminates in the associated phase diagram [152]. On the other hand, the doping evolution of SRM-2 is identical in both compounds where its intensity increases towards optimal doping [152]. Since the split SRM in $NaFe_{1-x}Co_xAs$ can be explained by an orbital selective pairing mechanism with different intra- (d_{zy}-d_{zy}) and inter-orbital (d_{zy}-d_{xy}/d_{xz}) scattering rates [151, 193] a similar mechanism must be at play in $Ba_{1-x}Na_xFe_2As_2$ as well. Furthermore, the identical behaviour of SRM-2 in $NaFe_{1-x}Co_xAs$ and $Ba_{1-x}Na_xFe_2As_2$ indicates that it resides on the same orbitals. Split SRMs in $Ba(Fe_{1-x}Co_x)_2As_2$ [47, 153, 155], $NaFe_{1-x}Co_xAs$ [152, 192]

[12] the corresponding phonons and the resulting fit vie Reslib are given in Fig.: A.2.4(a)(b)(c) for Na35b, Na39 and Na40, respectively

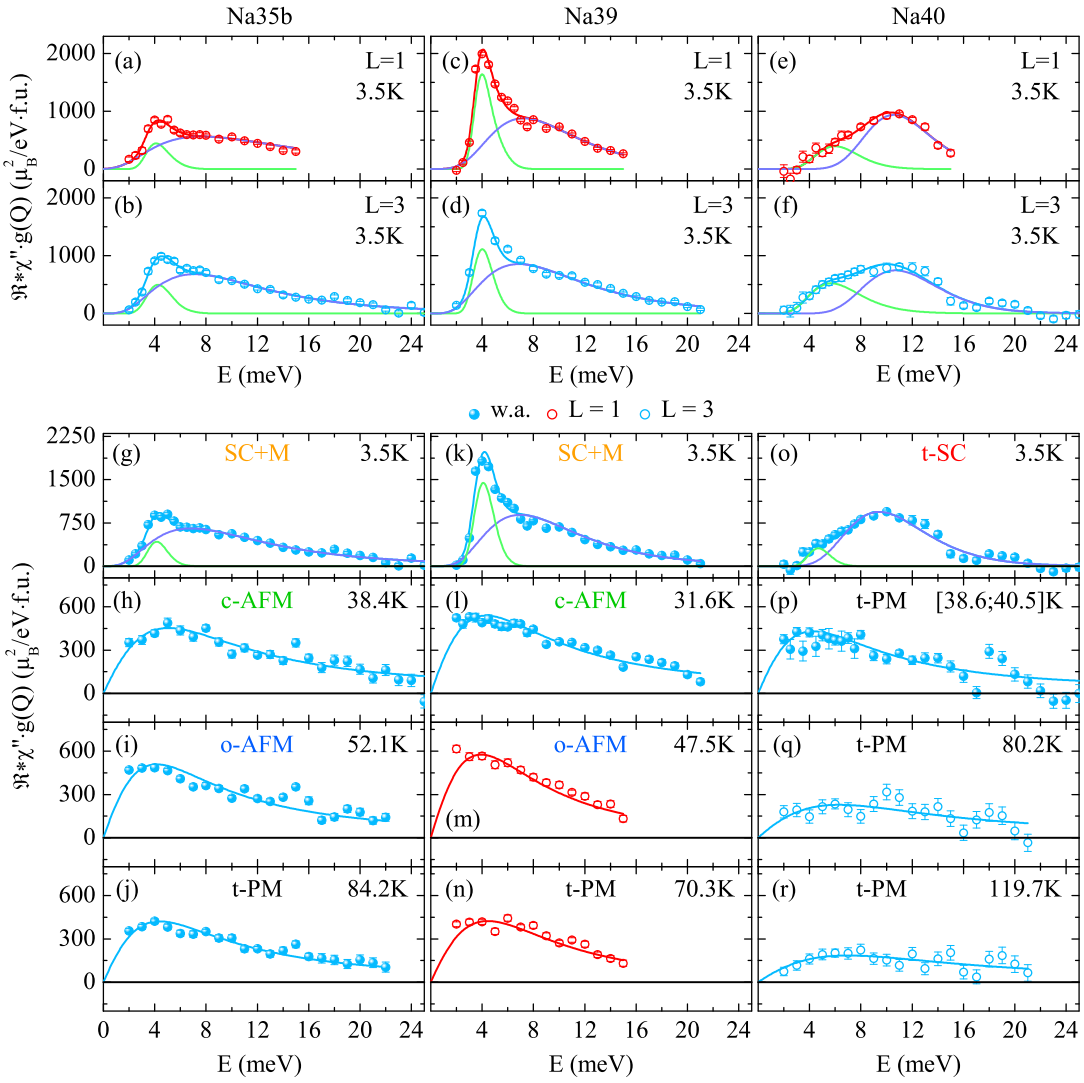

Figure 2.8: Excitation spectra for Na35b, Na39 and Na40 in their various phases and the corresponding Reslib fits based on a phenomenological model. **(a)-(f)** The SC state at $\boldsymbol{Q}$ = (0.5,0.5,L) with L = 1 and 3 displays a split SRM for Na35b, Na39 and Na40, respectively. Two log-normal functions provide a phenomenological model, whereas the low-energy mode, SRM-1, increases in intensity towards the AFM end-point and vanishes beyond. Consequently, SRM-1 in Na39 is the most intense SRM ever measured so far. **(g)-(r)** Summary of all excitation spectra in the SC and normal state, while data points at L = 1 and 3 were weighted averaged (w.a.), if available. The normal state, i.e. the c-AFM, o-AFM and t-PM phase, is always described by a single relaxor. Data points in (p) are the weighted average of two spectra taken at slightly different temperatures, 38.6 K and 40.5 K.

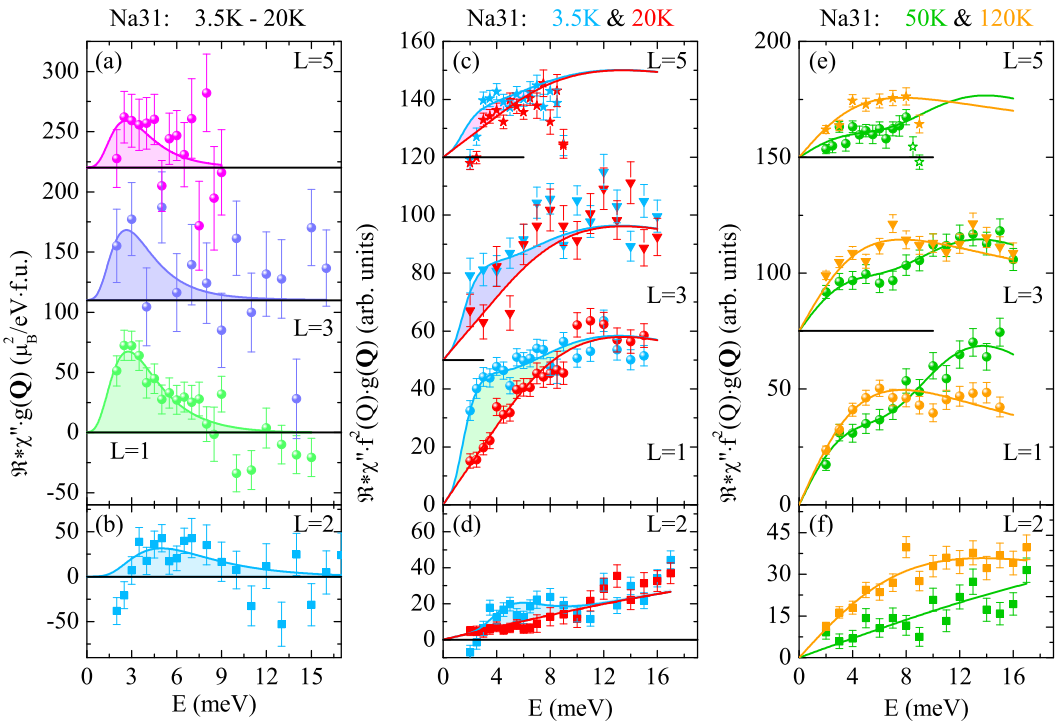

Figure 2.9: Excitation spectra of Na31. **(a)** The intensity difference of $\chi''(\boldsymbol{Q}, E)$ at 3.5 K and 20 K for L = 1, 3 and 5 defines the SRM, which is modelled by a log-normal function, fitted with the RESLIB routine and converted to an absolute scale. An offset of respectively 110 $\mu_B^2/\text{eV}\cdot\text{f.u.}$ is introduced for clarity. **(b)** Same as in (a) for L = 2. **(c)** Excitation spectra at 3.5 K and 20 K at $\boldsymbol{Q}$ = (0.5,0.5L) with L = 1, 3 and 5. The lines correspond to a relaxor plus log-normal function fit with global parameters, the SRM is added for $\chi''(\boldsymbol{Q}, E)$ at 3.5 K, and serve as guides for the eye. Again an offset is introduced for sake of clarity. **(d)** Same as in (c) for L = 2. **(e)** The excitation spectrum at 50 K is described in the same fashion as in (c), while the one at 120 K is fitted only by a single relaxor. In both cases serve the lines as guides to the eye. **(f)** Same as in (e) for L = 2.

and $Ba_{1-x}Na_xFe_2As_2$ bear one commonality: they are most pronounced in the underdoped regime where static AFM order reconstructs the Fermi surface and gaps parts of it. An extreme case is BaCo45 where the SRM is fully anisotropic, c.f. Chap. 3. By ARPES studies it was shown that the gapped density of states (DOS) at the Fermi surface by AFM order is orbital-dependent [76] and thus, in view of BCS theory, are the associated gaps Δ_{SC}, i.e. $\Delta_{xy} \neq \Delta_{yz} \neq \Delta_{xz}$. In oppos-

ite to the Co and thus electron-doped compounds $Ba_{1-x}Na_xFe_2As_2$ undergoes a spin reorientation which will re-reconstruct the Fermi surface, consequently alters the DOS and thus the intra-and inter-orbital scattering rates. This may provide an explanation for the opposite doping dependence of SRM-1. For the further analysis of the spin excitation spectra the data at L = 1 and 3 in Fig.: 2.8 (a)-(f) are weighted averaged and shown in (g), (k) and (o) for Na35b, Na39 and Na40 respectively. If available also the spectra in the normal state were weighted averaged and given in (h)-(j) for Na35b, in (l)-(n) for Na39 and in (p)-(r) for Na40, respectively. All spectra were transformed on an absolute scale, whereby the phenomenological model for the SC state consists of two log-normal functions and the normal state is described by single relaxors. Details for both models are listed in Sec. 2.4.2.
The normal state responses, i.e. in the t-PM, o-AFM and c-AFM phases, display only subtle changes in their amplitude and damping constants Γ, but otherwise, show no impact of the various phase transitions. Only for Na40 the NS intensity is more rapidly suppressed with increasing temperature than in Na35b and Na39, but compared at a temperature slightly above T_c their intensities are almost the same, c.f. Fig.: 2.8 (h), (l) and (p), respectively.

The remarkable doping evolution of the SRM between $0.35 \leq x \leq 0.40$ is extended further towards lower Na-doping concentrations, by exploring the spin excitations in Na31 and Na25 respectively. For Na31 the difference spectra $\chi''(3.5\,\mathrm{K}) - \chi''(20\,\mathrm{K})$ at L = 1, 3 and 5 display a SRM, which can be modelled by a single log-normal function within the Reslib routine, c.f. Fig.: 2.9(a). Whether this is the correct line-shape or just the envelope of two separate modes with distinct polarisation can only be differentiated by pINS. Like in underdoped $Ba(Fe_{1-x}Co_x)_2As_2$ un-polarised neutrons observed a single SRM [194], which could later be correctly resolved as two separate lines with different polarisations, c.f. Ref. [153] and Chap. 3. In Na31 the single SRM fit yielded an $E_{SRM} = 2.8(3)\,\mathrm{meV}$, which is one of the lowest value reported until today. Additionally, the same difference spectra was obtained at the BZ boundary at L = 2, where the fit with the same model yields a $E_{SRM-even} = 5.4(7)\,\mathrm{meV}$. This documents the L dispersion of the SRM and will be discussed later.
Comparing the resonance intensities shows that the SRM in Na31 is ten to 20 times weaker than those in Na35b, Na39 and Na40 although the corresponding T_c is only two to three times less. This massive and non-monotonic reduction of the SRM's intensity and T_c indicates that the magnetic phase dominates and only a few states are available for SC. As a consequence, $\chi''(\boldsymbol{Q}, E)$ at 3.5 K and 20 K in Fig.: 2.9(c)(d) are globally described, while an extra log-normal function is added in the SC spectra to account for the SRM. The underlying model for the magnetic states are purely phenomenological and consist of a single relaxor and a log-normal to serve as guides for the eye. In this way, the spectra at 50 K for odd

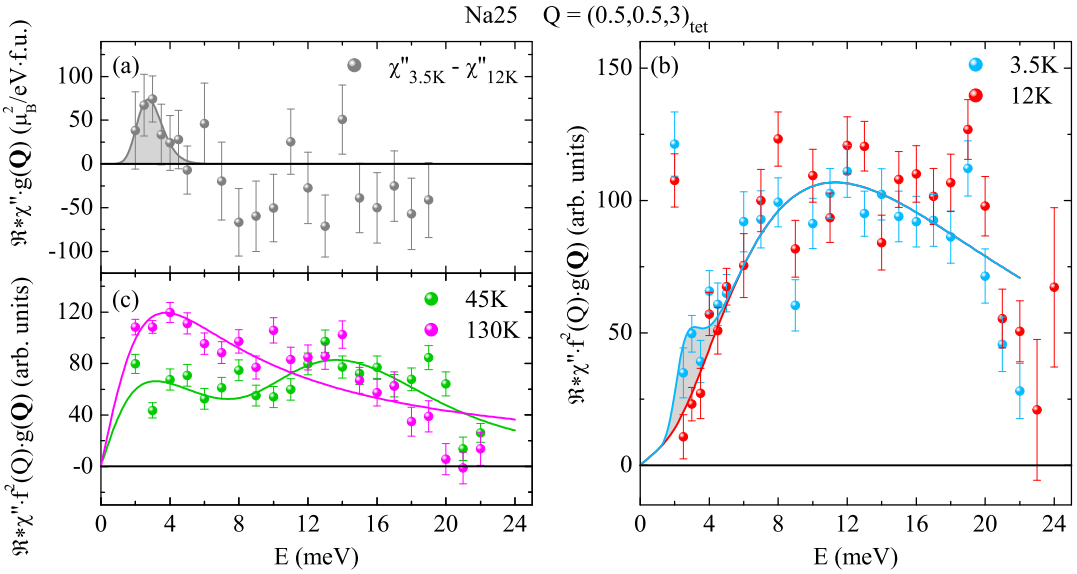

Figure 2.10: Excitation spectra of Na25 at $\boldsymbol{Q}$ = (0.5,0.5,3). **(a)** The intensity difference of $\chi''(\boldsymbol{Q}, E)$ at 3.5 K and 12 K defines the SRM, which is modelled by a log-normal function, fitted with the RESLIB routine and converted to an absolute scale. **(b)** Excitation spectra at 3.5 K and 12 K. The lines correspond to a relaxor plus log-normal function fit with global parameters, the SRM is added for $\chi''(\boldsymbol{Q}, E)$ at 3.5 K, and serve as guides for the eye. **(c)** The excitation spectrum at 45 K is described in the same fashion as in (b), while the one at 130 K is fitted only by a single relaxor. In both cases serve the lines as guides to the eye.

and even L in Fig.: 2.9(e)(f) are described respectively, while those at 130 K are given by a single relaxor only.
For Na25 with $x = 0.25$ the corresponding data are presented in Fig.: 2.10 and identically described as for Na31. Again, the difference spectrum $\chi''(3.5\,\mathrm{K}) - \chi''(12\,\mathrm{K})$ reveal a very faint SRM, whose existence can best be visualised by the corresponding $\boldsymbol{Q}$-scan Fig.: 2.11(n). Furthermore, the SRM intensity can be transformed on an absolute scale (which still contains the instrumental resolution) by the RESLIB routine, whereas $\chi''(\boldsymbol{Q}, E)$ is modelled by a log-normal function, again. Similar to Na31 the obtained intensity does not scale monotonically with the reduction of T_c. Once more, $\chi''(\boldsymbol{Q}, E)$ at 3.5 K and 12 K are globally and phenomenologically described by a single relaxor and a log-normal function, while an additional log-normal is added to account for the SRM in the SC state, c.f Fig.: 2.10(b). In the same fashion, the spectrum in Fig.: 2.10(c) at 45 K in the o-AFM phase is described, whereas the one at 130 K in the t-PM phase is given

by a single relaxor only.
For both compounds, Na25 and Na31, there is a discernible shoulder at low-energies in the excitation spectrum above T_{reo}, i.e. in the o-AFM phase. This feature is not recognisable in the c-AFM phase, which indicates that the spin reorientation redistributes some spectral weight. In this view, recent Raman studies on the related compound $Sr_{1-x}Na_xFe_2As_2$ with x $\sim$ 0.34 suggested an additional gap opening associated with the spin reorientation, however at much higher $260\,\mathrm{cm}^{-1} \approx 32\,\mathrm{meV}$ [195]. Most likely, the reported electronic gap opening corresponds to a two-magnon process, whereat in INS the gap would be observable at $\sim 16\,\mathrm{meV}$. Whether there is such an additional gap opening in the presented spectra for $Ba_{1-x}Na_xFe_2As_2$ cannot be deduced without ambiguity.

In order to confirm the observed signal and to explore the associated (h,h) width, or the a width in orthorhombic notation, several $\boldsymbol{Q}$-scans at selected energies were conducted and are presented in Fig.: 2.11. For Na35b this includes $\boldsymbol{Q}$-scans at L = 3 and 4 meV, 8 meV and 12 meV (a)(b)(c) for the SC+M phase at 3.5 K, the c-AFM phase at 38.4 K and in the t-PM one at 84.2 K, respectively. In the case of Na39 the scans were conducted at L = 1 at 4 meV, 7 meV and 11 meV (d)(e)(f) in all phases of the corresponding phase diagram. For Na40, $\boldsymbol{Q}$-scans at 2 meV and 11 meV were performed below T_c at 3.5 K and above it at 38.6 K, c.f. (g)(i). Additionally, $\boldsymbol{Q}$-scans at 6 meV at various temperatures were done (h), while the fit values of the amplitudes are added in Fig.: 2.14(l). Furthermore, $\boldsymbol{Q}$-scans at L = 1 and 3 meV in Na31 in the SC+M, c-AFM and o-AFM phase are shown in (m). The same is done for Na25 at 3 meV (n) and 8 meV (o).
All presented scans were fitted by Gaußians on a constant to quadratic background, while the obtained widths are summarised in (j) (k) (l) for Na35b, Na39 and Na40, respectively. Low-energy excitations at 3 meV or 4 meV for $0.25 \leq x \leq 0.39$ tend to sharpen below T_c as it is also observed in CuSCs [196, 197] and $Ba_{1-x}K_xFe_2As_2$ [198]. Theoretically, this effect is simply explained by the SC gap opening which enhances the quasiparticle lifetime due to a reduced inter-/intra-band scattering rate [199, 200]. On the other hand, such a behaviour is not observed for Na40 at 6 meV, where the obtained peak widths remain rather constant for all probed temperatures within error bars. In regard to the absolute unit calculation, the Reslib routine requires a model, which defines the (H,K) dependence. Consequently, each $\boldsymbol{Q}$-scan of the samples Na35b, Na39 and Na40 were fitted accordingly by assuming a Gaußian line shape. For simplicity, the energy and temperature dependence of the peak width will be ignored, and the obtained values are averaged to a global value of $w_{HK} = 0.023\,\mathrm{rlu}$. In the subsequent analysis, it is assumed that w_{HK} is isotropic in the (H,K)-plane.

The L dispersion of the SRM is explored by investigating the difference spectra between SC and NS state at odd (BZ centre) and even (BZ boundary) L values,

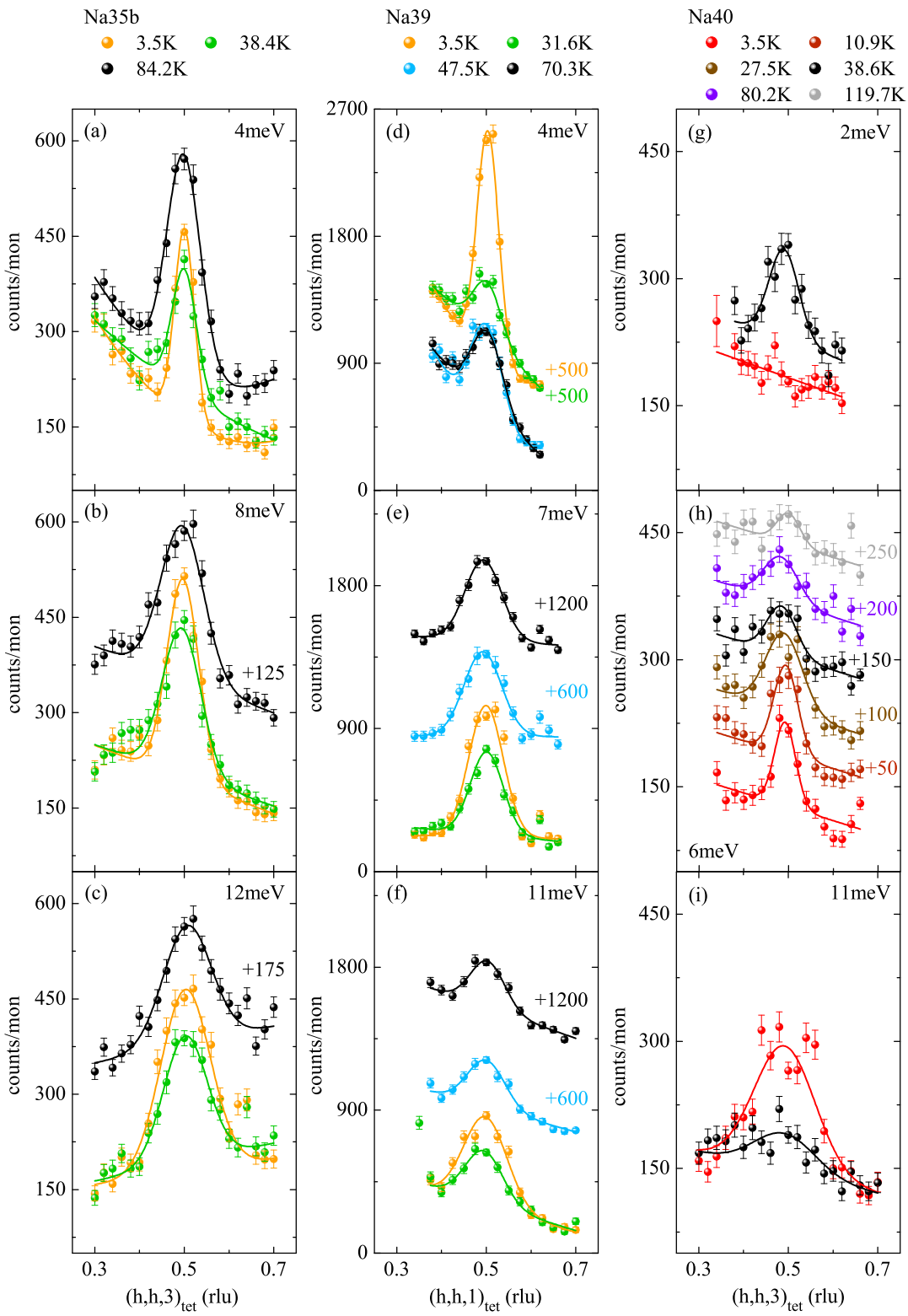
Na35b
3.5K
38.4K
84.2K
Na39
3.5K
31.6K
47.5K
70.3K
Na40
3.5K
10.9K
27.5K
38.6K
80.2K
119.7K
(a)
4meV
(b)
8meV
+125
(c)
12meV
+175
(d)
4meV
+500
+500
(e)
7meV
+1200
+600
(f)
11meV
+1200
+600
(g)
2meV
(h)
+250
+200
+150
+100
+50
6meV
(i)
11meV
counts/mon
(h,h,3)tet (rlu)
(h,h,1)tet (rlu)

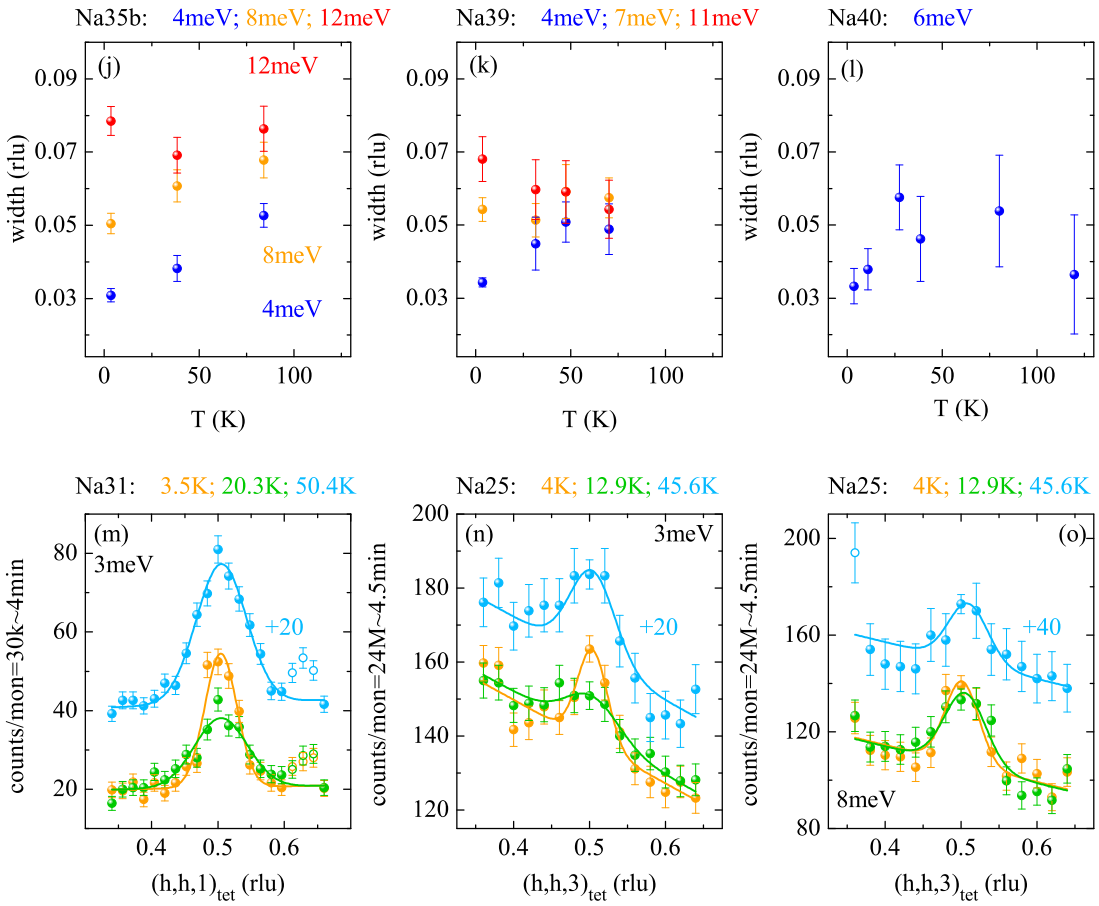

Figure 2.11: *Q*-scans along the (h,h) direction at various temperatures for Na25, Na31, Na35b, Na39 and Na40. (a)-(c) ***Q***-scans in the SC+M, c-AFM and t-PM phase at 4 meV, 8 meV and 12 meV for Na35b. **(d)-(f)** Same as in (a)-(c) for Na39 in all its phases at 4 meV, 7 meV and 11 meV. **(g)-(i)** Same as in (a)-(c) for Na40 in all its phases at 2 meV, 6 meV and 11 meV. The scan at 6 meV is conducted at additionally temperatures, in the t-SC as well as in the t-PM phase. All lines are Gaußian fits to the data on a linear or quadratic background. The obtained amplitudes values in (h) were added in the temperature dependence in Fig.: 2.14(l). **(j)-(l)** Summary of the obtained fit values for the peak widths as a function of temperature. Low-energy excitations, i.e. at 4 meV seems to sharpen below T_c. **(m)** For Na31 the ***Q***-scan at 3 meV also displays a sharpening and increase in amplitude below T_c. **(n)(o)** Same as in (m) for Na25 at 3 meV and 8 meV, while the sharpening with a slight increase of the amplitude can be observed for the former energy, excitations are unaffected by SC in the latter. Note that some scans are given an offset for clarity.

which are shown for Na35b, Na39 and Na40 in Fig.: 2.12(a)(b)(c), respectively. A comparison of the (raw) data is facilitated by correcting them for the corresponding Fe^{2+} magnetic form factor and normalising on Φ_{scale}[13] obtained from the absolute unit transformation process. While SRM-2 displays a weakly upward bending dispersion with no intensity loss, SRM-1 is absent at the BZ boundary. Accordingly, SRM-1 is a three-dimensional excitation in opposite to SRM-2 which is only weakly 3D. Moreover, the dispersion of SRM-1 is traced further by measuring at intermediate L values, i.e. at $1 \leq \mathrm{L} \leq 2$ for Na39 in Fig.: 2.12(d) and at $0 \leq \mathrm{L} \leq 1$ for Na35b in Fig.: 2.12(e) while the resulting E_{SRM-1} (L) values are summarised in Fig.: 2.12(f). The dispersion of the split SRM is modelled by

$$E_{Res-j}(L) = E_{Res-j}^{BZC} + 3.23(13) \cdot \sqrt{\cos^2\left(\pi \frac{L}{2}\right)}, \tag{2.2}$$

where the bandwidth $B_W = 3.23(13)\,\mathrm{meV}$ is a global fit parameter, E_{res-j} are a common for Na35b and Na39 but individual for Na40. Note that line colour of E_{SRM-1} (L) mimics its intensity variation between BZ centre (BZC) and boundary and is given by Eq.: (2.9).
However, the L dispersion of the SRM display the residual interlayer spin correlations although the associated magnetic coupling constant J_c is the smallest one in the parent compound [79, 201]. Intriguingly, the bandwidths in BaCo60 with $B_W \sim 2.8\,\mathrm{meV}$ and Na(31, 35b, 39, 40) with $3.23\,\mathrm{meV}$ are similar and agree both to an universal plot presented in Ref. [202]. In this plot, there is a linear relationship of $B_W/k_\mathrm{B}T$ and x/x_m, whereas x_m denotes the end-point of AFM order in the phase diagram. With increasing x the bandwidth decreases and is expected to have vanished when x_m is exceeded by $\sim 40\,\%$ [202]. Consequently, three-dimensional AFM correlations extend far beyond the critical end-point and thus support the view that SC in FeSCs is a $s^{\pm}$-wave mediated by paramagnons. On the other hand, if the relation $E_{res}/2\Delta_{SC} \approx 0.64$ [157] also holds for the L dependence then Δ_{SC} should increase towards the BZ boundary. However, ARPES data treating this issue is only scarcely available, but in $Ba_{0.6}K_{0.4}Fe_2As_2$, the closely related compound to Na40, such an experiment was conducted, and the opposite dependency was reported [203]. While the gap is constant on the electron pocket (γ, δ-band at the $\boldsymbol{M}$-point) it varies on the hole-pocket (α-band) and displays a maximum of 12 meV at the $\boldsymbol{\Gamma}$-point but a minimum of 9 meV at the $\boldsymbol{Z}$-point, BZ boundary. This would imply a downward bending dispersion, which is at odds with the corresponding L independent SRM [198] and in extent with Na40. Apparently this scaling relation $E_{res}/2\Delta_{SC} \approx 0.64$ [157] is too simple to link the dispersions of the SRM and Δ_{SC}.

[13] the corresponding values are listed in Tab.: A.2.1

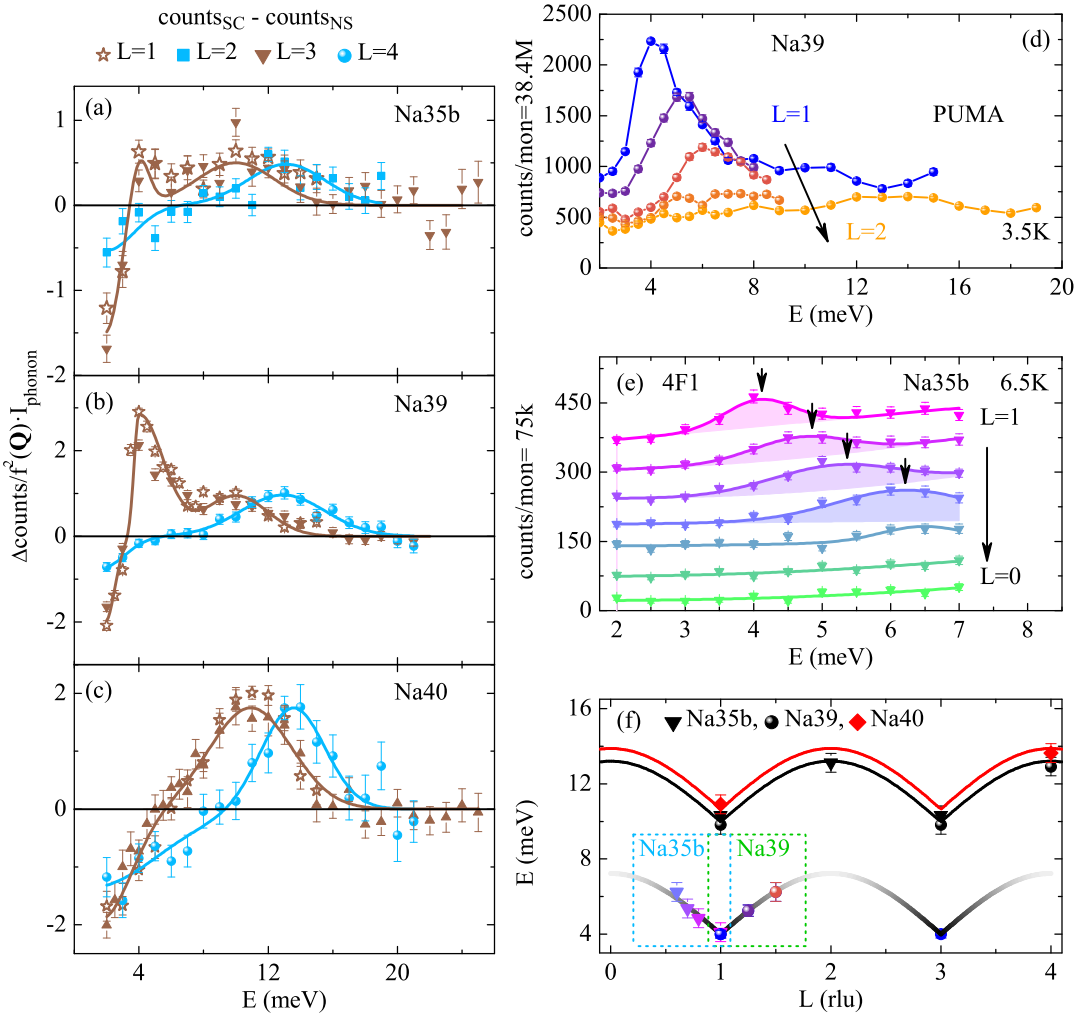

Figure 2.12: Dispersion of resonance modes in Na35b, Na39 and Na40. **(a),(b),(c)** Superconducting-normal-state-difference spectrum corrected for the Fe^{2+} magnetic form factor and normalised on phonon scattering for Na35b, Na39 and Na40 at odd and even L values, respectively. The resulting maxima are used to define E_{SRM-1}, E_{SRM-2} and $E_{SRM-even}$. **(d)** Energy scans at various L values between 1 and 2 on Na39 to define the c dispersion of SRM-1. **(e)** Same as in (d) but for Na35b between L = 1 and L = 0. **(f)** Fit of the dispersion as described in the main-text in which the data points for SRM-1 of Na35b and Na39 were combined. The corresponding colour strength should indicate the intensity dependence.

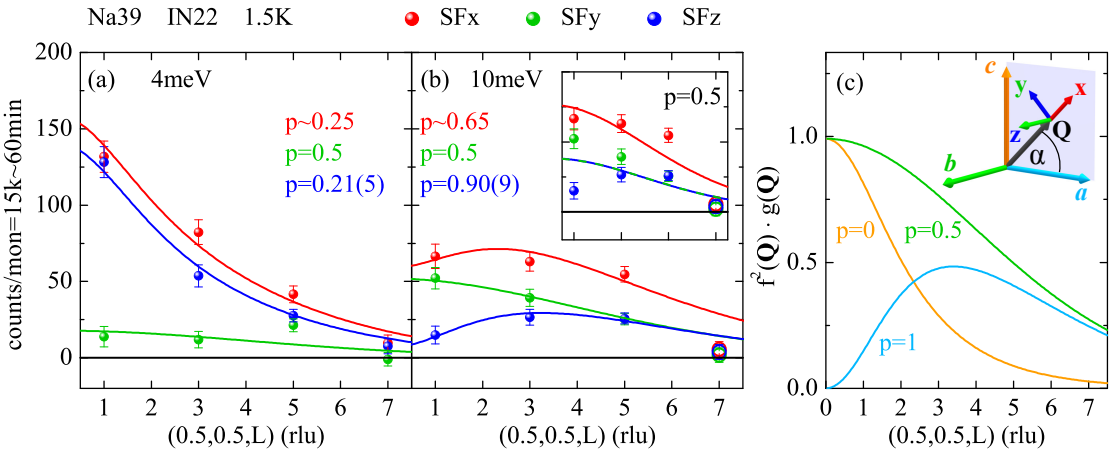

Figure 2.13: Polarisation of SRM-1 and SRM-2 in Na39. L-dependence at 1.5 K in all three spin-flip (SF) channels x, y and z at 4 meV and 10 meV in **(a)**, **(b)** respectively. Note that the background was estimated via BG = SFy + SFz - SFx and was subtracted from the data. Lines are fits according to Eq.: (2.1). The inset of (b) displays the L dependence if an isotropic model (p fixed at 0.5) is assumed. Open symbols were ignored in the fit. **(c)** schematically shows the L-dependence for polarisation along c ($p = 0$), a ($p = 1$) and the $f(Q)$ dependence alone ($p = 0.5$).

Polarisation analysis of excitations in Na39

Contrary to their electron-doped counterparts like $Ba(Fe_{1-x}Co_x)_2As_2$ from the *122* family and $NaFe_{1-x}Co_xAs$ from the *111* family, the superconducting state in Na35b and Na39 emerges from a magnetic phase with rotated moments. Naively this would cause concomitantly rotated low-energy spin fluctuation and thus a change in the paramagnons polarisation. When in $Ba(Fe_{1-x}Co_x)_2As_2$ [153, 155] and $NaFe_{1-x}Co_xAs$ [184] low-energy excitations are predominantly *t-out* and thus c polarised they should be rotated in the ab plane in underdoped $Ba_{1-x}Na_xFe_2As_2$. In order to attack this issue polarised inelastic neutron (pINS) experiments at SRM-1 and SRM-2 in Na39 were performed.

The frame of reference for the polarisation analysis is the same as in Sec. 2.1.4, while a more detailed description is given in Sec. 6.5. Briefly: $\boldsymbol{Q}$ is always parallel to $\boldsymbol{x}$ and lies in the $[1, 1, 0]/[0, 0, 1]$ scattering plane as well as $\boldsymbol{y}$ which is perpendicular to $\boldsymbol{x}$ while $\boldsymbol{z}$ is normal to the scattering plane. With the help of Tab.: 6.2 the contributions along the three magnetic axis a, b and c, corresponding to *long*, *t-in* and *t-out* can be extracted.

Due to the small sample masses and the resulting long counting times the polarisation analysis is restricted to the two resonance energies SRM-1 at 4 meV and SRM-2 at 10 meV. To extract the contributions along the three magnetic principal

axes the L dependence was explored and the results[14] are presented in Fig.: 2.13. The analysis with Eq.: (2.1) is identical to the one conducted for BaCo45 in Sec. 3.2 and given in Fig.: 3.4, i.e. the simultaneous fit of the three polarisation channels considers the boundary condition SFx = SFy + SFz. As guidelines the (squared) Fe^{2+} magnetic form factor times the geometry factor $g(\boldsymbol{Q})$ are given in Fig.: 2.13(c) for three different polarisations. Since the SFy channel and thus the contribution along the magnetic b axis does not depend on the scattering geometry p is by construction fixed at 0.5. At 4 meV there is only a minor contribution polarised along this axis, while the majority remains in the ac plane despite the spin reorientation. The analysis yields that $\sim 21\,\%$ are polarised along a and the remaining $\sim 79\,\%$ along c. This predominantly c polarised low-energy part of split SRMs is in line with those observed in BaCo60 [153, 155] (c.f. Chap. 3), in $NaFe_{1-x}Co_xAs$ [184] and even in overdoped $Ba_{1-x}K_xFe_2As_2$ [186, 187]. Despite the rotated magnetic order, the associated low-energy fluctuations do not follow suit. Apparently, c polarised low-energy fluctuations are a crucial ingredient for superconductivity to emerge in FeSCs as they were observed in many compounds [153,155,184,186,187] and even in FeSe [185,204]. Moreover, at 10 meV and thus for SRM-2 the situation is somehow unclear. Fitting the L dependence in Fig.: 2.13(b) yields $p = 0.90(9)$ for the SFz channel, which means that SRM-2 is a purely in-FeAs-layer mode and thus excitations at 10 meV are perpendicularly polarised to those at 4 meV. This would be an astonishing and unprecedented observation in FeSCs, as SRM-2 is reported to be isotropic in spin space in $NaFe_{1-x}Co_xAs$ [184,205], BaCo60 [153,155] and $Ba_{1-x}K_xFe_2As_2$ [186,187]. However, the result of this analysis must be taken with care as it crucially depends on the data points at L = 1. If the splitting at L = 1 originates from an artefact, the entire analysis is flawed and left as an undisclosed subject. Nonetheless, inset in Fig.: 2.13(b) indicates the L dependence in case of an isotropic SRM-2, like in all the other FeSCs. Apart from this, another question concerns the temperature evolution of the excitation spectra when the various phases in $Ba_{1-x}Na_xFe_2As_2$ are transited.

The temperature dependence at selected energies in Na25, Na31, Na35b, Na39 and Na40 is summarised in Fig.: 2.14. For comparison, the temperature dependence of the corresponding magnetic Bragg peaks, from Fig.: 2.2, are also shown. In Na25 and Na31 the temperature dependence of low-energy excitations at 3 meV can be described as follows: both peak at T_N, become suppressed upon decreasing temperature as the magnetic gaps start to open, display no further gapping at T_{reo} and eventually increase below T_c due to the SRM formation. Intensity peaking of low-energy excitations at the critical temperature for a phase transition is a well-known behaviour. Since Na25 and Na31 transit into the c-AFM phase without showing that peaking of intensity, the o-AFM order is their leading

[14] after the background BG = SFy + SFz - SFx was subtracted

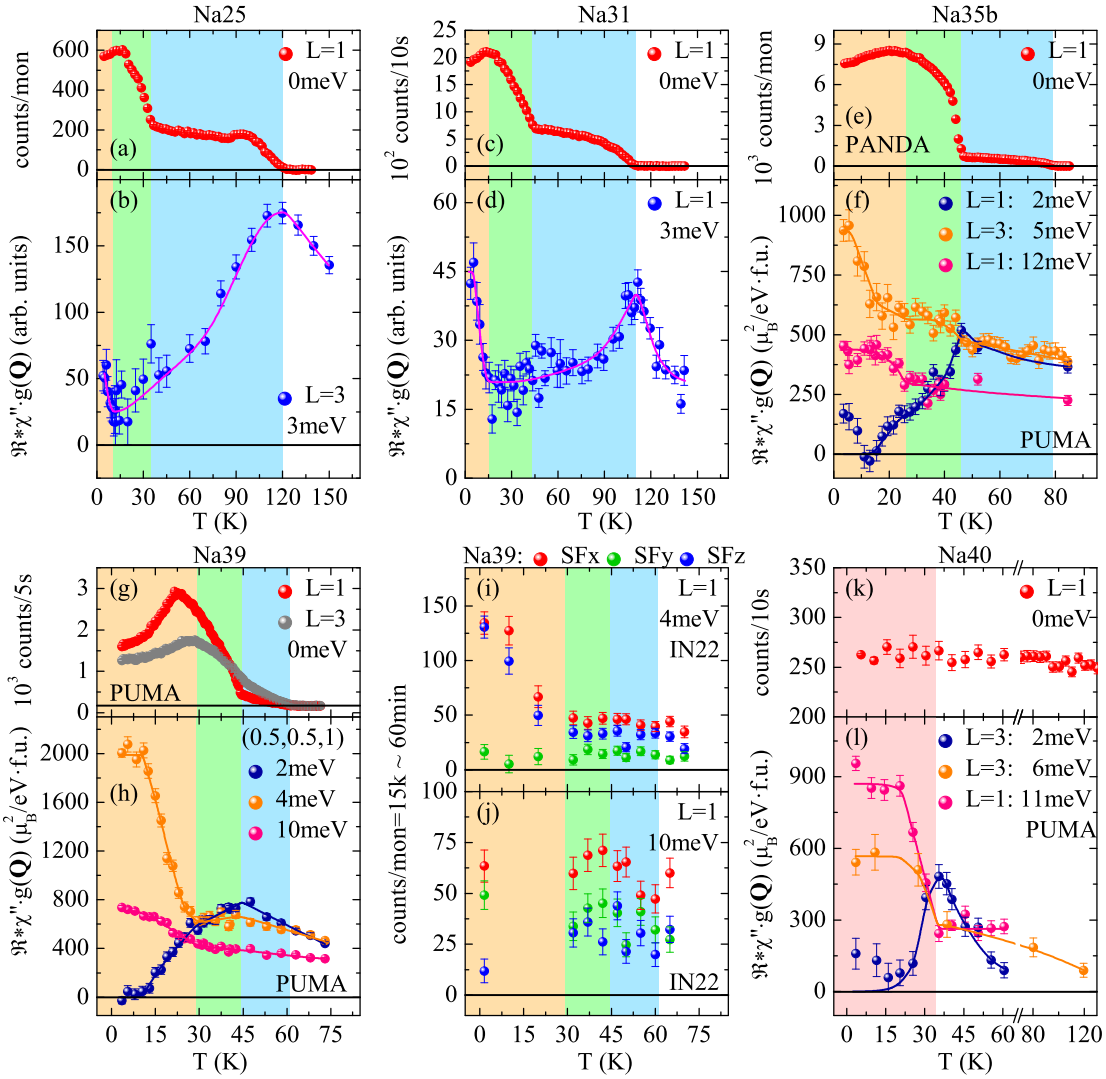

Figure 2.14: Temperature dependence of $Ba_{1-x}Na_xFe_2As_2$. **(a),(c),(g),(k)** non-normalised magnetic Bragg peak intensity of Na25, Na31, Na 39 and Na40, respectively, but otherwise same data as in Fig.: 2.2 and in Ref. [159] in order to facilitate a comparison with the inelastic response. **(e)** the temperature dependence of the $(0.5, 0.5, 1)$ magnetic Bragg peak intensity of Na35b is identical to the one in Na35a except that the former displays a slightly higher T_N of 79 K instead of 70 K. **(b),(d),(f),(h),(l)** display the inelastic response where low-energy excitations become gapped below T_N for Na25 and Na31, or below T_{reo} for NA35 and Na39 or below T_c for Na40, respectively Additionally, an intensity uptake below T_c signals the SRM formation. **(i),(j)** display the intensity dependence in the three spin-flip channels SFx, SFy and SFz at 4 meV and 10 meV for Na39. All lines are guides to the eye.

instability; meaning these samples enter a state whose free energy is close to the overall minimum already at T_N. In accordance, the spin reorientation is incomplete and the majority of the magnetic moments remain aligned in the FeAs-layers as can be seen in Fig.: 2.2(a')(b'). Whether there is any further gapping of low-energy excitations below T_c cannot be resolved due to the broad energy resolution ($\sim 1\,\text{meV}$) and the appearance of the SRM.
On the other hand, low-energy excitations in Na35b and Na39, i.e. at 2 meV, reveal that peaking in intensity at T_{reo} and thus the spin reorientation is their leading magnetic instability which minimises their free energy. Again, this is in agreement with the complete (major) realignment of the magnetic moments in Na35b (Na39), c.f. Sec. 2.1. In Na40 there is no magnetic order, and the leading instability is the SC phase transition at T_c where the corresponding low-energy excitations at 2 meV peak. A similar intensity peaking of low-energy fluctuations at T_c were reported for the CuSCs $La_{1.86}Sr_{0.14}CuO_4$ [196] and other FeSCs [131, 178, 192]. Furthermore, the temperature dependence at the corresponding resonance energies SRM-1 and SRM-2 for Na35b[15], Na39 and Na40 are respectively shown in Fig.: 2.14(f)(h)(l) and display the characteristic strong intensity uptake at T_c. The temperature dependence at 6 meV for Na40 is taken from the fits of the associated $\boldsymbol{Q}$-scans given in Fig.: 2.11(h).
Moreover, the temperature dependence of Na39 in the three spin flip channels at 4 meV and 10 meV are shown in Fig.: 2.14(i)(j), respectively. At 4 meV intensity in the SFy channel remains rather constant in all four phases. The SFz channels tend to be slightly more intense than the SFy one in the NS phases, which corresponds to the two magnetically soft directions a and c. Like the unpolarised data, there is no sizeable change neither in intensity nor polarisation when the system develops AFM order or rotates the moments. However, below T_c when SRM-1 emerges the intensity gain is exclusively found in the SFz channel. At 10 meV the temperature dependence in the NS phases is unaffected by the various phase transitions while excitations are isotropic in spin space. Due to a programming error, additional data points in the SC phase were missed which brings back the situation, where the analysis depends on a single data point. Changes in the spin space anisotropy, i.e. the suppression of intensity in the SFy channel or the increase in SFz are reported for several FeSCs in Ref. [184, 187, 205, 206] and in Fig.: 3.8(c).

Analysis of the SRM intensity

The presented data well characterises the (split) SRMs regarding intensity, polarisation, $\boldsymbol{Q}$-width and dispersion, which is summarised by the phenomenological model given in Sec. 2.4.2. Furthermore, the SRM itself must originate from a shift of spectral weight which displays a striking doping dependence for SRM-1

[15] 5 meV and 12 meV are a bit off from SRM-1 and SRM-2 defined in Fig.: 2.12(a) but fairly close to them

in particular, c.f. Fig.: 2.8(t). Upon approaching the end-point of static AFM order in the $x-T$ phase diagram, the intensity of SRM-1 strongly increases at the expense of the ordered magnetic moment, which indicates a shift of spectral weight from the one to the other. Accordingly, at $(0.5, 0.5, 1)$ the magnetic Bragg peak intensity reduction, normalised on phonon scattering, is twice as large for Na39 than in Na35b. To quantify this idea the magnetic moment and the spectral weight of SRM-1 in the first BZ are calculated within the RESLIB routine. Based on the model in Sec. 2.4.2 the spectral weight, associated with SRM-1, can be obtained via the sum rule

$$\begin{aligned}\int \chi''^{\mathrm{Na39}}_{\mathrm{SRM\text{-}1}} &= \frac{1}{N}\frac{\int_0^{20\,\mathrm{meV}}\int_0^2\int_{-1}^1\int_0^2 \chi''^{\mathrm{Na39}}_{\mathrm{SRM\text{-}1}}\frac{(2\pi)^3}{V}dEdHdKdL}{\int_0^2\int_{-1}^1\int_0^2\frac{(2\pi)^3}{V}dHdKdL} \\ &= 0.0124\ \mu_{\mathrm{B}}^2/\mathrm{Fe},\end{aligned} \tag{2.3}$$

whereas the integration runs over the orthorhombic unit cell with volume V, and N is a normalisation factor to obtain the result in $\mu_{\mathrm{B}}^2/\mathrm{Fe}$. Moreover, SRM-1 is assumed to be completely *t-out* polarised, and the corresponding geometric dependence is corrected by a factor of 2.

The ordered magnetic moment in Na39 and thus its reduction is calculated from the magnetic Bragg peaks. Therefore, the data was corrected for higher order counts in the monitor, while the geometry factor[16] $g(\boldsymbol{Q})$, determined in the previous section c.f. Fig.: 2.4(c), was treated appropriately. Correspondingly, the cross-section is given by Eq.: (6.7), where the delta functions are approximated by sharp Lorentzians. During the fit there are only two free parameters to describe the peak, its position and amplitude, whereas Fig.: A.2.5 depicts the results. Note that the amplitude contains the overall scaling factor Φ_{scale} obtained from the phonon fit and the squared magnetic moment μ^2. Accordingly the ordered magnetic moment at 3.5 K in the SC state is determined as $\mu_{\mathrm{Na39}}(3.5\,\mathrm{K}) = 0.1549\ \mu_{\mathrm{B}}$. The maximal ordered magnetic moment is obtained at 26 K, which is slightly below T_c, but where the magnetic Bragg peaks are most intense. Pursuing the same analysis, simply by taking the corresponding amplitudes values from Fig.: 2.2(d') and $g(\boldsymbol{Q})$ from Fig.: 2.4(c) yields $\mu_{\mathrm{Na39}}(26\,\mathrm{K}) = 0.1887\ \mu_{\mathrm{B}}$. For comparison the same analysis is conducted at 30 K and provides a magnetic moment of $\mu_{\mathrm{Na39}}(30\,\mathrm{K}) = 0.1844\ \mu_{\mathrm{B}}$. For Na35b the same analysis can be conducted, although there were no HK or rocking scans over the magnetic Bragg peaks performed in that particular experiment at PUMA spectrometer. Nonetheless, the temperature dependence of the $(0.5, 0.5, 1)$ magnetic Bragg peak was traced and by assuming that the peak profile is identical to the one in Na39 and $g(\boldsymbol{Q})$ does not change between SC

[16] the observed intensity is proportional to the perpendicular projection of μ with respect to $\boldsymbol{Q}$, c.f. Eq.: (6.7). The c-AFM/o-AFM phase mixture is captured in the obtained p value.

and NS phase as outlined before, the ordered magnetic moment is estimated as $\mu_{\text{Na35b}}(3.5\,\text{K}) = 0.2083\ \mu_\text{B}$ and $\mu_{\text{Na35b}}(20\,\text{K}) = 0.2220\ \mu_\text{B}$. Again, the maximal magnetic Bragg peak intensity is found at a slightly lower temperature than T_c. The results for both compounds are summarised in Tab.: 2.2. A detailed error estimation is not conducted since the systematic error of this method is in the range of 20-30 % [207].
The suppressed spectral weight associated with the ordered magnetic moment is fully recaptured in SRM-1 as both values fully agree with each other within the estimated systematic error of this method. Consequently, the reduction of static magnetic order is the motor of SRM-1, which highlights the intimate relation between AFM and SC. Whether this is a universal behaviour in FeSCs or a consequence of the spin reorientation in this compound is an open issue, since no data for comparison is reported in the literature. In particular, this would mean that for $NaFe_{1-x}Co_xAs$ where SRM-1 decreases in intensity towards the AFM end-point [152] the suppressed magnetic moment would decrease concomitantly. Intriguingly SRM-1 in $Ba(Fe_{1-x}Co_x)_2As_2$, $NaFe_{1-x}Co_xAs$ and $Ba_{1-x}Na_xFe_2As_2$ is predominantly c polarised, although the magnetic moments are aligned in the FeAs-layer for the two former compounds and out of them in the latter

Table 2.2: Calculated values of μ, $\int \chi''_{\text{SRM-1}}$ and $\int \Delta\chi''$. For Na35b and Na39 the ordered magnetic moment, its reduction below T_c and the spectral weight associated with SRM-1 are summarised. The static, ordered magnetic moment is calculated at 3.5 K and at 20 K $\lesssim T_c =$ 26 K for Na35b and at 26 K $\lesssim T_c =$ 29 K for Na39. In the calculation the c-AFM/o-AFM phase mixture is captured in the obtained p value from the analysis in Fig.: 2.4(c). Furthermore, the net gain of spectral weight in the SC state in comparison to the NS for Na25, Na31, Na35b, Na39 and Na40 are listed.

quantity	**Na35b**	**Na39**
$\mu(3.5\,\text{K})$ (μ_B)	0.2083	0.1549
$\mu(T \lesssim T_c)$ (μ_B)	0.2220	0.1887
$\Delta\mu^2$ (μ_B^2)	-0.0058	-0.0116
$\int \chi''_{\text{SRM-1}}$ $(\mu_\text{B}^2/\text{Fe})$	0.0037	0.0124
sample	$\int \Delta\chi''$	$(10^{-3}\mu_\text{B}^2/\text{Fe})$
Na25		0.4709
Na31		0.4998
Na35b		16.0
Na39		23.5
Na40		22.3

one [26, 72, 82, 153, 155, 184]. With respect to the magnetic ordering direction SRM-1 in the two electron-doped compounds is a transversal mode while it is a longitudinal one for hole doping. Apparently, the shifted spectral weight re-emerges in the channel where the AFM gap is lowest [78, 80, 153, 160]. Moreover, SRM-1 must also contain some orbital-dependent character (anisotropy due to SOC) as otherwise, it is hard to explain the lack of b polarised spectral weight in the absence of strong or any magnetic gaps, c.f. BaCo60 in Sec. 3.3. Apart from this, there are reports stating that at E_{SRM-1} a small but a polarised fraction of spectral weight is found [153, 184]. Consequently, at SRM-1 c polarised excitations are strongly enhanced, b polarised ones become suppressed and a polarised excitations are hardly affected (if these were not gapped by AFM order before). In the same fashion as in Eq.: (2.3) the net intensity gain of the SC state in comparison to the NS one can be calculated via

$$\int \Delta\chi'' = \frac{1}{N} \frac{\int_0^{20\,\mathrm{meV}} \int_0^2 \int_{-1}^1 \int_0^2 (\chi''_{SC} - \chi''_{NS}) \frac{(2\pi)^3}{V} dE dH dK dL}{\int_0^2 \int_{-1}^1 \int_0^2 \frac{(2\pi)^3}{V} dH dK dL}. \tag{2.4}$$

Thereby, SRM-2 was treated as isotropic, and the geometric dependence is corrected by a factor 3/2. Note, that $\int \Delta\chi''$ refers only to the model for the inelastic response without any contribution of the elastic, and static moment, although the integration starts at 0 meV. The obtained results are listed in Tab.: 2.2 as well. Furthermore, T_c values for Na35b (26 K) and $Ba(Fe_{0.925}Co_{0.075})_2As_2$ (25 K) [131] like their $\int \Delta\chi''$ values are almost identical. Comparing to the CuSC $YBa_2Cu_3O_{7-\delta}$ where T_c ranges from 52 K to 87 K the spectral weight of the SRM is also factor 2-4.5 larger than here [133], which underlines again the theoretical prediction that it is proportional to the SC change in exchange-energy and thus to T_c as well [118, 208, 209].

2.2.3 Section Summary

Inelastic neutron scattering experiments were conducted over a broad doping range $0.25 \leq x \leq 0.40$ in $Ba_{1-x}Na_xFe_2As_2$. The excitation spectrum in the SC state revealed a split SRM for Na35b, Na39 and Na40, while the splitting cannot be resolved in Na25 and Na31. Moreover, the low-energy part SRM-1 displays an intriguing doping dependence, as its intensity drastically increases towards the AFM end-point in the phase diagram and is abruptly suppressed to a small shoulder beyond that point. This behaviour is unprecedented in electron-doped FeSCs like $NaFe_{1-x}Co_xAs$ and $Ba(Fe_{1-x}Co_x)_2As_2$, which also display a split SRM, where SRM-1 is continuously suppressed towards the corresponding AFM end-point [152, 210]. In this regard, absolute unit calculation showed that SRM-1 in

Na39 is the most intense SRM in FeSCs ever observed until today. Furthermore, it could be proven that the spectral weight of SRM-1 originates from the suppressed static magnetic moment in the SC state. The amount of suppressed static moment below T_c increases with increasing doping, despite the ordered moment's reduction in general. In contrast to SRM-1, SRM-2 evolves gradually, and its intensity increases with increasing T_c values. This dependence is summarised in Fig.: 2.15 for both modes, as well as the scaling behaviour of E_{SRM-1}, E_{SRM-2} and $E_{SRM-even}$ with T_c. Note that the resonance energies were defined according to the difference spectra in the SC and NS. For Na25 and Na31, the split parts of SRM cannot be resolved, hence SRM-1 and SRM-2 coincide. Additionally, universal scaling values of E_{SRM}/k_BT ($\sim$ 4.3 for FeSCs and $\sim$ 5.3 for CuSCs [152]) are inserted as lines for comparison. However, a clear trend in the doping evolution is hardly discernible, since the interpretation is hampered by the very faint SRMs in Na25 and Na31. In particular, the SRM in Na31 could consist of two modes, whereas the second peaks at $\sim$ 5 meV. When this is the case, E_{SRM-2}/k_BT_c approaches the universal scaling value for FeSCs with increasing doping. Especially, the universal scaling ratio is only fulfilled close to optimal, but not for under-doped compounds. Furthermore, E_{SRM-1}/k_BT_c follows a much smaller scaling ratio, while $E_{SRM-even}/k_BT_c$ scales with a larger value, due to its upwards bending L dispersion. The universal scaling ratio of E_{SRM}/k_BT_c is a means from the early days in FeSC-research to facilitate a comparison between different compounds and their families, before split SRMs were discovered and much attention was paid to the L dispersion. Consequently,

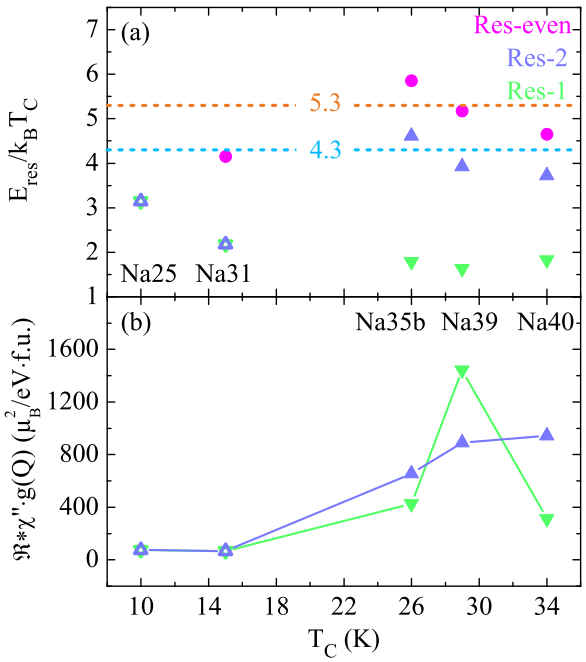

Figure 2.15:
Comparison of the resonance energies and intensities. **(a)** Ratio of E_{SRM}/k_BT as a function of T_c to indicate the compliance with universal scaling value of $\sim$ 4.3 for FeSCs and $\sim$ 5.3 for CuSCs [152]. **(b)** Peak values of SRM-1 and SRM-2 as a function of T_c. While SRM-2 gradually increases with increasing T_c, SRM-1 displays a non-monotonic behaviour as it peaks at (close to) the AFM end-point and vanishes abruptly beyond. For Na25 and Na31 SRM-1 and SRM-2 cannot be separated and thus coincide always in the plot.

this means is too rough to account for the details of the pairing mechanism with anisotropic and orbital-dependent Δ_{SC} [143,211–214], which ultimately determine the SRM.
Moreover, finite out of FeAs-layer spin correlations are still persistent as the SRM disperses upwards from the BZ centre to the BZ boundary, thereby displaying a bandwidth of $\sim 3\,\mathrm{meV}$ in agreement with the universal behaviour reported in Ref. [202]. Apart from that, SRM-1 and SRM-2 display different dimensionalities; while the former is 3D with strong intensity variations along the L direction, the latter is 2D and constant. In particular, SRM-1 is sensitive to the positions in $\boldsymbol{Q}$ space where magnetic order appears and vanishes at the BZ boundary which again underscores its deep relation to AFM order. Furthermore, the polarisation analysis at 4 meV in Na39 showed that this mode is also c polarised and thus longitudinal with respect to the reoriented moment. This is in clear opposition with electron-doped FeSC, where the spins remain aligned in the FeAs-layers and low-energy excitations in the SC state are *t-out* polarised [153, 155, 184]. Consequently, the polarisation of low-energy excitations are decoupled from the underlying magnetic order and do not follow the spin reorientation. In summary with other FeSCs, c polarised low-energy excitations seem to play a crucial role for the mediation of SC [153, 155, 184–187, 204] Although, the moments orientation can be determined without any doubt in the c-AFM phase, c.f. Sec. 2.1 and Ref. [82,84,163,165], the magnetic structure bears some uncertainty. Particularly, neutron scattering cannot distinguish between a single and a double $\boldsymbol{Q}$ structure. Due to its strong MEC, the spin reorientation is associated with a re-entrant phase, hence to a double $\boldsymbol{Q}$ structure which would cause half of the Fe sites to be non-magnetic. While μSR and infra-red spectroscopy studies [163, 165, 166] indeed observed/deduced that structure, recent pair distribution function (PDF) analysis revealed rapidly fluctuating orthorhombic domains on small length scales, approximately five unit cells. Consequently, if strong MEC effects prevail then the magnetic moments are also wildly fluctuating, which could ultimately explain why c polarised low-energy excitations are still observed despite the reorientation of the static and ordered part.

2.3 Discussion

X-ray, elastic and inelastic neutron scattering experiments were performed to study the magnetic structure, its coupling to the crystal lattice and the corresponding excitations. Thereby various single crystals of $Ba_{1-x}Na_xFe_2As_2$ with x = 0.25, 0.31, 0.35, 0.39 and 0.40 were probed which cover a broad range in the corresponding phase diagram. All samples become superconducting and display two consecutive magnetic phase transitions, except Na40. In the first magnetic phase (o-AFM) the moments are aligned within the FeAs-layers, as it was observed in many FeSCs [26, 72, 73, 215, 216], while in the second phase (c-AFM) they realign themselves along the c axis and thus perpendicular to the FeAs-layers. A spin reorientation of the Fe^{2+} moments has been observed before in the parent to under-doped compounds of the *1111* family, which is associated to the ordering of the *RE* moments at $T_{RE} \sim 10\,\mathrm{K}$ [217–220], and thus due to a different origin. In the *122* family the spin reorientation occurs at $T_{reo} \sim 5 \cdot T_{RE}$ and originates from SOC interactions ($\lambda_{\mathrm{SOC}} \sim 10\,\mathrm{meV}$ [221]), most likely.
Intriguingly a spin reorientation followed by a SC transition at lower temperatures is only observed for hole doping at the *AE*-site [46,47,82,83,163,165] and not on the Fe-site [85–89] as one could naively expect from simple electron counting. Nonetheless, with increasing substitution of Cr or Mn on the Fe-site the o-AFM phase is suppressed, while at advanced doping a novel AFM phase with G-type order, tetragonal lattice symmetry and moments along the c is stabilised [85–89]. However, there is no spin reorientation transition in the sense that the moments order first according to one scheme and then at a lower temperature according to a second. The substitution of Cr/Mn induces an entirely new magnetic order, but never SC. In this context, the local moments of Mn prevent SC to emerge [89], while it also yields to charge localisation as the end-compound $BaMn_2As_2$ is an insulator [222, 223].

The spin reorientation transition in $AE_{1-x}AM_xFe_2As_2$ documents the strong MEC in FeSCs as the orthorhombic distortion is reverted below T_{reo}. Moreover, it is necessarily of first order as there is no magnetic group-subgroup relation. Consequently, a phase mixture of o-AFM and c-AFM orders can form, whereby the o-AFM fraction is minimised in $Ba_{1-x}Na_xFe_2As_2$ around $x \sim 0.35$, where the spin reorientation is complete, similar to a martensitic transition. Note in this regard, that neutron scattering alone cannot distinguish between a phase mixture and moments pointing in an intermediate but arbitrary direction as only the overall moment (moment's direction) is sensed. However, such a continuous rotation of all moments seems unlikely as a o-AFM and c-AFM phase fractionalisation is also observed in diffraction experiments based on powder samples [45, 84] and by symmetry considerations. In that respect, c-AFM phase fractions from $\sim 10\,\%$ in $Ba_{0.76}K_{0.24}Fe_2As_2$ [84] to $\sim 60\,\%$ in $Ba_{0.76}Na_{0.24}Fe_2As_2$ [45] were reported in the

literature. In opposite to the here presented results and the literature, dilatometry measurements reported a complete reversion of the orthorhombic distortion and thus a complete spin reorientation with $\sim 100\,\%$ c-AFM phase [46, 47]. There are two options to resolve this discrepancy. First and utmost unlikely is the chance that the investigated samples display a broad doping level variation, which is in stark contradiction with the characterisation measurements and the observed sharp magnetic transitions. Second and also unlikely, the small pressure (a few MPa) exerted on the sample, which is required to measure thermal expansion with a capacitative dilatometer, massively boosts the c-AFM phase. Hassinger *et al.* [161, 162] could show that the c-AFM phase is stabilised when hydrostatic pressure of a few GPa is applied, which, however, is orders of magnitudes larger than the pressure reached in capacitative dilatometry.
Another particularity is the competition between c-AFM/o-AFM order and SC for the same electronic states. In Na39 the magnetic Bragg peak intensity at $(0.5, 0.5, 1)$ is reduced by roughly $50\,\%$ below T_c, while the penalty at L = 3 is $30\,\%$ and at L = 7 it is just $20\,\%$. This anisotropic suppression indicates that the c-AFM phase is less compatible, or interacts more severe, with SC than the o-AFM phase, as the former is predominately sensed at L = 1 and the latter at L = 7. Consequently, the release of free energy between the c-AFM phases and SC is in close competition with each other, which is also evidenced by specific heat measurements [46, 47].

The reversion of the orthorhombic distortion below T_{reo} documents once more the strong coupling between magnetic order and the lattice. In this regard, several studies reported on a complete (or fractional complete) restoration of C_4 symmetry [46, 47, 163, 165, 166], which imposes salient consequences on the magnetic structure, with moments along the c direction. Accordingly, half of the Fe-site become non-magnetic, while the other half carries the doubled moment. Indeed IR [163, 164], μSR [164, 165] and Mößbauer spectroscopy [166] interpreted their results in favour of a double-$\boldsymbol{Q}$ structure. Note, that the presented neutron scattering data measures only the averaged ordered moment hence cannot distinguish between a single-$\boldsymbol{Q}$ and a double-$\boldsymbol{Q}$ structure. However, in a recent pair distribution function (PDF) analysis, which allows investigating the local structure, rapidly fluctuating orthorhombic domains on the length scale of $\sim 20\,\text{Å} \approx 5$ unit cells were deduced, while the overall system appears tetragonal on mesoscopic length scales [167]. In particular, the orthorhombic model provides a slightly better fit to the data than the tetragonal one, basing on their goodness-of-fit values[17], which are 1.27 and 1.40[18], respectively [167]. Apart from that, the potential

[17] defined as $gof = \frac{\sum(G_{obs}-G_{cal})^2}{\sum(G_{obs})^2}$

[18] although the two values seem to be exchanged in the original supplementary material, which denotes the tetragonal model with the smaller value.

influence of mesoscopic phase separated c-AFM and o-AFM domains in the specimen is dropped in the discussion, because in a previous report dealing with the same composition no such separation was observed [83]. Since the Mößbauer experiment and PDF analysis partially contains the same authors, they tried to reconcile their observations by focussing on the different characteristic measurement time scales. As PDF data cannot distinguish between local and dynamic orthorhombic regions and Mößbauer is sensitive to times scales of $\sim 10^{-7}$ s, they concluded that the orthorhombic regions fluctuate on a time scale between 10^{-7} s and 10^{-13} s [167]. Furthermore, IR spectroscopy and μSR would be insensitive to such small and rapidly oscillating orthorhombic domains [163–165], as the first technique lacks the spatial and the latter the time resolution. Accordingly, rapidly fluctuating orthorhombic domains relax the C_4 symmetry condition and by strong MEC would thus generate a rapidly fluctuating ordered moment in the *ac* plane, i.e. the two soft magnetic directions. In addition, this must also somehow affect the elastic constants, e.g. the Young's modulus, which hardens below T_{reo} as the orthorhombic distortion and the associated softening is reverted [102]. Nonetheless, the impact of rapidly fluctuating orthorhombic domains in the c-AFM, in particular on Young's modulus, requires a thorough theoretical model, which is not yet established.

Another consequence of magnetic ordering is the reconstruction, or re-reconstruction, of the Fermi surface [48–50,224] forming the basis from which SC will emerge eventually. In that context Yi *et al.* [49] observed a splitting of the d_{zy} and d_{xz} orbitals [49] while Shimojima *et al.* [76] reported a change in the DOS at the FS which can be attributed to the d_{xz} orbital almost exclusively below T_N in $BaFe_2As_2$. In that context, ARPES measurements on $BaFe_2As_2$ observed a splitting of the degenerate d_{zy} and d_{xz} orbitals below T_N, while only the d_{xz} orbital preserves some residual electronic DOS [49, 76]. Of course, these effects become washed out with increasing doping, but it highlights the highly orbital selective character of the Fermi surface which again is the basis from which superconductivity emerges (in the region of phase coexistence). This particularity is well exemplified by the SRM in BaCo45, where it is highly anisotropic and low-energy *long* spin fluctuations/paramagnons cannot contribute to the pairing, as the associated magnetic order gaps them, c.f. Chap. 3 and Ref. [153]. Regarding $Ba_{1-x}Na_xFe_2As_2$, the situation is more intricate as the spin reorientation will reconstruct the reconstructed Fermi surface, but so far no detailed ARPES experiments to elaborate this issue have been conducted. Presumably, these experiments would be very hard to interpret in case of a c-AFM/o-AFM phase coexistence and the corresponding superposition of both structures in the spectra. Changes in the electronic structure were recently corroborated by Raman scattering experiments, where an additional electronic feature is formed below T_{reo} at 32 meV [195], which is most likely a two-magnon excitation.

Table 2.3: Summary of the doping levels, sample masses, transition temperatures and gain of spectral weight in the superconducting state of the investigated $Ba_{1-x}Na_xFe_2As_2$ samples.

	Na25	Na31	Na35a	Na35b	Na39	Na40
x_{EDX} (%)	25	31	35	35	39	40
m (mg)	66	125	90	294	172	42
T_n (K)	120	110	70	79	61	–
T_{reo} (K)	35	43	46	46	44.5	–
T_c (K)	10	~ 15	26	26	29	34
$\int \Delta\chi''$ ($10^{-3}\mu_B^2$/Fe)	0.4709	0.4998	–	16.0	23.5	22.3

Moreover, the two parts of the split SRM in $Ba_{1-x}Na_xFe_2As_2$ display a distinct doping dependence. The part at higher energies SRM-2 increases monotonically in intensity with advanced doping, i.e. concomitantly with T_c. On the other hand, the low-energy part SRM-1 displays a non-monotonic doping dependence, as it intensifies massively towards the AFM end-point and vanishes abruptly beyond it. In the related but electron-doped compounds, which do not display a spin reorientation but still a split SRM, the opposite trend for the doping intensity evolution of SRM-1 is observed [152, 210]. Nonetheless, the intensity of SRM-2 is increasing with advanced doping, or concomitantly with T_c, which is a general feature in FeSCs [152, 178, 210]. Furthermore, the abrupt vanishing of SRM-1, within a very narrow doping range between Na39 ($T_N = 61$ K) and Na40, concomitantly with static AFM order shows that it is strongly coupled to it. This relationship is elaborated further by absolute unit calculation within the Reslib routine, which proves that the suppressed spectral weight from static AFM order, below T_c, is recaptured by SRM-1. Despite the reduction of the ordered moment with increasing doping the amount suppressed by SC is also increasing; an observation which, due to strong MEC, resembles the suppression of orthorhombicity in $Ba(Fe_{1-x}Co_x)_2As_2$ with increasing x [31]. If both quantities are directly proportional to each other, then a similar and yet to be confirmed behaviour of SRM-1 in $Ba(Fe_{1-x}Co_x)_2As_2$ should be observable.
There is another particularity in the relation between magnetic order and its associated low-energy fluctuations for mediating the Cooper-pair formation. As the spins rotate in hole-doped FeSCs, their low-energy fluctuations should follow this rotation and thus be differently polarised in comparison to the electron-doped compounds. However, this is not the case as for both magnetic orders from which SC emerges SRM-1 remains predominantly c and partially a polarised [97, 153, 155, 184]. Consequently, low-energy spin excitations are decoupled from the underlying magnetic order, which still resembles the AFM gap anisotropy

of the non-SC parent compound. Note in that context, that the ordered moment itself is already strongly reduced and is of the order of $\sim 0.2\ \mu_B$ in Na35b and Na39.
Intriguingly, the shifted spectral weight associated with the suppressed magnetic moment in BaCo45 is purely a polarised (ordering direction) and reappears in the c (*t-out*) and b (*t-in*) channel, c.f. Chap. 3 and Ref. [153]. Consequently the suppressed spectral weight changes its polarisation. When there is a one-to-one correspondence between certain orbitals and the crystallographic axes, the shift of spectral weight must also happen between orbitals. However, in $Ba_{1-x}Na_xFe_2As_2$ the spectral weight is shifted on the same orbitals, just to higher energies, as the moments and low-energy spin excitations are in parallel alignment. Apparently, c polarised low-energy fluctuations are crucial for SC to emerge, disregarding the underlying magnetic order and putting interesting constraints on orbital-selective pairing mechanism which, however, needs to be derived theoretically. Moreover, the strong MEC effects need to be considered as well as the rapidly fluctuating orthorhombic domains in the c-AFM phase. Once more, the properties of the investigated $Ba_{1-x}Na_xFe_2As_2$ samples are summarised in Tab.: 2.3.

2.4 Methods

The investigated samples in this chapter were all synthesised via the self-flux method which is in detail outlined by Aswartham *et al.* in Ref. [32]. To estimate the sample quality energy-dispersive X-ray (EDX) analyses were conducted yielding an accuracy of 1-2 %. Thereby single crystalline samples were obtained, and their corresponding masses are listed in Tab.: 2.3. While T_s, T_N and T_{reo} were easily measured by neutron scattering T_c was determined by their susceptibility curves by a superconducting quantum interference device (SQUID) magnetometer. All susceptibility curves showed sharp SC transitions, which documents the high quality of the investigated samples. In order to avoid any potential deterioration of the sample quality due to air exposure, they were constantly kept under Argon-atmosphere with an oxygen content below 5 ppm. Accordingly, the sample alignment for the neutron scattering experiments was conducted with the aid of a custom-designed can whose Kapton-foil window is permeable for X-rays from the Laue camera. For all neutron scattering experiments in this chapter, the scattering plane is $[1, 1, 0]/[0, 0, 1]$ in tetragonal notation, corresponding to $[1, 0, 0]/[0, 0, 1]$ in the orthorhombis notation. The sample itself was attached to a thin L-shaped aluminium holder and fixed by wrapping thin aluminium wire around it. Moreover, it was air-tightly sealed with an indium gasket in an aluminium can for the neutron scattering experiments. On the other hand, the sample Na35a was shortly exposed to air as it was transferred into the cryostat of our custom-designed X-ray diffractometer D5000 for the temperature dependent measurements. However,

there was no negative impact on the crystal quality. The D5000 diffractometer operates in Bragg-Brentano geometry, while the X-rays with $\lambda = 2.289\,760$ Å were generated from a Cr-anode, which is provided by 40 kV acceleration voltage and 30 mA heating current from a high-voltage generator. Low-temperatures with a stability of $\Delta T = 0.5$ K were reached with a helium-flow cryostat.

The neutron scattering experiments were conducted at the LLB in Saclay, France, at the ILL in Grenoble, France, as well as at the FRM-II in Garching, Germany. All instruments were operated in fixed $\boldsymbol{k}_f$ mode and in order to suppress higher order contaminations either PG or cooled Be filters were installed additionally. Table 2.4 summarises which instruments at which facility with which fixed $\boldsymbol{k}_f$, monochromator, analyser and filter were used. Concerning the experiments with polarisation analysis, the corresponding polarisation quality of the set-up was estimated by measuring the flipping ratios (FR) on nuclear Bragg peaks. Thereby a FR of ~ 31 at 4F1 spectrometer in LLB and FR ~ 14 at IN22 at ILL were obtained. Note that the former one was operated with Helmholtz coils and the latter with the CryoPAD.

2.4.1 M: Spin Reorientation Transitions

The temperature dependence for the magnetic and nuclear Bragg peaks in Fig.: 2.2 is obtained by constantly cooling and counting at the corresponding position. Since the cooling rate was low and the counting time short, meaning that in the given time frame the temperature does not change significantly, a lot of data points were generated, which eventually were binned within certain intervals listed in Tab.: 2.5.

Table 2.4: Instruments settings of the employed spectrometers/ diffractometer.

instrument	facility	$\boldsymbol{k}_f$	mono.	ana.	filter
2T	LLB	2.662 Å^{-1}	PG(002)	PG(002)	PG
3T1	LLB	2.662 Å^{-1}	PG(002)	PG(002)	PG
4F1 (pol.)	LLB	2.57 Å^{-1}	PG(002)[19]	Heusler(111)	PG
4F1 (unpol.)	LLB	1.55 Å^{-1}	PG(002)	PG(002)	cooled Be
G43	LLB	1.97 Å^{-1}	PG(002)	PG(002)	PG
PANDA	FRM-II	1.55 Å^{-1}	PG(002)	PG(002)	cooled Be
PUMA	FRM-II	2.662 Å^{-1}	PG(002)	PG(002)	PG
IN22	ILL	2.662 Å^{-1}	Heusler(111)	Heusler(111)	PG

[19] a PG filter, the polarising suppermirror and a Mezei flipper were installed between the monochromator and the sample.

Table 2.5: Binning intervals for the temperature dependence of magnetic and nuclear Bragg peak intensity.

sample	binning interval	Instrument
Na25	2K (unpol); as measured (pol)	2T & 4F1
Na31	2K	2T
Na35a	1K	PANDA
Na35b[20]	1K	PANDA
Na39	1K	PUMA
Na40	2K nuc; 5K mag	3T1 & PUMA

2.4.2 M: Magnetic Excitations in $Ba_{1-x}Na_xFe_2As_2$

The RESLIB fits are based on phenomenological models for $\chi''(\boldsymbol{Q}, E)$ in the SC and NS. For simplicity, and since a temperature, energy and sample independent (H,K)-width $w_{HK} = 0.023\,\text{rlu}$ was assumed, $\chi''(\boldsymbol{Q}, E)$ is decomposed into two parts, one is purely (H,K)-dependent $\mathfrak{Q}(H, K)$ the other is purely energy dependent $\mathfrak{E}(E(L))$. The energy-dependent part considers the L dispersion as well. Consequently, the entire phenomenological model is summarised in Eq.: (2.5)-(2.2):

$$\chi''(\boldsymbol{Q}, E) = \mathfrak{Q}(H, K) \cdot \mathfrak{E}(E(L)), \tag{2.5}$$

$$\begin{aligned}\mathfrak{Q}(H, K) = \frac{1}{2\pi w_{HK}^2} \cdot \exp\left(-\frac{1}{2} \cdot \left(\frac{H - h_c}{w_{HK}}\right)^2\right) \times \\ \exp\left(-\frac{1}{2} \cdot \left(\frac{K - k_c}{w_{HK}}\right)^2\right),\end{aligned} \tag{2.6}$$

$$\mathfrak{E}_{NS}(E) = \frac{\chi'(\boldsymbol{Q}, 0)}{\pi} \cdot \frac{E\Gamma}{E^2 + \Gamma^2}, \tag{2.7}$$

$$\begin{aligned}\mathfrak{E}_{SC}(E(L)) = \sum_{j=1}^{2} \frac{A_j(L)}{\sqrt{2\pi} \cdot E \cdot \Gamma_j} \times \\ \exp\left(-\frac{1}{2}\left(\frac{\ln(E_{Res-j}(L)) - \ln(E)}{\Gamma_j}\right)^2\right),\end{aligned} \tag{2.8}$$

$$A_1(L) = A_1 \cdot \left(1 - 0.88(4) \cdot \cos^2\left(\pi \frac{L}{2}\right)\right), \tag{2.9}$$

$$A_2(L) = A_2. \tag{2.10}$$

[20] shown in Fig.: 2.14(e)

Furthermore, the instrumental parameters of PUMA spectrometer to estimate the resolution within the Cooper-Nathans approximation [189–191] are listed in Tab.: 2.6.
In order to transform the experimental data to $\chi''(\boldsymbol{Q}, E)$, the background estimated appropriately away from $\boldsymbol{Q}_{AFM}$ was subtracted, while the results were subsequently corrected for the Bose factor and higher order contaminations in the monitor. Details for each sample are listed below, and the corresponding raw data can be found in the Appendix.

2.4.2.1 Data Treatment Na25

The presented data for sample Na25 are the combination of two consecutive measurements at PUMA spectrometer. It is the same sample and all instrumental conditions, like aperture slits opening, were tried to be reproduced. Nonetheless, the striking difference between both experiments concerns the monochromator, whose motors to adjust the focus were broken, and thus its curvature was fixed at a certain value in the second experiment. Note, that a focusing monochromator needs to readjust its curvature to maintain maximum flux at every $\boldsymbol{Q}$-position. In order to deal with this issue, a phonon is used as a reference. Consequently, the data could be corrected and were combined by a weighted averaged.
The background was estimated sufficiently away from the signal and fitted by a polynomial. The phonons, E-scans and their weighted average are shown in Fig.: A.3.1 in the appendix.

2.4.2.2 Data Treatment Na31

The data for sample Na31 are the combination of two consecutive measurements at 2T spectrometer with the same sample. Furthermore, the spectrometer configurations for both experiments Exp1 and Exp2 were identical. The raw data, background estimation and for L = 5 the weighted average are given in Fig.: A.3.2 in the appendix.

2.4.2.3 Data Treatment Na35b

The data for sample Na35b were measured in a single experiment at PUMA spectrometer whereas the raw data and estimated background are given in Fig.: A.2.1 in the appendix.

2.4.2.4 Data Treatment Na39

The unpolarised neutron scattering data for sample Na39 were obtained in two experiments on PUMA spectrometer. However, for the analysis only the E-scan

at L = 1 at 3.5 K and the phonon scans overlap. In both cases the data were combined, after background subtraction. Note, that the instrumental configurations of the first experiment were restored in the second one. Nonetheless, the obtained raw data, background estimation and phonon scans are presented in Fig.: A.2.2.

The polarised data for sample Na39 were obtained in two experiments in IN22 spectrometer at ILL, Grenoble. Combining the data of both experiments is allowed, as the same sample and its setup were identical. The corresponding experimental background was estimated by BG = SFy + SFz - SFx, as given in Tab.: 6.2.

2.4.2.5 Data Treatment Na40

The data for sample Na40 were obtained in two experiments on PUMA spectrometer. However, only phonon scans overlap. Note, that the instrumental configurations of the first experiment were restored in the second one. Nonetheless, the obtained raw data, background estimation and phonon scans are presented in Fig.: A.2.3.

Table 2.6: Reslib parameters for absolute unit calculation in Sec. 2.2
Parameters of PUMA and 2T spectrometer as well as for the samples Na25, Na31, Na35b, Na39 and Na40 used for absolute unit calculations. All components are treated as they would be of rectangular shape which yields to a factor of $1/\sqrt{12}$ in the square root of the variance for each dimension and is taken into account within the RESLIB routine.

Component	Property	Value				
		PUMA				2T
beam	width (cm)	2.5				9
	height (cm)	13				15
mono. PG(002)	width (cm)	16.2				15
	height (cm)	26				12
	depth (cm)	2				2.5
	hor. mosaic	24′				24′
	ver. mosaic	24′				24′
	τ (Å^{-1})	1.87325				1.87325
monitor	width (cm)	5				45
	height (cm)	10				80
ana. PG(002)	width (cm)	15				17
	height (cm)	21				11
	depth (cm)	2				2.5
	hor. mosaic	24′				24′
	ver. mosaic	24′				24′
	τ (Å^{-1})	1.87325				1.87325
detector	width (cm)	2.53				3
	height (cm)	10				10
collimation horizontal & vertical	source - mono.	120′				60′
	mono. - sample	120′				60′
	sample - ana.	120′				120′
	ana. - detector	120′				120′
distances (cm)	source - mono.	209				480
	mono. - sample	215				210
	sample - ana.	91.3				95
	ana. - detector	76.2				65
	mono. - monitor	100				120
samples		Na25	Na35b	Na39	Na40	Na31
	height (cm)	0.65	1.4	1.4	0.873	1.1
	width (cm)	0.50	0.7	0.7	0.689	0.59
	depth (cm)	0.04	0.08	0.04	0.043	0.04
	hor. mosaic	100′	60′	60′	60′	60′
	ver. mosaic	60′	52′	52′	52′	52′

3 Magnetic Excitations in $Ba(Fe_{1-x}Co_x)_2As_2$

Info

The data presented in this section are already partially published in Waßer *et al.*., Scientific Reports, **7**, 10307 (2017) [153]. This chapter is partially based on this publication.

Abstract

In iron-based superconductors, there are two strong arguments which favour a paramagnon mediated Cooper-pair formation with $s^{\pm}$-symmetry over a phonon-assisted para-orbiton mechanism with s^{++}-symmetry. The first argument is the closeness of the antiferromagnetic and superconducting domes in the corresponding temperature vs. doping phase diagram, while the second one is the emergence of the spin resonance mode below T_c. Superconductivity in $Ba(Fe_{1-x}Co_x)_2As_2$ emerges upon Co doping at the expense of the antiferromagnetic order, and there is a regime where both orders coexist microscopically. Consequently, paramagnons as the bosonic glue must stamp the virtues of the suppressed magnetic order on the spin resonance mode. However, despite intense research, the question of how superconductivity emerges from an antiferromagnetically ordered state is almost unanswered. In order to attack this issue, polarised inelastic neutron scattering is employed to identify the nature of the spin resonance mode, and thus of superconductivity in the presence of magnetic order with large moments. The excitation spectrum in the normal state of Co underdoped $Ba(Fe_{1-x}Co_x)_2As_2$ shows broad magnetic gaps opening in all three spin directions, which reflect the spin-space anisotropy of the parent compound $BaFe_2As_2$. Moreover, and in contrast to the isotropic spin resonance modes observed in the optimal to overdoped regime these modes are fully anisotropic and appear only in the two transversal channels. This anisotropy, where longitudinal contributions to the spin resonance mode of the magnetic excitation spectra are gapped, due to the static order, is attributed to a band- and orbital-selective pairing mechanism. Additionally, fingerprints of this mechanism are still retained for optimum doping, where the low-energy excitations develop a remarkable in-FeAs-Layer spin-space anisotropy below T_c.

Contents

3.1	Introduction	**62**
3.2	Anisotropic Magnetic Excitations in Underdoped $Ba(Fe_{1-x}Co_x)_2As_2$	**64**
3.3	Spin Resonance Mode in $Ba(Fe_{0.94}Co_{0.06})_2As_2$	**71**
3.4	Summary and Discussion	**77**
3.5	Methods	**80**

3.1 Introduction

One hallmark observation of superconductivity mediated by spin fluctuations is the emergence of the spin resonance mode (SRM) in inelastic neutron scattering (INS) experiments [57, 59, 116, 118, 225]. The spin resonance mode itself can be understood as a spin exciton which results from a divergence in the susceptibility. Thereby, large parts of the hole and electron pockets of the Fermi surface (FS) sheets are connected by a wave-vector $\boldsymbol{q}$, while the corresponding SC gap function changes its sign in between. For this reason, the SRM is deeply connected to the pairing symmetry, details of the FS, and appears as an isotropic feature in spin-space when spin-orbit coupling (SOC) is neglected, c.f. Sec. 1.3. On the other hand, the heavy-fermion superconductor $CeCoIn_5$ with $4f$ electrons has strong SOC which causes an Ising-like SRM [226]. However, iron-based superconductors (FeSCs) display a more intricate situation due to their multi-band, multi-orbital character of the FS plus an intermediate strength of SOC, approximate 10 meV [221]. For example in Co underdoped NaFeAs the electron pocket at the FS consists of d_{xy}, d_{xz} and d_{zy} orbitals, yet, $\Delta_{xz}, \Delta_{yz} \geq 4\,\text{meV}$ and $\Delta_{xy} = 7\,\text{meV}$ [143] and thus the overall gap structure is orbital dependent and anisotropic. Moreover, in the microscopic AFM/SC phase coexistence regime for underdoped $Ba(Fe_{1-x}Co_x)_2As_2$ and $NaFe_{1-x}Co_xAs$ alike [39–43], AFM order reconstructs and gaps parts of the FS from which SC emerges, eventually. Accordingly, one may ask what is the difference when SC is formed out of the t-PM or the o-AFM phase. Furthermore, the importance of SOC is documented by the remarkable anisotropy gaps of the magnon dispersion in the AFM ordered parent compounds [78–80, 160]. For the parent compound $BaFe_2As_2$ the anisotropy gaps at $T \ll T_N$ can be ordered as $\Delta^a_{long} > \Delta^b_{t-in} > \Delta^c_{t-out}$, whereas a is the ordering direction[1] of the magnetic moment with *longitudinal* (*long*) spin excitations, b is the other direction in the FeAs-layers with *transversal* (*t-in*) excitations, and c is

[1] parallel to $[1,0,0]_{\text{ort}} = [1,1,0]_{\text{tet}}$

perpendicular to the FeAs-layer yielding the second *transversal* (*t-out*) direction for excitations [78]. This anisotropy means that it is easier to rotate the spins out of the FeAs-layer than within, counter-intuitive for a layered magnet, and indicative of a lifted tetragonal orbital degeneracy. Since the superconducting state is intimately related to magnetic order reminiscent signatures of the AFM gap anisotropy can be found in the SRMs. In optimally Co-doped $BaFe_2As_2$, polarised inelastic neutron scattering (pINS) experiments observed a split SRM emerging below T_c where the lower part is sharp in energy and anisotropic in spin-space, while the upper part is broader in energy but isotropic [155]. Furthermore, pINS experiments on K-optimum and Ni-doped $BaFe_2As_2$ established qualitatively the same picture; an anisotropic and sharp part is peaking at a lower energy than the broader and isotropic one. This picture holds even for 50 % K-doping, which is twice the value to fully suppress AFM order, which thus discards the option that this anisotropy arises from the presence of quasi-static moments [186]. The most extreme cases of split SRMs are found in underdoped $NaFe_{1-x}Co_xAs$ [61,184,192] and $Ba_{1-x}Na_xFe_2As_2$, c.f. Chap. 2, where the part at low energies (SRM-1) dominates the spectra.

Theoretically, various models were proposed to explain the split of the anisotropic part form the isotropic part of the SRM. One model is based on the idea that the isotropic mode (SRM-2) is the usual singlet to triplet spin-exciton, while the anisotropic mode (SRM-1) is attributed to quasi-static correlations in the magnetic phase [227,228]. Another model takes the orbital dependence of the SC gaps into account by constructing an orbital and band selective pairing mechanism, which retains some well defined orbital character in SRM-1 [151]. Based on INS data of $Ba(Fe_{1-x}Co_x)_2As_2$ a more recent study claimed that the anisotropic part of the SRM is an overdamped magnon, which becomes undamped in the SC state and is thus not a true SRM [210].

To test these theoretical ideas pINS experiments in the intermediate doping regime of $Ba(Fe_{1-x}Co_x)_2As_2$ at $x = 4.5\,\%$ (abbreviated as BaCo45) where AFM and SC microscopically coexist were conducted. Contrary to most pINS studies, which were predominantly focussed on the optimum to the over-doped regime, the emergence of the superconducting state from an antiferromagnetically ordered one with sizeable moments $\mu \sim 0.2\,\mu_B$ [22,39] provides a unique platform to study the interplay between both orders. Although many INS studies were already performed on almost the same doping level and reported a SRM appearing at 4.5 meV [40,194,210,229–231], solely the polarisation analysis can provide details of the SC/AFM interplay and can tell whether there is a fundamental difference in comparison to the non-magnetic side of the SC dome in the phase diagram.

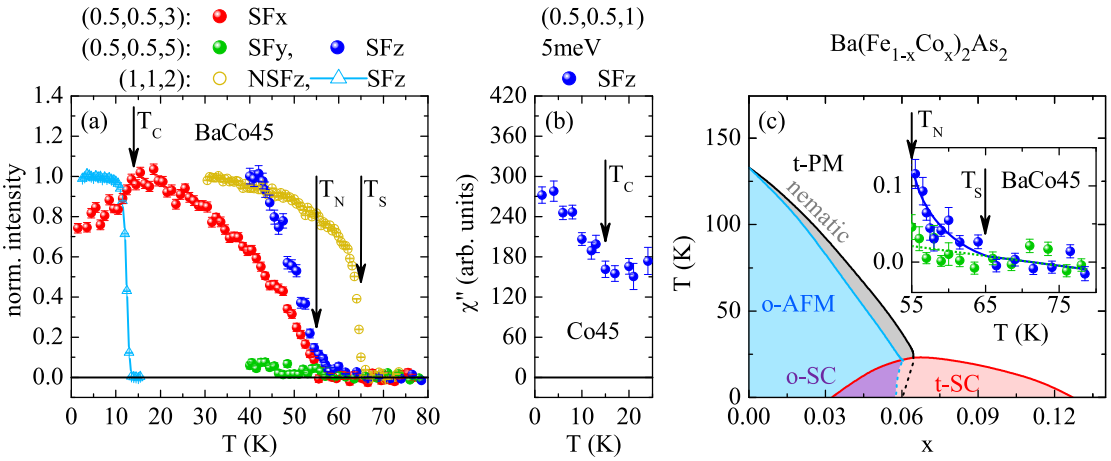

Figure 3.1: Transition temperatures of BaCo45 and schematic phase diagram of $Ba(Fe_{1-x}Co_x)_2As_2$. **(a)** Temperature dependence on the magnetic and nuclear Bragg peaks to define the transition temperatures as $T_s \sim 65\,\mathrm{K}, T_N \sim 55\,\mathrm{K}$ and $T_c \sim 14\,\mathrm{K}$. **(b)** Intensity increase below T_c due to the formation of the spin resonance mode. **(c)** Schematic phase diagram of $Ba(Fe_{1-x}Co_x)_2As_2$, based on Ref. [31], displays the various phases in $Ba(Fe_{1-x}Co_x)_2As_2$, i.e. tetragonal paramagnetic (t-PM), orthorhombic AFM (o-AFM), orthorhombic SC (o-SC) and tetragonal SC (t-SC). The inset magnifies the nematic region in (a) and shows anisotropic diffuse scattering in the spin flip (SF) y and z-channel. Lines are guide to the eyes and data points are published in [153].

3.2 Anisotropic Magnetic Excitations in Underdoped $Ba(Fe_{1-x}Co_x)_2As_2$

Polarised inelastic neutron scattering is employed to elucidate the nature of the SRMs, whereby the corresponding frame of reference for the polarisation analysis is defined in Sec. 6.5. In short, x is parallel to $\boldsymbol{Q}$, y stands perpendicular to x but lies within the scattering plane and z points along its normal. Varying the L component of $\boldsymbol{Q}$ alters the *long*/*t-out* contribution in the SFz channel, with *t-out* being dominant for small L values and *long* for large. In this way, *long* and *t-out* contributions can be disentangled, while the *t-in* component appears in the SFy channel exclusively. Although *long*, *t-in* and *t-out*, respectively a, b and c, are the natural directions to describe the spin-space anisotropy, the actual $\boldsymbol{Q}$ positions, where the spectra were taken, are labelled within the tetragonal notation. Figure 3.2(a)(b) links the different notations in real and reciprocal space.
The various phase transitions in BaCo45 were determined by tracing the tem-

perature dependence of Bragg peak's intensity and are summarised in Fig.: 3.1. Entering the orthorhombic phase causes the domain formation and yields a lower crystal quality which reduces the extinction effects. Consequently, this is observable as an intensity increase of the nuclear Bragg peaks. Accordingly, the intensity uptake of the $(1, 1, 2)$ nuclear Bragg peak at 65 K defines T_s. Similarly, the sharp rise of intensity at the magnetic Bragg peaks $(0.5, 0.5, 3)$ and $(0.5, 0.5, 5)$ is attributed to the formation of long range order, hence $T_N = 55\,\mathrm{K}$, while the ordered moment in BaCo45 is $\mu \sim 0.2\,\mu_\mathrm{B}$ [22,40]. Magnetic scattering at $(0.5, 0.5, 5)$ in the nematic regime is magnified in the inset of Fig.: 3.1(c) and shows that an anisotropy between the SFy and SFz channel is formed below T_s. The nematic phase is characterised by a broken four-fold rotation but a preserved translation symmetry in spin-space. Consequently, the magnetic diffuse scattering in the SFz channel corresponds to *long* magnetic correlations consistent with the ordering direction below T_N. This is also consistent with the spin-space anisotropy which the parent compound $BaFe_2As_2$ develops above T_s [232]. Moreover, the superconducting phase transition is determined by tracing the neutron beam depolarisation in the SFz channel of the $(1, 1, 2)$ nuclear Bragg peak. Since a Helmholtz-coil set-up was used to generate the neutron's polarisation at the sample position via a small magnetic field, this field can be trapped within the sample by cooling below T_c and will be released by heating above. When in this case the polarisation of the incident neutrons is perpendicular to the trapped field direction, experimentally realised by rotating the field below T_c, there will be a abrupt field change and the neutron beam will de-polarise. Therefore, nuclear Bragg peak intensity in the forbidden SF channel can be detected, and the sudden intensity drop upon heating defines $T_c = 14\,\mathrm{K}$. Furthermore the competition between o-SC and o-AFM order for the same electronic state is visualised by the $\sim 26\,\%$ reduction of intensity at the $(0.5, 0.5, 3)$ magnetic Bragg peak, while on the other side the SRM at 5 meV emerges below T_c, c.f. Fig.: 3.1(b). Despite the AFM/SC competition, both phases coexist on a microscopic scale [39–41]. Figure 3.1(c) displays the phase diagram of $Ba(Fe_{1-x}Co_x)_2As_2$, based on the data from Nandi *et al.* [31], whereat here all defined transition temperatures, the suppression of AFM order and the SRM emergence are all in perfect agreement with the literature [31,40,60,116,194,233].

The *long*, *t-in* and *t-out* contributions of the magnetic excitation spectra were separated by neutron-polarisation analysis. Within the given frame of reference, the *t-in* contributions are exclusively found in the SFy channel. To disentangle the *long* and *t-out* contributions which are both found in the SFz channel, scans at $(0.5, 0.5, \mathrm{L})$ with L = 1, 3 and 5 were conducted, c.f. Fig.: 3.2. These $\boldsymbol{Q}$-positions correspond all to the AFM Brillouin zone (BZ) centre, while the variation of L changes the projection of scattering vector $\boldsymbol{Q}$ on a and c, and thus respectively promotes(discriminate) the *long* (*t-out*) component due to the geometry factor $\sin^2(\alpha)(\cos^2(\alpha))$. Note that in a pINS experiment only the perpendicular part

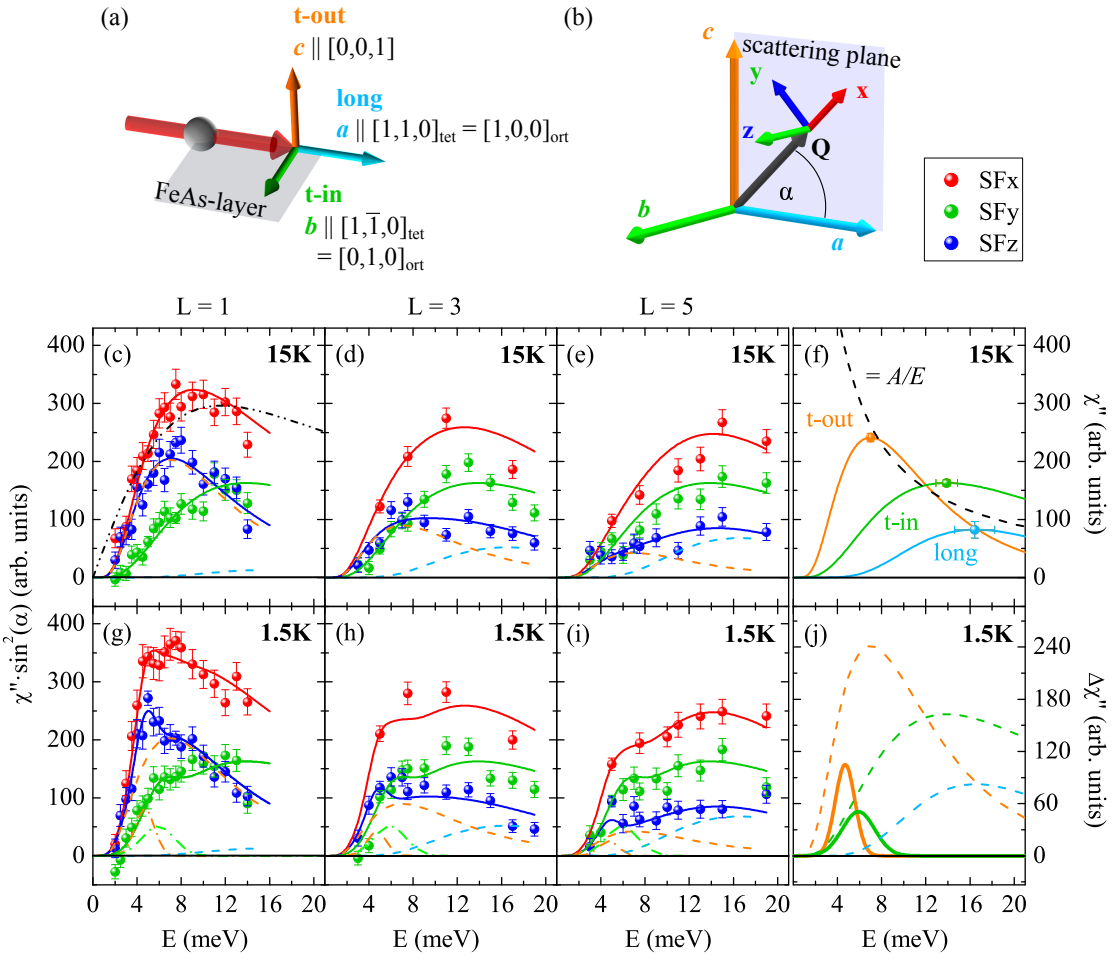

Figure 3.2: Spectra of magnetic excitations in the normal and superconducting state at various L values. Frame of reference in real space **(a)** to define χ''_{long}, χ''_{t-in} and χ''_{t-out}, and in reciprocal space **(b)** to show how the susceptibilities can be extracted via pINS. **(c)-(e)** The imaginary part of the dynamical susceptibility at 15K is fitted by three log-normal functions, which take the corresponding geometry factors at (0.5,0.5,L) with L = 1, 3 and 5 into account, respectively. For comparison a single relaxor function is added in (c) to show that this function describes the spectra improperly. **(f)** Summary of the extracted anisotropic AFM gap values following a simple $1/E$ relation. **(g)-(i)** Same scans as in (c)-(e), respectively, in the SC phase at 1.5 K where only two additional components in χ''_{t-in} and χ''_{t-out} are required to consistently describe the data. The SRM as well as the AFM gaps (dashed lines and same as in (f)) are presented in **(j)**. The data points are published in [153].

of $\boldsymbol{Q}$ and neutron polarisation $\boldsymbol{P}$ contributes to the SF channel, c.f. Tab.: 6.2. Therefore, the spectrum in the SFz channel at $(0.5, 0.5, 1)$ is dominated by the *t-out* component and at $(0.5, 0.5, 5)$ by the *long* one. A direct measure for the background is given by SFy + SFz - SFx, which was fitted by a polynomial and subtracted from the data. Furthermore, the data were corrected for the Fe^{2+} magnetic form factor[2], the Bose factor and for higher-order contaminations in the monitor. Consequently, the data corresponding to the imaginary part of the dynamical susceptibility, however in arbitrary units, multiplied by the geometry factor $\sin^2(\alpha)$. The spectra at 15 K contain only the response of the AFM gaps and were self-consistently fitted by the three susceptibilities χ''_{long}, χ''_{t-in}, and χ''_{t-out}, while the response in the SFx channel is always the sum of SFy and SFz. Thereby, each anisotropy gap is phenomenologically well described by a log-normal function

$$L_N(E) = A\mathrm{e}^{-\frac{1}{2}\left(\frac{\ln(E_c)-\ln(E)}{w}\right)^2}, \tag{3.1}$$

whereas each function has only three free parameters. Additionally, the intrinsic asymmetric line-shape of the log-normal function takes the distortion due to the convolution process with the instrumental resolution[3] as well as a disorder induced broadening of the spectra into account. Moreover, there is a crossover from spin-waves to diffusive spin excitations when the AFM gap closes towards optimal doping [234]. In the latter scenario, spin excitations would be described by the relaxor function, which is illustratively fitted to the SFx channel in Fig.: 3.2(c), black dashed line. As there are still sizeable AFM gaps present, the relaxor model inappropriate to describe the data. Therefore, the spectra in the o-AFM phase of BaCo45 can be well understood as a spin-wave-like response with disorder [40, 78, 234].
The fit-results of the anisotropy gaps are summarised in Fig.: 3.2(f) and their intensity follow a $1/E$-relation, which is expected for simple magnons. In the two transversal directions, χ''_{t-out} and χ''_{t-in}, the well-defined anisotropy gaps of the parent compound at 11.6 meV and 18.9 meV are renormalised to 7 meV and 13.9 meV, respectively [78]. Furthermore, there is a sizeable amount of signal in the *long* channel, and the corresponding gap is determined at ~ 16 meV. The anisotropy gaps of BaCo45 and $BaFe_2As_2$ are listed in Tab.: 3.1. Here the estimate from Qureshi *et al.* [78] for Δ_{long} is given and not the 24 meV reported by Wang *et al.* [79] as there is still some uncertainty. For the two transversal gaps, both reports are consistent with each other. However, the intensity relation with $1/E$ for simple magnons not fulfilled for Δ_{long} compared to Δ_{t-out} and Δ_{t-in} in $BaFe_2As_2$ [78, 79].

[2] numerically approximated by three Gaußians, whereas the corresponding values are tabulated at `https://www.ill.eu/sites/ccsl/ffacts/ffachtml.html`, or in the International Tables of Crystallography C, Chap. 4, J. P. Brown (3rd edition, 2004)

[3] the finite volume of the resolution ellipsoid captures the beginning of the steep spin-wave dispersion and thus the partial integration of many symmetric curves appears as an asymmetric feature at energies above the AFM gap [230, 234]

Table 3.1: AFM gaps of BaCo45 and $BaFe_2As_2$.

Gap	BaCo45	$BaFe_2As_2$ [78]
Δ_{t-out}	7 meV	11.6 meV
Δ_{t-in}	13.9 meV	18.9 meV
Δ_{long}	$\sim$ 16 meV	$\gtrsim$ 35 meV

Consequently, χ''_{long} misses spectral weight and thus the gap must extend to energies $\gtrsim 35$ meV according to [78] and density functional theory (DFT) studies [235, 236]. The signal observed at ~ 24 meV in the *long* channel is alternatively interpreted as a two-magnon process [237], whose polarisation is always longitudinal but with much less intensity. Nonetheless, in BaCo45 Δ_{long} does not miss intensity, since it increases with increasing L, as expected. Consequently, there is a large renormalisation of the longitudinal gap and it, like the two transversal ones, follows a $1/E$ relation.
The structural phase transition at 65 K in BaCo45 leads to the formation of orthorhombic twin domains, which are measured simultaneously. As a result, the observed spectra are the superposition of the responses from the BZ centre of the one twin and the BZ boundary of the other twin. False signals from the "wrong" twin domain can be excluded in the probed energy regime, since the steep magnon dispersion could only lead to contributions around 200 meV [201, 234], which is further supported by recent measurements on detwinned samples of $Ba(Fe_{1.935}Ni_{0.065})_2As_2$ [238]. For this reason, the presented data do not incorporate false signal from the second twin, whose response can thus be ignored safely.

The response in the SC phase and its corresponding analysis is presented in Fig.: 3.2(g)(h)(i). Assuming that the AFM anisotropy gaps are unaffected by the SC transition, the nine spectra at the three probed scattering vectors are described identically by the susceptibilities at 15 K, while all additional intensity is attributed to the SRMs, solely. The presence of two distinct SRMs in the SFz and SFy channel can be best visualised in Fig.: 3.3. In the SFy channel, only χ''_{t-in} can contribute with full geometry factor. Accordingly, the data at L = 1, 3, and 5 were (weighted) averaged and the emerging SRM is fitted by a Gaußian peaking at 5.9 meV. On the other hand, χ''_{long} and χ''_{t-out} contribute both to the SFz channel according to their geometry factors, c.f. Tab.: 6.2. However, concerning the SRM the χ''_{long} component can be ignored since longitudinal fluctuations are suppressed below 8 meV, c.f. Fig.: 3.2. Thus the SRM in the SFz channel is *t-out* polarised, which is further corroborated by the L dependence in Fig.: 3.4. Therefore, the spectra at (0.5,0.5,L) with L = 1, 3 and 5 in the SFz channel were fitted by those log-normal function, obtained from the normal state at 15 K, and a Gaußian resonance mode whose geometry factor corresponds to the *t-out* polarisation. Figure 3.3(c) shows that the SRM in χ''_{t-out} at L = 1 peaks at 4.7 meV, while the SRM in SFy channel is given in Fig.: 3.3(d). Although both resonance modes display a different polarisation and peak at different energies, their sum perfectly agrees

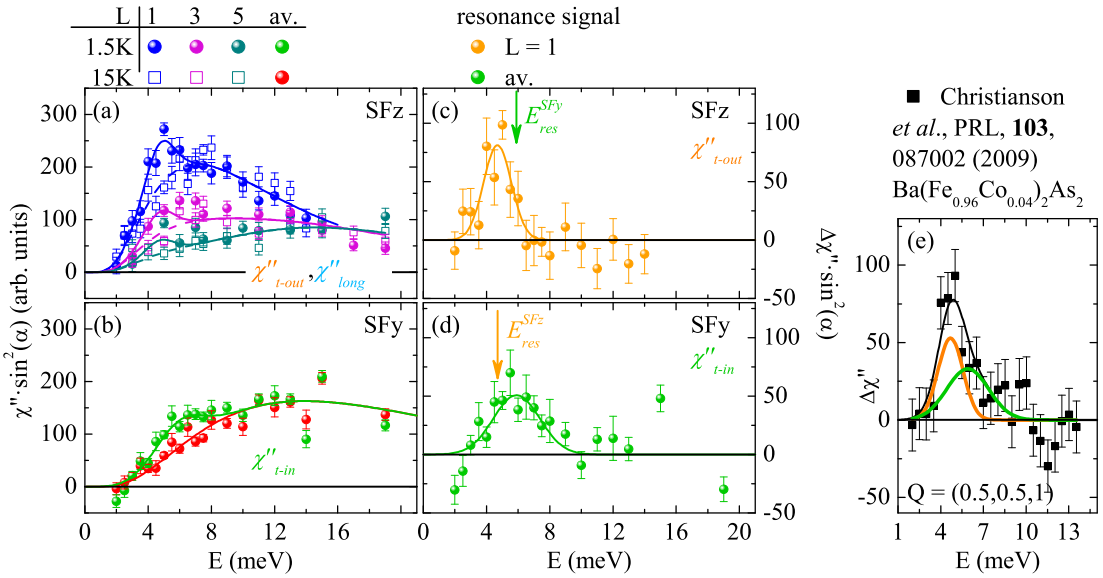

Figure 3.3: Two anisotropic resonance modes below T_c. **(a)** Summary of the SFz data at 1.5 K and 15 K with the corresponding fits from Fig.: 3.2. **(b)** The SFy channel at $L = 1, 3$ and 5 in Fig.: 3.2 contains only χ''_{t-in} contributions allowing all L values to be averaged and to be described as one, respectively for 1.5 K and 15 K. **(c)(d)** The intensity difference between 1.5 K and 15 K reveal that the SRMs peak at different energies; for SFz at 4.7 meV (χ''_{t-out}) and for SFy at 5.9 meV (χ''_{t-in}), respectively. The data points are published in [153].

with the unpolarised data from Christianson *et al.* [194], c.f. Fig.: 3.3, and other reports in the literature [40,229,230,239]. The polarisation analysis of the SRMs of χ''_{t-out} and χ''_{t-in} can be further corroborated by inspecting the L-dependence, c.f. Fig.: 3.4. Again, the given frame of reference promotes χ''_{t-out} and discriminates χ''_{long} for small L values in the SFz channel, while promotion and discrimination are reversed at large L values. Therefore, the fraction of χ''_{long} can be determined via

$$I\left(\alpha(\mathrm{L})\right) = S \cdot f^2(Q)\left((1-p)\cos^2\left(\alpha(\mathrm{L})\right) + p\sin^2\left(\alpha(\mathrm{L})\right)\right),$$
$$p = \frac{\chi''_{long}}{\chi''_{long} + \chi''_{t-out}},$$

with scaling factor S, Fe^{2+} magnetic form factor $f(Q)$ and $\alpha(\mathrm{L})$ the angle between $\boldsymbol{Q}$ and $\boldsymbol{a}$ as defined in Fig.: 3.2(b). The L dependence in the SFy channel can be described by the same formula, but p is always fixed to 0.5 as there is no geometrical dependence next to the magnetic form factor. In the orthorhombic

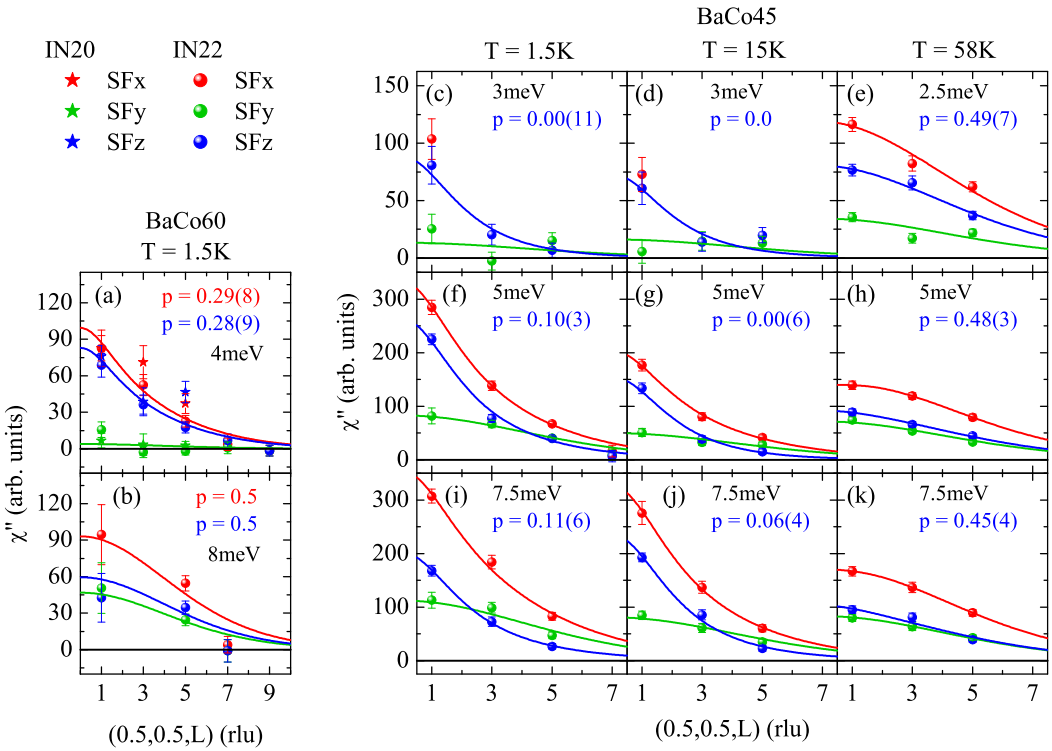

Figure 3.4: Polarisation analysis of the spin resonance modes in BaCo45 and BaCo60. The polarisation of the SRMs is extracted by analysing the L dependence via Eq.: (2.1), whereas p describes the χ''_{long} contribution. **(a)(b)** Analysis of the L dependence for BaCo60 at 4 meV and 8 meV, respectively. While the lower mode contains 28 % of χ''_{long} and a negligible fraction of χ''_{t-in}, the upper mode is isotropic. **(c)-(k)** Same analysis for BaCo45 in the SC phase at 3 meV, 5 meV and 7.5 meV, when not labelled differently, at 1.5 K, above T_c but with in the o-AFM phase at 15 K and above T_N at 58 K. The data points are published in [153].

state at $T_N < T = 58$ K this fit yields $p = 0.5$ within errorbars at 2.5 meV, 5 meV and 7.5 meV. Although there is no $\chi''_{long}/\chi''_{t-out}$ anisotropy χ''_{t-in} has 50 % less intensity at 2.5 meV, which documents the accumulation of spectral weight in the two magnetically soft directions before the actual AFM order sets in. The lack of $\chi''_{long}/\chi''_{t-out}$ anisotropy just 3 K above T_N indicate how close o-AFM and c-AFM order in configuration-space are. In addition to that, spectra at $(0.5, 0.5, 1)$ were taken in the "nematic" regime at 58 K $> T_N$ and at 70 K $> T_s$ in the t-PM phase, which are presented in Fig.: 3.5. All SF and NSF channels were fitted simultaneously and compliant with Tab.: 6.2 by a single relaxor. Above T_s in the t-PM

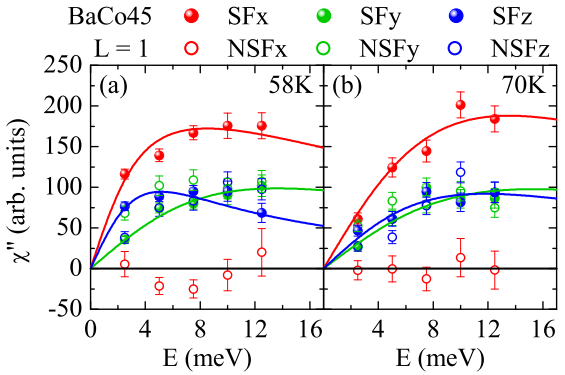

Figure 3.5:
Normal state response in BaCo45. (a) The spectra at 58 K in the SFy and SFz channel is described by a relaxor function, which shows an anisotropic response. **(b)** Above T_s at 70 K the response becomes isotropic.

phase (SFy/NSFz) and (SFz/NSFy) display identical relaxation energies Γ and intensities, which documents that the spin-space anisotropy has vanished. Below T_s, Γ is unaffected in the (SFy/NSFz) channel, while it shifts to lower energies in the (SFz/NSFy) channel indicating the AFM ordering direction. However, at 15 K in the o-AFM and at 1.5 K in the o-SC phase there is only a negligible *long* component, which is consistent with the interpretation that longitudinal low-energy spin excitations are gapped below T_N due to the ordering of sizeable magnetic moments, c.f. Fig.: 3.4(c)-(j). Accordingly, $p \sim 0$ and the SRM in SFz channel appears only in χ''_{t-out}. Furthermore, the same analysis of the L dependence is conducted for the two resonance energies of BaCo60, i.e. at $E_{\text{Res-1}} = 4$ meV and $E_{\text{Res-2}} = 8$ meV, c.f. Fig.: 3.4(a)(b). At E_{SRM-1} χ''_{t-in} is almost zero, while the slower decay of intensity with increasing L in SFz channel reveals a *long* contribution of 28 %. Similar results are reported in optimum doped $Ba(Fe_{1-x}Ni_x)_2As_2$ [97], overdoped $Ba_{1-x}K_xFe_2As_2$ [186] and underdoped $NaFe_{1-x}Co_xAs$ [184]. On the other hand at E_{SRM-2}, SFy and SFz are almost equal in intensity and $p = 0.5$, which proves that the resonance mode is fully isotropic in spin-space as it is expected from theory [57].
The SRM in BaCo60 is explored in more details in the next section.

3.3 Spin Resonance Mode in $Ba(Fe_{0.94}Co_{0.06})_2As_2$

In order to explore details of the spin resonance mode in BaCo60 further, the same sample was used as in the report of Steffens *et al.* [155], where the split and anisotropic SRM in $Ba(Fe_{0.94}Co_{0.06})_2As_2$ was observed for the first time. BaCo60 is the optimal Co-doped $Ba(Fe_{1-x}Co_x)_2As_2$ compound and directly located at the quantum critical point (QCP) in the phase diagram, c.f. Fig.: 3.1(c). Upon decreasing temperature, at this doping level in the phase diagram, the transition lines delineating the nematic regime and the t-SC phase are crossed. A particularity of the T_s transition line is its back-bending below T_c, i.e. SC suppresses magnetic fluctuations, which cause the orthorhombic distortion due to strong mag-

netoelastic coupling (MEC). Accordingly, the intensity on a nuclear Bragg peak increases towards T_c as the orthorhombic distortion reduces multiple scattering and extinction effects, and decreases below T_c when the orthorhombic distortion is reverted. Therefore, T_c can easily be determined by tracing the $(1,1,2)$ nuclear Bragg peak intensity, c.f. Fig.: 3.8. The line is a Gaußian fit to the data which yields $T_c = 23.85(10)\,\mathrm{K}$ in agreement with its previous value [155]. Although the T_c value is unaffected by time, the 2.88 g heavy single crystal is cracked into (presumably) three pieces, as the rocking scan over the $(1,1,0)$ nuclear Bragg peak in Fig.: 3.6 clearly shows. On the one hand side, the sample is wrapped tightly in aluminium foil, which makes an easy realignment more complicated. On the other hand, this wrapping keeps all pieces together especially if the sample is cracked multiple times instead of three. This cracking can also be observed in the phonon scan in Fig.: 3.7(a) as there are three peaks instead of one, which would be the normal case, c.f. phonon scans in $LiFe_{1-x}Co_xAs$ (Chap. 4) and in $Ba_{1-x}Na_xFe_2As_2$ (Fig.: A.2.4). Nonetheless, the phonon at $(0.2, 0.2, 8)$ in BaCo60 is fitted via the Reslib routine by assuming the acoustic limit, i.e. a linear dispersion. In order to model the cracked sample, the dispersion is split into three parts by adding a constant offset

$$\omega_1(q) = cq - \Delta_1, \quad \omega_2(q) = cq, \quad \omega_3(q) = cq + \Delta_3 \tag{3.2}$$

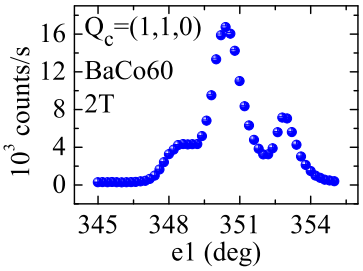

Figure 3.6: Rocking scan over $(1,1,0)$ in BaCo60.

which corresponds to a constant shift in $\boldsymbol{Q}$ and thus accounts for the misaligned cracked pieces. Accordingly, the dispersion is shown in Fig.: 3.7(b), while the yellow ellipsoids are the instrumental resolution of 2T spectrometer within the Cooper-Nathans approximation [189–191]. Thereby, the overall scaling factor for absolute unit normalisation is determined as $\Phi_{scale} = SCALE \cdot (A_1 + 1 + A_3)$. However, magnetic excitations are not affected noticeably as Reslib fits to the $\boldsymbol{Q}$-scans at 2 meV, 4 meV and 7.5 meV in Fig.: 3.7(c)-(e) indicate. Two different models were employed, first the $\boldsymbol{Q}$-width in the [H,K]-plane is described by a single Gaußian (blue dashed line), while in the second model, the $\boldsymbol{Q}$-width is given by three Gaußians, whose centres are shifted from each other according to the phonon scan (grey solid line). In the second model the width is a global fit-parameter, and the amplitudes are weighted with respect to the phonon scan. Despite the differences in both models, the actual Reslib-fit is almost identical in both cases. Only at energies below ~ 4 meV a slightly distorted line-shape is obtained by the triple-Gaußian model. Therefore, any effect on the inelastic spectra of magnetic excitations, due to the cracked sample can be safely neglected.

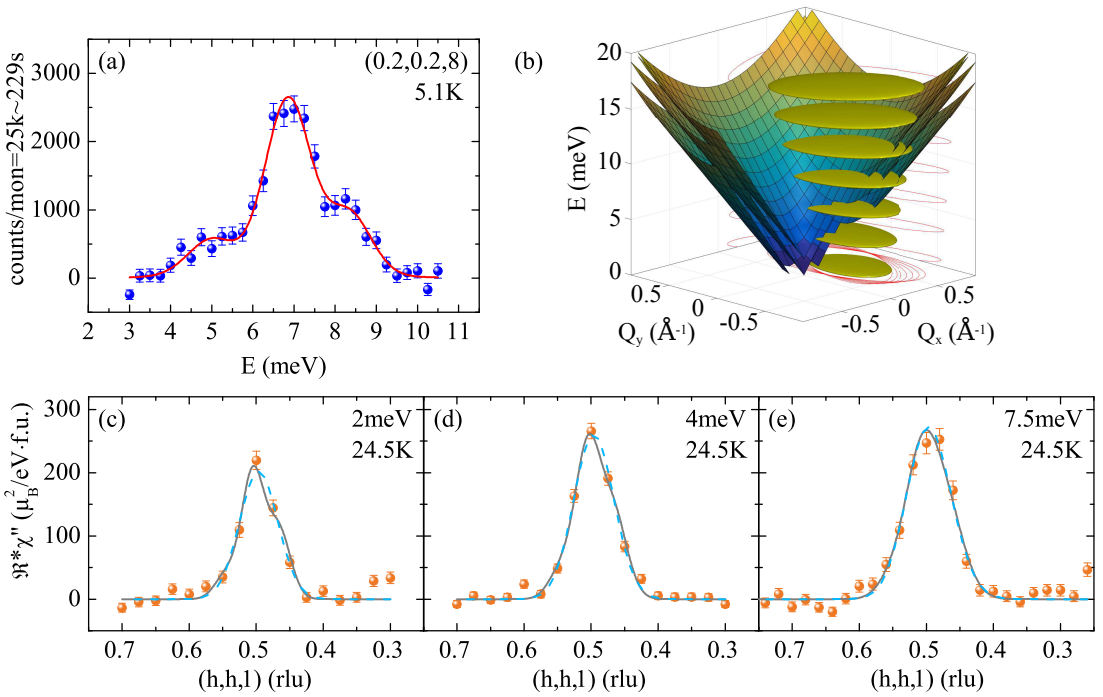

Figure 3.7: Phonon and Q-scans in BaCo60. **(a)** Fit of the convolution of instrumental resolution and the modelled dispersion to the phonon scan via RESLIB at $(0.2, 0.2, 8)$ and 5.1 K. Since the sample consists of three crystallites the corresponding linear phonon dispersion is modelled as three linear functions with equal slope but off-setted against each other. **(b)** Modelled phonon dispersion and the resolution ellipsoid of 2T spectrometer. **(c)(d)(e)** $\boldsymbol{Q}$-scans at 24.5 K and at 2 meV, 4 meV and 7.5 meV, respectively. In each case the model for the RESLIB fit is either a simple Gaußian (blue dashed line), or three Gaußians where each centre is shifted according to the phonon scan in (a) (solid grey line).

Transport experiments, like susceptibility measurements in a SQUID, observed the SC transition at 24 K. To check by neutron scattering, whether this value has changed with time, the temperature dependence of the $(1, 1, 2)$ nuclear Bragg peak is traced, c.f. Fig.: 3.8(a). In a previous experiment on the same sample, Steffens *et al.* [155] observed an increase of intensity, which is reverted at T_c and is thus easily observable as a maximum. The dependence can be understood as extinction effects[4], which are reduced when orthorhombic domains are formed and

[4] a measure for multiple scattering

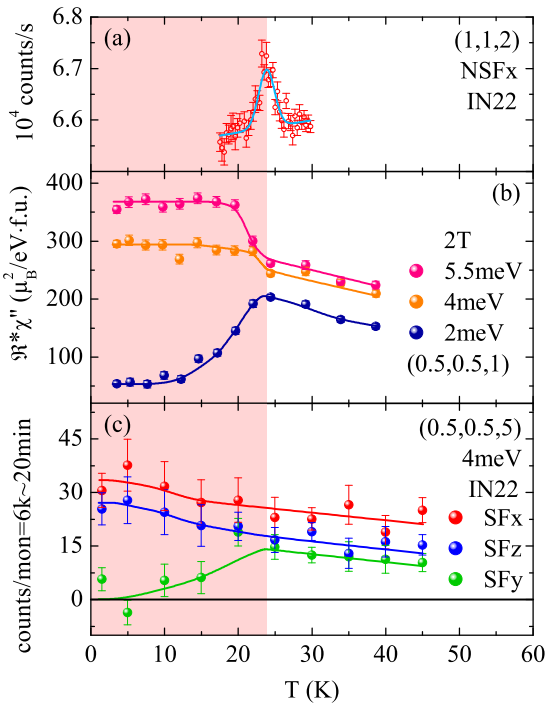

Figure 3.8: Temperature dependence in BaCo60. **(a)** The SC transition can be seen as an extinction effect on the nuclear Bragg peak $(1, 1, 2)$, due to residual fluctuating magnetic order and it's suppression below T_c. **(b)** SC gap opening and SRM formation yields a reduction low-energy magnetic excitations, 2 meV, while there is a promotion of scattering intensity at 4 meV and 5.5 meV below T_c. **(c)** At 4 meV pINS shows that excitations are rather isotropic above T_c while a remarkable anisotropy develops below; χ''_{t-in} becomes almost completely suppressed.

consequently yield an intensity increase. In that context, Nandi *et al.* [31] showed that the orthorhombic distortion is reverted below T_c, i.e. the extinction coefficient increases, the nuclear Bragg peak intensity decreases and a maximum at T_c = 23.90(10) K is formed. Below T_c the SRM in BaCo60 is formed at the expense of low-energy spin fluctuations. Consequently, excitations at 2 meV become gapped and additional spectral weight is accumulated at higher energies, c.f. Fig.: 3.8(b). Moreover, a particular spin-space anisotropy at $E_{SRM-1} = 4$ meV develops at T_c as *t-in* fluctuations become almost completely suppressed and thus the signal changes from isotropic to *long*/*t-out* polarised as shown in Fig.: 3.8(c). This is consistent with the results from the L-dependence in Fig.: 3.4(a). However, since the SFz channel at $\boldsymbol{Q} = (0.5, 0.5, 5)$ senses to $\sim 82\,\%$ the *long* component it is remarkable that even in the absence of strong symmetry breaking fields, like magnetic order or large orthorhombic distortions, a huge C_2 anisotropy is developed in the SC-phase, although the FeAs-layers display C_4 symmetry. This anisotropy can solely be assigned to the SC phase, as the very small orthorhombic distortion is even reverted below T_c [31], while long-range AFM order is not realised. Figure 3.9 displays the corresponding E-scans at $(0.5, 0.5, 5)$ in the SC and NS phase, respectively in (a) and (b). For both scans the background was determined by SFy + SFz - SFx, linearly fitted and subtracted from the data which were further corrected for the Bose-factor. In the SC phase, the spin-space anisotropy extends up to ~ 6 meV, while it is still perceptible in the NS state at 29.9 K. Single relaxor functions were fitted to SFy and SFz in the NS state with the boundary condition

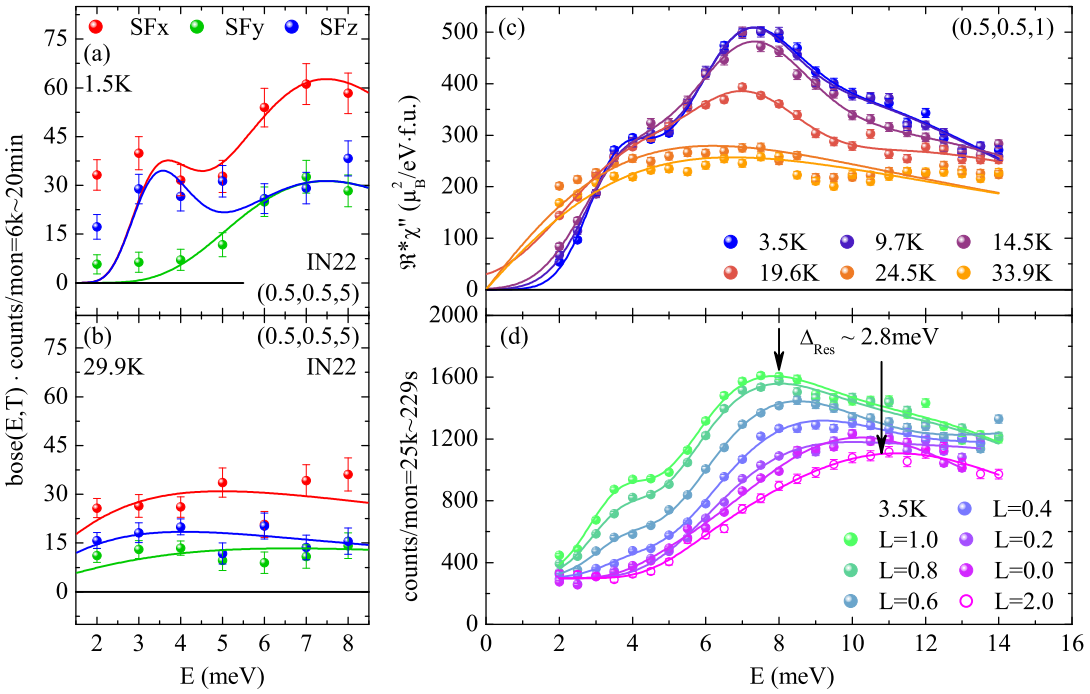

Figure 3.9: Energy dependence in BaCo60. **(a)** Anisotropic and isotropic part of the SRM at $(0.5, 0.5, 5)$ and 1.5 K obtained with polarised neutrons on IN22 spectrometer. Lines are log-normal functions and serve as guides for the eye to indicate that the low-energy spin-space anisotropy extents to ~ 6 meV. **(b)** Same scan as in (a) but in the normal state at 29.9 K. Sizeable low-energy spin-space anisotropy is absent. The lines are relaxor fits. **(c)** E scans at $(0.5, 0.5, 1)$ with unpolarised neutrons at 2T spectrometer at various temperatures to show how the SRM evolves with temperature. Solid lines are single relaxors fitted by the RESLIB routine to the data, while the dashed lines serve as a guide for the eye. **(d)** Same set-up as in (c) to show how the mode disperses from the Brillouin zone centre to the boundary. The dashed lines serve a guide for the eye.

of SFx = SFy + SFz. Thereby, the anisotropic behaviour of the two SF channels is revealed, which is a precursor of the anisotropy below T_c.
Generally, the origin of the spin-space anisotropy in the SC phase must be found at the multi-band and multi-orbital Fermi surface (FS), where the d_{xz} and d_{zy} orbitals are degenerate in the t-PM phase [50, 76]. This orbital degeneracy is lifted in the o-AFM phase [49, 50, 76, 240] and presumably orbital dependent SC-gaps $\Delta_{d_{xy}} \neq \Delta_{d_{yz}} \neq \Delta_{d_{xz}}$ open below T_c as it is reported for the related compound $NaFe_{1-x}Co_xAs$ [143]. Consequently, within an orbital selective pairing mechan-

ism [151] intra- and inter-orbital scattering is very different, thus the resonance energies will be different, though both scatterings/resonance modes take place at the same wave-vector $\boldsymbol{Q}$ [193]. Although, the orbital anisotropy decreases towards optimal and over-doping [143, 145, 210, 211] this scenario can be reconciled with the presented data here if the orbital degeneracy is still lifted to generate the anisotropic low-energy SRM in BaCo60.
The split SRM in BaCo60 can be best observed with polarised neutrons [155] and has been overlooked in an initial and unpolarised study [131]. Nonetheless, SRM-1 is clearly visible Fig.: 3.9(c) as a shoulder at 4 meV in the excitation spectrum at $(0.5, 0.5, 1)$ even by unpolarised neutrons. The solid lines in the normal state are Reslib-fits of the single relaxor to the data, while the dashed lines correspond to the data below T_c and serve as guides to the eye. By normalising the normal state response to absolute units (convolution of instrumental resolution and $\chi''(\boldsymbol{Q}, E)$) and rescaling the SC data accordingly, identical values (within error bars) of SRM-2 in comparison with Inosov *et al.* [131] are obtained. Additionally, SRM-2 disperses along L as given in Fig.: 3.9(d) and possesses a band-width of ~ 2.8 meV, which is consistent with the dispersion in $Ba_{1-x}Na_xFe_2As_2$ in Sec. 2.2.2 as well as the universal doping vs. band-width behaviour in Ref. [202]. On the other hand, SRM-1 is suppressed at the BZ boundary, similar to underdoped $Ba_{1-x}Na_xFe_2As_2$, but an identical bandwidth with SRM-2 cannot be deduced from the data. In Appendix A.4 a more detailed analysis of the intensity dependence and L dispersion is attempted, but still no dispersion of SRM-1 can be resolved. The L dispersion of the SRM indicates that residual interlayer spin correlations still play a role [202], which in the parent compounds cause upwards dispersing AFM gaps [79, 201]. Although, data is scarcely available which trace the L dependence of the SC gap an intriguing relation was reported by an ARPES study on $Ba_{0.6}K_{0.4}Fe_2As_2$ [203]. While the gap is constant on the electron pocket (γ, δ-band at the $\boldsymbol{X}$-point) it varies on the hole-pocket (α-band) and displays a maximum of 12 meV at the $\boldsymbol{\Gamma}$-point but a minimum of 9 meV at the $\boldsymbol{Z}$-point, BZ boundary. In a naive picture, E_{SRM} scales with Δ_{SC} which consequently would correspond to a downward dispersion of the SRM from the $\boldsymbol{\Gamma}$-point (BZ centre, odd L values) to the $\boldsymbol{Z}$-point (BZ boundary, even L values), contrary to the experimental observation in $Ba_{0.67}K_{0.33}Fe_2As_2$, where the SRM is L independent [198]. Therefore, the L dispersions of E_{SRM} and Δ_{SC} are not trivially related to each other, which is an open issue to be explored in the future, both theoretically and experimentally.

3.4 Summary and Discussion

The spin resonance modes in BaCo45 and BaCo60 are fundamentally different from each other; hence it is crucial whether superconductivity emerges from an antiferromagnetically ordered state or from a paramagnetic one. In BaCo45 with microscopical coexisting AFM/SC order [39–43] the SRM is fully anisotropic, while in non-magnetic BaCo60 the SRM displays an anisotropic shoulder at low energies next to an isotropic mode at larger energies. Particularly, in BaCo45 the SRM emerges only in the two transversal directions and peaks in χ''_{t-out} at 4.7 meV hence at a lower energy than in χ''_{t-in} where it peaks at 5.9 meV. The longitudinally polarised signal does not contribute to the SRM. Additionally, the origin of this spin-space anisotropy can be associated with the AFM gaps opening below T_N. Like in "simple" Chromium [224] the onset of AFM order reconstructs Fermi surface (FS) and gaps parts of it. Indeed ARPES experiments observed that the FS in $BaFe_2As_2$ undergoes a massive reconstruction below T_N where the degeneracy of the d_{zy} and d_{xz} orbitals are lifted [49, 50]. Consequently, the electronic density of states (DOS) is partially gapped, while the remaining part is almost exclusively found in the d_{xz} orbital [76]. In $Ba(Fe_{0.955}Co_{0.045})_2As_2$ the d_{zy} and d_{xz} orbitals are split by ~ 20 meV [49], which yields an orbital-polarised C_2 symmetric FS. This implies the observed strong magnetic anisotropy [76]. Disregarding these details for a second, less DOS at ε_F causes a smaller Δ_{SC} and thus a reduced T_c in BCS theory [113]. Within this simple picture, it is easy to understand why T_c is small for underdoped $Ba(Fe_{1-x}Co_x)_2As_2$ and there is no longitudinal contribution to the SRM in BaCo45. In comparison to the parent compound $BaFe_2As_2$ Δ_{long} is strongly renormalised, but still much larger than the SC gap value $\Delta_{SC} = 8\,\text{meV} < \Delta_{long}$ determined in ARPES experiments [210]. Therefore, *long* fluctuations cannot interplay with SC and thus cannot contribute to the exchange energy minimisation [118]. However, high-energy *long* fluctuations still do contribute to the pairing. On the other hand, in BaCo60 long-range static magnetic order is absent and the anisotropic part at 4 meV, SRM-1, displays 28 % of *long* contribution. Accordingly, a sizeable *long* signal would thus be observable at low energies in BaCo45 if AFM and SC order were mesoscopically phase separated. This is not the case, and once again the microscopic phase coexistence of both orders is confirmed in line with NMR and μSR studies [39, 41].
Table 3.2 summarises the responses of BaCo45 and BaCo60. While the spin excitations for both compounds can be described by an in spin-space isotropic relaxor at elevated temperatures above their prime order, they gradually turn to be anisotropic upon approaching the ordering transition. The developing anisotropy can easily be explained theoretically within a random phase approximation (RPA) which takes SOC into account [81, 241]. In the spin-triplet superconductor Sr_2RuO_4, which is close to an incommensurate magnetic ordering transition, but not reaching it, pINS experiments also observed such anisotropic relaxor

responses [242]. The FeSC-version of a compound close to but not reaching magnetic order, where also a spin-space anisotropy is observed is LiFeAs [243].
Here in the two Co-doped samples BaCo45 and BaCo60 the relaxor with the smaller relaxation energy Γ is observed in the SFz channel, which senses *long* and *t-out* contributions, meaning the contributions along the two magnetically soft directions a and c. Additionally, in both cases, the relaxor in the SFy channel always displays the larger relaxation energy and thus documents that b is the magnetically hard axis. Furthermore, this spin-space anisotropy is carried forward into the SC phase, i.e. the SRMs, as the anisotropic shoulder at low-energies in BaCo60 is polarised in the same way. On the other hand, a sizeable signal, polarised along the hard axis, is suppressed for low energies and peaks at 8 meV, which is precisely the energy determined from the universal scaling ratio Eq.: (1.5). In contrast, the SRM in BaCo45 appears only in the two transversal directions b and c, while longitudinal fluctuations along a are missing due to the large AFM gap. Consequently, the spin resonance modes in BaCo45 and BaCo60 are fundamentally different depending on whether SC emerges from the t-PM, or from the o-AFM phase.
In BaCo45 the magnetic anisotropy gap Δ_{t-out} and the anisotropic SRM are unambiguously determined. Therefore, a recent explanation on the origin of the split SRM, stating that SRM-1 and Δ_{t-out} are the same excitations, is discarded clearly [210]. Moreover, the definitive explanation for the anisotropic SRMs, their evolution with increasing doping/decreasing AFM order, must reconsider an orbitally resolved multi-band structure and the orbital-selective pairing which arises therein. In addition to that, the SRM-2 displays a L dependence, which resembles the one for the AFM dispersion in the parent compound and thus points to non-negligible inter-FeAs-layer coupling. Intriguingly, SRM-1 in BaCo60 seems not to

Table 3.2: Comparison of magnetic excitations in BaCo45 and BaCo60. The evolution of the spin-space anisotropy from the t-PM to the SC phase for under doped BaCo45 and optimal doped BaCo60 are summarised.

	superconducting		**normal state**
	$\boldsymbol{E_{res}}$	**character**	$\boldsymbol{T > T_c}$
under dop. BaCo45	4.7 meV	χ''_{t-out}	$T < T_N$ gapped $T_N \lesssim T$ anisotropic relaxor
	5.9 meV	χ''_{t-in}	$T_S < T$ isotropic relaxor
optimum dop. BaCo60	4 meV	28 % χ''_{long} + 72 % χ''_{t-out}	$T_c \lesssim T$ anisotropic relaxor
	8 meV	isotropic	$T_c \ll T$ isotropic relaxor

disperse along L, in stark contrast to SRM-2 and the SRMs in $Ba_{1-x}Na_xFe_2As_2$. While the L bandwidth $B_w \sim 2.8\,\text{meV}$ in BaCo60 is directly observed here, Pratt *et al.* reported $B_w = 3\,\text{meV}$ and $B_w < 0.8\,\text{meV}$ for 4.7 % and 8 % Co doping respectively [229]. Apparently, and in line with the results for $Ba_{1-x}Na_xFe_2As_2$ in Chap. 2 the L dispersion quickly levels off when the system is moved away from the critical doping concentration as indicated by the plot from Lee *et al.* [202]. Note that in the heavy-fermion system UPd_2Al_3 with coexisting AFM/SC order [244, 245] the SRM is also L dispersive as well as in the non-magnetic compound $CeCoIn_5$ with strong interlayer spin couplings [226].
In a broader view, the behaviour of the SRM is directly related to the details of the pairing mechanism when superconductivity is mediated by paramagnons. Accordingly, the L dependence is related to residual interlayer spin correlations (assuming L is perpendicular to the relevant layers). However, when this observation is reconciled with an orbital-dependent pairing mechanism in FeSCs, the situation becomes intricate. On the one hand side, the resonance energy is related to the SC gap linearly, and hence its upwards dispersion indicates a larger SC gap at the $\boldsymbol{Z}$-point than at the $\boldsymbol{\Gamma}$-point. On the other hand, the L dependence of the SC gap is scarcely studied, and in $Ba_{1-x}K_xFe_2As_2$ it intriguingly displays the opposite behaviour; Δ_{SC} is constant on the (γ, δ)-electron pockets, but it disperses downwards on the (α)-hole pocket [246]. Despite being a fine detail in the complete theory to describe superconductivity in FeSCs, it is nonetheless an open issue.

The spin-space anisotropy of the SRM in BaCo45 and its evolution with increasing doping towards BaCo60 highlights the complexity when superconductivity emerges from an antiferromagnetic state. Particularly, when AFM order reconstructs the FS, gaps parts of it and rearrange the DOS in an orbital-dependent fashion. Note, even if the α-band (hole-pocket at $\boldsymbol{\Gamma}$-point) would undergo a Lifshitz transition superconductivity can still be mediated by paramagnons, nevertheless [55]. Contrary to a phonon-mediated multi-band superconductor like MgB_2 where different SC gaps open on separated bands [247]; here, the addition of SOC and the microscopical phase coexistence with AFM order frame the theoretical description of the SC state and mechanism by much tighter constraints. The orbital-resolved and spin-dependent band structure must form the theoretical basis out of which the superconducting state emerges. However, this band structure is yet known insufficiently to this day. The general theoretical description must include SOC as there would be no antiferromagnetic gap opening in the two transversal directions $(\Delta_{t-out}, \Delta_{t-in})$, otherwise. Furthermore and despite the strong renormalisation of Δ_{long} in BaCo45 in comparison to its parent compound, *long* fluctuations remain gapped by AFM order and thus prevent any interplay with SC. Presumably, this gives an explanation why T_c is much higher in BaCo60 although the corresponding doping level is not much higher. Ultimately,

any generalised theory to describe the anisotropic SRM and its doping evolution must necessarily take the band- and orbital-selective aspects of the SC pairing mechanism into account. Finally, this theory would not only be limited to the FeSCs but could also be extended to the HFSCs with $4f$ and $5f$ electrons, where the knowledge of the band structure is much less advanced.

3.5 Methods

Single crystalline samples of $Ba(Fe_{1-x}Co_x)_2As_2$ were synthesised via the self-flux method, and the corresponding details are outlined in Ref. [248]. Thereby, three single crystals of $Ba(Fe_{0.955}Co_{0.045})_2As_2$ were obtained, co-aligned in the $[1,1,0]/[0,0,1]$ scattering plane and combined to sample BaCo45 with a total mass of 2.12 g. BaCo60 is one single crystal of $Ba(Fe_{0.94}Co_{0.06})_2As_2$ with a total mass of 2.88 g and the same sample as used in Ref. [155]. However, as shown in Sec. 3.3, it is presumably cracked into three pieces, which are slightly misaligned. Otherwise, this does not affect the quality magnetic inelastic signal, as the broad instrumental resolution integrates over all crystallites. The same argument holds for BaCo45 also. For both samples, the crystals were mounted on L-shaped aluminium holders and attached with aluminium wire to them.
The polarised inelastic neutron scattering experiments were conducted at the IN20 and IN22 triple-axis spectrometer (TAS) at the Institute Laue-Langevin (ILL) in Grenoble, France. Additionally, unpolarised INS experiments at the BaCo60 sample were performed at 2T TAS in the Laboratoire Léon Brillouin (LLB) in Saclay, France. At the IN20 and IN22 TAS spectrometer, Heusler monochromators and analysers were employed while the polarisation at the sample is defined by Helmholtz coils in the first case and via the CryoPAD in the latter. Furthermore, a PG-filter is installed between the sample and the analyser to discriminate higher order contaminations. Therefore, most scans were operated in constant $k_f = 2.662\,\text{Å}^{-1}$ mode. The overall neutron polarisation was estimated by measuring the flipping-ratios on nuclear Bragg peaks in the SC phase. For IN20 (IN22) this yields $FR \sim 14(16)$ corresponding to $\Pi \sim 86(88)\%$. At 2T TAS spectrometer PG monochromator and analyser were used, while a PG-filter on the secondary spectrometer arm between sample and analyser was installed to, again, discriminate higher order contaminations.

All $Ba(Fe_{1-x}Co_x)_2As_2$ samples were synthesised in and provided by the AIST in Tsukuba, Japan, in particular by Kunihiro Kihou and Chul-Ho Lee.

4 Incommensurate to Commensurate Magnetic Excitations in $LiFe_{1-x}Co_xAs$

Abstract
Incommensurate spin excitations in LiFeAs become commensurate with increasing Co doping, and perfect nesting conditions are recovered at 12 % which is simultaneously the end-point of the superconducting dome. Here inelastic neutron scattering is used to explore the spin response at intermediate doping, i.e. in superconducting $LiFe_{0.95}Co_{0.05}As$ (LiCo05) with $T_c = 9.5\,K$ and in overdoped and thus non-superconducting $LiFe_{0.82}Co_{0.18}As$ (LiCo18) with still enhanced nesting. In that context, clear commensurate magnetic excitations are observed in LiCo18, while, however, the interpretation of the signal in LiCo05 is less clear, as magnetic signal and background cannot be distinctly separated. Despite the improving nesting conditions with increasing Co doping, T_c is gradually suppressed, which documents that ideal nesting conditions are necessary but not paramount for superconductivity in iron-based superconductors.

Contents

4.1 Introduction **81**
4.2 Magnetic Excitations in $LiFe_{0.82}Co_{0.18}As$ **85**
4.3 Discussion **89**
4.4 Methods **90**

4.1 Introduction

The *first* iron-based superconductor is LiFeAs as it was synthesized already back in 1968 [249]. However, that compound did not attract much attention[1] most likely because resistivity measurements were omitted. Therefore, its superconducting and interesting physical properties were hidden for 40 years until 2008 when the boom of iron-based superconductor (FeSC) research sets in leading

[1] only 15 citing articles before 2008 are listed on `http://onlinelibrary.wiley.com/doi/10.1002/zaac.19683610107/full` in the CrossRef section

to its rediscovery. Today, LiFeAs is a very interesting material as it is on the verge of realising many phases, whereby experiments and theoretical studies report on (partially) conflicting properties. Moreover, on the way to a unified theory, valid for all FeSCs, LiFeAs paved and continues to pave it with stumbling blocks, as it is very different from members of the *1111* and *122* family, as well as its directly related compound NaFeAs in the *111* family. For example NaFeAs shows a tetragonal to orthorhombic phase transition at ∼60 K and AFM order at ∼45 K [27, 250], while LiFeAs remains tetragonal and paramagnetic to the lowest temperatures [24, 25, 251]. Moreover, NaFeAs displays weak[2] superconductivity at $T_c \sim 10$ K [27, 250] contrary to the strong SC phase emerging at $T_c \sim 18$ K in LiFeAs [24, 25, 251, 252]. In a recent study, both compounds were connected by exploring the doping dependence of $Na_{1-x}Li_xFeAs$ [253]. In opposition to the other FeSCs where T_c is promoted by applying pressure or doping it is only reduced in LiFeAs to date. This is exemplified when *(i)* electrons are added to the system by replacing Fe for e.g. Co, where SC is completely suppressed at $x \sim 12\,\%$ [60,150,254], *(ii)* doping holes by substituting Fe for V which drives the system toward a magnetic instability and away from SC already at 2 % [255], or *(iii)* an external pressure of 13 GPa is applied [256, 257]. Additionally, SC is very sensitive to Li-deficiencies as it is totally suppressed for $y \sim 2\,\%$ in $Li_{1-y}Fe_{1+y}As$ [258]. Furthermore, the T_c-value ranges between 16 K and 18 K in the literature [25, 251, 254, 258–264]. A recent STM/S study may resolve this issue, as it can trace the SC phase transition at locally pure positions. It reports on two distinct SC transitions, where the gap partially opens at $T^* = 18$ K and fully opens at $T_c = 16$ K [252], which is attributed to the multi-band nature of the compound. At T^* the SC gaps open on the α-band at $k_z \sim \pi$, while the rest of the FS becomes gapped at T_c [252]. The FS itself contains a particularity, for the hole and electron pockets are badly nested, as revealed in an early ARPES study from Borisenko *et al.* [148] and confirmed by later studies [150, 212, 213, 265]. The absence of (π, π) nesting is in contrast to other FeSCs and questions it's significance for superconductivity.

Moreover, the FS of LiFeAs is similar to an electron-doped FeSC as the α-band at the $\mathbf{\Gamma}$-point barely crosses the Fermi level [148]. Figure 4.1. shows the FS for pure and 3 % Co-doped $LiFe_{1-x}Co_xAs$ reproduced from Miao *et al.* [213]. At very low doping, i.e. at $\sim 0.4\,\%$ Co, the α-pocket in $LiFe_{1-x}Co_xAs$ undergoes a Lifshitz-transition as it sinks below the Fermi level [213]. However, 3 % Co-doping does not change the SC-gap size in comparison to the pure compound [213]. Therefore, the anisotropic Δ_{SC} values reported by Umezawa *et al.* [212], are added as colour code to Fig. 4.1. However, despite the bad nesting conditions, Taylor *et*

[2] weak means, despite vanishing resistivity there is only small SC volume fraction (5 % − 10 %) indicated by a faint diamagnetic response in the magnetic susceptibility measurements, c.f. data in Refs. [27, 250]

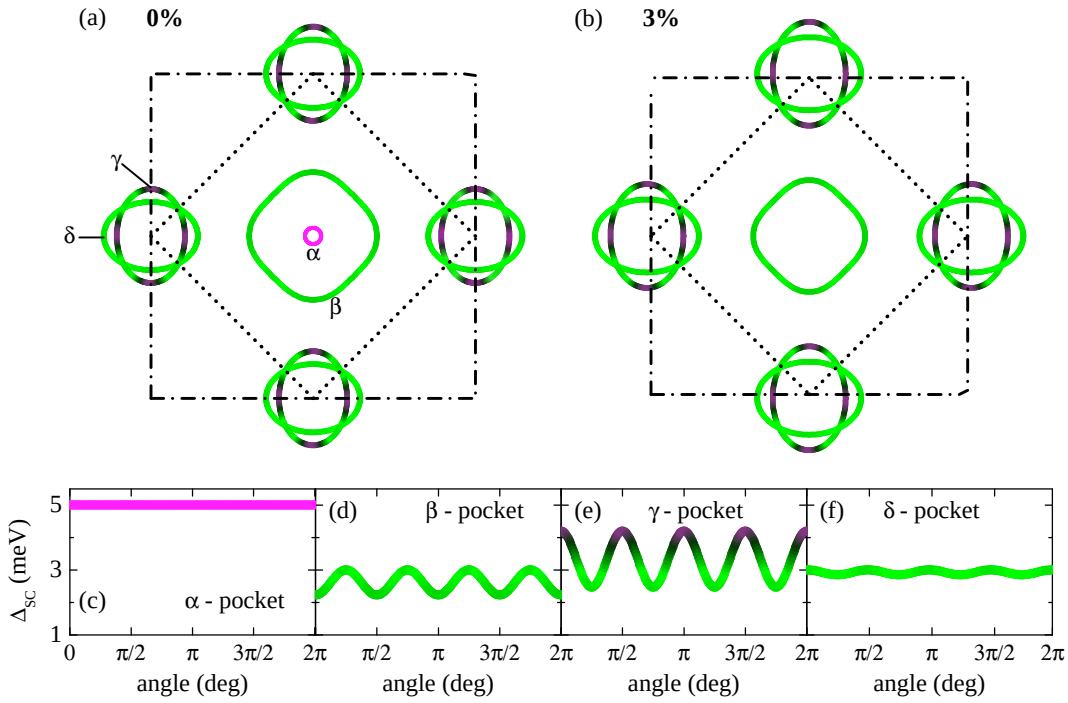

Figure 4.1: Fermi surface and SC gap energies of pure and 3 % Co-doped LiFeAs. **(a)(b)** Fermi surface (FS) and the corresponding colour coded SC gap energies for pure and 3 % Co-doped $LiFe_{1-x}Co_xAs$. The shape of the FS is reproduced from the report of Miao *et al.* [213]. Upon 3 % Co-doping the nesting conditions between the hole β-pocket and the electron γ/δ-pocket is increased. **(c)-(f)** SC gap energies for the $\alpha-, \beta-, \gamma-$ and δ-pocket as a function of angle reproduced from the report of Umezawa *et al.* [212].

al. found strong AFM fluctuations, which even show a resonance-like increase in intensity below T_c, in their TOF experiment on polycrystalline LiFeAs [266]. In a subsequent study on single crystalline LiFeAs Qureshi *et al.* discovered in-layer transversal[3] incommensurate magnetic excitations [267], which are a characteristic feature for electron-doped FeSCs [268]. This confirms that LiFeAs is situated somewhere at the end of the SC dome in the schematic phase diagram in Fig.: 1.2. On the other side, Qureshi *et al.* could not confirm the resonance-like increase of intensity below T_c, but a gradual uptake at 7.5 meV accompanied by an intensity decrease at low energies [267]. Note, according to the universal scaling relation from Eq.: (1.5) a resonance mode at ∼7 meV is expected for $T_c = 18$ K which, however, comes along with a strong intensity uptake below T_c. Further-

[3] transversal with respect to the ordering direction of the magnetic moment (in other FeSCs)

more, magnetic excitations are slightly broadened but persistent in non-SC Li-deficient samples [269]. Within experimental error-bars, the FS topology between SC LiFeAs and non-SC $Li_{0.94}FeAs$ is not altered [269]; and thus Li vacancies are non-magnetic impurity scattering potentials, which are strongly pair-breaking if the underlying SC gap symmetry is $s^{\pm}$ [54, 64, 116].
The actual pairing mechanism in LiFeAs is object of an intensive debate. As LiFeAs is on the verge to a ferromagnetic instability [270, 271] SC could alternatively be mediated by ferromagnetic instead of antiferromagnetic fluctuations. As a consequence LiFeAs would be a p-wave superconductors [272] as it is proposed for Sr_2RuO_4 [273, 274]. Support for such a scenario was experimentally provided by a non-vanishing Knight-shift in a NMR experiment [270] and deduced from quasi-particle interference (QPI) pattern [275]. However, these observations have not been confirmed in consecutive studies [276, 277] and are refuted, e.g. by measuring the spin susceptibility with polarised neutrons, where spin-singlet pairing is clearly proved [278]. Moreover, there are many theoretical approaches to account for the pairing mechanism, the SC-gap structure and the magnetic excitation spectra. Despite the bad nesting conditions in LiFeAs, scattering processes between the β hole and the (γ, δ) electron pockets are the origin of incommensurate magnetic intensity [279], observed in INS [267, 269]. Therefore, strong magnetic fluctuations prevail and are available for SC-pairing with $s^{\pm}$ symmetry [280], in agreement with the *1111* [281, 282] and *122* [58, 131, 178, 210, 283] families as well as $NaFe_{1-x}Co_xAs$ [61, 284]. In addition, this pairing symmetry is also deduced in other theoretical studies [277, 285, 286]. On the other side, theories based on phonon-assisted orbital fluctuations were applied for LiFeAs and resulted in sign-preserving s^{++} SC-pairing symmetry [65, 287]. This is the old conflict between the pairing mechanism of FeSCs in general, c.f. Chap. 1.3, and a delicate issue for samples in the overdoped regime. In this regime the mismatch of hole and electron FS increases, spin excitations become weak, and no clear spin resonance mode develops below T_c like in KFe_2As_2 [178].
However, the nesting conditions initially improve with increasing Co-doping in $LiFe_{1-x}Co_xAs$ as the β hole pocket shrinks and the (γ, δ) electron pockets expand [60, 150, 213]. Concomitantly to the FS nesting conditions, spin fluctuations observed in NMR are enhanced and cause a Fermi liquid (FL) to non-Fermi liquid (NFL) to Fermi liquid crossover [60]. Consequently, around $\sim 12\,\%$ Co-doping, where the nesting conditions are optimised and spin fluctuations in NMR are strongest [60] commensurate magnetic excitations are observed in TOF neutron scattering [154]. Although the FS nesting conditions improve towards $\sim 12\,\%$ T_c is gradually suppressed to zero [60, 150, 258]. However, the questions are *(i)* what happens at intermediate Co-doping levels, i.e at $5\,\%$, where the nesting conditions are enhanced and a sizeable $T_c \sim 10\,\mathrm{K}$ remains; *(ii)* what happens at overdoping, i.e. at $18\,\%$, where nesting conditions are still enhanced but T_c is already suppressed to zero?

4.2 Magnetic Excitations in $LiFe_{0.82}Co_{0.18}As$

The Fermi surfaces (FS) revealed by ARPES indicated improved nesting conditions with increasing Co doping [60, 150, 213], which would result in enhanced and commensurate magnetic excitations compared to the parent compound where they are incommensurate [186, 267]. Thereby, the large hole pocket shrinks and the electron pockets expand, which decreases the incommensuration $\boldsymbol{\delta}$ and yields an increased overlap when both pockets are connected by $\boldsymbol{Q} \pm \boldsymbol{\delta}$ [60, 150, 213]. To explore the resulting spin excitations, one intermediate doped compound, which is still superconducting below $T_c \sim 9.5\,\mathrm{K}$, namely LiCo05, and one overdoped and non-superconducting compound, namely LiCo18, were investigated. Unfortunately, in the obtained data for LiCo05 magnetic signal and background cannot unambiguously separated, which is why its tentative attempt of analysis is shifted to Appendix A.5. In the following, only the result for LiCo18 are presented.
Figure 4.2(a)-(j) displays the rocking scans through the centres at $(0.5, 0.5, 0)$ and $(1.5, 0.5, 0)$ at 1.5 K in two symmetry equivalent Brillouin zones (BZ) for LiCo18. Each commensurate magnetic peak was fitted by a Gaußian on a linear background. If there would be an incommensurate magnetic signal, it would be detectable in Fig.: 4.2(a)-(e) as the scan paths of the rocking and transversal scans are almost parallel to each other. Moreover, Fig.: 4.2(a')-(e') show the same scan as those in (a)-(e), but at 250 K where there is no magnetic signal resolvable. To trace the temperature evolution scans at intermediate temperatures, 80 K and 160 K, at 8 meV were run and are depicted in (k). The fitted amplitudes and widths are summarised in (m) and show a linear increase, respectively decrease, with temperature. Both values were interpolated to 250 K and used as fixed parameters to describe the corresponding signal in (d'). As a result, the magnetic signal is described by a Gaußian, whose amplitude is in the corresponding error bar, entirely, and thus it is not resolvable.
Fitting the magnetic excitations at $(1.5, 0.5, 0)$ in Fig.: 4.2(f)-(j) yielded much smaller rocking widths due to the scattering geometry, i.e. since $\boldsymbol{Q}$ is much larger than for $(0.5, 0.5, 0)$ a small angular deviation causes a much larger $\Delta\boldsymbol{Q}$, as well. In order to enable a comparison between the two $\boldsymbol{Q}$ positions, the obtained widths are normalised on their corresponding value at 8 meV and summarised in (l). These values roughly scatter around one and indicate no broadening in that energy regime due to dispersion. This is not in conflict with the reported dispersive low-energy spin excitations, observed in a TOF experiment by Li *et al.* [154], because the energy range probed here is too narrow.
Furthermore, the obtained amplitudes were corrected for the Bose, monitor and Fe^{2+} magnetic form factor. In order to facilitate a comparison with the parent compound [243], these were normalised on integrated phonon intensity, which is given by the coloured peak in Fig.: 4.3(c)(d), respectively for both compounds. The energy dependence of the normalised amplitudes can be described by a single

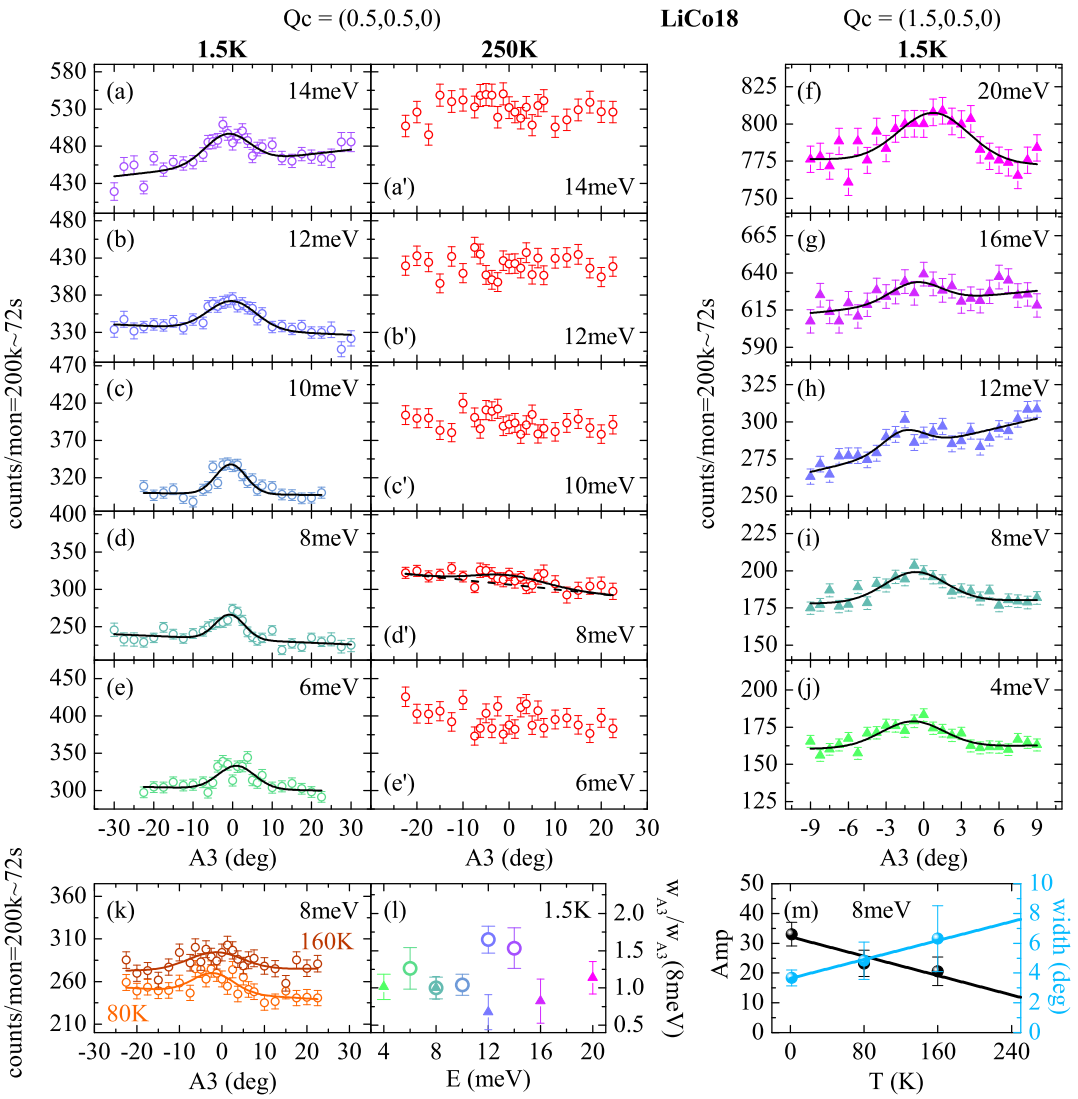

Figure 4.2: Rocking scans in LiCo18. **(a)-(e)** Rocking scans through Qc = $(0.5, 0.5, 0)$ at 1.5 K and between 14 meV and 6 meV in 2 meV steps, respectively. **(a')-(e')** are the same as in (a)-(e), but at 250 K. **(f-j)** Rocking scans through Qc = $(1.5, 0.5, 0)$ at 1.5 K and between 20 meV and 4 meV in 4 meV steps, respectively. **(k)** displays the same as in (d),(d') at intermediate temperatures of 80 K and 160 K. **(l)** Widths of the rocking scans over both $\boldsymbol{Q}$ values normalised on 8 meV for reasons of comparison. **(m)** Temperature dependent increase (decrease) of the width (amplitude) at 8 meV, resulting from the corresponding fits. The Gaußian in (d') is based on these results and cannot be resolved within the statistics.

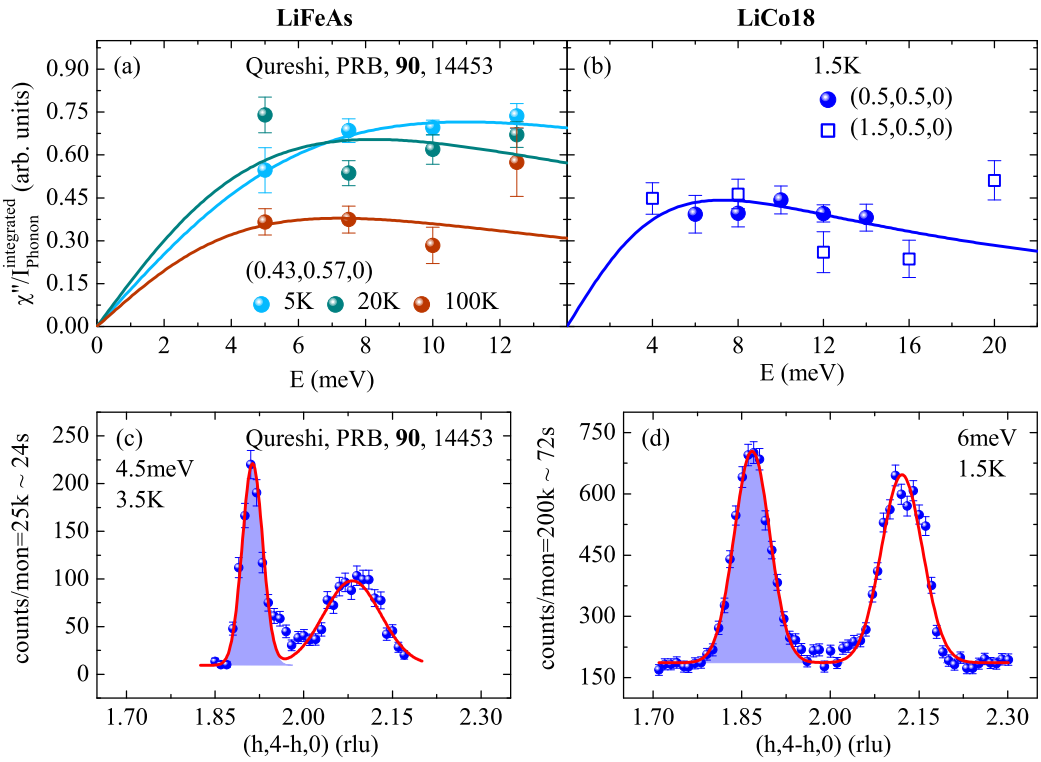

Figure 4.3: Energy dependence in $LiFe_{1-x}Co_xAs$ normalised on phonon intensity. **(a)(b)** E-scans at the incommensurate/commensurate maxima of the magnetic excitations at various temperatures in LiFeAs and LiCo18, respectively. For reasons of comparison each spectra is normalized on the integrated intensity of a corresponding phonon, coloured peaks in **(c)(b)** respectively. Besides, the $1/E$-dependence of the phonon intensity is corrected as well. The data in (a) and (c) are taken from Qureshi *et al.* [186].

relaxor function and is shown in Fig.: 4.3(a)(b).

However, comparing the normalised peak values of the magnetic excitations with each other is insufficient, because a portion is ignored, due to the incommensurate nature, at least in the parent compound LiFeAs. In this context, the ignored portion can be captured by transversal[4] integration of the magnetic signal. Figure 4.3(a)(b) shows the low-energy, low-temperature magnetic excitations in $LiFe_{1-x}Co_xAs$ with x = 0 and 0.18, respectively, whereas the data for x = 0 are taken from Qureshi *et al.* [186]. The scan for LiFeAs is fitted by four Gaußians, and the one for LiCo18 is fitted by one Gaußian, while the associated fit results are

[4]transversal with respect to the scattering vector $\boldsymbol{Q}$, i.e. parallel to the scan direction

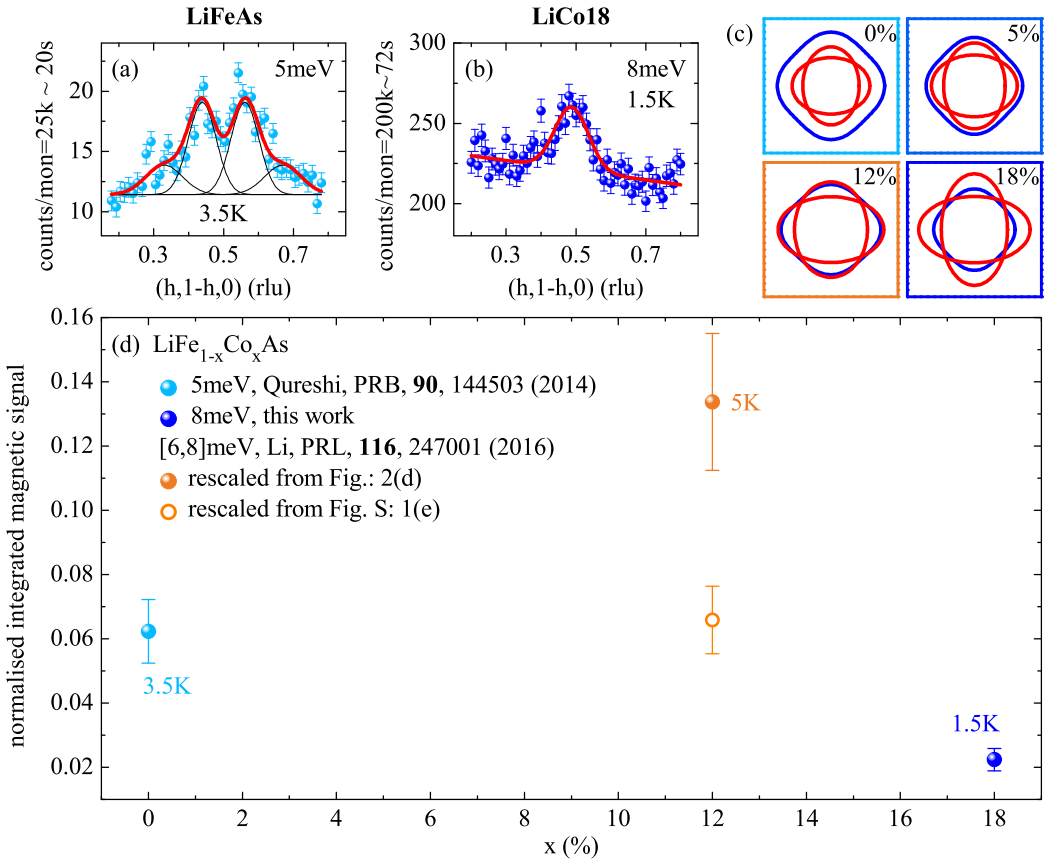

Figure 4.4: Doping dependence in $LiFe_{1-x}Co_xAs$ of integrated magnetic signal normalised on phonon intensity. **(a)(b)** Transversal $\boldsymbol{Q}$-scans with Gaußian fits to the data in LiFeAs and LiCo18, respectively. **(c)** Hole (blue) and electron (red) FSs are laid on top of each other to visualise how the nesting conditions change with increasing Co doping; reproduced from Dai *et al.* [60]. **(d)** Doping dependence of the integrated magnetic signal from (a)(b), normalized on the corresponding phonon from Fig.: 4.3(c)(d). The data points at 12 % Co-doping are extracted from Ref. [154] while those in (a) are from Ref. [186].

used for the integration. Furthermore, the doping dependence of the integrated intensity, normalised on integrated phonon scattering, is depicted in Fig.: 4.4(d). Note that the given error bars result from the fitting process. Additionally, the hole (blue) and electron (red) FSs, which are reproduced from Dai *et al.* [60] and laid on top of each other to visualise the nesting with increasing Co doping, are given in Fig.: 4.4(c). When the nesting conditions are ideal at $x = 12\,\%$ magnetic excitations, i.e. spin fluctuations, are strongest as the data points taken from Li

et al. [154] indicate. Thereby, the expression $[6, 8]$ meV represents an integration from 6 meV to 8 meV resulting from a line cut along the [1,K]-direction in their TOF data. In order to add the their results to Fig.: 4.4(d), they were scaled by the excitations for $x = 0\,\%$ which Li *et al.* also showed in their paper [154]. Intriguingly, the same scan is shown twice in their paper, once in Fig.: 2(d) and once in Fig. S: 1(e), and does not possess the same intensity. Maybe, they used different binning widths along [1,K] direction, which thus yield different intensities, although this remains puzzling. In this context, to transform the scattering intensities to double differential cross sections, Li *et al.* [154] normalised their TOF data on a vanadium standard, while Qureshi *et al.* [186] normalised their TAS data on phonon scattering. Both normalisation processes are well established [207], and in both reports consistent double differential cross sections for LiFeAs were deduced. Nonetheless, the spin excitation intensity increases with increasing doping as the nesting conditions are improved, but they also become more rapidly[5] suppressed beyond the SC end-point. Naively, one would expect in FeSCs, that increasing spin fluctuations lead to a higher T_c, but the opposite behaviour is observed in LiFeAs; the spin fluctuations are most intense at $x = 12\,\%$ Co-doping which coincides with the SC end-point in the corresponding phase diagram. Consequently, ideal nesting conditions are not necessary to promote T_c in FeSCs.

4.3 Discussion

Superconductivity mediated by spin fluctuations is the most prominent theory for FeSCs. In this regard, Dai *et al.* measured the doping dependence in $LiFe_{1-x}Co_xAs$ of the ^{75}As spin-lattice relaxation rate $1/T_1T$, which is a weighted sum over the first BZ of sub-meV low-energy spin fluctuations. The quality of FS nesting determines the strength of low-energy spin fluctuations and thus $1/T_1T$, in a naive picture. Although T_c gradually decreases with Co-doping, FS nesting increases up to $x_c \sim 0.12$, where it is optimal but T_c almost zero, and decreases towards overdoping, as the hole and electron FS mismatch is increased again [60]. Consequently, $1/T_1T$, observed by Dai *et al.*, follows this behaviour [60] similar to the presented INS data, which means that enhanced spin fluctuations do not promote T_c. In this context, in the INS spectrum, not only the spin excitation intensity increases up to x_c also the signal itself undergoes an incommensurate to commensurate crossover, as a consequence of improved nesting conditions. How much the incommensuration is reduced, and by how much spin excitations are enhanced in LiCo05 cannot be deduced, as the corresponding signal cannot be separated from the background, unfortunately. In LiCo18, spin excitations are still commensurate although the associated ARPES measurements show an increased FS

[5] rapidly refers to the (absolute value of the) rate with which the intensity increased, respectively decreases.

mismatch [60]. Furthermore, the corresponding intensity in LiCo18 is already lower than the one in LiFeAs, whereas the $1/T_1T$ spin-lattice relaxation rate is still higher at $x = 0.18$ than at $x = 0$ [60]. Possibly, sub-meV spin excitations are still enhanced due to the better nesting conditions in LiCo18 than in LiFeAs, but spin excitations in the meV-regime are stronger suppressed. Moreover, the spin fluctuations in LiFeAs are already about eight times weaker than in optimally Co-doped $Ba(Fe_{1-x}Co_x)_2As_2$ at the resonance energy [131], although a factor of two can be recovered due to the incommensurability [186]. Since LiFeAs behaves intrinsically as an overdoped material, weak spin fluctuations are expected as those are a common feature and were observed in $Ba_{1-x}K_xFe_2As_2$ [178] and $Ba(Fe_{1-x}Co_x)_2As_2$ [288, 289] as well. Additionally, there is no clear spin resonance mode in overdoped materials anymore, as reported by Lee *et al.* [178]. That may be the possible reason why a clear resonance mode is not detected in LiFeAs [186, 267], and why it would be even harder to detect in LiCo05 (if the corresponding data would be easier to analyse).
Although NMR and INS data cannot be related to each other directly, since different energy scales, sub-meV in the former and meV in the latter, are probed by both techniques, their results reveal comparable trends. This is at odds with theory, where enhanced spin fluctuations do promote T_c [279,280,286]. In order to reconcile this observation with a unified theory, an orbital resolved pairing mechanism is required, as indicated by Li *et al.* [154]. Within this mechanism, some of the d_{xy}, d_{xz}, and d_{zy} orbitals must somehow behave differently in LiFeAs than in other FeSCs, in order to provide an overall explanation where enhanced spin fluctuations, i.e. paramagnons, do indeed provide a higher T_c.

4.4 Methods

The single crystalline samples LiCo05[6] and LiCo18 were synthesized, characterised and provided by the IFW in Dresden. The synthesis process is a self-flux technique, where all steps are performed under Ar-atmosphere; for details see Refs. [254, 290]. In order to characterise the samples, EDX, XRD and susceptibility measurements in a SQUID were conducted. From the EDX measurements the actual doping level, i.e. 5 % and 18 %, were extracted. Note that the experimental error of the method it typically 1-2 %. The XRD measurements were performed (at the IFW) to compare the c lattice parameters with the work of Pitcher *et al.* [258] and show very good agreement. In addition, the susceptibility measurements showed no ferromagnetic phase transition and a $T_c \sim 9.5\,\mathrm{K}$ for the sample LiCo05. However, Aswartham *et al.* noted that Co-doped LiFeAs is fragile and more sensitive to air and moisture than the parent compound [254]. On that score,

[6] although not shown in this chapter, but in Appendix A.5

quantity	LiCo05	LiCo18
x	0.05	0.18
number of pieces	2	4
total mass (mg)	~ 300	~ 800
orientation	[100]/[010]	[100]/[010]
accuracy	$\sim 3°$	$\sim 3°$
a (Å) @ IN8	3.789	3.761
T_c (K)	~ 9.5	–

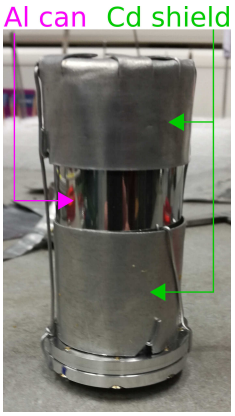

Figure 4.5: List of the properties of LiCo05 and LiCo18th next to a picture of the sample-can containing LiCo05.

the samples were strictly kept under Ar-atmosphere, for the orientation procedure and for the experiment as well. In order to explore the magnetic signal by inelastic neutron scattering (INS) several single crystal pieces from badge SE3785 for LiCo05 and from badge SE4184 for LiCo18 were co-aligned in $[1,0,0]/[0,1,0]$ scattering geometry. LiCo05 consists of two pieces with total mass ~ 300 mg while LiCo18 consists of four pieces with a combined mass ~ 800 mg. LiFeAs cleaves perpendicular to the c axis, hence the demanded scattering plane is visible, easily. However, the largest pieces are circular and flat plates without any edge indicating a direction in the ab-plane, due to the synthesis process. Pieces of each sample were mounted on a thin aluminium sample-holder and carefully attached with Al-wire. For the co-alignment an air-tight Al-can with a Kapton-foil window was used, which is transparent for X-rays from the Cologne Laue-camera. After the individual Laue-photos are evaluated, the Al-can is transferred back into the Ar-box, where the sample orientation can be adjusted by hand. Due to the crystal shape, this is a time and labour intensive procedure.
The INS experiments for both samples were performed at the IN8 triple axis spectrometer (TAS) in ILL, Grenoble, France. Although, the Laue-photos displayed an accurate alignment for the pieces of each sample, the IN8 revealed a mismatch by $\sim 3°$. The properties of both samples are summarised in Tab. 4.5.
For both experiments a top-loading ILL "Orange"-type cryostat was utilised; a non-standard one with a sample-access diameter of 70 mm for LiCo18 and a standard one with a sample-access diameter of 49 mm for LiCo05. Both samples were mounted in air-tightly sealed Al-cans with Ar-atmosphere. Chronologically the experiment with LiCo18 was conducted first and weak signals on a high background level were found. In order to suppress the background, the Al-can containing LiCo05 was framed by a Cd-shield Fig.: 4.5. If not mentioned differently a double focussing PG monochromator and analyser were used, and k_f is fixed to $2.662\,\text{Å}^{-1}$.

The momentum transfer $\boldsymbol{Q}$ is defined as $\boldsymbol{Q} = H\boldsymbol{a}^* + K\boldsymbol{b}^* + L\boldsymbol{c}^*$, where H, K and L are the Miller indices and $(\boldsymbol{a}^*, \boldsymbol{b}^*, \boldsymbol{c}^*) = \left(\hat{\boldsymbol{a}}\frac{2\pi}{a}, \hat{\boldsymbol{b}}\frac{2\pi}{b}, \hat{\boldsymbol{c}}\frac{2\pi}{c}\right)$, respectively. Moreover, the a lattice constant was adjusted at the IN8 spectrometer, resulting in 3.789 Å for LiCo05 and 3.761 Å for LiCo18, c.f. Tab.: 4.5; while the c lattice parameter cannot be adjusted due to the chosen scattering plane. Note, that the IN8 TAS is not designed to measure the lattice parameter with high accuracy.

5 The Quest for the Resonance Mode in $NdFeAsO_{1-x}F_x$

Abstract
The spin resonance mode is the hallmark excitation in iron-based superconductors, which is insufficiently explored in the *1111* family, although the highest bulk T_c values are found there. To search for the resonance mode in $NdFeAsO_{0.87}F_{0.13}$ ($T_c = 50\,K$) neutron time-of-flight experiments on polycrystalline samples were performed. However, the energy regime where this excitation should emerge is superimposed by strong Nd^{3+} crystal field excitations, which inhibit the observation of the spin resonance mode. Therefore, it was not observed in $NdFeAsO_{0.87}F_{0.13}$ meaning that its existence and exploration remain an open issue.

Contents

5.1 Introduction **93**
5.2 Results **94**
5.3 Summary and Discussion **100**
5.4 Methods **101**

5.1 Introduction

$NdFeAsO_{1-x}F_x$ belongs to the *1111* family from which the first iron-based superconductors $LaFePO_{1-x}F_x$ and $LaFeAsO_{1-x}F_x$ were synthesised by Kamihara *et al.*[1] [13, 14]. The corresponding crystal structure is shown in Fig.: 1.1. Although this family contains the highest bulk T_c-values, up to 56 K in $Gd_{1-x}Th_xFeAsO$ [17], detailed neutron scattering studies, especially on the SRM, are lacking This is due to two reasons. First, in the *RE-1111* family, were *RE* is a rare earth like La, Ce, Pr, Nd, Sm and Gd [14, 17, 100, 216, 218, 219, 292–296], no single crystal in the size suited for INS studies could be synthesised to date. Although, the most recent attempts accomplished high-quality and low-millimetre sized single crystals [297]. Second, Sm and Gd are generally unsuited for neutron scattering experiments due to their huge (isotope averaged) neutron absorption cross section $\sigma_{abs} = 5922(56)$

[1] to be precise, the first who induced superconductivity by doping as the parent compounds were already synthesised e.g. by Zimmer *et al.* in 1995 [291]

and 47 900(125) barn, respectively [298]. However, by use of the time-of-flight (TOF) neutron scattering technique Christianson *et al.* could measure the first spin resonance mode in polycrystalline $Ba_{1-x}K_xFe_2As_2$ in 2008 at a very early stage of this research field [134]. Moreover, the TOF technique proved to be a powerful tool to extract spin fluctuations at the AFM-ordering vector in polycrystalline samples as reported by Rahn *et al.* for FeSe [104]. On the other side, Shamoto *et al.* were able to show the resonance mode at $E_{res} \sim 13\,\text{meV}$ and $Q = 1.15\,\text{Å}^{-1}$ in $LaFeAsO_{0.92}F_{0.08}$ by a TAS experiment, in spite of a peak in the phonon density of states at this $(\boldsymbol{Q}, E)$-position [281]. However, this is the only compound in the *1111*-family in which the SRM is reported so far. Although, Goremychkin *et al.* [299] and Cheng *et al.* [300] performed TOF, respectively TAS, experiments on polycrystalline $NdFeAsO_{1-x}F_x$, in both reports the possible existence of the SRM is not even mentioned. Instead, both reports agree on a Nd^{3+} crystal field (CF) excitation at 20 meV, where the spin resonance mode would be expected, due to the universal scaling law $E_{res} = 4.3 k_B T_c$, c.f. Eq.: (1.5). Despite the CF excitation, signatures of the SRM should be observable in a TOF experiment, and the quest for the resonance mode in $NdFeAsO_{0.87}F_{0.13}$ (NdF13) is revisited here.

5.2 Results

In order to investigate the excitation spectrum, about 10 g of polycrystalline NdF13 were filled into a small sachet made of aluminium foil. NdF13 consists of two batches with only marginal impurity phases, which will not affect the obtained results, c.f. methods section for more details. Moreover, the sachet was clamped in an aluminium frame and inserted into the IN4 cryostat. Consequently, the excitation spectrum of NdF13 was explored by taking (Q, E)-maps at 10 K, 38 K and 50 K. For the further analysis, a linear background was subtracted from the data, and the obtained intensities were subsequently corrected for the Bose factor. Those maps are displayed in Fig.: 5.1, where the neutron's energy gain side, i.e. negative energy transfers, are omitted. This omission results from the Bose-factor correction which results in erroneously high intensities. In the (smeared) elastic line the high-intensity spots correspond to nuclear Bragg peaks, which would be observed in a powder diffraction experiment also. Furthermore, the several excitation levels can be split into two parts roughly. On the left-hand side, i.e. at low Q values, their origin is more likely magnetic, because the corresponding form factor dependence suppresses scattering intensity at large Q values. On the right-hand side, i.e. at large Q values, their origin is more likely phononic, as the phonon intensity scales as Q^2. In order to analyse the excitations further constant Q cuts at $2.478\,\text{Å}^{-1}$ and $3.1\,\text{Å}^{-1}$ are presented in Fig.: 5.2. This corresponds to vertical sections in Fig.: 5.1 and for each section data points within the (total) interval

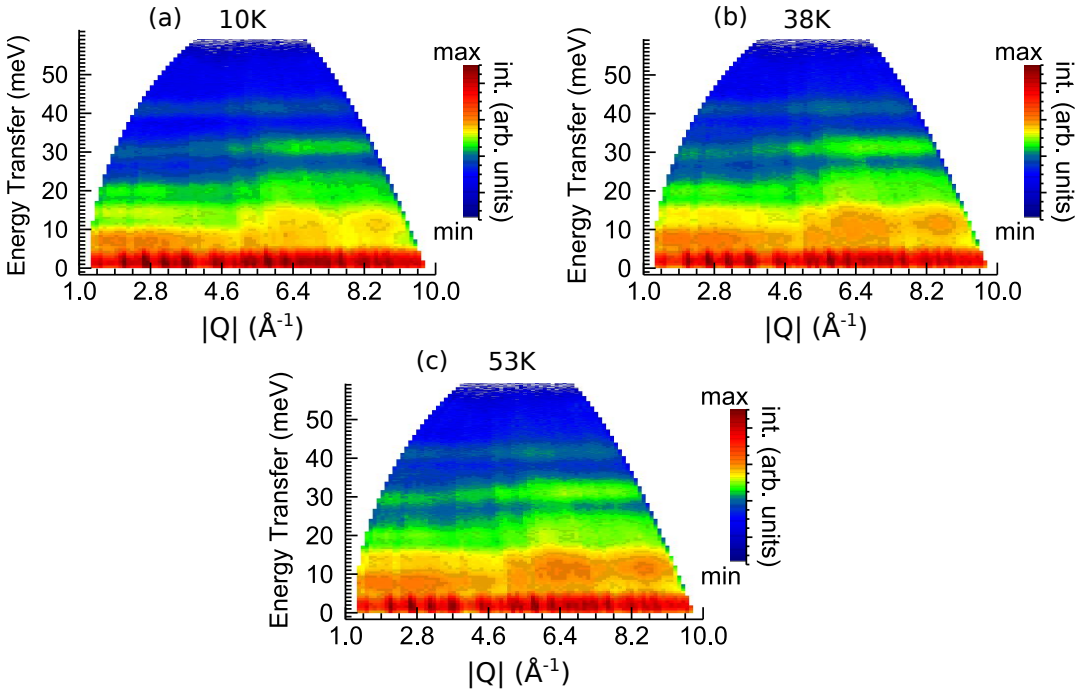

Figure 5.1: (Q,*E*)-maps at 10, 38 and 53 K of $NdFeAsO_{0.87}F_{0.13}$. (Q,E)-maps of $NdFeAsO_{0.87}F_{0.13}$ taken with an initial wavelength of $\lambda = 1.1$ Å at 10, 38 and 53 K, respectively shown in **(a)**, **(b)** and **(c)**.

$\Delta Q = 0.2\,\text{Å}^{-1}$ and $\Delta E = 0.5$ meV are binned. The resulting spectra were fitted by 11 or 12 Gaußians, where every single mode, except the elastic line, is displayed in Fig.: 5.2(a)-(d). Although the first three excitation lines **A-C** could not be resolved here, Goremychkin *et al.* reported them in their TOF study with higher resolution [299]. Additionally, the generalised phonon density of states (*gdos*) from Xiao *et al.* [301] for the undoped parent-compound is inserted in Fig.: 5.2(a). Assuming that the partial substitution of oxygen by fluorine does not affect the *gdos* significantly, it is used as a measure to estimate which excitations contain a strong phononic contribution. In particular, these are the excitations at ~ 24 meV, 30 meV and 41 meV which are shown in Fig.: 5.2(e) as green dashed lines. This sub-figure summarises all extracted CF excitations and compares them to those in the undoped parent-compound at 160 K as reported in [301]. According to Hund's rules, the ground state of Nd^{3+} contains three f-electrons and is ${}^4I_{9/2}$. The tetragonal crystal electric field splits the tenfold degenerate ground state into five Kramers degenerate doublets, which were analysed by Xiao *et al.* within the Stevens operator formalism [301]. Since there is no structural/ magnetic phase transition for 13 %, F-doping the CF transitions should be identical to those in the

t-PM phase of the undoped parent-compound, because the surrounding electrical field determines the CF excitations. However, this can only be true for $\sim 57\,\%$ of the Nd^{3+}-ions within the O_4-tetrahedrons, because 13 % fluorine doping leaves that fraction unaffected. 34 % of the (O_{4-n},F_n)-tetrahedrons contain one fluorine ion, 7.7 % contain two, and the remaining fraction possesses three or four. Although both F^{1-} and O^{2-} contain ten electrons, they do not generate identical crystal fields and thus explain why there are more than five CF excitations in Fig.: 5.2(e). Nonetheless the CF-levels at $\sim 7.5\,\text{meV}$, 20.7 meV and 35.5 meV in NdFeAsO are well reproduced in the extracted CF excitation scheme for NdF13. On the other hand, an additional mode (**K**) at $\sim 12\,\text{meV}$ appears, as shown in Fig.: 5.2(b)(c). The intensity of this mode increases with increasing temperature, c.f. Fig.: 5.3(b), and is thus interpreted as an excitation between excited levels. Note, while the phonon (thermal) population is governed by Bose statistics, CF excitations are populated according to the Boltzmann statistics and correcting the data for the Bose factor does not cancel inter excited-level transitions (IETs). Therefore, the **K**-mode is interpreted as a transition between two excited levels, most likely from $\sim 9\,\text{meV}$ to $\sim 21\,\text{meV}$, and is represented as a dashed orange line in Fig.: 5.2(e). In total Fig.: 5.2(e) shows 11 excitations; seven CF transitions **A-E**, **H** and **J**, three phonon lines **F**, **G** and **I**, and one inter-excitations transition **K**. Table 5.1 summarises the excitation levels and compares them to those reported by Goremychkin *et al.* [299] and Cheng *et al.* [300] for similarly doped compounds. Furthermore, the values for the parent compound NdFeAsO in the t-PM phase at 160 K and in the o-AFM phase at 5 K reported by Xiao *et al.* [301] are given as well. For energy transfers up to 20 meV all studies on the doped compounds agree fairly with each other and Cheng *et al.* [300] also report an IET at 11 meV. However, there is disagreement on the origin of the mode at $\sim 41\,\text{meV}$. Cheng *et al.* attributed it to another crystal-field excitation although they observe two spurious peaks in the energy range from 40 meV to 45 meV and an increased instrument background [300]. Although the phononic contribution and the background were subtracted the remaining intensity in this region seems too high [300], but a superposition of the phonon mode and a CF excitation cannot be ultimately ruled out in this study here. Intriguingly, Cheng *et al.* reported an additional IET at 26 meV [300], which is not observed here. On the other hand, the level at $\sim 35\,\text{meV}$ is absent in their report, although it must be present since half of the NdO_4-tetrahedrons are unaffected by the doping. A possible reason to explain this discrepancy could be that in their TAS study the signal above 36 meV was attributed to the instrumental background. This could mask the $\sim 35\,\text{meV}$ mode and cause deviations in the phonon and CF contributions.

In order to elucidate the spin resonance mode (SRM) in NdF13 the temperature difference from 10 K to 53 K at various Q values is displayed in Fig.: 5.3(a). The negative signal at 12 meV indicates the inter-excitation transition as evidenced by the temperature dependence in Fig.: 5.3(b). Furthermore, there is a positive

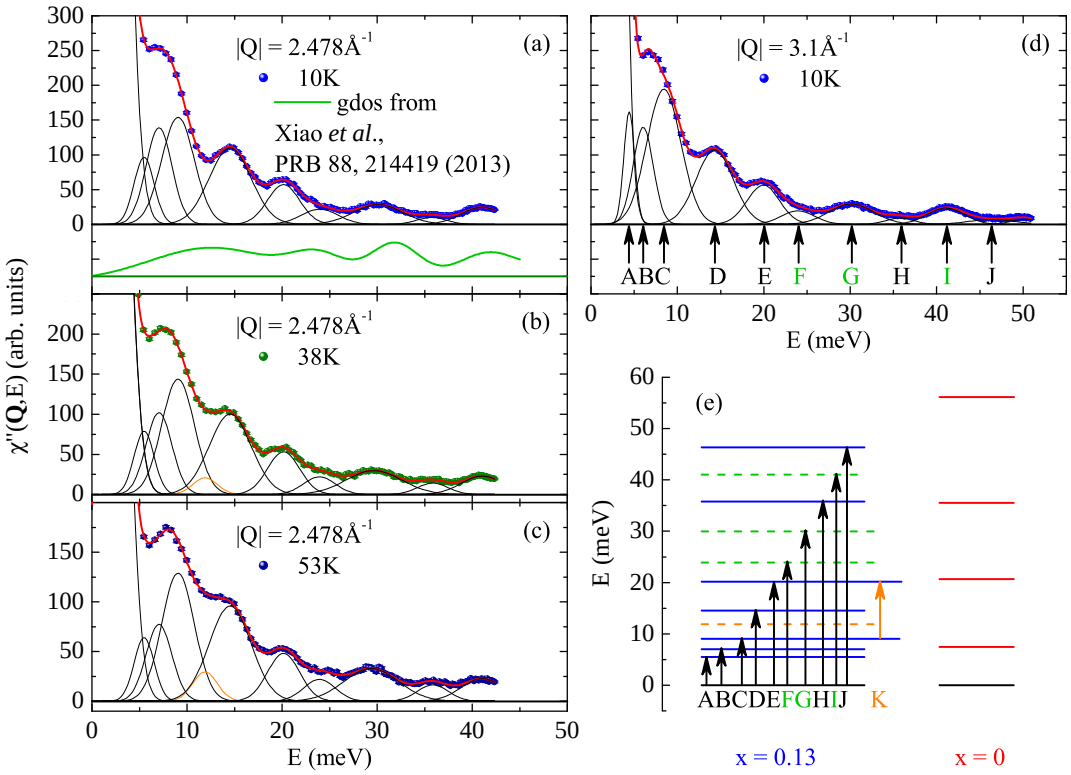

Figure 5.2: Excitation scheme in $NdFeAsO_{0.87}F_{0.13}$. **(a-c)** sections from Fig. 5.1 along $Q = 2.478\,\text{Å}^{-1}$ within $\Delta Q = 0.2\,\text{Å}^{-1}$ and $\Delta E = 0.5\,\text{meV}$ at 10 K, 38 K and 53 K, respectively. The *gdos* in (a) indicates the phononic contribution obtained from the parent compound [301]. **(d)** same as in (a) at $Q = 3.1\,\text{Å}^{-1}$. **(e)** resulting excitation scheme with CF excitations (blue lines), phonons (green dashed lines) and an inter-excitation transition (orange dashed line). For comparison the CF scheme of the parent-compound at 160 K from Xiao *et al.* [301] is shown.

(difference) signal in the energy range from 14 meV to 22 meV, where the resonance signal would be expected according to the universal scaling law, and at 41 meV. Figure 5.3(b) shows that the intensity of the levels at 14.6 meV, 20 meV and 41 meV decrease with increasing temperature. For the resonance mode as well as for a CF excitation such a behaviour is expected. However, the temperature dependence of the SRM should be more order parameter-like at T_c, while for a CF excitation the intensity follows the Boltzmann distribution and thus changes gradually over T_c. Although the intensity increase at 20 meV, with decreasing temperature, seems steeper than the CF excitations at 14.6 meV and 41 meV, a concluding statement based on three points is not possible. On the other side, the

Q dependence of the difference signal should follow the Fe^{2+} magnetic form factor in case of a resonance excitation whereas the Nd^{3+} CF excitations follows the Nd^{3+} magnetic form factor. For 12 meV, 14.6 meV, 20 meV and 41 meV this Q dependence is displayed in Fig.: 5.3(c)-(f), respectively. Each cut is fitted by the Nd^{3+}, Fe^{2+} and a weighted sum of both form factors, $(1-p)\cdot f^2(Nd^{3+}) + p\cdot f^2(Fe^{2+})$. In all cases the weighted fit coincides with the Nd^{3+} magnetic form factor fit and thus the corresponding weights are $p = 0.00(14), p = 0.00(14), p = 0.00(14)$ and $p = 0.00(46)$ for Fig.: 5.3(c)-(f) respectively. Due to the low intensity and thus relatively large error bars, the fit uncertainty of the 41 meV signal in Fig.: 5.3(f) is bloated. In particular the Q dependence of the 12 meV signal confirms that this is a transition between two Nd^{3+} CF excited states. Concerning the result

Table 5.1: Comparison of the excitation levels in $NdFeAsO_{1-x}F_x$. Summary and comparison of the extracted excitation levels to those reported in Ref. [299,300]. Additionally, the crystal-field levels reported by Xiao *et al.* [301] of the parent compound NdFeAsO are given in the t-PM phase at 160 K and in the o-AFM phase at 5 K. The origin of each mode is either attributed to a Nd^{3+} crystal field (CF) excitation, phonon (PH), or inter excited-level transitions (IET).

this study			**Goremychkin**		**Cheng**		**Xiao**		
			***et al.* [299]**		***et al.* [300]**		***et al.* [301]**		
$x = 0.13$			**$x = 0.15$**		**$x = 0.15$**		**$x = 0$**		
all T			**7 K & 50 K**		**3 K & 150 K**		**5 K**	**160 K**	
mode	meV	type	meV	type	meV	type	meV	meV	type
A	5.49	CF	4.71	CF	4.49	CF	2.81	–	CF
B	7.04	CF	7.34	CF	7.34	CF	7.38	7.45	CF
C	9.06	CF	9.13	CF	8.97	CF	8.56	–	CF
D	14.56	CF	15.46	CF	15.17	CF	–	–	
E	20.15	CF	21.06	CF	19.79	CF	19.86	20.69	CF
F	23.91	PH	–	–	26	IET	22.16	–	CF
G	29.98	PH	–	–	–	–	–	–	
H	35.79	CF	–	–	–	–	36.44	35.51	CF
I	41.04	PH	–	–	41.50	CF	37.55	–	CF
J	46.25	CF	–	–	44.51	CF	47.86	–	CF
K	11.91	IET	–	–	11	IET	49.75	56.12	CF

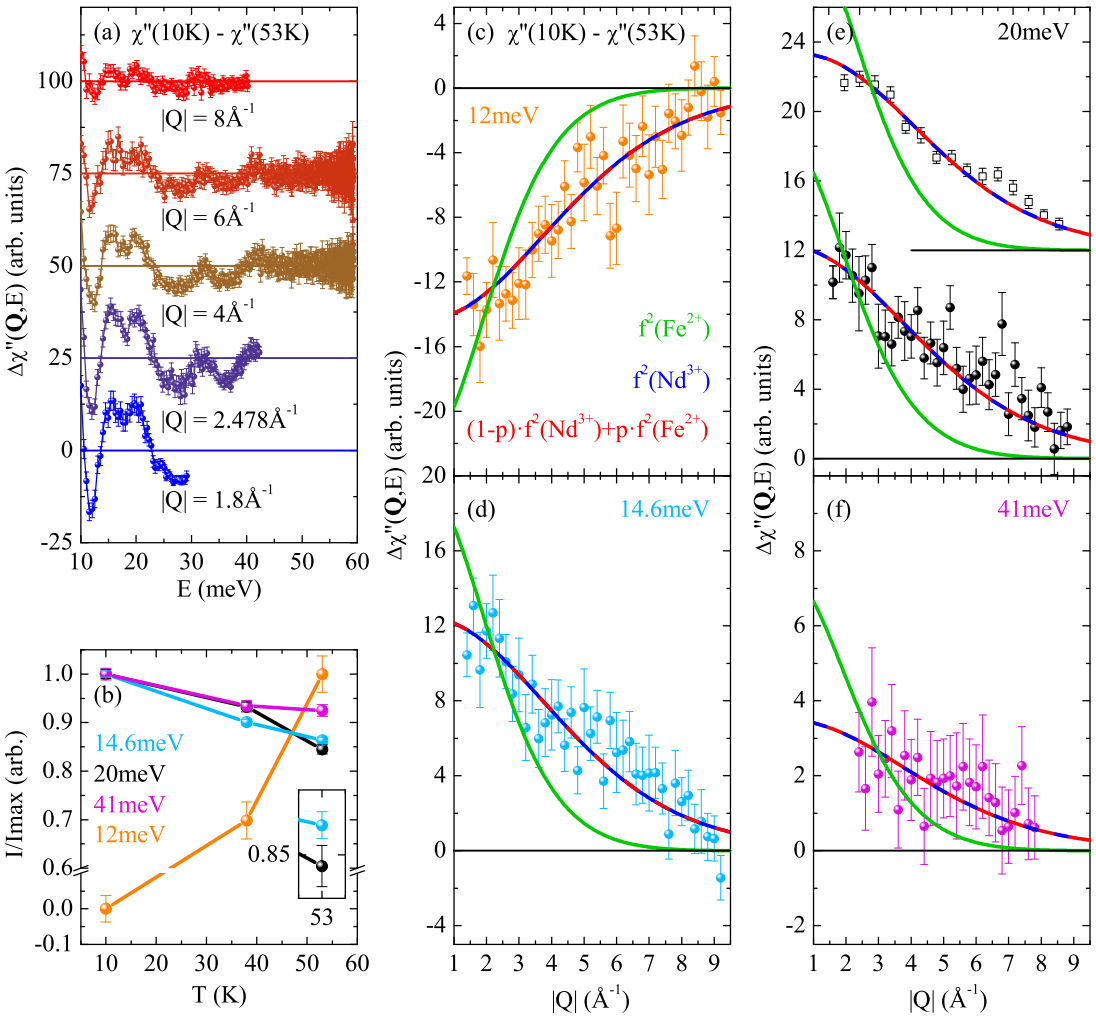

Figure 5.3: Constant Q- and *E*-cuts at various temperatures. **(a)** Intensity change between 10 and 53 K at various Q values. **(b)** Temperature dependence of the 12 meV, 14.6 meV, 20 meV and 41 meV modes normalised on their corresponding maximum. The inset magnifies the region at 53 K for 14.6 meV and 20 meV. **(c)-(f)** Q-cuts of the temperature difference at 12 meV, 14.6 meV, 20 meV and 41 meV, respectively. The lines are fits of the magnetic form factor, Nd^{3+} (blue), Fe^{2+} (green), and a weighted sum of both (red). Open symbols in (e) display the intensity integrated over $\Delta E = 3$ meV and $\Delta Q = 0.5$ Å^{-1}.

at 20 meV, where the resonance energy is expected, there is no contribution stemming from the Fe-ions and thus no resonance signal. In order to exclude that the

presented slice in Fig.: 5.3(e) is too narrow, the integration interval was extended from $\Delta E = 0.5\,\text{meV}$ to 3 meV and from $\Delta\text{Q} = 0.2\,\text{Å}^{-1}$ to $0.5\,\text{Å}^{-1}$. However, the fit result is unaffected, c.f. Fig.: 5.3(e). Additionally, other energies around 20 meV with various integration intervals were analysed in the same way (not shown), but the result is identical to the presented one.

5.3 Summary and Discussion

The excitation levels in NdF13 were investigated by a TOF experiment. In total there are seven CF levels reported for NdF13, thereby the five lowest levels observed here are in perfect agreement with those reported by Goremychkin *et al.* [299] and Cheng *et al.* [300]. Nd^{3+} is in a $^4I_{9/2}$ state, and one would expect five Kramers degenerate CF excitations, which do not split since the fluorine-doping suppresses the magneto-structural phase transition, identical with the t-PM phase of the undoped parent-compound. However, doping changes the electrical potential surrounding $\sim 43\,\%$ of the Nd^{3+}-ions and thus the corresponding CF levels. Therefore, the spectra contain a superposition of different Nd^{3+} CF excitations next to phonons. The phononic contribution to the excitation lines should be independent of doping and was estimated from the phonon *gdos* reported by Xiao *et al.* for the parent compound [301]. There is some disagreement with the reported CF scheme by Cheng *et al.* [300] for the 41 meV excitations. This level was attributed to be a phonon, while Cheng *et al.* assigned it to a CF excitation. Note, that in their study there is spurious scattering in this energy window and increased instrumental background, which could lead to an overestimation of the signal.
Furthermore, the SRM has been expected at $\sim 20\,\text{meV}$ according to the universal scaling relation in Eq.: (1.5) which, however, is coinciding with a CF excitation. The corresponding intensity of the CF must be much stronger than the one of the SRM as the Q dependence adheres to the Nd^{3+} form factor almost exclusively. However, the error of the weighted Nd^{3+}, Fe^{2+} magnetic form factor fit leaves some space for a very weak SRM. A putative indication to the formation of that weak SRM is given by the temperature dependence in Fig.: 5.3(b), as the relative intensity increase with decreasing temperature at 20 meV is larger compared to the one at 14.6 meV and 41 meV. In general, the (relative) intensity dependence for the CF excitations is given by the Boltzmann statistics, i.e. with increasing temperature states at higher energies become more populated at the expense of those states at lower energies. For this reason, the intensity reduction with increasing temperature should be strongest at 14.6 meV followed by the one at 20 meV and finally by 41 meV. Since this is not the case, an additional temperature dependent contribution, e.g. a relative to the CF excitation weak SRM, could be present at 20 meV. Nonetheless, there must be a SRM in this material and a detailed

temperature dependence at 20 meV might show the expected order parameter-like intensity increase at T_c.

5.4 Methods

Two different batches, SE3941 and SE4085, of NdF13 were prepared by using a two-step solid-state reaction method, similar to that described in Ref. [302] at the IFW in Dresden. Moreover, samples were characterised by WDX, XRD and SQUID measurements, also at the IFW and the results are summarised in Tab.: 5.2. The WDX measurement on SE3941 yields a fluorine doping level of 13(3) %, as well as NdAs and FeAs as possible impurity phases. In order to estimate their portions powder XRD analysis reveals less than 1 % and ∼ 2 % of NdAs in SE3941 and SE4085, respectively. This small amount is too weak to produce any detectable CF excitations, which could affect the presented results. The portion of the FeAs impurity phase is not mentioned as it contributes undetectably to the diffractogram. Additionally, the determined a and c lattice constants for SE3941 are respectively 0.25 ‰ and 0.41 ‰ larger than in SE4085, which almost coincides within error bars. However, these subtle differences do not influence their SC properties as both susceptibility curves, taken by SQUID measurements, lay perfectly on top of each other and show a T_c of 50 K. Therefore, in order to increase the sample volume, both samples were mixed for the TOF experiment while the individual parameters of each sample are summarised in Tab. 5.2.

Table 5.2: Properties of the F-doped NdFeAsO samples.

	SE3941	**SE4085**
x	0.13(3)	–
mass (g)	∼ 6	∼ 4
a (Å)	3.9651(5)	3.9641(5)
c (Å)	8.5644(10)	8.5609(10)
T_c (K)	50	50
impurity phase		
NdAs	≤ 1 %	∼ 2 %
FeAs	–	–

$NdFeAsO_{1-x}F_x$ is a not well-studied compound as there are only a few phase diagrams published [303–305]. Comparing the T_c values to those in the literature [303–305] shows that the observed value is slightly larger for 13 % F-doping. On the other side Ren *et al.* reported a T_c of 50 K, when there is a nominal oxygen deficiency of 15 % in $NaFeAsO_{1-\delta}$ [16]. As both, oxygen deficiency and fluorine doping, add electrons to the system a combined effect could cause the deviation. Malavasi *et al.* also refined the (O,F)-occupation in their neutron data, while X-ray techniques like WDX are less accurate for light elements like oxygen and fluorine than for heavy ones as their cross-section scales quadratically with the

electron number. A possible and more reliable way to compare the samples would be a phase diagram based on charge carrier density as abscissa rather than the fluorine doping level.

The TOF neutron scattering experiment was performed at IN4 spectrometer in the Institute Laue Langevin (ILL) in Grenoble, France. Therefore, the sample was filled into a $\sim 2\,\mathrm{cm} \times 4\,\mathrm{cm}$ sized sachet, made of commercial Al-foil, which was clamped into an Al-frame. The entire experiment lasted for four days, and the beamtime was roughly equally distributed on the three different temperatures, 10 K, 38 K and 53 K at which the spectra were taken. Throughout the experiment the incident wave-length was fixed to $\lambda = 1.1\,\text{Å} \sim 67.6\,\mathrm{meV}$. In order to analyse the spectra the large array manipulation programme (LAMP) provided by the ILL was used. LAMP converts the raw-data, detected as a function of time and angle, into $S(\boldsymbol{Q}, E)$ after removing bad detector banks and subtracting a constant background. Data points within an interval of 0.6 meV are rebinned. Since the resulting points in $(\boldsymbol{Q}, E)$-scape are not regularly spaced the Delaunay triangulation method is applied for interpolation on a regular grid. Finally $S(\boldsymbol{Q}, E)$ is converted into $\chi''(\boldsymbol{Q}, E)$ by correcting for the Bose factor.

6 Methods: Neutron Scattering

Neutron scattering is a powerful tool to probe lattice and magnetic structures as well as their corresponding excitations, e.g. phonons, magnons, crystal field (CF) transitions, spin resonance modes, etc.. The thorough analysis of all these observations aides to understand the underlying physics of this particular compound, material class and in extend the holistic phenomena. Throughout this thesis neutron scattering is the principal means of investigation. Despite the complexity of this technique, only some key points are given here, as there are many textbooks available, which provide a more detailed overview [306–311]. On a basic level, the theoretical background of neutron scattering is summarised in Sec. 6.1. Furthermore, the central tool of observation, the triple-axis spectrometer (TAS), is introduced in Sec. 6.2 and the time-of-flight technique is briefly reviewed in Sec. 6.3 However, two key aspects in this thesis are absolute unit calculation highlighted in Sec. 6.4 and polarisation analysis in Sec. 6.5 on the other hand side.

6.1 Basics

When a system is probed by neutron scattering the actual scattering process is a weak perturbation which theoretically can be described within the Born approximation. Therefore, the incident neutrons with momentum $\boldsymbol{k}_i$ and the outgoing neutrons with momentum $\boldsymbol{k}_f$ are treated as plane waves. The difference between $\boldsymbol{k}_i$ and $\boldsymbol{k}_f$ defines the scattering vector $\boldsymbol{Q} = \boldsymbol{k}_i - \boldsymbol{k}_f$ while the energy difference between incident and outgoing neutrons defines the energy transfer to the sample $E = E_i - E_f$, i.e. both quantities define the probed point in $(\boldsymbol{Q}, E)$-space. Accordingly, the variation of these parameters generates a cut through $(\boldsymbol{Q}, E)$-space which eventually displays, for example, the reciprocal lattice, dispersions relations, crystal field excitation schemes, etc.. Furthermore, during the scattering process, the probed system may undergo a transition from its initial state i to another state, called final state f. The transition rate between these two states are obtained by Fermi's Golden Rule and the corresponding double differential cross section is defined as

$$\begin{aligned}\left.\frac{d^2\sigma}{d\Omega dE}\right|_{i\to f} =& \frac{k_i}{k_f}\left(\frac{m_n}{2\pi\hbar^2}\right)\left|\langle \boldsymbol{k}_f, f|\, U\, |\boldsymbol{k}_i, i\rangle\right|^2 \times \\ & \delta\left(E + E_i - E_f\right),\end{aligned} \tag{6.1}$$

with U the interaction potential and the delta-distribution for energy conversation. Certainly, the double differential cross section is proportional to the measured

intensity, c.f. Sec. 6.4. In order to foster a relation between observed intensities and theoretical models the transition matrix elements $|\langle \boldsymbol{k}_f, f| U |\boldsymbol{k}_i, i\rangle|^2$ must be evaluated and thus the corresponding scattering potentials U be defined. For nuclear scattering this is described by delta-functions

$$U(\boldsymbol{r}) = \frac{2\pi\hbar^2}{m_n} \sum_l b_l^{scat} \delta\left(\boldsymbol{r} - \boldsymbol{R}_l\right) \tag{6.2}$$

with isotope specific scattering length b^{scat} and l runs over all scattering centres $\boldsymbol{R}_l$. Additionally, the neutron's magnetic moment $\boldsymbol{\mu}_n$ can scatter off local magnetic fields $\boldsymbol{B}$ via dipole-dipole interaction which yields for the associated potential

$$U = -\boldsymbol{\mu}_n \cdot \boldsymbol{B} = -\boldsymbol{\mu}_n \cdot \mu_0 \left(\nabla \times \left(\frac{\boldsymbol{\mu}_e \times \boldsymbol{R}}{R^3} \right) - \frac{2\mu_\mathrm{B}}{\hbar} \frac{\boldsymbol{p} \times \boldsymbol{R}}{R^3} \right). \tag{6.3}$$

Thereby the local fields are generated by the magnetic moments from the electrons $\boldsymbol{\mu}_e$, whereas the first part in Eq.: (6.3) originates from the electron's spin while the second part is due to its orbital motion with momentum $\boldsymbol{p}$. A particularity for magnetic neutron scattering, i.e. of the dipole-dipole interaction, is that the corresponding double differential cross section is proportional to the local magnetic field perpendicular to the scattering vector $\boldsymbol{Q}$. Accordingly, only the perpendicular part of the magnetic signal with respect to $\boldsymbol{Q}$ can contribute to the measured intensity which aides to determine its polarisation, c.f. Sec. 6.5.
In general, the evaluation of the transition matrix elements spawn pair correlation functions which are directly related to the imaginary part of the dynamical susceptibility $\chi''(\boldsymbol{Q}, E)$ via the fluctuation-dissipation theorem. The calculation of $\chi''(\boldsymbol{Q}, E)$ in absolute units is presented in Sec. 6.4. There only the results for the corresponding double differential cross sections are quoted, as more detailed information on the theoretical aspects of neutron scattering, in particular, the derivation of $\frac{d^2\sigma}{d\Omega dE}$ can be found in various textbooks like in Ref. [309–311].

6.2 Triple Axis Spectrometer

The most versatile tool to map large portions of $(\boldsymbol{Q}, E)$-space is the triple-axis spectrometer (TAS) which is extensively used in this thesis and schematically depicted in Fig.: 6.1. In reactor based neutron sources, like FRM-II, LLB and ILL, free neutrons are obtained by nuclear fission processes of ^{235}U similar to a nuclear power plant, however in very small scale. For experimental usage the self-supported chain reaction generates in average 1.7 neutrons per fission[1] whose energies are in the MeV regime, typical for nuclear processes but much too high for

[1] $1.7 = 2.7 - 1$ as one generated neutron is needed to sustain the self-supported chain reaction

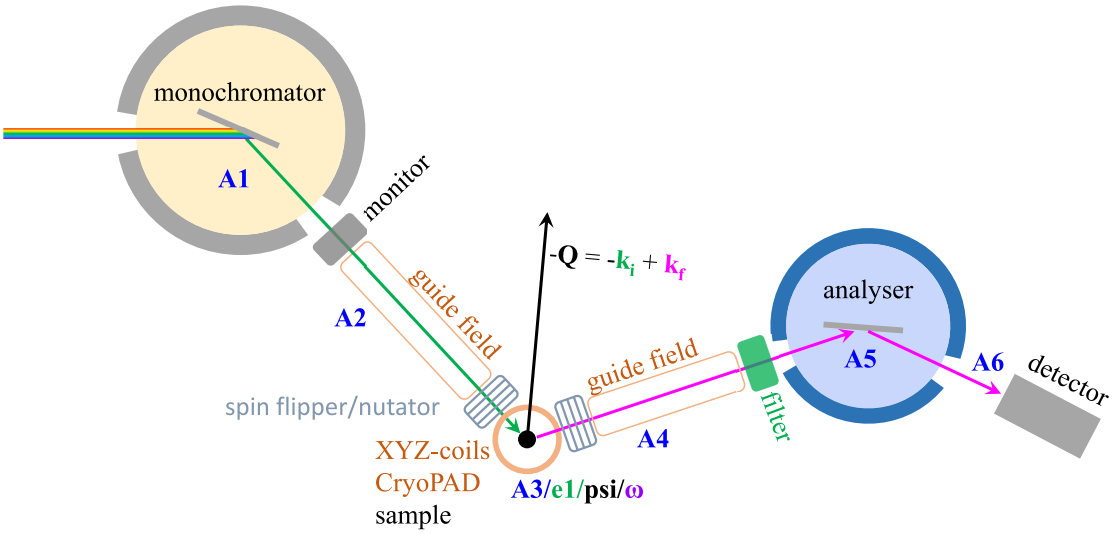

Figure 6.1: Basic layout of a Triple-Axis Spectrometer. The monochromator (A1) defines $\boldsymbol{k}_i$ while the monitor on the primary spectrometer arm estimates the incident flux on the sample (A3). For polarisation analysis guide fields and spin flippers/nutators are installed before and after the sample stage which contains the XYZ-Helmholtz coil or CryoPAD in that case. Higher order contaminations are suppressed by a filter as those scattered neutrons with $\boldsymbol{k}_f$ are picked by the analyser (A5) to be counted in the detector. A broad region of $(\boldsymbol{Q}, E)$-space can be accessed by rotating all parts of the spectrometer, which are according to ILL labelling: (A1) monochromator, (A2) spectrometer parts beyond A1, (A3) sample which is also called e1, psi or ω depending on the neutron facility, (A4) spectrometer parts beyond A3, (A5) analyser and (A6) detector.

solid state spectroscopy in the meV regime. Therefore, a moderator with temperature T_{mod} is employed in which the neutrons thermalise via scattering processes. According to the moderator temperature neutrons are called *cold* for $T_{mod} \lesssim 50\,\mathrm{K}$, *thermal* for $T_{mod} \sim 300\,\mathrm{K}$ and *hot* for $T_{mod} \gtrsim 1000\,\mathrm{K}$ and their corresponding energy distribution is given by the Maxwell-Boltzmann distribution. Consequently, the moderator tailors the neutron flux to optimise the experimental conditions for specific tasks, i.e. as a rule of thumb cold neutrons to explore the low-energy regime, thermal for the mid- to high-energies and hot for structure determination. Although these neutrons adhere to the Maxwell-Boltzmann distribution, now, they are still a white beam. Selecting a particular initial momentum $\boldsymbol{k}_i$ is obtained by Bragg scattering from the monochromator crystal (*first TAS axis*). For experiments without polarisation analysis, which are presented in this thesis, the neutron beam was monochromatised by the $(0, 0, 2)$ or $(0, 0, 4)$ nuclear Bragg peak of

pyrolytic graphite, abbreviated as PG(002) or PG(004). The same abbreviations hold for the analyser as well. In case of an experiment with polarisation analysis, the magneto-nuclear $(1, 1, 1)$ Bragg peak of the Heusler alloy Cu_2MnAl is used. Moreover, a strong magnetic field $\sim 1\,\mathrm{T}$ is applied at the monochromator/analyser crystal to saturate their magnetic moments and to align/pin the neutron's spin polarisation[2]. Due to a magnetic-nuclear interference term, only neutrons with, say, spin up are scattered, c.f. Sec. 6.5, and thus a polarised beam is generated or analysed.
A monitor is installed behind the monochromator and is nothing less than a very inefficient detector in order to estimate the incident flux on the sample, by e.g. capturing only every 10.000^{th} neutron. Note that the incident flux on the sample varies over time as the neutron source fluctuates and that the reflectivity of the monochromator depends on $\boldsymbol{k}_i$. Therefore, monitoring the incident flux prevents the observation of artefacts, and is essential for absolute unit calculation, c.f. Sec. 6.4. However, higher order neutrons, i.e. lambda-halves contaminations, are captured in the monitored incident flux also and must be corrected via a monitor-correction, which is provided by the corresponding local contact.
On the primary spectrometer arm, a guide field to preserve the neutron's polarisation and spin flippers/nutators to adjust it in the desired direction can be installed in case of an experiment with polarisation analysis. The spin flipper/nutator consist at least of one coil whose magnetic field is tuned to the incident neutrons velocity to fulfil the required precession. Otherwise, there can be collimators or aperture slits for background discrimination. At the sample stage (*second TAS axis*) the sample and its experimental environment are installed, e.g. cryostats, high-pressure cells, furnaces, time-resolved switching devices, magnets, etc.. In any case the scattered neutrons will have a final momentum $\boldsymbol{k}_f$ which is "defined" by the analyser (*third TAS axis*), meaning only those neutrons with the targeted $\boldsymbol{k}_f$ will be detected. Again, a guide field and spin flippers/nutators can be installed on the secondary spectrometer-arm, in order to rotate the to-be analysed polarisation direction of the scattered neutrons in such a way that only these will be scattered by the analyser. A brief summary of the spectrometers used in this thesis, their names, locations, moderator classifications, employed monochromators and analysers as well as the corresponding filters are listed in Tab.: 6.1.

By the rotation of all three axes, a large portion of $(\boldsymbol{Q}, E)$-space can be accessed. According to the notation at ILL[3] the monochromator rotation angle is labelled with A1, A2 for the primary spectrometer arm and everything beyond, A3 is the sample stage, or e1 at LLB, psi at FRM-II or ω in some textbooks, A4 is the sec-

[2]since the neutron is a spin-1/2 particle there are only to discrete possibilities, i.e. spin up or down with respect to the field direction and no spontaneous transitions (spin-flip) in between
[3]different at different facilities

ondary spectrometer arm and everything attached to it, A5 rotates the analyser and A6 the detector. Note that there are facility-dependent notations for the angle which rotates the sample, and thus there are different notations for the rocking scans in this thesis as well as in the literature. Technically, monochromator and analyser, and thus $\boldsymbol{k}_i$ and $\boldsymbol{k}_f$ are confined on a plane, as those components are not lifted due to their heavy shieldings. The plane in which $\boldsymbol{k}_i$ and $\boldsymbol{k}_f$ are confined is called scattering plane and set by the sample orientation, which thus provides a well-defined $\boldsymbol{Q}$. Therefore, any $(\boldsymbol{Q}, E)$-position confined to the scattering plane can be accessed by varying $\boldsymbol{k}_i$ and $\boldsymbol{k}_f$, i.e. by moving the spectrometer arms and rotating the sample appropriately.

More detailed information on the instrumentation of a TAS can be found in Ref. [306–308].

Table 6.1: Used neutron scattering instruments and their corresponding configurations.

instrument	facility	sort	mono	ana	filter
PANDA	FRM-II	cold	PG(002)	PG(002)	cooled Be
PUMA	FRM-II	thermal	PG(002)	PG(002)	PG
IN4	ILL	thermal	PG(004)	TOF	–
IN8	ILL	thermal	PG(002) Si(111)	PG(002)	PG
IN20	ILL	thermal	Heusler(111) Si(111)	Heusler(111) PG(002)	PG
IN22	ILL	thermal	Heusler(111)	Heusler(111)	PG
2T	LLB	thermal	PG(002)	PG(002)	PG
3T1	LLB	thermal	PG(002)	PG(002)	PG
4F1 4F2	LLB	cold	PG(002)	PG(002) Heusler(111)	cooled Be
G43	LLB	cold	PG(002)	PG(002)	colled Be

6.3 Time-of-Flight Spectrometer, IN4

The data presented in Chap. 5 are obtained at the time-of-flight (TOF) spectrometer IN4 at ILL. Although this is the only experiment conducted at a TOF spectrometer its principle of work is outlined in the following. The main difference between a TOF spectrometer and a TAS is that the latter contains a analyser crystal in order to investigate $\boldsymbol{k}_f$, while the former does not. Instead, the TOF spectrometer consists of a large detector unit and measures the neutrons' time of flight after the scattering process; to be precise by knowing the distance between sample and detector the time of flight and thus the energy E can be classically calculated. Furthermore, the large detector unit consists of many single detectors, which are grouped into several banks to cover a certain solid angle. Accordingly, the neutron's detection position allows to recalculate the corresponding $\boldsymbol{Q}$, and thus large portions of $(\boldsymbol{Q}, E)$-space can be mapped simultaneously.
Obviously, this kind of spectrometer cannot operate with a continuous neutron flux as this would obfuscate information on the transferred energy. Therefore, the TOF spectrometer is either operated at a spallation source which intrinsically supplies a pulsed neutron flux or, as it is the case for the IN4 TOF spectrometer at ILL, a continuous neutron flux from the reactor source is chopped into short pulses. The incident neutron momentum $\boldsymbol{k}_i$[4] is defined by a velocity selector, or at IN4 by a monochromator crystal. Note that the thermal neutron beam is monochromatised before it is chopped.

More detailed information about the TOF technique and the IN4 spectrometer can be found in Ref. [306, 307] and on the corresponding webpage[5].

6.4 Absolute Unit Calculation

In a neutron scattering experiment, the reciprocal space is probed, and the resulting information is encoded in (detector) counts either per time interval or monitor counts. To decode the information knowledge of the intensity distribution in reciprocal space and in energy, $I(\boldsymbol{Q}, E)$, is sufficient in most cases, e.g. for structural refinements or tracing intensity changes when an external control parameter, like temperature T, magnetic field B, pressure p, etc. is varied. However, a quantitative comparison of the intensities between different experiments is impeded as each dataset is "individual"; meaning it contains instrument specific resolution effects, sample illumination, counting time, etc.. Therefore, the comparable quantity is the double differential cross section $d^2\sigma/d\Omega dE$ which is related to the measured

[4] or with an elaborated chopper system several $\boldsymbol{k}_i$ can be selected simultaneously [312]

[5] `https://www.ill.eu/users/instruments/instruments-list/in4c/description/instrument-layout/`

intensity $I(\boldsymbol{Q}, E)$ via a four-dimensional convolution with the instrumental resolution $\mathfrak{R}$

$$I(\boldsymbol{Q}, E) = \Phi_{scale} \left(\mathfrak{R} * \frac{d^2\sigma}{d\Omega dE} \right) (\boldsymbol{Q}, E) \,, \tag{6.4}$$

$$\mathfrak{R}(\boldsymbol{Q}, E) = R_0(\boldsymbol{Q}, E) \exp\left(-\frac{1}{2} \boldsymbol{\Delta} \cdot \boldsymbol{M}(\boldsymbol{Q}, E) \cdot \boldsymbol{\Delta}^t \right),$$

$$\boldsymbol{\Delta} = \left(Q'_x - Q_x, Q'_y - Q_y, Q'_z - Q_z, E' - E \right)$$

with $\boldsymbol{M}(\boldsymbol{Q}, E)$ being the resolution matrix within the Cooper-Nathans or Popovici approximation[6] [190, 313], $\boldsymbol{\Delta}$ is the four-dimensional difference vector in $(\boldsymbol{Q}, E)$-space, $R_0(\boldsymbol{Q}, E)$ accounts for the instrumental efficiency and, among other factors, the resolution-volume normalisation, and Φ_{scale} is an overall scaling factor, which includes among other factors the sample volume and illumination, incident flux and counting time [189, 243, 308]. In order to calculate the double differential cross section, in particular, $\chi''(\boldsymbol{Q}, E)$ and thus the scattering intensity of the spin resonance mode of Na-doped $BaFe_2As_2$, c.f. Chap. 2, Φ_{scale} must be determined and the convolution process be dealt with. Reslib, a Matlab routine, realises this by fitting the convolution of a model for the double differential cross section and the resolution to the data [189]. Consequently, Φ_{scale} can be determined if it is the only free parameter concerning the overall intensity, i.e. when $d^2\sigma/d\Omega dE$ is completely determined. In this context, calculating the intensity of an acoustic phonon is very suitable, as it is an intrinsic property of the sample [207]. In addition, there are two alternative methods for absolute unit determination; one is based on sample elastic incoherent scattering the other on using a reference standard as discussed in detail by Xu *et al.* [207]. Using the reference standard, e.g. Vanadium, is seldom done for TAS experiments as it requires the repetition of all performed scans which is too time-consuming. On the other hand, this is the *modus operandi* in TOF experiments (though not conducted in Chap. 5). Normalising on incoherent scattering is difficult as to the measured intensity, the sample, as well as its environment, contributes. This results easily in an overestimated reference and thus in an underestimated signal; which would explain why Wang *et al.* [210] observed a 6 times less intense SRM in optimally doped $Ba(Fe_{1-x}Co_x)_2As_2$ in comparison to Inosov *et al.* [131] who normalised on phonon scattering.

Following various textbooks on neutron scattering [306, 308, 309, 311] the double

[6] The Popovici approximation describes the resolution in terms of beam divergences due to Soller collimators as well as shape and dimension of the source, monochromator, sample, analyser, and detector. In the Cooper-Nathans approximation the resolution is entirely determined by the (beam) divergences of each spectrometer component. Additionally, the corresponding reflection and transmission coefficients are considered [189–191, 313].

differential cross section for phonons is defined as

$$\left(\frac{d^2\sigma}{d\Omega dE}\right)_{phon} = N_{nuc}\hbar^2\frac{k_f}{k_i}\frac{n(E)+1}{2E(q)}\left|F_{dyn}\left(Q\right)\right|^2\delta\left(E-E(q)\right), \tag{6.5}$$
$$F_{dyn}\left(Q\right) = \sum_j \frac{b_j^{scat}}{\sqrt{m_j}}\boldsymbol{Q}\cdot\boldsymbol{\xi}_{j,s}\left(\boldsymbol{q}\right)\mathrm{e}^{i\boldsymbol{Q}\cdot\boldsymbol{r}_j}\mathrm{e}^{-W_j(Q)},$$

where F_{dyn} denotes the dynamical structure factor, N_{nuc} the number of nuclear unit cells, b_j^{scat} the scattering length and m_j the mass of atom j, $\boldsymbol{\xi}$ is the polarisation vector, s labels the phonon branch, $\mathrm{e}^{-W_j(Q)}$ the Debye-Waller factor and $n(E)$ the Bose population factor (at fixed temperature). The Reslib routine incorporates the final/initial momentum ratio k_f/k_i to the resolution, however, here it is written explicitly to keep consistency with wide-spread literature. In case of acoustic phonons F_{dyn} simplifies further for $\boldsymbol{q}\to 0$ as

$$\lim_{\boldsymbol{q}\to 0}\frac{\boldsymbol{\xi}_{j,s}(\boldsymbol{q})}{\sqrt{m_j}} = \frac{\hat{\boldsymbol{e}}(\boldsymbol{q})}{\sqrt{M}},$$
$$\Rightarrow F_{dyn}(Q) = \frac{Q\cos(\varphi)}{\sqrt{M}}\sum_j b_j^{scat}\mathrm{e}^{i\boldsymbol{Q}\cdot\boldsymbol{r}_j}\mathrm{e}^{-W_j(Q)},$$

while M is the total mass of all atoms in the unit cell [243, 308] and the angle between scattering vector $\boldsymbol{Q}$ and polarisation of the phonon mode is given by $\cos(\varphi)$, which is close to 1 if the scan path is reasonably chosen. Therefore, $d^2\sigma/d\Omega dE$ for acoustic phonon scattering can be written as

$$\begin{aligned}\left(\frac{d^2\sigma}{d\Omega dE}\right)_{phon} =& N_{nuc}\frac{k_f}{k_i}\frac{\left(\hbar Q\right)^2}{2m_n}\frac{n(E)+1}{E(q)}\frac{m_n}{M}\cos(\varphi)\times \\ & \left|\sum_j b_j^{scat}\mathrm{e}^{i\boldsymbol{Q}\cdot\boldsymbol{r}_j - W_j(Q)}\right|^2\delta\left(E-E(q)\right).\end{aligned} \tag{6.6}$$

In the numerical implementation the delta-distribution is approximated by a Gaußian with a small but finite width of 0.05 meV while the acoustic phonon dispersion for small $\boldsymbol{q}$ is given by $E=\alpha q$. Only phonons adhering to this approximation were treated in this thesis, for the general case $E(q)$ must be modelled by the holistic phonon dispersion.
Furthermore, the differential cross section for elastic magnetic Bragg scattering is defined as

$$\begin{aligned}\left(\frac{d\sigma}{d\Omega}\right)_{mag} =& \left(\frac{\gamma r_0}{2}\right)^2 N_{mag}\frac{\left(2\pi\right)^3}{V_{mag}}\sum_{\boldsymbol{Q}}\delta\left(\boldsymbol{k}-\boldsymbol{Q}\right)\times \\ & \left|\sum_j g\boldsymbol{S}_\perp f(\boldsymbol{Q})\mathrm{e}^{i\boldsymbol{Q}\cdot\boldsymbol{r}_j}\right|^2\mathrm{e}^{-2W(Q)},\end{aligned} \tag{6.7}$$

with $\gamma r_0/2 = p = 2.695\,\text{fm}$ corresponds to the scattering length of a single magnetic moment of $1\,\mu_\text{B}$, while γ is the gyromagnetic ratio of the neutron and r_0 the classical electron radius. $f(\boldsymbol{Q})$ the magnetic form factor, g denotes the Landé factor and $g\boldsymbol{S}_\perp = \boldsymbol{\mu}_\perp$ is the perpendicular projection with respect to the scattering vector $\boldsymbol{Q}$ of the ordered moment in units of μ_B. Note that in a (unpolarised) neutron experiment only this projected component contributes to the measured intensity. N_{mag} and V_{mag} account for the number and volume of the magnetic unit cells, respectively. Within the Reslib routine the delta-distributions in Eq.: (6.7) are approximated by Lorentzians. Additionally, a very sharp Lorentzian with width = 0.01 meV for the energy dependence was inserted, as Reslib erroneously would treat the Bragg peak as energy independent otherwise. Thereby, the cross section of elastic magnetic scattering, and thus the measured intensity is fully modelled in the Reslib routine with only two free parameters, the magnetic moment $\boldsymbol{\mu}$ and the overall scaling factor Φ_{scale}. When the latter is terminated, e.g. via a phonon scan in the acoustic limit, the magnetic moment of the sample can be estimated, as it is done for Na39 in Sec. 2.2.2.

In case of inelastic magnetic scattering the imaginary part of the dynamical susceptibility $\chi''(\boldsymbol{Q}, E)$ can be calculated from the double differential cross section, which is defined as [306, 308–311]

$$\begin{aligned}\frac{d^2\sigma}{d\Omega dE} = &\left(\frac{\gamma r_0}{2}\right)^2 \frac{k_f}{k_i} \frac{N}{\pi\mu_B^2} \frac{\mathrm{e}^{-2W(\boldsymbol{Q})}}{1-\mathrm{e}^{-\frac{E}{k_B T}}} f^2(\boldsymbol{Q}) \times \\ &\sum_{\alpha,\beta} \left(\delta_{\alpha\beta} - \hat{\boldsymbol{Q}}_\alpha \cdot \hat{\boldsymbol{Q}}_\beta\right) \cdot \chi''_{\alpha,\beta}(\boldsymbol{Q}, E),\end{aligned} \tag{6.8}$$

where N accounts for the number of unit cells again. $\left(\delta_{\alpha\beta} - \hat{\boldsymbol{Q}}_\alpha \cdot \hat{\boldsymbol{Q}}_\beta\right)$ is the polarisation factor, which states that only the perpendicular part of the magnetic signal with respect to the scattering vector $\boldsymbol{Q}$ contributes to the double differential cross section. For an isotropic signal the sum over the spatial coordinates α and β would result in a factor 2, but in case of anisotropy it must be evaluated appropriately. To transform $\chi''(\boldsymbol{Q}, E)$ to an absolute scale requires two things: first the overall scaling factor Φ_{scale} must again be known, i.e. be terminated from phonon scattering in the acoustic limit, and second, a model for $\chi''(\boldsymbol{Q}, E)$ must be defined. Consequently, Reslib convolutes the given model with the instrumental resolution and fits it to the data[7]. Note that the in this way fitted data still contain the convolution with the resolution and the geometry factor, even after normalising with Φ_{scale}. Therefore the fitted data is not $\chi''(\boldsymbol{Q}, E)$ but $\Re * \frac{d^2\sigma}{d\Omega dE}$, however in units of $\mu_\text{B}^2/\text{eV}\cdot\text{f.u.}$. The systematic error of this method is estimated

[7]data format must be (H, K, L, E, I, dI), with H, K, L in reciprocal lattice units, E the transferred energy and I, dI the intensity in counts, respectively its corresponding error.

to be 20-30 % [207], but error-bars in all figures of this work correspond to the standard deviation of the count-rate and do not include the errors caused by the normalisation process.

6.5 Polarisation Analysis

Polarised neutron scattering is a powerful tool to separate nuclear and magnetic scattering components and to spatially resolve the orientation of magnetic signals. Accordingly, the neutron's spin must be analysed and the corresponding double differential cross section[8] is defined as

$$\left.\frac{d^2\sigma}{d\Omega dE}\right|_{s_i\to s_f} = \frac{k_f}{k_I}\sum_{i,f} P(i)\left|\langle f|\sum_l e^{i\boldsymbol{Q}\cdot\boldsymbol{r}_l} U_l^{s_i s_f}|i\rangle\right|^2 \times \delta\left(E+E_i-E_f\right), \tag{6.9}$$

with $s_i(s_f)$ the initial(final) neutron spin, $P(i)$ the probability factor of the initial state and $U^{s_i s_f}$ the spin-dependent scattering amplitude, while l labels the associated scattering centres. The scattering amplitudes are defined as

$$U^{s_i s_f} = \langle s_f|\, b_l^{scat} - \pi_l \boldsymbol{S}_\perp\cdot\boldsymbol{\sigma} + B_l \boldsymbol{I}_l\cdot\boldsymbol{\sigma}\,|s_i\rangle\,, \tag{6.10}$$

whereby b_l^{scat} denotes the coherent nuclear scattering length, $\pi_l\boldsymbol{S}_\perp = p\cdot f(\boldsymbol{Q})\cdot\boldsymbol{\mu}_\perp$ the magnetic scattering amplitude[9], $p = 2.695\,\mathrm{fm}$ and B_l the spin-dependent nuclear magnetic scattering amplitude. In a pioneering work of Moon, Riste and Koehler [314] the spin-dependent scattering amplitudes in Eq.: (6.10) were derived as[10]

$$U^{\uparrow\uparrow} = b^{scat} - pS_{\perp,x} + BI_x \tag{6.11a}$$
$$U^{\downarrow\downarrow} = b^{scat} + pS_{\perp,x} - BI_x \tag{6.11b}$$
$$U^{\uparrow\downarrow} = -p\left(S_{\perp,y}+iS_{\perp,z}\right) + B\left(I_y+iI_z\right) \tag{6.11c}$$
$$U^{\downarrow\uparrow} = -p\left(S_{\perp,y}-iS_{\perp,z}\right) + B\left(I_y-iI_z\right) \tag{6.11d}$$

where x is parallel to $\boldsymbol{Q}$. Close examination of these equations yields that nuclear scattering is always a non-spin-flip (NSF) process, ($\uparrow\uparrow$) or ($\downarrow\downarrow$), when nuclear magnetic scattering is neglected. Moreover, when the neutron's polarisation $\boldsymbol{P}$ is

[8] holds for elastic and inelastic scattering alike, but only the spin-dependence is considered here

[9] the index $\perp$ symbols that only the perpendicular part of the magnetic signal with respect to $\boldsymbol{Q}$ contributes to the intensity

[10] the indices are cyclically exchanged as in the original publication in order to match the frame of reference here

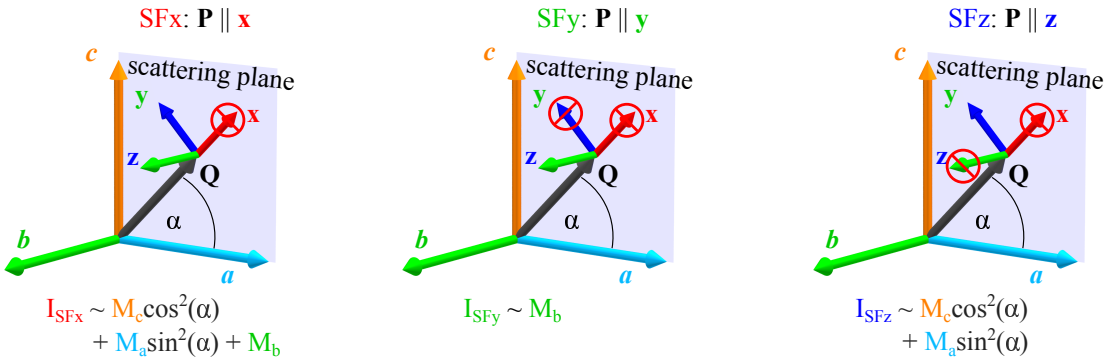

Figure 6.2: Frame of reference for polarisation analysis. The polarisation analysis allows to differentiate the intensity contributions in the SFx, SFy and SFz channels, respectively, along the three principal directions $\boldsymbol{a}$, $\boldsymbol{b}$ and $\boldsymbol{c}$. For each SF channel the corresponding contributions are derived, based on the selection rules for neutron scattering. In the given frame of reference $\boldsymbol{Q}||x$, y is perpendicular to x, but still in the scattering plane, while z is normal to it.

along x and parallel to $\boldsymbol{Q}$ magnetic scattering is always a spin-flip (SF) process, ($\uparrow\downarrow$) or ($\downarrow\uparrow$). In particular the SF channel contains only the part of magnetic scattering which is perpendicular to both, the scattering vector $\boldsymbol{Q}$ and the neutron's polarisation $\boldsymbol{P}$ as it is summarised in Fig.: 6.2 and Tab.: 6.2. In this example, the scattering plane is spanned by $\boldsymbol{a}$ and $\boldsymbol{c}$, while the neutron's polarisation superimposes a second frame of reference where x is always parallel to $\boldsymbol{Q}$, y in the scattering plane, z perpendicular and thus parallel to $\boldsymbol{b}$. With this second frame of reference and the corresponding additional "selection rules" the magnetic signal in the SF and NSF channels can be decomposed along the three principal axes $\boldsymbol{a}$, $\boldsymbol{b}$

Table 6.2: Contributions in the various SF and NSF channels. According to the frame of reference as defined in Fig.: 6.2 the various contributions to the SF and NSF channels are resolved.

Polarisation	spin-flip (SF)	non-spin-flip (NSF)
$\mathbf{P}\|\|\boldsymbol{x}$	$M_c \cos^2(\alpha) + M_a \sin^2(\alpha)$ $+M_b$ + BG	N + BG′
$\mathbf{P}\|\|\boldsymbol{y}$	M_b + BG	$M_c \cos^2(\alpha) + M_a \sin^2(\alpha)$ + N + BG′
$\mathbf{P}\|\|\boldsymbol{z}$	$M_c \cos^2(\alpha) + M_a \sin^2(\alpha)$ + BG	M_b + N + BG′

and $\boldsymbol{c}$. The angle α is given by $\boldsymbol{Q}$ and $\boldsymbol{a}$ and the corresponding $\cos^2(\alpha)$ ($\sin^2(\alpha)$) is summarised in the *geometry factor* $g(\boldsymbol{Q})$. For the polarisation analysis in Chap. 2 and Chap. 3 $\boldsymbol{a}$ is the magnetic ordering direction of the pure host compound $BaFe_2As_2$ in the o-AFM phase, i.e. along $[1,1,0]_{\mathrm{tet}} = [1,0,0]_{\mathrm{ort}}$, while $\boldsymbol{c}$ denotes the directions perpendicular to the FeAs-layers.

Furthermore, Eqs.: (6.11) are the theoretical basis to generate a polarised and monochromatic neutron beam as nuclear and magnetic scattering amplitudes are contributing coherently. If a magnetic field $\boldsymbol{B}$ polarises the neutrons perpendicular to $\boldsymbol{Q}$ and magnetises the ferromagnetic monochromator crystal accordingly, then the scattering amplitudes are given by

$$\left(\frac{\mathrm{d}\sigma}{\mathrm{d}\Omega}\right)^{(\uparrow\uparrow)} = |F_N(Q) + F_M(Q)|^2$$
$$\left(\frac{\mathrm{d}\sigma}{\mathrm{d}\Omega}\right)^{(\downarrow\downarrow)} = |F_N(Q) - F_M(Q)|^2 .$$

Consequently, a monochromatised and polarised beam results at hkl positions of equal nuclear and magnetic structure factors, which is the case at the $(1,1,1)$ reflection of the Heusler alloy Cu_2MnAl, for example. The polarisation of the scattered neutrons is analysed in the same way. A measure for the polarisation quality is the flipping ratio (FR) i.e. the intensity ratio of I_{SF}/I_{NSF} which is directly related to the total polarisation Π via

$$\Pi = \frac{I_{SF} - I_{NSF}}{I_{SF} + I_{NSF}} = \frac{FR - 1}{FR + 1}. \tag{6.12}$$

For Heusler - Heusler set-up typical flipping ratios are $FR \sim 14$ which corresponds to a total polarisation of $\Pi \sim 86\,\%$. Technically, guide-fields and spin-flippers/nutators are installed additionally on the spectrometer arms in order to preserve the neutrons polarisation and to adjust it in the desired direction of examination. At the sample stage this is realised by either a XYZ-Helmholtz coil or the CryoPAD[11]. The XYZ-Helmholtz coil always generates a small magnetic field at the sample and only the three diagonal[12] terms of the polarisation matrix can be analysed. On the other hand, the CryoPAD shields off all magnetic fields at the sample via a Meißner shield, and thus the off-diagonal terms can be assessed. Further technical options to polarise the neutron beam are the $(2,0,0)$ Bragg peak in $Co_{0.92}Fe_{0.08}$ or Fe/Si supermirrors, for example. However, experiments which were conducted at IN20 and IN22 with polarisation analysis employed a Heusler crystal for monochromatisation and analysis, while at 4F1 a supermirror was used

[11] **Cryo**genic **P**olarisation **A**nalysis **D**evice

[12] xx, yy and zz, but in all, up down SF and NSF combinations

for the polarisation and again a Heusler for the analysis.

More details about the neutron polarisation technique can be found in various textbooks like in Ref. [307–311].

Appendix

A.1 Spin Reorientation transitions

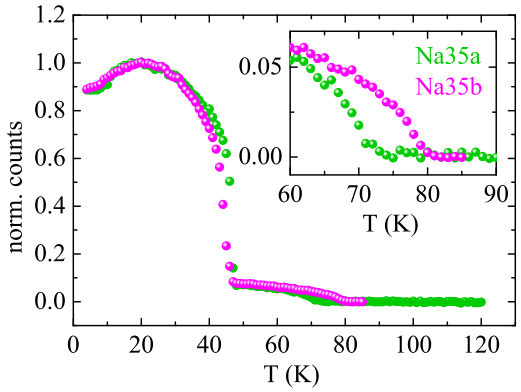

Figure A.1.1:
Temperature dependence of $(0.5, 0.5, 1)$ magnetic Bragg peak in Na35a and Na35b. Temperature dependence of the normalised $(0.5, 0.5, 1)$ Bragg peak intensity of Na35a and Na35b. Both samples behave very similar except that T_N in Na35b is $\sim 8\,\mathrm{K}$ higher than in Na35a as shown in the inset.

Although the samples Na35a and Na35b should be nominal of the same composition, Na35b displays a T_N which is $\sim 8\,\mathrm{K}$ higher than the T_N in Na35a. Despite a thorough characterisation, the EDX method contains an intrinsic error of 1-2 %. The observed discrepancy in T_N must be within the EDX error and can be explained by the steepness of the corresponding phase boundary in the phase diagram. Note on this occasion, the phase boundary of c-AFM and SC+M domes are rather flat, and thus will only be marginally affected by a slight deviation of x, in this region. However, when normalised on their maximum the temperature dependence of Na35a and Na35b are very identical in regard to T_{reo} and the suppression of the ordered magnetic moment below T_c as Fig.: A.1.1 clearly documents.

A.2 Magnetic Excitations in $Ba_{1-x}Na_xFe_2As_2$

The raw data of the E-scans at L = 1 and 3 at PUMA spectrometer for Na35b and the corresponding background estimations are shown in Fig.: A.2.1. The $\boldsymbol{Q}$ positions to estimate the background were $(0.4, 0.4, 1.74)$ for L = 1 and $(0.4, 0.4, 3.32)$ as well as $(0.6, 0.6, 2.55)$ for L = 3. Note that the given $\boldsymbol{Q}$ positions were chosen in such a way that Q is kept constant. Additionally, background points which result from the $\boldsymbol{Q}$-scans were inserted as well. Moreover, the background is described by a polynomial.

The raw data of the E-scans at L = 1 and 3 at PUMA spectrometer for Na39 and the corresponding background estimations are shown in Fig.: A.2.2. The raw

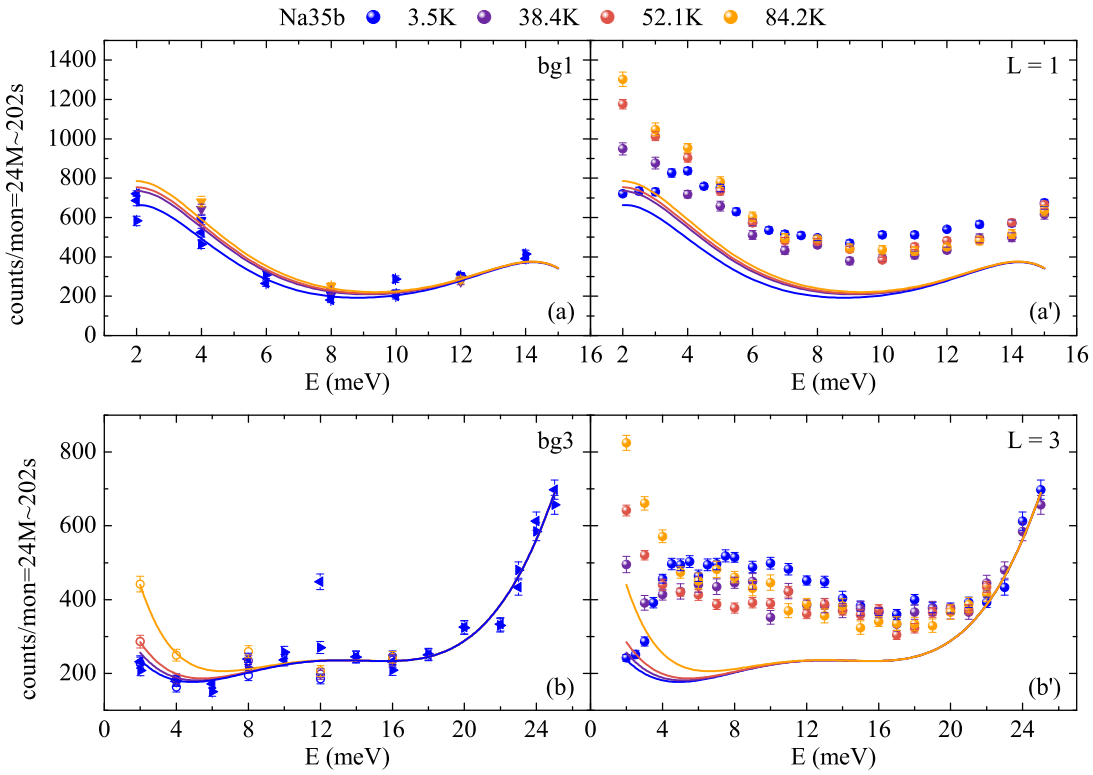

Figure A.2.1: Raw data and estimated background for Na35b. **(a)** Background (bg) scan for L = 1 at $(0.4, 0.4, 1.74)$ for various temperatures. Lines correspond to a polynomial fit. **(a')** E-scan at L = 1 for the same temperatures as in (a). **(b)** Background scans for L = 3 at $(0.4, 0.4, 3.32)$ and at $(0.6, 0.6, 2.55)$ for various temperatures. **(b')** E-scan at L =3 for the same temperatures as in (b).

data of the E-scans at L = 1 and 3 at PUMA spectrometer for Na39 and the corresponding background estimations are shown in Fig.: A.2.2. The $\boldsymbol{Q}$ positions to estimate the background were $(0.36, 0.36, 1.92)$ for L = 1 and $(0.254, 0.254, 3.634)$ as well as $(0.685, 0.685, 2.005)$ for L = 3. Note that the given $\boldsymbol{Q}$ positions were chosen in such a way that Q is kept constant. Additionally, background points which result from the $\boldsymbol{Q}$-scans were inserted as well. Moreover, the background is described by a polynomial. In particular, the phonon scans and the background subtracted spectra at 3.5 K for L = 1 lie perfectly on top of each other, which documents clearly that both experiments can be combined in the analysis.

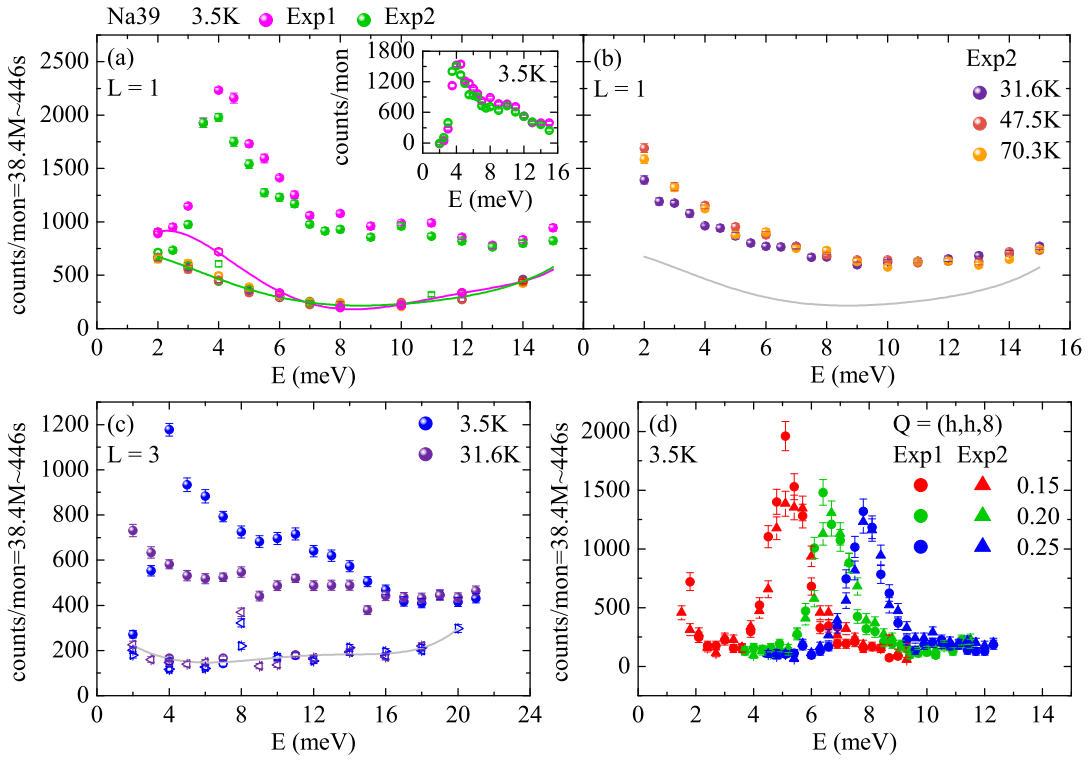

Figure A.2.2: Raw data and estimated background for Na39. **(a)** E-scan and background at $(0.36, 0.36, 1.92)$ for L = 1 at 3.5 K for both experiments. The lines correspond to polynomial fits. After background subtraction both spectra lie perfectly on top of each other as the inset shows. **(b)** E-scan at L = 1 at various temperatures but always in the normal state. **(c)** E-scan and background scans at $(0.254, 0.254, 3.634)$ and at $(0.685, 0.685, 2.005)$ for L = 3 at 3.5 K and 31.6 K. **(d)** Phonon scans of Exp1 and Exp2 at 3.5 K which lie perfectly on top of each other in both cases.

The raw data of the E-scans at L = 1 and 3 at PUMA spectrometer for Na40 and the corresponding background estimations are shown in Fig.: A.2.3. The raw data of the E-scans at L = 3 and 1 at PUMA spectrometer for Na40 and the corresponding background estimations are shown in Fig.: A.2.3. The $\boldsymbol{Q}$ positions to estimate the background were $(0.36, 0.36, 1.92)$ for L = 1 and $(0.254, 0.254, 3.634)$ for L = 3. Note that the given $\boldsymbol{Q}$ positions were chosen in such a way that Q is kept constant. Additionally, background points which result from the $\boldsymbol{Q}$-scans were inserted as well. Moreover, the background is described by a polynomial. In particular, the phonon scans lie perfectly on top of each other, which documents clearly that both experiments can be combined in the analysis.

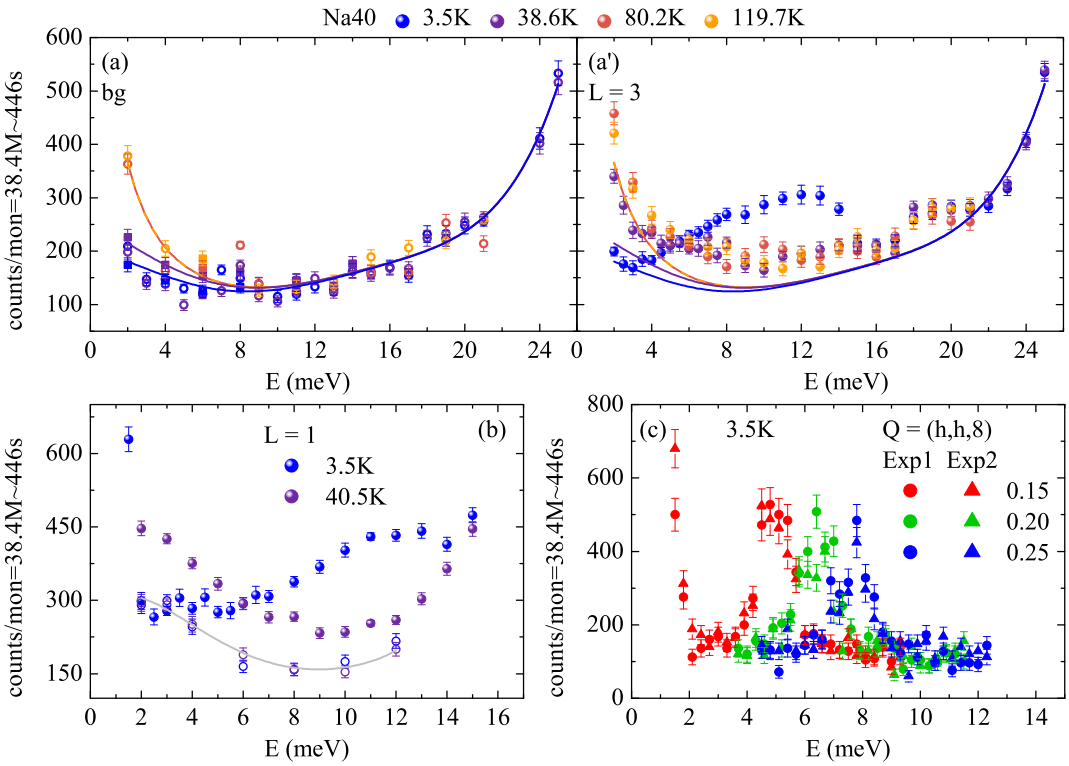

Figure A.2.3: Raw data and estimated background for Na40. **(a)** Background (bg) scan for L = 3 at $(0.254, 0.254, 3.634)$ for various temperatures. Lines correspond to a polynomial fit. **(a')** E-scan at L = 3 for the same temperatures as in (a). **(b)** E-scan at L = 1 and its corresponding background at $(0.36, 0.36, 1.92)$ at 3.5 K and 40.5 K. Again, the solid line is a polynomial fit to the bg. **(c)** Phonon scans of Exp1 and Exp2 at 3.5 K which lie perfectly on top of each other in both cases.

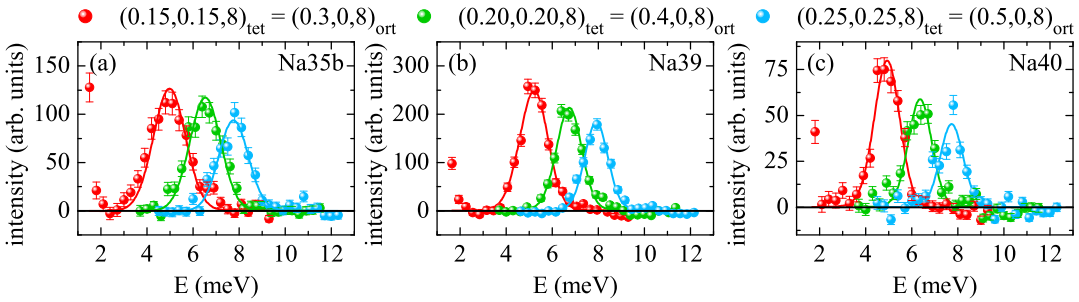

Figure A.2.4: Phonon scans in Na35b, Na39 and Na40. The presented phonons are described by Lorentzians in the RESLIB routine, respectively for Na35b, Na39 and Na40 in **(a)(b)(c)**.

The phonon scans, which were used for the absolute unit calculation are shown in Fig.: A.2.4. For Na39 and Na40 the presented data points result from the combination of the two scans shown in Fig.: A.2.2(d) and Fig.: A.2.3(d), respectively. Nonetheless, the obtained phonons were described by Lorentzians in the RESLIB routine. Thereby, the different scaling factors Φ_{scale}, summarised in Tab.: A.2.1 were obtained, which were used to transform the INS data to an absolute scale.

The magnetic Bragg peaks in Na39 and their corresponding description by the RESLIB routine are given in Fig.: A.2.5. Since the RESLIB routine cannot deal with δ-functions, which were given in the cross section for magnetic Bragg scattering in Eq.: (6.7), these were modelled by sharp Lorentzians. Furthermore, the broadening due to the convolution with the experimental resolution is indicated, by inserting the (normalised) Lorentzian model for the magnetic Bragg peak in Fig.: A.2.5. In addition, the model parameters and the obtained ordered magnetic moments for Na35b and Na39 are listed in the table on the right-hand side of the figure.

Table A.2.1: Scaling factors obtained from phonon scattering

sample	Φ_{scale}
Na35b	228(14)
Na39	429(8)
Na40	107(7)

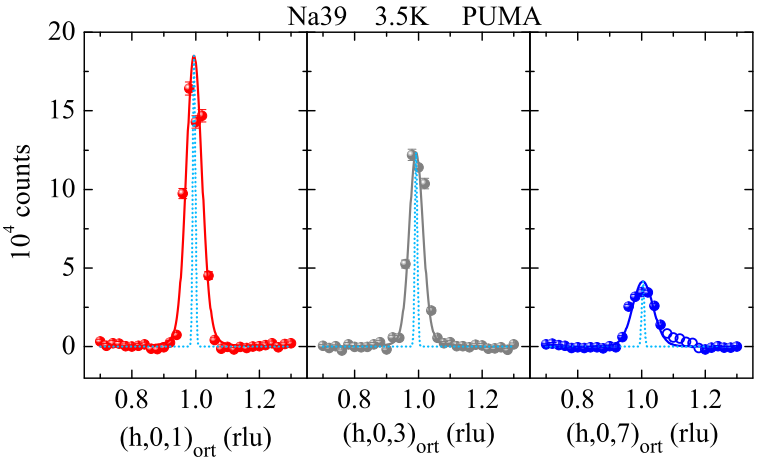

entity	value
H_c	1
L_c	1, 3, 7*
E_c	0 meV*
w_{HK}	0.004 rlu*
w_L	0.012 rlu*
w_E	0.01 meV*
$\mu(3.5\,\mathrm{K})$	0.1549 μ_B
$\mu(26\,\mathrm{K})$	0.1887 μ_B

* fixed

Figure A.2.5: Reslib fits to magnetic Bragg peaks in Na39. The magnetic Bragg peaks were modelled by Lorentzians, while the solid lines are the RESLIB fit and the dotted lines the pure model. On the right hand side is a table summarising the employed parameters.

A.3 Spin Excitations in Na25 and Na31

For Na25 the raw data, estimated background, the phonon scan as a reference to combine the two experiments Exp1 and Exp2 at PUMA spectrometer and their weighted average are shown in Fig.: A.3.1. The positions to estimate the back-

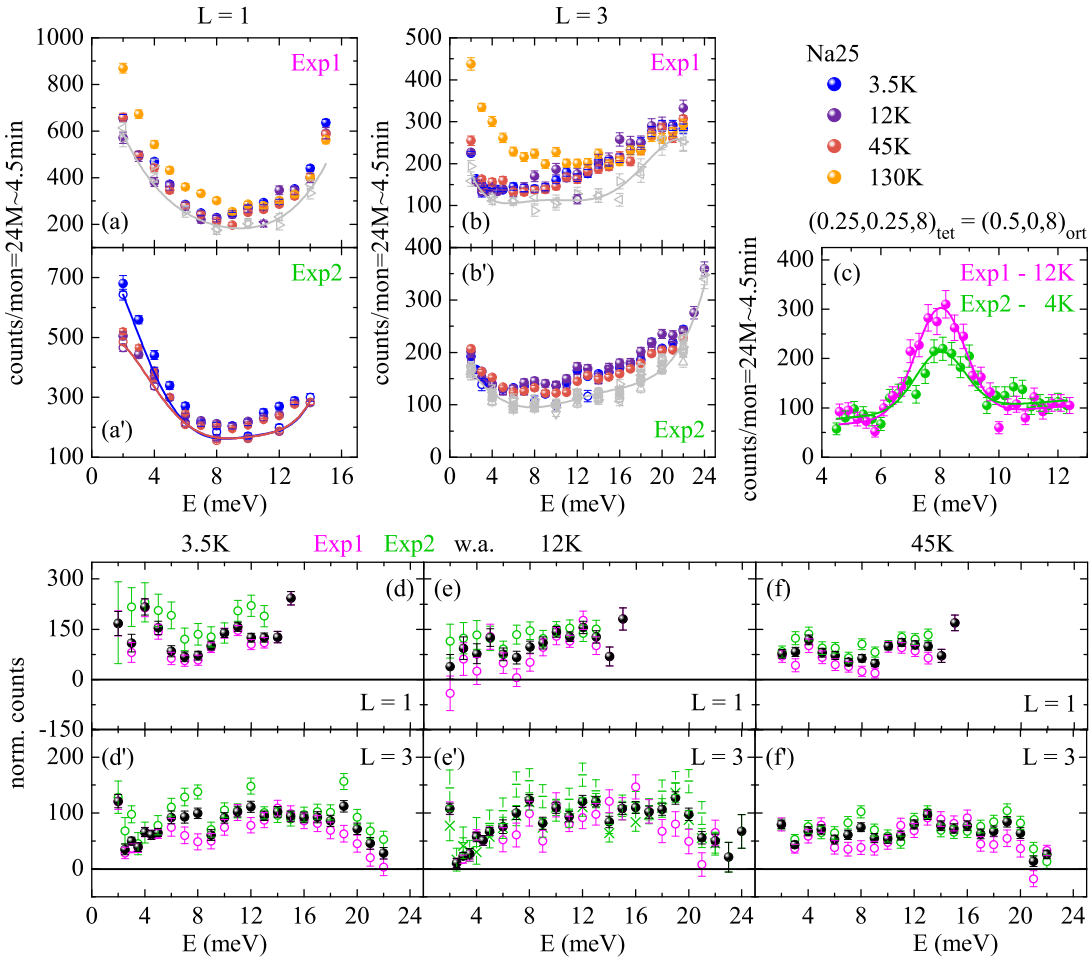

Figure A.3.1: Raw data of Na25 and their weighted average. **(a)(a')** E-scan at L = 1 at various temperatures whereas the open symbols indicate the background, respectively for Exp1 and Exp2. **(b)(b')** same as in (a)(a') but for L = 3. **(c)** Phonon scans to enable the combination of Exp1 and Exp2. **(d)(d')** Corrected and renormalised spectra at 3.5 K at L = 1 and 3 respectively. **(e)(e')** Same as in (d)(d') but at 12 K. Note that the weighted average also includes scans at $(0.5, 0.5, 3)$ and $(\overline{0.5}, \overline{0.5}, 3)$ from Exp2 which are symbolised by (x) and (-). **(f)(f')** Same as in (d)(d') but at 130 K.

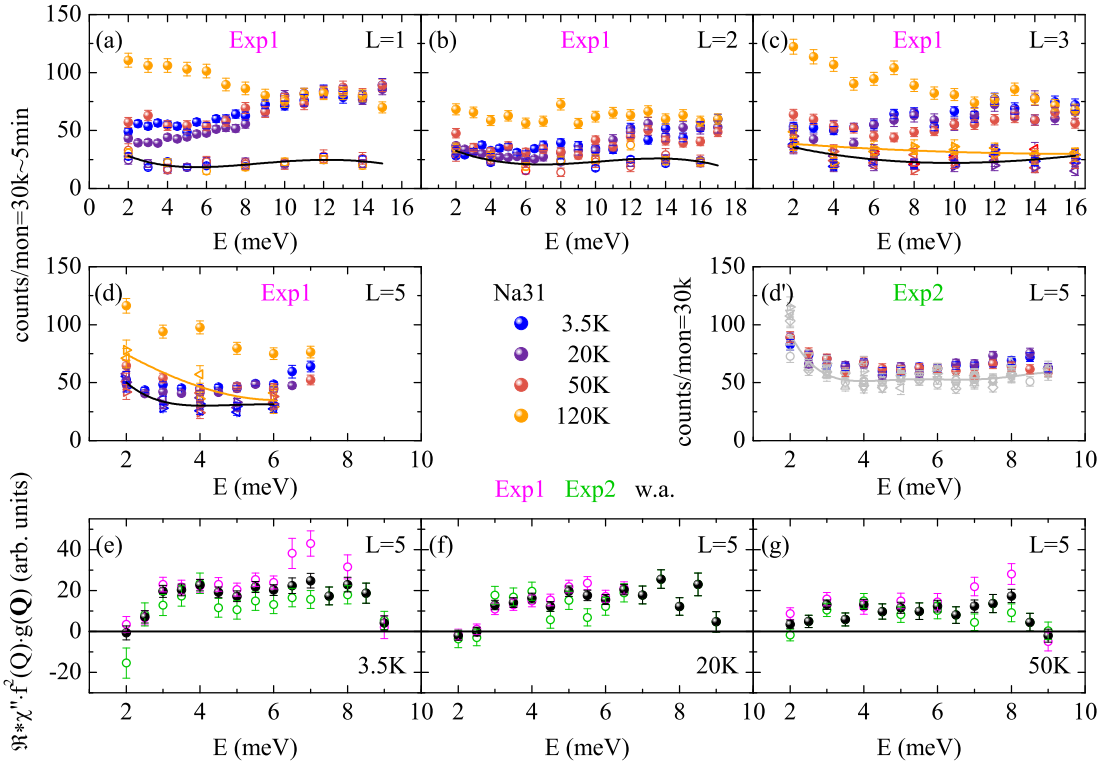

Figure A.3.2: Raw data of Na31 and their weighted average. **(a)-(d)** *E*-scan at L = 1, 2, 3 and 5 at various temperatures whereas the open symbols indicate the background for Exp1. **(d')** same as in (d') but in Exp2. **(e)-(g)** Corrected and renormalised spectra for L = 5 at 3.5 K, 20 K and 50 K, respectively.

ground for L = 1 in Fig.: A.3.1(a) are $(0.458, 0.458, 1.375)$ and $(0.542, 0.542, 0.180)$[13] for Exp1 while those for Exp2 are given in (a') at $(0.3, 0.3, 2.13)$. The same for L = 3 is given in Fig.: A.3.1(b) $(0.36, 0.36, 3.415)$ and $(0.64, 0.64, 2.339)$ for Exp1 and in (b') $(0.3, 0.3, 3.54)$ and $(0.7, 0.7, 1.92)$ for Exp2. Note that the data at L = 1 were not discussed in the main text and are displayed here for the sake of completeness.

The raw data and the background estimation for Na31 measured at 2T spectrometer are shown in Fig.: A.3.2(a)-(d'), respectively. To estimate the background scans sufficiently away from the signal were conducted, i.e. for L = 1 at $(0.3, 0.3, 2.12)$, for L = 2 at $(0.3, 0.3, 2.74)$, for L = 3 at $(0.3, 0.3, 3.54)$ and $(0.7, 0.7, 1.93)$ and for L = 5 at $(0.3, 0.3, 5.34)$ and $(0.7, 0.7, 4.44)$. For L = 5 the

[13] this estimation is based on a clockwise and counter-clockwise rotation away from the central position and is not a clever choice as some residual signal still may be contained.

data at 3.5 K, 20 K and 50 K were weighted averaged in order to increase statistics. The corrected data for Exp1 and Exp2 as well as their averaged are depicted in Fig.: A.3.2(e)(f)(g) respectively.

A.4 Magnetic Excitations in $Ba(Fe_{1-x}Co_x)_2As_2$

The L dispersion of SRM-1 and its intensity dependence in BaCo60 are attempted to elucidate by fitting the data from Fig.: 3.9(d) with two log-normal functions, one for SRM-1 and SRM-2 each, on top of a constant but L dependent background. Accordingly, the fits are shown in Fig.: A.4.1(a) and the region around SRM-1 is magnified in (a'). Note that this is rather an attempt than a thorough analysis, as the excitation spectra most likely contain more features than to be captured by two log-normal functions, and a detailed background estimation is missing. Moreover, the width for both modes are a global fit parameter, and for L = 0 and 2, the resonance energies are set to be identical, due to symmetry. In this context, the obtained and Fe^{2+} magnetic form factor corrected intensity dependence of SRM-1 and SRM-2 is given in Fig.: A.4.1(b). For SRM-1, the in-

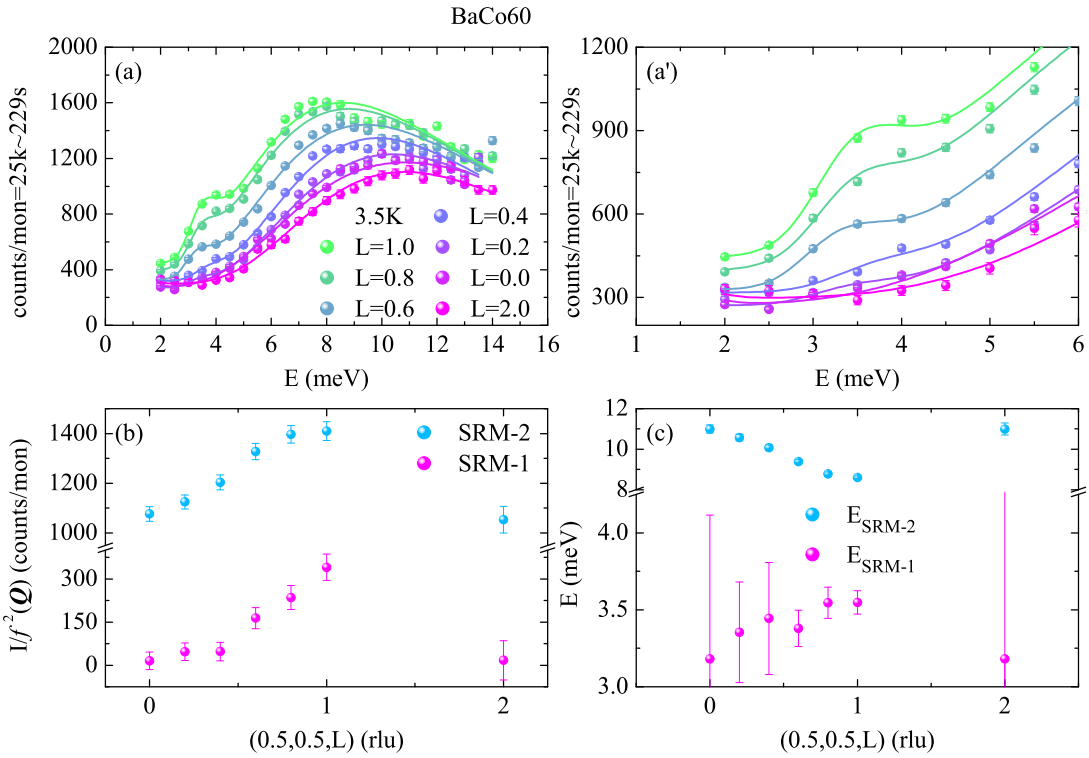

Figure A.4.1: Attempt to elucidate $E_{SRM-1}(L)$ in BaCo60. **(a)** Same data as in Fig.: 3.9(d), but fitted with two log-normal functions. **(a')** Magnified part from (a) around SRM-1. **(b)** L dependence of the obtained amplitudes from the fits in (a). **(c)** L dispersion of SRM-1, based on the fit results from (a).

tensity decreases away from the $\mathbf{\Gamma}$-point, similar to SRM-1 in $Ba_{1-x}Na_xFe_2As_2$. Additionally, SRM-2 seems also decreasing in intensity away from the $\mathbf{\Gamma}$-point, but only a thorough analysis of the SC-NS difference spectra, i.e. when the normal state contributions are removed, can tell whether there is a L dependence of the intensity.
Another aspect is the L dispersion. In $Ba_{1-x}Na_xFe_2As_2$ both SRMs dispersed upwards and showed identical bandwidths. While SRM-2 in BaCo60 is clearly in line with this observation, the situation for SRM-1 is different as there is dispersion resolvable.

The same analysis is attempted by modelling SRM-1 with a Gaußian and SRM-2 again with a log-normal, which, however, provided the same result.

A.5 Incommensurate to Commensurate Magnetic Excitations in $LiFe_{0.95}Co_{0.05}As$

Magnetic excitation in LiCo05 were investigated by transversal scan, i.e. along (h, 1-h), similar to the procedure Qureshi *et al.* performed for LiFeAs [186]. Thereby, excitations at 5 meV, 7.5 meV, 10 meV and 12.5 meV and in each case at 1.5 K, 12 K and 70 K were probed. The results are summarised in Fig.: A.5.1(a)-(d), where apparently commensurate excitations are observed on an intriguingly incommensurate mountain-like background of undeclared origin. However, a tentative attempt to analyse the observed spectra is given below.
Although the scan paths in reciprocal space are almost identical, rocking scans were performed, meaning scans where the absolute value of Q is not changed, c.f. Fig.: A.5.1(e), whereas the corresponding centre-positions are marked as coloured arrows in (a)-(d). As a rule of thumb, those scans provide a better signal and background estimation than a scan where the magnitude of $\boldsymbol{Q}$ is changed. In this context, the rocking scan over the peak centred at $\boldsymbol{Q}_c = (0.2, 0.8, 0)$ and $E = 5$ meV is only a flat line, which indicates it is background signal. Moreover, this mountain-like spectra was simulated with Reslib in Matlab, by assuming that the incommensurate magnetic excitations, as in the parent compound, were unaltered by doping. The spectra could not be reproduced, even if both samples are rotated against each other by as much as 10° (not shown). As a consequence, the additional peaks in Fig.: A.5.1(a)(d) at 12 K were fitted by Gaußians, indicated by the dashed lines, and treated as background. The temperature dependence of the background is captured by adjusting the constant off-set and keeping the remaining parameters fixed. In this context, the background for scans at 7.5 K and 10 meV in Fig.: A.5.1(b)(c) was inspired, although not the entire scan path was measured. Furthermore, the chosen approach to analyse the data, displays a flaw, next to its questionable assumptions, when the obtained peak width of the signal is plotted as a function of energy, c.f. (b). Typically, the width increases with increasing energy transfer, as the associated TAS $\boldsymbol{Q}$-resolution becomes broader, instead spin excitations at 12 meV are the sharpest.
Trying to analyse whether the *background* subtracted signal at 5 meV and 1.5 K, given Fig.: A.5.1(f), is already commensurate or still incommensurate, despite of the enhanced nesting conditions, a corresponding model was fit to it with the Reslib routine. Although, both models seem to describe the data equally well, the resulting incommensurability has an error of 0.1 rlu, which is almost as big as the incommensurability in LiFeAs itself [186, 267]. Consequently, the commensurate model seems better suited, however, since signal and experimental background cannot be separated unambiguously, this is not a clear statement. Furthermore, when the obtained integrated and normalised intensity is inserted in Fig.: 4.4(d) it would erroneously indicate a decrease of the spin fluctuation strength, in con-

tradiction to the $1/T_1T$ data from Dai *et al.* [60].

Unfortunately, since signal and background cannot be separated unambiguously, the corresponding analysis reaches a dead end.

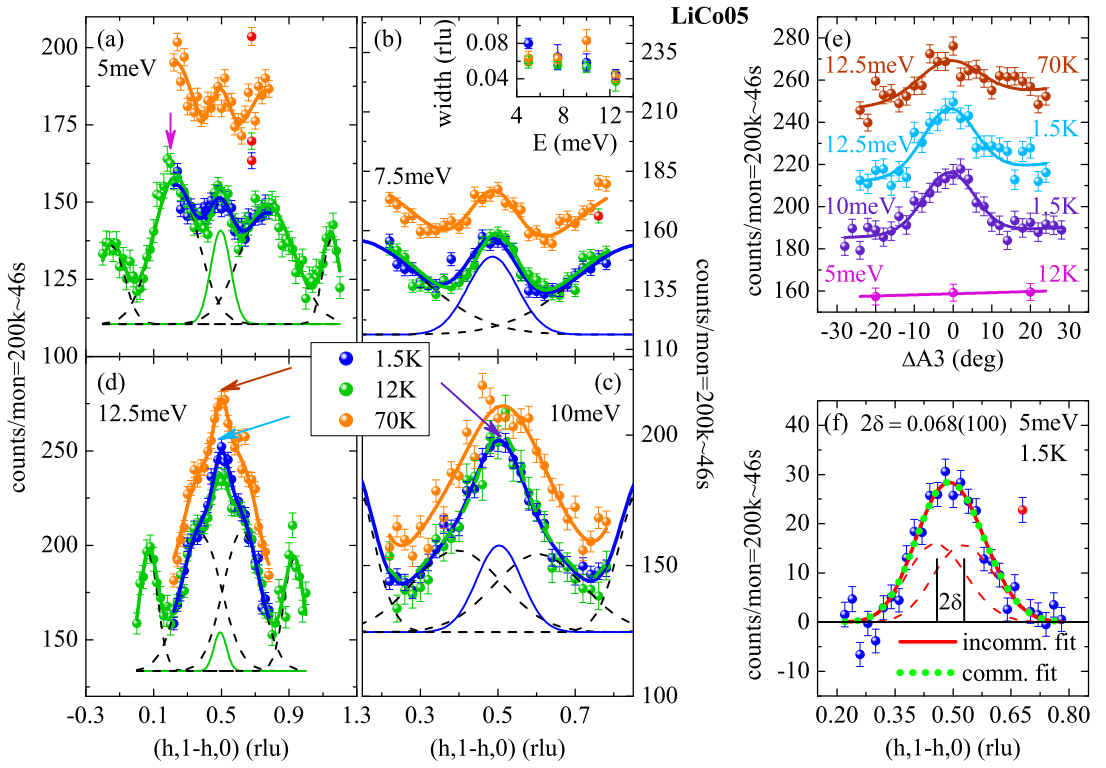

Figure A.5.1: Q-scans at various energies and temperatures of LiCo05. **(a)-(d)** Transversal $\boldsymbol{Q}$-scans at 1.5 K $< T_c$, 12 K $\gtrsim T_c$ and 70 K $\gg T_c$ with energy transfers of 5 meV, 7.5 meV, 10 meV and 12.5 meV, respectively. Each spectra is fitted by three to five Gaußians, whereas dotted lines denote the background level and solid lines the signal. The inset in (b) shows the extracted widths. **(c)** Rocking scans over the peak positions at 10 meV and 12.5 meV at 1.5 K and 70 K, and over an additional peak at 5 meV. This proves that the extracted signal is real in the former case and the additional peak is purely background in the latter case. Central positions in (e) are indicated by arrows in (a), (c) and (d) respectively. **(e)** Fit with the RESLIB routine in MATLAB by convolving the experimental resolution with either a commensurate or an incommensurate model after background subtraction.

A.6 List of Samples

Table A.6.1: Investigated samples in this thesis. Sample masses which are written in red do not exist any more. The given masses refer to those during the presented experiments.

sample ID	composition	mass (mg)	badge number
	$Ba_{1-x}Na_xFe_2As_2$		
Na25	$Ba_{0.75}Na_{0.25}Fe_2As_2$	66	SE2029
Na31	$Ba_{0.69}Na_{0.31}Fe_2As_2$	125	?? (IFW1104)
Na35a	$Ba_{0.65}Na_{0.35}Fe_2As_2$	90	SE1961-A
Na35b	$Ba_{0.65}Na_{0.35}Fe_2As_2$	294	SE2074
Na39	$Ba_{0.61}Na_{0.39}Fe_2As_2$	172	SE3402
Na40	$Ba_{0.60}Na_{0.40}Fe_2As_2$	42	SE1969
	$Ba(Fe_{1-x}Co_x)_2As_2$		
BaCo45	$Ba(Fe_{0.955}Co_{0.045})_2As_2$	756.8	#140904-1-A
		686.4	#140904-1-B
		679.1	#140904-1-C
BaCo60	$Ba(Fe_{0.94}Co_{0.06})_2As_2$	2880	#090601-A
	$LiFe_{1-x}Co_xAs$		
LiCo05	$LiFe_{0.95}Co_{0.05}As$	185	SE3785
		113	
LiCo18	$LiFe_{0.82}Co_{0.18}As$	373.8	SE4184
		205.2	
		103.3	
		101.3	
	$NdFeAsO_{1-x}F_x$		
NdF13	$NdFeAsO_{0.87}F_{0.13}$	$\sim$ 6000	SE3941
		$\sim$ 4000	SE4085

List of Figures

Fig. 1.1 Room temperature crystal structures of FeSC families. . . . 2
Fig. 1.2 Generic phase diagrams of FeSCs. 3
Fig. 1.3 Schematic sketch of the spin-nematic and magnetic transition. 5
Fig. 1.4 Pairing symmetry and spin resonance mode. 9

Fig. 2.1 Schematic phase diagram of $Ba_{1-x}Na_xFe_2As_2$. 14
Fig. 2.2 Temperature dependence of the nuclear and magnetic Bragg peaks in $Ba_{1-x}Na_xFe_2As_2$. 17
Fig. 2.3 Lattice constants of the $Ba_{1-x}Na_xFe_2As_2$ samples investigated in this thesis. 19
Fig. 2.4 Suppression of magnetic Bragg peak intensity in SC state. 21
Fig. 2.5 Polarisation analysis of the magnetic signal in Na25. 23
Fig. 2.6 Line-shape of the magnetic Bragg peaks in Na35a, Na39 and Na40. 25
Fig. 2.7 Orthorhombicity in Na35a. 26
Fig. 2.8 Excitation spectra for Na35b, Na39 and Na40 in their various phases and the corresponding RESLIB fits based on a phenomenological model. 32
Fig. 2.9 Excitation spectra of Na31. 33
Fig. 2.10 Excitation spectra of Na25 at $\boldsymbol{Q}$ = (0.5,0.5,3). 35
Fig. 2.11 $\boldsymbol{Q}$-scans along the (h,h) direction at various temperatures for Na25, Na31, Na35b, Na39 and Na40. 38
Fig. 2.12 Dispersion of resonance modes in Na35b, Na39 and Na40. . 40
Fig. 2.13 Polarisation of SRM-1 and SRM-2 in Na39. 41
Fig. 2.14 Temperature dependence of $Ba_{1-x}Na_xFe_2As_2$. 43
Fig. 2.15 Comparison of the resonance energies and intensities. . . . 48

Fig. 3.1 Transition temperatures of BaCo45 and schematic phase diagram of $Ba(Fe_{1-x}Co_x)_2As_2$. 64
Fig. 3.2 Spectra of magnetic excitations in the normal and superconducting state at various L values. 66
Fig. 3.3 Two anisotropic resonance modes below T_c. 69
Fig. 3.4 Polarisation analysis of the spin resonance modes in BaCo45 and BaCo60. 70

Fig. 3.5 Normal state response in BaCo45. 71
Fig. 3.6 Rocking scan over $(1, 1, 0)$ in BaCo60. 72
Fig. 3.7 Phonon and $\boldsymbol{Q}$-scans in BaCo60. 73
Fig. 3.8 Temperature dependence in BaCo60. 74
Fig. 3.9 Energy dependence in BaCo60. 75

Fig. 4.1 Fermi surface and SC gap energies of pure and 3 % Co-doped LiFeAs. 83
Fig. 4.2 Rocking scans in LiCo18. 86
Fig. 4.3 Energy dependence in $LiFe_{1-x}Co_xAs$ normalised on phonon intensity. 87
Fig. 4.4 Doping dependence in $LiFe_{1-x}Co_xAs$ of integrated magnetic signal normalised on phonon intensity. 88
Fig. 4.5 List of the properties of LiCo05 and LiCo18th next to a picture of the sample-can containing LiCo05. 91

Fig. 5.1 (Q,E)-maps at 10, 38 and 53 K of $NdFeAsO_{0.87}F_{0.13}$. 95
Fig. 5.2 Excitation scheme in $NdFeAsO_{0.87}F_{0.13}$. 97
Fig. 5.3 Constant Q- and E-cuts at various temperatures. 99

Fig. 6.1 Basic layout of a Triple-Axis Spectrometer. 105
Fig. 6.2 Frame of reference for polarisation analysis. 113
Fig. A.1.1 Temperature dependence of $(0.5, 0.5, 1)$ magnetic Bragg peak in Na35a and Na35b. 117
Fig. A.2.1 Raw data and estimated background for Na35b. 118
Fig. A.2.2 Raw data and estimated background for Na39. 119
Fig. A.2.3 Raw data and estimated background for Na40. 120
Fig. A.2.4 Phonon scans in Na35b, Na39 and Na40. 121
Fig. A.2.5 Reslib fits to magnetic Bragg peaks in Na39. 122
Fig. A.3.1 Raw data of Na25 and their weighted average. 123
Fig. A.3.2 Raw data of Na31 and their weighted average. 124
Fig. A.4.1 Attempt to elucidate $E_{SRM-1}(L)$ in BaCo60. 126
Fig. A.5.1 Q-scans at various energies and temperatures of LiCo05. . 129

List of Tables

Tab. 2.1 Transition temperatures of the $Ba_{1-x}Na_xFe_2As_2$ samples. . 17
Tab. 2.2 Calculated values of μ, $\int \chi''_{\text{SRM-1}}$ and $\int \Delta\chi''$. 46
Tab. 2.3 Summary of the doping levels, sample masses, transition temperatures and gain of spectral weight in the superconducting state of the investigated $Ba_{1-x}Na_xFe_2As_2$ samples. 54
Tab. 2.4 Instruments settings of the employed spectrometers/ diffractometer. 56
Tab. 2.5 Binning intervals for the temperature dependence of magnetic and nuclear Bragg peak intensity. 57
Tab. 2.6 RESLIB parameters for absolute unit calculation in Sec. 2.2 60

Tab. 3.1 AFM gaps of BaCo45 and $BaFe_2As_2$. 68
Tab. 3.2 Comparison of magnetic excitations in BaCo45 and BaCo60. 78

Tab. 5.1 Comparison of the excitation levels in $NdFeAsO_{1-x}F_x$. . . . 98
Tab. 5.2 Properties of the F-doped NdFeAsO samples. 101

Tab. 6.1 Used neutron scattering instruments and their corresponding configurations. 107
Tab. 6.2 Contributions in the various SF and NSF channels. 113
Tab. A.2.1 Scaling factors obtained from phonon scattering 121
Tab. A.6.1 Investigated samples in this thesis. 130

Bibliography

[1] J. G. Bednorz and K. A. Müller, Zeitschrift für Physik B Condensed Matter, **64**, 189 (1986).

[2] N. P. Armitage, P. Fournier and R. L. Greene, Rev. Mod. Phys., **82**, 2421 (2010).

[3] M. Eschrig, Advances in Physics, **55**, 47 (2006).

[4] M. Le Tacon, G. Ghiringhelli, J. Chaloupka, M. M. Sala, V. Hinkov, M. W. Haverkort, M. Minola, M. Bakr, K. J. Zhou, S. Blanco-Canosa, C. Monney, Y. T. Song, G. L. Sun, C. T. Lin, G. M. De Luca, M. Salluzzo, G. Khaliullin, T. Schmitt, L. Braicovich and B. Keimer, Nat. Phys., **7**, 725 (2011).

[5] N. D. Mathur, F. M. Grosche, S. R. Julian, I. R. Walker, D. M. Freye, R. K. W. Haselwimmer and G. G. Lonzarich, Nature, **394**, 39 (1998).

[6] P. Monthoux, A. V. Balatsky and D. Pines, Phys. Rev. Lett., **67**, 3448 (1991).

[7] T. Dahm, V. Hinkov, S. V. Borisenko, A. A. Kordyuk, V. B. Zabolotnyy, J. Fink, B. Büchner, D. J. Scalapino, W. Hanke and B. Keimer, Nat. Phys., **5**, 217 (2009).

[8] P. Thalmeier and A. Akbari, Quantum Criticality in Condensed Matter - World scientific, 44 (2015).

[9] L. Taillefer, Annu. Rev. Condens. Matter Phys., **1**, 51 (2010).

[10] N. Doiron-Leyraud, P. Auban-Senzier, S. René de Cotret, C. Bourbonnais, D. Jérome, K. Bechgaard and L. Taillefer, Phys. Rev. B, **80**, 214531 (2009).

[11] A. Ardavan, S. Brown, S. Kagoshima, K. Kanoda, K. Kuroki, H. Mori, M. Ogata, S. Uji and J. Wosnitza, J. Phys. Soc. Jpn., **81**, 1, 011004 (2011).

[12] L. Boeri, O. Dolgov and A. A. Golubov, Phys. Rev. Lett., **101**, 026403 (2008).

[13] Y. Kamihara, H. Hiramatsu, M. Hirano, R. Kawamura, H. Yanagi, T. Kamiya and H. Hosono, J. Am. Chem. Soc., **128**, 10012 (2006).

[14] Y. Kamihara, T. Watanabe, M. Hirano and H. Hosono, J. Am. Chem. Soc., **130**, 3296 (2008).

[15] R. Zhi-An, L. Wei, Y. Jie, Y. Wei, S. Xiao-Li, Zheng-Cai, C. Guang-Can, D. Xiao-Li, S. Li-Ling, Z. Fang and Z. Zhong-Xian, Chin. Phys. Lett., **25**, 2215 (2008).

[16] Z.-A. Ren, G.-C. Che, X.-L. Dong, J. Yang, W. Lu, W. Yi, X.-L. Shen, Z.-C. Li, L.-L. Sun, F. Zhou and Z.-X. Zhao, EPL (Europhysics Letters), **83**, 17002 (2008).

[17] C. Wang, L. Li, S. Chi, Z. Zhu, Z. Ren, Y. Li, Y. Wang, X. Lin, Y. Luo, S. Jiang, X. Xu, G. Cao and Z. Xu, EPL (Europhysics Letters), **83**, 67006 (2008).

[18] P. Cheng, L. Fang, H. Yang, X. Zhu, G. Mu, H. Luo, Z. Wang and H. Wen, Science in China Series G: Physics, Mechanics and Astronomy, **51**, 719 (2008).

[19] M. Rotter, M. Tegel and D. Johrendt, Phys. Rev. Lett., **101**, 107006 (2008).

[20] S. Avci, O. Chmaissem, E. A. Goremychkin, S. Rosenkranz, J.-P. Castellan, D. Y. Chung, I. S. Todorov, J. A. Schlueter, H. Claus, M. G. Kanatzidis, A. Daoud-Aladine, D. Khalyavin and R. Osborn, Phys. Rev. B, **83**, 172503 (2011).

[21] A. S. Sefat, R. Jin, M. A. McGuire, B. C. Sales, D. J. Singh and D. Mandrus, Phys. Rev. Lett., **101**, 117004 (2008).

[22] C. Lester, J.-H. Chu, J. G. Analytis, S. C. Capelli, A. S. Erickson, C. L. Condron, M. F. Toney, I. R. Fisher and S. M. Hayden, Phys. Rev. B, **79**, 144523 (2009).

[23] P. C. Canfield, S. L. Bud'ko, N. Ni, J. Q. Yan and A. Kracher, Phys. Rev. B, **80**, 060501 (2009).

[24] J. H. Tapp, Z. Tang, B. Lv, K. Sasmal, B. Lorenz, P. C. W. Chu and A. M. Guloy, Phys. Rev. B, **78**, 060505 (2008).

[25] M. J. Pitcher, D. R. Parker, P. Adamson, S. J. C. Herkelrath, A. T. Boothroyd, R. M. Ibberson, M. Brunelli and S. J. Clarke, Chem. Commun., **45**, 5918 (2008).

[26] S. Li, C. de la Cruz, Q. Huang, G. F. Chen, T.-L. Xia, J. L. Luo, N. L. Wang and P. Dai, Phys. Rev. B, **80**, 020504 (2009).

[27] D. R. Parker, M. J. P. Smith, T. Lancaster, A. J. Steele, I. Franke, P. J. Baker, F. L. Pratt, M. J. Pitcher, S. J. Blundell and S. J. Clarke, Phys. Rev. Lett., **104**, 057007 (2010).

[28] F.-C. Hsu, J.-Y. Luo, K.-W. Yeh, T.-K. Chen, T.-W. Huang, P. M. Wu, Y.-C. Lee, Y.-L. Huang, Y.-Y. Chu, D.-C. Yan and M.-K. Wu, Proceedings of the National Academy of Sciences, **105**, 14262 (2008).

[29] E. Pomjakushina, K. Conder, V. Pomjakushin, M. Bendele and R. Khasanov, Phys. Rev. B, **80**, 024517 (2009).

[30] S. Avci, O. Chmaissem, D. Y. Chung, S. Rosenkranz, E. A. Goremychkin, J.-P. Castellan, I. S. Todorov, J. A. Schlueter, H. Claus, A. Daoud-Aladine, D. D. Khalyavin, M. G. Kanatzidis and R. Osborn, Phys. Rev. B, **85**, 184507 (2012).

[31] S. Nandi, M. G. Kim, A. Kreyssig, R. M. Fernandes, D. K. Pratt, A. Thaler, N. Ni, S. L. Bud'ko, P. C. Canfield, J. Schmalian, R. J. McQueeney and A. I. Goldman, Phys. Rev. Lett., **104**, 057006 (2010).

[32] S. Aswartham, M. Abdel-Hafiez, D. Bombor, M. Kumar, A. U. B. Wolter, C. Hess, D. V. Evtushinsky, V. B. Zabolotnyy, A. A. Kordyuk, T. K. Kim, S. V. Borisenko, G. Behr, B. Büchner and S. Wurmehl, Phys. Rev. B, **85**, 224520 (2012).

[33] S. Jiang, H. Xing, G. Xuan, C. Wang, Z. Ren, C. Feng, J. Dai, Z. Xu and G. Cao, Journal of Physics: Condensed Matter, **21**, 382203 (2009).

[34] S. Kasahara, T. Shibauchi, K. Hashimoto, K. Ikada, S. Tonegawa, R. Okazaki, H. Shishido, H. Ikeda, H. Takeya, K. Hirata, T. Terashima and Y. Matsuda, Phys. Rev. B, **81**, 184519 (2010).

[35] F. Rullier-Albenque, D. Colson, A. Forget, P. Thuéry and S. Poissonnet, Phys. Rev. B, **81**, 224503 (2010).

[36] E. Colombier, M. S. Torikachvili, N. Ni, A. Thaler, S. L. Bud'ko and P. C. Canfield, Supercond. Sci. Technol., **23**, 054003 (2010).

[37] S. K. Kim, M. S. Torikachvili, E. Colombier, A. Thaler, S. L. Bud'ko and P. C. Canfield, Phys. Rev. B, **84**, 134525 (2011).

[38] K. Kothapalli, A. E. Bohmer, W. T. Jayasekara, B. G. Ueland, P. Das, A. Sapkota, V. Taufour, Y. Xiao, E. Alp, S. L. Bud/'ko, P. C. Canfield, A. Kreyssig and A. I. Goldman, Nat. Commun., **7**, (2016).

[39] Y. Laplace, J. Bobroff, F. Rullier-Albenque, D. Colson and A. Forget, Phys. Rev. B, **80**, 140501 (2009).

[40] D. K. Pratt, W. Tian, A. Kreyssig, J. L. Zarestky, S. Nandi, N. Ni, S. L. Bud'ko, P. C. Canfield, A. I. Goldman and R. J. McQueeney, Phys. Rev. Lett., **103**, 087001 (2009).

[41] P. Marsik, K. W. Kim, A. Dubroka, M. Rössle, V. K. Malik, L. Schulz, C. N. Wang, C. Niedermayer, A. J. Drew, M. Willis, T. Wolf and C. Bernhard, Phys. Rev. Lett., **105**, 057001 (2010).

[42] P. Cai, X. Zhou, W. Ruan, A. Wang, X. Chen, D.-H. Lee and Y. Wang, Nat. Commun., **4**, 1596 (2013).

[43] S. Oh, A. M. Mounce, J. A. Lee, W. P. Halperin, C. L. Zhang, S. Carr, P. Dai, A. P. Reyes and P. L. Kuhns, Phys. Rev. B, **88**, 134518 (2013).

[44] M. G. Kim, R. M. Fernandes, A. Kreyssig, J. W. Kim, A. Thaler, S. L. Bud'ko, P. C. Canfield, R. J. McQueeney, J. Schmalian and A. I. Goldman, Phys. Rev. B, **83**, 134522 (2011).

[45] S. Avci, O. Chmaissem, J. Allred, S. Rosenkranz, I. Eremin, A. Chubukov, D. Bugaris, D. Chung, M. Kanatzidis, J.-P. Castellan, J. Schlueter, H. Claus, D. Khalyavin, P. Manuel, A. Daoud-Aladine and R. Osborn, Nat. Commun., **5**, 3845 (2014).

[46] A. E. Böhmer, F. Hardy, L. Wang, T. Wolf, P. Schweiss and C. Meingast, Nat. Commun., **6**, 7911 (2015).

[47] L. Wang, F. Hardy, A. E. Böhmer, T. Wolf, P. Schweiss and C. Meingast, Phys. Rev. B, **93**, 014514 (2016).

[48] M. Yi, D. H. Lu, J. G. Analytis, J.-H. Chu, S.-K. Mo, R.-H. He, M. Hashimoto, R. G. Moore, I. I. Mazin, D. J. Singh, Z. Hussain, I. R. Fisher and Z.-X. Shen, Phys. Rev. B, **80**, 174510 (2009).

[49] M. Yi, D. Lu, J.-H. Chu, J. G. Analytis, A. P. Sorini, A. F. Kemper, B. Moritz, S.-K. Mo, R. G. Moore, M. Hashimoto, W.-S. Lee, Z. Hussain, T. P. Devereaux, I. R. Fisher and Z.-X. Shena, Proceedings of the National Academy of Sciences, **108**, 6878 (2011).

[50] M. Yi, Y. Zhang, Z.-X. Shen and D. Lu, npj Quantum Materials, **2**, 57 (2017).

[51] C.-H. Lee, A. Iyo, H. Eisaki, H. Kito, M. T. Fernandez-Diaz, T. Ito, K. Kihou, H. Matsuhata, M. Braden and K. Yamada, J. Phys. Soc. Jpn., **77**, 083704 (2008).

[52] C. Lee, K. Kihou, A. Iyo, H. Kito, P. Shirage and H. Eisaki, Solid State Communications, **152**, 644 (2012).

[53] A. V. Chubukov, M. Khodas and R. M. Fernandes, Phys. Rev. X, **6**, 041045 (2016).

[54] P. J. Hirschfeld, C. R. Phys., **17**, 197 (2016).

[55] V. Mishra, D. J. Scalapino and T. A. Maier, Scientific Reports, **6**, 32078 (2016).

[56] I. I. Mazin, D. J. Singh, M. D. Johannes and M. H. Du, Phys. Rev. Lett., **101**, 057003 (2008).

[57] M. M. Korshunov and I. Eremin, Phys. Rev. B, **78**, 140509 (2008).

[58] M. M. Korshunov, V. A. Shestakov and Y. N. Togushova, Phys. Rev. B, **94**, 094517 (2016).

[59] T. A. Maier, S. Graser, D. J. Scalapino and P. Hirschfeld, Phys. Rev. B, **79**, 134520 (2009).

[60] Y. M. Dai, H. Miao, L. Y. Xing, X. C. Wang, P. S. Wang, H. Xiao, T. Qian, P. Richard, X. G. Qiu, W. Yu, C. Q. Jin, Z. Wang, P. D. Johnson, C. C. Homes and H. Ding, Phys. Rev. X, **5**, 031035 (2015).

[61] C. Zhang, H.-F. Li, Y. Song, Y. Su, G. Tan, T. Netherton, C. Redding, S. V. Carr, O. Sobolev, A. Schneidewind, E. Faulhaber, L. W. Harriger, S. Li, X. Lu, D.-X. Yao, T. Das, A. V. Balatsky, T. Brückel, J. W. Lynn and P. Dai, Phys. Rev. B, **88**, 064504 (2013).

[62] Y. Mizukami, M. Konczykowski, Y. Kawamoto, S. Kurata, S. Kasahara, K. Hashimoto, V. Mishra, A. Kreisel, Y. Wang, P. J. Hirschfeld, Y. Matsuda and T. Shibauchi, Nat. Commun., **5**, (2014).

[63] K. Cho, M. Kończykowski, J. Murphy, H. Kim, M. A. Tanatar, W. E. Straszheim, B. Shen, H. H. Wen and R. Prozorov, Phys. Rev. B, **90**, 104514 (2014).

[64] R. Prozorov, M. Kończykowski, M. A. Tanatar, A. Thaler, S. L. Bud'ko, P. C. Canfield, V. Mishra and P. J. Hirschfeld, Phys. Rev. X, **4**, 041032 (2014).

[65] T. Saito, Y. Yamakawa, S. Onari and H. Kontani, Phys. Rev. B, **92**, 134522 (2015).

[66] S. Onari, H. Kontani and M. Sato, Phys. Rev. B, **81** (2010).

[67] H. Kontani, T. Saito and S. Onari, Phys. Rev. B, **84**, 024528 (2011).

[68] R. Tazai, Y. Yamakawa, M. Tsuchiizu and H. Kontani, Phys. Rev. B, **94**, 115155 (2016).

[69] H. Nakaoka, Y. Yamakawa and H. Kontani, arXiv: cond-mat, 1805.10578 (2018).

[70] L. Takeuchi, Y. Yamakawa and H. Kontani, arXiv: cond-mat (2018).

[71] M. D. Lumsden and A. D. Christianson, Journal of Physics: Condensed Matter, **22**, 203203 (2010).

[72] Q. Huang, Y. Qiu, W. Bao, M. A. Green, J. Lynn, Y. C. Gasparovic, T. Wu, G. Wu and X. H. Chen, Phys. Rev. Lett., **101**, 257003 (2008).

[73] N. Qureshi, Y. Drees, J. Werner, S. Wurmehl, C. Hess, R. Klingeler, B. Büchner, M. T. Fernández-Díaz and M. Braden, Phys. Rev. B, **82**, 184521 (2010).

[74] Y. Hu, X. Ren, R. Zhang, H. Luo, S. Kasahara, T. Watashige, T. Shibauchi, P. Dai, Y. Zhang, Y. Matsuda and Y. Li, Phys. Rev. B, **93**, 060504 (2016).

[75] S. Avci, J. M. Allred, O. Chmaissem, D. Y. Chung, S. Rosenkranz, J. A. Schlueter, H. Claus, A. Daoud-Aladine, D. D. Khalyavin, P. Manuel, A. Llobet, M. R. Suchomel, Kanatzidis and R. Osborn, Phys. Rev. B, **88**, 094510 (2013).

[76] T. Shimojima, K. Ishizaka, Y. Ishida, N. Katayama, K. Ohgushi, T. Kiss, M. Okawa, T. Togashi, X.-Y. Wang, C.-T. Chen, S. Watanabe, R. Kadota, T. Oguchi, A. Chainani and S. Shin, Phys. Rev. Lett., **104**, 057002 (2010).

[77] C. Liu, T. Kondo, R. M. Fernandes, A. D. Palczewski, E. D. Mun, N. Ni, A. N. Thaler, A. Bostwick, E. Rotenberg, J. Schmalian, S. L. Bud/'ko, P. C. Canfield and A. Kaminski, Nat. Phys., **6**, 419 (2010).

[78] N. Qureshi, P. Steffens, S. Wurmehl, S. Aswartham, B. Büchner and M. Braden, Phys. Rev. B, **86**, 060410 (2012).

[79] C. Wang, R. Zhang, F. Wang, H. Luo, L. P. Regnault, P. Dai and Y. Li, Phys. Rev. X, **3**, 041036 (2013).

[80] Y. Song, L.-P. Regnault, C. Zhang, G. Tan, S. V. Carr, S. Chi, A. D. Christianson, T. Xiang and P. Dai, Phys. Rev. B, **88**, 134512 (2013).

[81] D. D. Scherer and B. M. Andersen, Phys. Rev. Lett., **121**, 037205 (2018).

[82] F. Waßer, A. Schneidewind, Y. Sidis, S. Wurmehl, S. Aswartham, B. Büchner and M. Braden, Phys. Rev. B, **91**, 060505 (2015).

[83] K. M. Taddei, J. M. Allred, D. E. Bugaris, S. Lapidus, M. J. Krogstad, R. Stadel, H. Claus, D. Y. Chung, M. G. Kanatzidis, S. Rosenkranz, R. Osborn and O. Chmaissem, Phys. Rev. B, **93**, 134510 (2016).

[84] J. M. Allred, S. Avci, D. Y. Chung, H. Claus, D. D. Khalyavin, P. Manuel, K. M. Taddei, M. G. Kanatzidis, S. Rosenkranz, R. Osborn and O. Chmaissem, Phys. Rev. B, **92**, 094515 (2015).

[85] J. Nayak, K. Filsinger, G. H. Fecher, S. Chadov, J. Minár, E. D. L. Rienks, B. Büchner, S. P. Parkin, J. Fink and C. Felser, Proceedings of the National Academy of Sciences, **114**, 12425 (2017).

[86] K. Marty, A. D. Christianson, C. H. Wang, M. Matsuda, H. Cao, L. H. VanBebber, J. L. Zarestky, D. J. Singh, A. S. Sefat and M. D. Lumsden, Phys. Rev. B, **83**, 060509 (2011).

[87] Y. Singh, M. A. Green, Q. Huang, A. Kreyssig, R. J. McQueeney, D. C. Johnston and A. I. Goldman, Phys. Rev. B, **80**, 100403 (2009).

[88] D. S. Inosov, G. Friemel, J. T. Park, A. C. Walters, Y. Texier, Y. Laplace, J. Bobroff, V. Hinkov, D. L. Sun, Y. Liu, R. Khasanov, K. Sedlak, P. Bourges, Y. Sidis, A. Ivanov, C. T. Lin, T. Keller and B. Keimer, Phys. Rev. B, **87**, 224425 (2013).

[89] Y. Texier, Y. Laplace, P. Mendels, J. T. Park, G. Friemel, D. L. Sun, D. S. Inosov, C. T. Lin and J. Bobroff, EPL (Europhysics Letters), **99**, 17002 (2012).

[90] C. Fang, H. Yao, W.-F. Tsai, J. Hu and S. A. Kivelson, Phys. Rev. B, **77**, 224509 (2008).

[91] R. M. Fernandes, A. V. Chubukov and J. Schmalian, Nat. Phys., **10**, 97 (2014).

[92] J.-H. Chu, J. G. Analytis, K. D. Greve, P. L. McMahon, Z. Islam, Y. Yamamoto and I. R. Fisher, Science, **329**, 824 (2010).

[93] E. C. Blomberg, M. A. Tanatar, R. M. Fernandes, I. I. Mazin, B. Shen, H.-H. Wen, M. D. Johannes, J. Schmalian and R. Prozorov, Nat. Commun., **4**, 1914 (2013).

[94] Q. Deng, J. Liu, J. Xing, H. Yang and H.-H. Wen, Phys. Rev. B, **91**, 020508 (2015).

[95] J.-H. Chu, H.-H. Kuo, J. G. Analytis and I. R. Fisher, Science, **337**, 710 (2012).

[96] S. Kasahara, H. J. Shi, K. Hashimoto, S. Tonegawa, Y. Mizukami, T. Shibauchi, K. Sugimoto, T. Fukuda, T. Terashima, A. H. Nevidomskyy and Y. Matsuda, Nature, **486**, 382 (2012).

[97] H. Luo, M. Wang, C. Zhang, X. Lu, L.-P. Regnault, R. Zhang, S. Li, J. Hu and P. Dai, Phys. Rev. Lett., **111**, 107006 (2013).

[98] S. Ishida, M. Nakajima, T. Liang, K. Kihou, C. H. Lee, A. Iyo, H. Eisaki, T. Kakeshita, Y. Tomioka, T. Ito and S. Uchida, Phys. Rev. Lett., **110**, 207001 (2013).

[99] R. M. Fernandes and J. Schmalian, Supercond. Sci. Technol., **25**, 084005 (2012).

[100] A. Jesche, C. Krellner, M. de Souza, M. Lang and C. Geibel, Phys. Rev. B, **81**, 134525 (2010).

[101] M. P. Allan, T.-M. Chuang, F. Massee, Y. Xie, N. Ni, S. L. Bud'ko, G. S. Boebinger, Q.Wang, D. S. Dessau, P. C. Canfield, M. S. Golden and J. C. Davis, Nat. Phys., **9**, 220 (2013).

[102] L. Wang, M. He, F. Hardy, P. Adelmann, T. Wolf, M. Merz, P. Schweiss and C. Meingast, Phys. Rev. B, **97**, 224518 (2018).

[103] S.-H. Baek, D. V. Efremov, J. M. Ok, J. S. Kim, J. van den Brink and B. Büchner, Nat. Mater., **14**, 210 (2015).

[104] M. C. Rahn, R. A. Ewings, S. J. Sedlmaier, S. J. Clarke and A. T. Boothroyd, Phys. Rev. B, **91**, 180501 (2015).

[105] F. Wang, S. A. Kivelson and D.-H. Lee, Nat. Phys., **11**, 959 (2015).

[106] T. Hashimoto, Y. Ota, H. Q. Yamamoto, Y. Suzuki, T. Shimojima, S. Watanabe, C. Chen, S. Kasahara, Y. Matsuda, T. Shibauchi, K. Okazaki and S. Shin, Nat. Commun., **9**, 282 (2018).

[107] Q. Wang, Y. Shen, B. Pan, X. Zhang, K. Ikeuchi, K. Iida, A. D. Christianson, H. C. Walker, D. T. Adroja, M. Abdel-Hafiez, X. Chen, D. A. Chareev, A. N. Vasiliev and J. Zhao, Nat. Commun., **7**, (2016).

[108] P. S. Wang, S. S. Sun, Y. Cui, W. H. Song, T. R. Li, R. Yu, H. Lei and W. Yu, Phys. Rev. Lett., **117**, 237001 (2016).

[109] Y. Sato, S. Kasahara, H. Murayama, Y. Kasahara, E.-G. Moon, T. Nishizaki, T. Loew, J. Porras, B. Keimer, T. Shibauchi and Y. Matsuda, Nat. Phys., **13**, 1074 (2017).

[110] H. Ikeda, M.-T. Suzuki, R. Arita, T. Takimoto, T. Shibauchi and Y. Matsuda, Nature Physics, **8**, 528 (2012).

[111] E. Fradkin, S. A. Kivelson, M. J. Lawler, J. P. Eisenstein and A. P. Mackenzie, Annu. Rev. Condens. Matter Phys., **1**, 153 (2010).

[112] S. Yonezawa, K. Tajiri, S. Nakata, Y. Nagai, Z. Wang, K. Segawa, Y. Ando and Y. Maeno, Nat. Phys., **13**, 123 (2016).

[113] J. Bardeen, L. N. Cooper and J. R. Schrieffer, Phys. Rev., **108**, 1175 (1957).

[114] A. P. Drozdov, M. I. Eremets, I. A. Troyan, V. Ksenofontov and S. I. Shylin, Nature, **525**, 73 (2015).

[115] F. Steglich, O. Stockert, S. Wirth, C. Geibel, H. Q. Yuan, S. Kirchner and Q. Si, Journal of Physics: Conference Series, **449**, 012028 (2013).

[116] P. J. Hirschfeld, M. M. Korshunov and I. I. Mazin, Rep. Prog. Phys., **74**, 124508 (2011).

[117] P. Monthoux, D. Pines and G. G. Lonzarich, Nature, **450**, 1177 (2007).

[118] D. J. Scalapino, Rev. Mod. Phys., **84**, 1383 (2012).

[119] H. Woo, P. Dai, S. M. Hayden, H. A. Mook, T. Dahm, D. J. Scalapino, T. Perring and F. Doğan, Nat. Phys., **2**, 600 (2006).

[120] O. Stockert, J. Arndt, E. Faulhaber, C. Geibel, H. S. Jeevan, S. Kirchner, M. Loewenhaupt, K. Schmalzl, W. Schmidt, Q. Si and F. Steglich, Nat. Phys., **7**, 119 (2011).

[121] D. J. Scalapino, E. Loh and J. E. Hirsch, Phys. Rev. B, **34**, 8190 (1986).

[122] K.-J. Zhou, Y.-B. Huang, C. Monney, X. Dai, V. N. Strocov, N.-L. Wang, Z.-G. Chen, C. Zhang, P. Dai, L. Patthey, J. van den Brink, H. Ding and T. Schmitt, Nat. Commun., **4**, 1470 (2013).

[123] M. Liu, L. W. Harriger, H. Luo, M. Wang, R. A. Ewings, T. Guidi, H. Park, K. Haule, G. Kotliar, S. M. Hayden and P. Dai, Nat. Phys., **8**, 376 (2012).

[124] M. Wang, C. Zhang, X. Lu, G. Tan, H. Luo, Y. Song, M. Wang, X. Zhang, E. Goremychkin, T. Perring, T. Maier, Z. Yin, K. Haule, G. Kotliar and P. Dai, Nat. Commun., **4**, 2874 (2013).

[125] F. Steglich, J. Arndt, S. Friedemann, C. Krellner, Y. Tokiwa, T. Westerkamp, M. Brando, P. Gegenwart, C. Geibel, S. Wirth and O. Stockert, Journal of Physics: Condensed Matter, **22**, 164202 (2010).

[126] H. Ding, M. R. Norman, J. C. Campuzano, M. Randeria, A. F. Bellman, T. Yokoya, T. Takahashi, T. Mochiku and K. Kadowaki, Phys. Rev. B, **54**, R9678 (1996).

[127] C. C. Tsuei and J. R. Kirtley, Rev. Mod. Phys., **72**, 969 (2000).

[128] A. A. Kalenyuk, A. Pagliero, E. A. Borodianskyi, A. A. Kordyuk and V. M. Krasnov, Phys. Rev. Lett., **120**, 067001 (2018).

[129] C. Pfleiderer, Rev. Mod. Phys., **81**, 1551 (2009).

[130] J. Rossat-Mignod, L. Regnault, C. Vettier, P. Bourges, P. Burlet, J. Bossy, J. Henry and G. Lapertot, Physica C: Superconductivity, **185-189**, 86 (1991).

[131] D. S. Inosov, J. T. Park, P. Bourges, D. L. Sun, Y. Sidis, A. Schneidewind, K. Hradil, D. Haug, C. T. Lin, B. Keimer and V. Hinkov, Nat. Phys., **6**, 178 (2009).

[132] C. Stock, C. Broholm, J. Hudis, H. J. Kang and C. Petrovic, Phys. Rev. Lett., **100**, 087001 (2008).

[133] H. F. Fong, P. Bourges, Y. Sidis, L. P. Regnault, J. Bossy, A. Ivanov, D. L. Milius, I. A. Aksay and B. Keimer, Phys. Rev. B, **61**, 14773 (2000).

[134] A. D. Christianson, E. A. Goremychkin, R. Osborn, S. Rosenkranz, M. D. Lumsden, C. D. Malliakas, I. S. Todorov, H. Claus, D. Y. Chung, M. G. Kanatzidis, R. I. Bewley and T. Guidi, Nature, **456**, 930 (2008).

[135] H. A. Mook, M. Yethiraj, G. Aeppli, T. E. Mason and T. Armstrong, Phys. Rev. Lett., **70**, 3490 (1993).

[136] A. Damascelli, Z. Hussain and Z.-X. Shen, Rev. Mod. Phys., **75**, 473 (2003).

[137] M. R. Norman, Science, **332**, 196 (2011).

[138] T. Hanaguri, S. Niitaka, K. Kuroki and H. Takagi, Science, **328**, 474 (2010).

[139] C.-T. Chen, C. C. Tsuei, M. B. Ketchen, Z.-A. Ren and Z. X. Zhao, Nat. Phys., **6**, 260 (2010).

[140] S. Chi, S. Johnston, G. Levy, S. Grothe, R. Szedlak, B. Ludbrook, R. Liang, P. Dosanjh, S. A. Burke, A. Damascelli, D. A. Bonn, W. N. Hardy and Y. Pennec, Phys. Rev. B, **89**, 104522 (2014).

[141] H. Ding, P. Richard, K. Nakayama, K. Sugawara, T. Arakane, Y. Sekiba, A. Takayama, S. Souma, T. Sato, T. Takahashi, Z. Wang, X. Dai, Z. Fang, G. F. Chen, J. L. Luo and N. L. Wang, EPL (Europhysics Letters), **83**, 47001 (2008).

[142] P. Richard, T. Qian and H. Ding, Journal of Physics: Condensed Matter, **27**, 293203 (2015).

[143] Q. Q. Ge, Z. R. Ye, M. Xu, Y. Zhang, J. Jiang, B. P. Xie, Y. Song, C. L. Zhang, P. Dai and D. L. Feng, Phys. Rev. X, **3**, 011020 (2013).

[144] V. B. Zabolotnyy, D. S. Inosov, D. V. Evtushinsky, A. Koitzsch, A. A. Kordyuk, G. L. Sun, J. T. Park, D. Haug, V. Hinkov, A. V. Boris, C. T. Lin, M. Knupfer, A. N. Yaresko, B. Buchner, A. Varykhalov, R. Follath and S. V. Borisenko, Nature, **457**, 569 (2009).

[145] K. Terashima, Y. Sekiba, J. H. Bowen, K. Nakayama, T. Kawahara, T. Sato, P. Richard, Y.-M. Xu, L. J. Li, G. H. Cao, Z.-A. Xu, H. Ding and T. Takahashi, Proceedings of the National Academy of Sciences, **106**, 7330 (2009).

[146] Y.-Z. You and Z.-Y. Weng, *Coexisting Itinerant and Localized Electrons*, 377–408, (Springer International Publishing, Cham2015).

[147] N. Xu, P. Richard, X. Shi, A. van Roekeghem, T. Qian, E. Razzoli, E. Rienks, G.-F. Chen, E. Ieki, K. Nakayama, T. Sato, T. Takahashi, M. Shi and H. Ding, Phys. Rev. B, **88**, 220508 (2013).

[148] S. V. Borisenko, V. B. Zabolotnyy, D. V. Evtushinsky, T. K. Kim, I. V. Morozov, A. N. Yaresko, A. A. Kordyuk, G. Behr, A. Vasiliev, R. Follath and B. Büchner, Phys. Rev. Lett., **105**, 067002 (2010).

[149] T. Qian, X.-P. Wang, W.-C. Jin, P. Zhang, P. Richard, G. Xu, X. Dai, Z. Fang, J.-G. Guo, X.-L. Chen and H. Ding, Phys. Rev. Lett., **106**, 187001 (2011).

[150] Z. R. Ye, Y. Zhang, F. Chen, M. Xu, J. Jiang, X. H. Niu, C. H. P. Wen, L. Y. Xing, X. C. Wang, C. Q. Jin, B. P. Xie and D. L. Feng, Phys. Rev. X, **4**, 031041 (2014).

[151] R. Yu, J.-X. Zhu and Q. Si, Phys. Rev. B, **89**, 024509 (2014).

[152] C. Zhang, W. Lv, G. Tan, Y. Song, S. V. Carr, S. Chi, M. Matsuda, A. D. Christianson, J. A. Fernandez-Baca, L. W. Harriger and P. Dai, Phys. Rev. B, **93**, 174522 (2016).

[153] F. Waßer, C. H. Lee, K. Kihou, P. Steffens, K. Schmalzl, N. Qureshi and M. Braden, Scientific Reports, **7**, 10307 (2017).

[154] Y. Li, Z. Yin, X. Wang, D. W. Tam, D. L. Abernathy, A. Podlesnyak, C. Zhang, M. Wang, L. Xing, C. Jin, K. Haule, G. Kotliar, T. A. Maier and P. Dai, Phys. Rev. Lett., **116**, 247001 (2016).

[155] P. Steffens, C. H. Lee, N. Qureshi, K. Kihou, A. Iyo, H. Eisaki and M. Braden, Phys. Rev. Lett., **110**, 137001 (2013).

[156] D. S. Inosov, J. T. Park, A. Charnukha, Y. Li, A. V. Boris, B. Keimer and V. Hinkov, Phys. Rev. B, **83**, 214520 (2011).

[157] G. Yu, Y. Li, E. M. Motoyama and M. Greven, Nat. Phys., **5**, 873 (2009).

[158] J. Paglione and R. L. Greene, Nat. Phys., **6**, 645 (2010).

[159] F. Waßer, S. Wurmehl, S. Aswartham, Y. Sidis, J. T. Park, A. Schneidewind, B. Büchner and M. Braden, physica status solidi (b), **254**, 1600181 (2017).

[160] J. T. Park, G. Friemel, T. Loew, V. Hinkov, Y. Li, B. H. Min, D. L. Sun, A. Ivanov, A. Piovano, C. T. Lin, B. Keimer, Y. S. Kwon and D. S. Inosov, Phys. Rev. B, **86**, 024437 (2012).

[161] E. Hassinger, G. Gredat, F. Valade, S. R. de Cotret, A. Juneau-Fecteau, J.-P. Reid, H. Kim, M. A. Tanatar, R. Prozorov, B. Shen, H.-H. Wen, N. Doiron-Leyraud and L. Taillefer, Phys. Rev. B, **86**, 140502 (2012).

[162] E. Hassinger, G. Gredat, F. Valade, S. R. de Cotret, O. Cyr-Choinière, A. Juneau-Fecteau, J.-P. Reid, H. Kim, M. A. Tanatar, R. Prozorov, B. Shen, H.-H. Wen, N. Doiron-Leyraud and L. Taillefer, Phys. Rev. B, **93**, 144401 (2016).

[163] B. P. P. Mallett, P. Marsik, M. Yazdi-Rizi, T. Wolf, A. E. Böhmer, F. Hardy, C. Meingast, D. Munzar and C. Bernhard, Phys. Rev. Lett., **115**, 027003 (2015).

[164] B. P. P. Mallett, C. N. Wang, P. Marsik, E. Sheveleva, M. Yazdi-Rizi, J. L. Tallon, P. Adelmann, T. Wolf and C. Bernhard, Phys. Rev. B, **95**, 054512 (2017).

[165] B. P. P. Mallett, Y. G. Pashkevich, A. Gusev, T. Wolf and C. Bernhard, EPL (Europhysics Letters), **111**, 57001 (2015).

[166] J. M. Allred, K. M. Taddei, D. E. Bugaris, M. J. Krogstad, S. H. Lapidus, D. Y. Chung, H. Claus, M. G. Kanatzidis, D. E. Brown, J. Kang, R. M. Fernandes, I. Eremin, S. Rosenkranz, O. Chmaissem and R. Osborn, Nat. Phys., **12**, 493 (2016).

[167] B. A. Frandsen, K. M. Taddei, M. Yi, A. Frano, Z. Guguchia, R. Yu, Q. Si, D. E. Bugaris, R. Stadel, R. Osborn, S. Rosenkranz, O. Chmaissem and R. J. Birgeneau, Phys. Rev. Lett., **119**, 187001 (2017).

[168] C. Dhital, Z. Yamani, W. Tian, J. Zeretsky, A. S. Sefat, Z. Wang, R. J. Birgeneau and S. D. Wilson, Phys. Rev. Lett., **108**, 087001 (2012).

[169] R. Cortes-Gil, D. R. Parker, M. J. Pitcher, J. Hadermann and S. J. Clarke, Chem. Mater., **22**, 4304 (2010).

[170] M. H. Christensen, J. Kang, B. M. Andersen, I. Eremin and R. M. Fernandes, Phys. Rev. B, **92**, 214509 (2015).

[171] W. R. Meier, Q.-P. Ding, A. Kreyssig, S. L. Bud'ko, A. Sapkota, K. Kothapalli, V. Borisov, R. Valenti, C. D. Batista, P. P. Orth, R. M. Fernandes, A. I. Goldman, Y. Furukawa, A. E. Böhmer and P. C. Canfield, npj Quantum Materials, **3**, 5 (2018).

[172] A. Kreyssig, J. M. Wilde, A. E. Böhmer, W. Tian, W. R. Meier, B. Li, B. G. Ueland, M. Xu, S. L. Bud'ko, P. C. Canfield, R. J. McQueeney and A. I. Goldman, Phys. Rev. B, **97**, 224521 (2018).

[173] D. K. Pratt, M. G. Kim, A. Kreyssig, Y. B. Lee, G. S. Tucker, A. Thaler, W. Tian, J. L. Zarestky, S. L. Bud'ko, P. C. Canfield, B. N. Harmon, A. I. Goldman and R. J. McQueeney, Phys. Rev. Lett., **106**, 257001 (2011).

[174] H. Luo, R. Zhang, M. Laver, Z. Yamani, M. Wang, X. Lu, M. Wang, Y. Chen, S. Li, S. Chang, J. W. Lynn and P. Dai, Phys. Rev. Lett., **108**, 247002 (2012).

[175] X. Lu, H. Gretarsson, R. Zhang, X. Liu, H. Luo, W. Tian, M. Laver, Z. Yamani, Y.-J. Kim, A. H. Nevidomskyy, Q. Si and P. Dai, Phys. Rev. Lett., **110**, 257001 (2013).

[176] J.-P. Castellan, S. Rosenkranz, E. A. Goremychkin, D. Chung, I. S. Todorov, M. G. Kanatzidis, I. Eremin, J. Knolle, A. Chubukov, S. Maiti, M. R. Norman, F. Weber, H. Claus, T. Guidi, R. I. Bewley and R. Osborn, Phys. Rev. Lett., **107**, 177003 (2011).

[177] C. H. Lee, K. Kihou, H. Kawano-Furukawa, T. Saito, A. Iyo, H. Eisaki, H. Fukazawa, Y. Kohori, K. Suzuki, H. Usui, K. Kuroki and K. Yamada, Phys. Rev. Lett., **106**, 067003 (2011).

[178] C. H. Lee, K. Kihou, J. T. Park, K. Horigane, K. Fujita, F. Waßer, N. Qureshi, Y. Sidis, J. Akimitsu and M. Braden, Scientific Reports, **6**, 23424 (2016).

[179] M. N. Gastiasoro and B. M. Andersen, Phys. Rev. B, **92**, 140506 (2015).

[180] X. Ren, L. Duan, Y. Hu, J. Li, R. Zhang, H. Luo, P. Dai and Y. Li, Phys. Rev. Lett., **115**, 197002 (2015).

[181] G. R. Stewart, Rev. Mod. Phys., **83**, 1589 (2011).

[182] R. M. Fernandes, D. K. Pratt, W. Tian, J. Zarestky, A. Kreyssig, S. Nandi, M. G. Kim, A. Thaler, N. Ni, P. C. Canfield, R. J. McQueeney, J. Schmalian and A. I. Goldman, Phys. Rev. B, **81**, 140501 (2010).

[183] T. J. Liu, J. Hu, B. Qian, D. Fobes, Z. Q. Mao, W. Bao, M. Reehuis, S. A. J. Kimber, K. Prokeš, S. Matas, D. N. Argyriou, A. Hiess, A. Rotaru, H. Pham, L. Spinu, Y. Qiu, V. Thampy, A. T. Savici, J. A. Rodriguez and C. Broholm, Nat. Mater., **9**, 718 (2010).

[184] C. Zhang, Y. Song, L.-P. Regnault, Y. Su, M. Enderle, J. Kulda, G. Tan, Z. C. Sims, T. Egami, Q. Si and P. Dai, Phys. Rev. B, **90**, 140502 (2014).

[185] M. Ma, P. Bourges, Y. Sidis, Y. Xu, S. Li, B. Hu, J. Li, F. Wang and Y. Li, Phys. Rev. X, **7**, 021025 (2017).

[186] N. Qureshi, C. H. Lee, K. Kihou, K. Schmalzl, P. Steffens and M. Braden, Phys. Rev. B, **90**, 100502 (2014).

[187] Y. Song, H. Man, R. Zhang, X. Lu, C. Zhang, M. Wang, G. Tan, L.-P. Regnault, Y. Su, J. Kang, R. M. Fernandes and P. Dai, Phys. Rev. B, **94**, 214516 (2016).

[188] S. Ideta, T. Yoshida, I. Nishi, A. Fujimori, Y. Kotani, K. Ono, Y. Nakashima, S. Yamaichi, T. Sasagawa, M. Nakajima, K. Kihou, Y. Tomioka, C. H. Lee, A. Iyo, H. Eisaki, T. Ito, S. Uchida and R. Arita, Phys. Rev. Lett., **110**, 107007 (2013).

[189] A. Zheludev, *Manual: ResLib 3.4*, Neutron Scattering Sciences Division, Oak Ridge National Laboratory, Oak Ridge, TN 37831-6393, USA (2007).

[190] M. J. Cooper and R. Nathans, Acta Crystallographica, **23**, 357 (1967).

[191] N. J. Chesser and J. D. Axe, Acta Crystallographica Section A, **29**, 160 (1973).

[192] C. Zhang, R. Yu, Y. Su, Y. Song, M. Wang, G. Tan, T. Egami, J. A. Fernandez-Baca, E. Faulhaber, Q. Si and P. Dai, Phys. Rev. Lett., **111**, 207002 (2013).

[193] W. Wang, J. T. Park, R. Yu, Y. Li, Y. Song, Z. Zhang, A. Ivanov, J. Kulda and P. Dai, Phys. Rev. B, **95**, 094519 (2017).

[194] A. D. Christianson, M. D. Lumsden, S. E. Nagler, G. J. MacDougall, M. A. McGuire, A. S. Sefat, R. Jin, B. C. Sales and D. Mandrus, Phys. Rev. Lett., **103**, 087002 (2009).

[195] L. Yue, X. Ren, T. Han, J. Guo, Z. Wu, Y. Zhang and Y. Li, Phys. Rev. B, **96**, 180505 (2017).

[196] T. E. Mason, A. Schröder, G. Aeppli, H. A. Mook and S. M. Hayden, Phys. Rev. Lett., **77**, 1604 (1996).

[197] B. Lake, G. Aeppli, T. E. Mason, A. Schröder, D. F. McMorrow, K. Lefmann, M. Isshiki, M. Nohara, H. Takagi and S. M. Hayden, Nature, **400**, 43 (1999).

[198] C. Zhang, M. Wang, H. Luo, M. Wang, M. Liu, J. Zhao, D. L. Abernathy, T. A. Maier, K. Marty, M. D. Lumsden, S. Chi, S. Chang, J. A. Rodriguez-Rivera, J. W. Lynn, T. Xiang, J. Hu and P. Dai, Scientific Reports, **1**, 115 (2011).

[199] N. Bulut and D. J. Scalapino, Phys. Rev. B, **47**, 3419 (1993).

[200] D. Manske, I. Eremin and K. H. Bennemann, Phys. Rev. B, **63**, 054517 (2001).

[201] L. W. Harriger, H. Q. Luo, M. S. Liu, C. Frost, J. P. Hu, M. R. Norman and P. Dai, Phys. Rev. B, **84**, 054544 (2011).

[202] C. H. Lee, P. Steffens, N. Qureshi, M. Nakajima, K. Kihou, A. Iyo, H. Eisaki and M. Braden, Phys. Rev. Lett., **111**, 167002 (2013).

[203] Y.-M. Xu, Y.-B. Huang, X.-Y. Cui, E. Razzoli, M. Radovic, M. Shi, G.-F. Chen, P. Zheng, N.-L. Wang, C.-L. Zhang, P.-C. Dai, J.-P. Hu, Z. Wang and H. Ding, Nat. Phys., **7**, 198 (2011).

[204] Q. Wang, Y. Shen, B. Pan, Y. Hao, M. Ma, F. Zhou, P. Steffens, K. Schmalzl, T. R. Forrest, M. Abdel-Hafiez, X. Chen, D. A. Chareev, A. N. Vasiliev, P. Bourges, Y. Sidis, H. Cao and J. Zhao, Nat. Mater., **15**, 159 (2016).

[205] Y. Song, W. Wang, C. Zhang, Y. Gu, X. Lu, G. Tan, Y. Su, F. Bourdarot, A. D. Christianson, S. Li and P. Dai, Phys. Rev. B, **96**, 184512 (2017).

[206] D. Hu, W. Zhang, Y. Wei, B. Roessli, M. Skoulatos, L. P. Regnault, G. Chen, Y. Song, H. Luo, S. Li and P. Dai, Phys. Rev. B, **96**, 180503 (2017).

[207] G. Xu, Z. Xu and J. M. Tranquada, Rev. Sci. Instrum., **84**, 083906 (2013).

[208] E. Demler and S.-C. Zhang, Nature, **396**, 733 (1998).

[209] D. J. Scalapino and S. R. White, Phys. Rev. B, **58**, 8222 (1998).

[210] M. Wang, M. Yi, H. L. Sun, P. Valdivia, M. G. Kim, Z. J. Xu, T. Berlijn, A. D. Christianson, S. Chi, M. Hashimoto, D. H. Lu, X. D. Li, E. Bourret-Courchesne, P. Dai, D. H. Lee, T. A. Maier and R. J. Birgeneau, Phys. Rev. B, **93**, 205149 (2016).

[211] J.-P. Reid, M. A. Tanatar, X. G. Luo, H. Shakeripour, S. R. de Cotret, A. Juneau-Fecteau, J. Chang, B. Shen, H.-H. Wen, H. Kim, R. Prozorov, N. Doiron-Leyraud and L. Taillefer, Phys. Rev. B, **93**, 214519 (2016).

[212] K. Umezawa, Y. Li, H. Miao, K. Nakayama, Z.-H. Liu, P. Richard, T. Sato, J. B. He, D.-M. Wang, G. F. Chen, H. Ding, T. Takahashi and S.-C. Wang, Phys. Rev. Lett., **108**, 037002 (2012).

[213] H. Miao, T. Qian, X. Shi, P. Richard, T. K. Kim, M. Hoesch, L. Y. Xing, X.-C. Wang, C.-Q. Jin, J.-P. Hu and H. Ding, Nat. Commun., **6**, 6056 (2015).

[214] P. O. Sprau, A. Kostin, A. Kreisel, A. E. Böhmer, V. Taufour, P. C. Canfield, S. Mukherjee, P. J. Hirschfeld, B. M. Andersen and J. C. S. Davis, Science, **357**, 75 (2017).

[215] J. Zhao, W. Ratcliff, J. W. Lynn, G. F. Chen, J. L. Luo, N. L. Wang, J. Hu and P. Dai, Phys. Rev. B, **78**, 140504 (2008).

[216] J. Zhao, Q. Huang, C. de la Cruz, S. Li, J. W. Lynn, Y. Chen, M. A. Green, G. F. Chen, G. Li, Z. Li, J. L. Luo, N. L. Wang and P. Dai, Nat. Mater., **7**, 953 (2008).

[217] D. Bhoi, P. Mandal, P. Choudhury, S. Pandya and V. Ganesan, Journal of Applied Physics, **110**, 113722 (2011).

[218] W. Tian, W. Ratcliff, M. G. Kim, J.-Q. Yan, P. A. Kienzle, Q. Huang, B. Jensen, K. W. Dennis, R. W. McCallum, T. A. Lograsso, R. J. McQueeney, A. I. Goldman, J. W. Lynn and A. Kreyssig, Phys. Rev. B, **82**, 060514 (2010).

[219] Y. Qiu, W. Bao, Q. Huang, T. Yildirim, J. M. Simmons, M. A. Green, J. W. Lynn, Y. C. Gasparovic, J. Li, T. Wu, G. Wu and X. H. Chen, Phys. Rev. Lett., **101**, 257002 (2008).

[220] H. Maeter, H. Luetkens, Y. G. Pashkevich, A. Kwadrin, R. Khasanov, A. Amato, A. A. Gusev, K. V. Lamonova, D. A. Chervinskii, R. Klingeler, C. Hess, G. Behr, B. Büchner and H.-H. Klauss, Phys. Rev. B, **80**, 094524 (2009).

[221] S. V. Borisenko, D. V. Evtushinsky, Z.-H. Liu, I. Morozov, R. Kappenberger, S. Wurmehl, B. Büchner, A. N. Yaresko, T. K. Kim, M. Hoesch, T. Wolf and N. D. Zhigadlo, Nat. Phys., **12**, 311 (2016).

[222] M. Merz, P. Schweiss, P. Nagel, M.-J. Huang, R. Eder, T. Wolf, H. von Löhneysen and S. Schuppler, J. Phys. Soc. Jpn., **85**, 044707 (2016).

[223] J. An, A. S. Sefat, D. J. Singh and M.-H. Du, Phys. Rev. B, **79**, 075120 (2009).

[224] E. Fawcett, Rev. Mod. Phys., **60**, 209 (1988).

[225] S. Graser, A. F. Kemper, T. A. Maier, H.-P. Cheng, P. J. Hirschfeld and D. J. Scalapino, Phys. Rev. B, **81**, 214503 (2010).

[226] S. Raymond and G. Lapertot, Phys. Rev. Lett., **115**, 037001 (2015).

[227] J. Knolle, I. Eremin, J. Schmalian and R. Moessner, Phys. Rev. B, **84**, 180510 (2011).

[228] W. Lv, A. Moreo and E. Dagotto, Phys. Rev. B, **89**, 104510 (2014).

[229] D. K. Pratt, A. Kreyssig, S. Nandi, N. Ni, A. Thaler, M. D. Lumsden, W. Tian, J. L. Zarestky, S. L. Bud'ko, P. C. Canfield, A. I. Goldman and R. J. McQueeney, Phys. Rev. B, **81**, 140510 (2010).

[230] G. S. Tucker, R. M. Fernandes, H.-F. Li, V. Thampy, N. Ni, D. L. Abernathy, S. L. Bud'ko, P. C. Canfield, D. Vaknin, J. Schmalian and R. J. McQueeney, Phys. Rev. B, **86**, 024505 (2012).

[231] C. Zhang, J. T. Park, X. Lu, R. Yu, Y. Li, W. Zhang, Y. Zhao, J. W. Lynn, Q. Si and P. Dai, Phys. Rev. B, **91**, 104520 (2015).

[232] Y. Li, W. Wang, Y. Song, H. Man, X. Lu, F. Bourdarot and P. Dai, Phys. Rev. B, **96**, 020404 (2017).

[233] D. C. Johnston, Advances in Physics, **59**, 803 (2010).

[234] G. S. Tucker, R. M. Fernandes, D. K. Pratt, A. Thaler, N. Ni, K. Marty, A. D. Christianson, M. D. Lumsden, B. C. Sales, A. S. Sefat, S. L. Bud'ko, P. C. Canfield, A. Kreyssig, A. I. Goldman and R. J. McQueeney, Phys. Rev. B, **89**, 180503 (2014).

[235] J. Knolle, I. Eremin, A. V. Chubukov and R. Moessner, Phys. Rev. B, **81**, 140506 (2010).

[236] E. Kaneshita and T. Tohyama, Phys. Rev. B, **82**, 094441 (2010).

[237] Fidrysiak, Maciej, Eur. Phys. J. B, **89**, 41 (2016).

[238] W. Zhang, J. T. Park, X. Lu, Y. Wei, X. Ma, L. Hao, P. Dai, Z. Y. Meng, Y.-f. Yang, H. Luo and S. Li, Phys. Rev. Lett., **117**, 227003 (2016).

[239] Q. Zhang, R. M. Fernandes, J. Lamsal, J. Yan, S. Chi, G. S. Tucker, D. K. Pratt, J. W. Lynn, R. W. McCallum, P. C. Canfield, T. A. Lograsso, A. I. Goldman, D. Vaknin and R. J. McQueeney, Phys. Rev. Lett., **114**, 057001 (2015).

[240] M. Yi, D. H. Lu, R. G. Moore, K. Kihou, C.-H. Lee, A. Iyo, H. Eisaki, T. Yoshida, A. Fujimori and Z.-X. Shen, New Journal of Physics, **14**, 073019 (2012).

[241] K.-K. Ng and M. Sigrist, J. Phys. Soc. Jpn., **69**, 3764 (2000).

[242] M. Braden, P. Steffens, Y. Sidis, J. Kulda, P. Bourges, S. Hayden, N. Kikugawa and Y. Maeno, Phys. Rev. Lett., **92**, 097402 (2004).

[243] N. Qureshi, P. Steffens, D. Lamago, Y. Sidis, O. Sobolev, R. A. Ewings, L. Harnagea, S. Wurmehl, B. Büchner and M. Braden, Phys. Rev. B, **90**, 144503 (2014).

[244] N. Bernhoeft, N. Sato, B. Roessli, N. Aso, A. Hiess, G. H. Lander, Y. Endoh and T. Komatsubara, Phys. Rev. Lett., **81**, 4244 (1998).

[245] A. Hiess, N. Bernhoeft, N. Metoki, G. H. Lander, B. Roessli, N. K. Sato, N. Aso, Y. Haga, Y. Koike, T. Komatsubara and Y, Journal of Physics: Condensed Matter, **18**, R437 (2006).

[246] Z. Xu, J. Wen, G. Xu, S. Chi, W. Ku, G. Gu and J. M. Tranquada, Phys. Rev. B, **84**, 052506 (2011).

[247] S. Souma, Y. Machida, T. Sato, T. Takahashi, H. Matsui, S.-C. Wang, H. Ding, A. Kaminski, J. C. Campuzano, S. Sasaki and K. Kadowaki, Nature, **423**, 65 (2003).

[248] M. Nakajima, S. Ishida, K. Kihou, Y. Tomioka, T. Ito, Y. Yoshida, C. H. Lee, H. Kito, A. Iyo, H. Eisaki, K. M. Kojima and S. Uchida, Phys. Rev. B, **81**, 104528 (2010).

[249] R. Juza and K. Langer, Zeitschrift für anorganische und allgemeine Chemie, **361**, 58 (1968).

[250] A. F. Wang, X. G. Luo, Y. J. Yan, J. J. Ying, Z. J. Xiang, G. J. Ye, P. Cheng, Z. Y. Li, W. J. Hu and X. H. Chen, Phys. Rev. B, **85**, 224521 (2012).

[251] X. Wang, Q. Liu, Y. Lv, W. Gao, L. Yang, R. Yu, F. Li and C. Jin, Solid State Commun., **148**, 538 (2008).

[252] P. K. Nag, R. Schlegel, D. Baumann, H.-J. Grafe, R. Beck, S. Wurmehl, B. Büchner and C. Hess, Scientific Reports, **6**, 27926 (2016).

[253] S. H. Baek, D. Bhoi, W. Nam, B. Lee, D. V. Efremov, B. Büchner and K. H. Kim, Nat. Commun., **9**, 2139 (2018).

[254] S. Aswartham, G. Behr, L. Harnagea, D. Bombor, A. Bachmann, I. V. Morozov, V. B. Zabolotnyy, A. A. Kordyuk, T. K. Kim, D. V. Evtushinsky, S. V. Borisenko, A. U. B. Wolter, C. Hess, S. Wurmehl and B. Büchner, Phys. Rev. B, **84**, 054534 (2011).

[255] L. Y. Xing, X. Shi, P. Richard, X. C. Wang, Q. Q. Liu, B. Q. Lv, J.-Z. Ma, B. B. Fu, L.-Y. Kong, H. Miao, T. Qian, T. K. Kim, M. Hoesch, H. Ding and C. Q. Jin, Phys. Rev. B, **94**, 094524 (2016).

[256] S. J. Zhang, X. C. Wang, R. Sammynaiken, J. S. Tse, L. X. Yang, Z. Li, Q. Q. Liu, S. Desgreniers, Y. Yao, H. Z. Liu and C. Q. Jin, Phys. Rev. B, **80**, 014506 (2009).

[257] M. Gooch, B. Lv, J. H. Tapp, Z. Tang, B. Lorenz, A. M. Guloy and P. C. W. Chu, EPL (Europhysics Letters), **85**, 27005 (2009).

[258] M. J. Pitcher, T. Lancaster, J. D. Wright, I. Franke, A. J. Steele, P. J. Baker, F. L. Pratt, W. T. Thomas, D. R. Parker, S. J. Blundell and S. J. Clarke, J. Am. Chem. Soc., **132**, 10467 (2010).

[259] O. Heyer, T. Lorenz, V. B. Zabolotnyy, D. V. Evtushinsky, S. V. Borisenko, I. Morozov, L. Harnagea, S. Wurmehl, C. Hess and B. Büchner, Phys. Rev. B, **84**, 064512 (2011).

[260] G. Li, R. R. Urbano, P. Goswami, C. Tarantini, B. Lv, P. Kuhns, A. P. Reyes, C. W. Chu and L. Balicas, Phys. Rev. B, **87**, 024512 (2013).

[261] T. Hanaguri, K. Kitagawa, K. Matsubayashi, Y. Mazaki, Y. Uwatoko and H. Takagi, Phys. Rev. B, **85**, 214505 (2012).

[262] U. Stockert, M. Abdel-Hafiez, D. V. Evtushinsky, V. B. Zabolotnyy, A. U. B. Wolter, S. Wurmehl, I. Morozov, R. Klingeler, S. V. Borisenko and B. Büchner, Phys. Rev. B, **83**, 224512 (2011).

[263] S. Chi, S. Grothe, R. Liang, P. Dosanjh, W. N. Hardy, S. A. Burke, D. A. Bonn and Y. Pennec, Phys. Rev. Lett., **109**, 087002 (2012).

[264] S. Khim, B. Lee, J. W. Kim, E. S. Choi, G. R. Stewart and K. H. Kim, Phys. Rev. B, **84**, 104502 (2011).

[265] H. Miao, L.-M. Wang, P. Richard, S.-F. Wu, J. Ma, T. Qian, L.-Y. Xing, X.-C. Wang, C.-Q. Jin, C.-P. Chou, Z. Wang, W. Ku and H. Ding, Phys. Rev. B, **89**, 220503 (2014).

[266] A. E. Taylor, M. J. Pitcher, R. A. Ewings, T. G. Perring, S. J. Clarke and A. T. Boothroyd, Phys. Rev. B, **83**, 220514 (2011).

[267] N. Qureshi, P. Steffens, Y. Drees, A. C. Komarek, D. Lamago, Y. Sidis, L. Harnagea, H.-J. Grafe, S. Wurmehl and B. B. andM. Braden, Phys. Rev. Lett., **108**, 117001 (2012).

[268] J. T. Park, D. S. Inosov, A. Yaresko, S. Graser, D. L. Sun, P. Bourges, Y. Sidis, Y. Li, J.-H. Kim, D. Haug, A. Ivanov, K. Hradil, A. Schneidewind, P. Link, E. Faulhaber, I. Glavatskyy, C. T. Lin, B. Keimer and V. Hinkov, Phys. Rev. B, **82**, 134503 (2010).

[269] M. Wang, M. Wang, H. Miao, S. V. Carr, D. L. Abernathy, M. B. Stone, X. C. Wang, L. Xing, C. Q. Jin, X. Zhang, J. Hu, T. Xiang, H. Ding and P. Dai, Phys. Rev. B, **86**, 144511 (2012).

[270] S. H. Baek, H. J. Grafe, F. Hammerath, M. Fuchs, C. Rudisch, L. Harnagea, S. Aswartham, S. Wurmehl, J. van den Brink and B. Büchner, The European Physical Journal B, **85**, 159 (2012).

[271] X. Wang, Q. Liu, Y. Lv, Z. Deng, K. Zhao, R. Yu, J. Zhu and C. Jin, Science China Physics, Mechanics and Astronomy, **53**, 1199 (2010).

[272] P. M. R. Brydon, M. Daghofer, C. Timm and J. van den Brink, Phys. Rev. B, **83**, 060501 (2011).

[273] K. Ishida, H. Mukuda, Y. Kitaoka, K. Asayama, Z. Q. Mao, Y. Mori and Y. Maeno, Nature, **396**, 658 (1998).

[274] Y. Maeno, S. Kittaka, T. Nomura, S. Yonezawa and K. Ishida, J. Phys. Soc. Jpn., **81**, 011009 (2011).

[275] T. Hänke, S. Sykora, R. Schlegel, D. Baumann, L. Harnagea, S. Wurmehl, M. Daghofer, B. Büchner, J. van den Brink and C. Hess, Phys. Rev. Lett., **108**, 127001 (2012).

[276] J. D. Wright, M. J. Pitcher, W. Trevelyan-Thomas, T. Lancaster, P. J. Baker, F. L. Pratt, S. J. Clarke and S. J. Blundell, Phys. Rev. B, **88**, 060401 (2013).

[277] M. P. Allan, K. Lee, A. W. Rost, M. H. Fischer, F. Massee, K. Kihou, C.-H. Lee, A. Iyo, H. Eisaki, T.-M. Chuang, J. C. Davis and E.-A. Kim, Nat. Phys., **11**, 177 (2015).

[278] J. Brand, A. Stunault, S. Wurmehl, L. Harnagea, B. Büchner, M. Meven and M. Braden, Phys. Rev. B, **89**, 045141 (2014).

[279] J. Knolle, V. B. Zabolotnyy, I. Eremin, S. V. Borisenko, N. Qureshi, M. Braden, D. V. Evtushinsky, T. K. Kim, A. A. Kordyuk, S. Sykora, C. Hess, I. V. Morozov, S. Wurmehl, R. Moessner and B. Büchner, Phys. Rev. B, **86**, 174519 (2012).

[280] Y. Wang, A. Kreisel, V. B. Zabolotnyy, S. V. Borisenko, B. Büchner, T. A. Maier, P. J. Hirschfeld and D. J. Scalapino, Phys. Rev. B, **88**, 174516 (2013).

[281] S.-i. Shamoto, M. Ishikado, A. D. Christianson, M. D. Lumsden, S. Wakimoto, K. Kodama, A. Iyo and M. Arai, Phys. Rev. B, **82**, 172508 (2010).

[282] S. Wakimoto, K. Kodama, M. Ishikado, M. Matsuda, R. Kajimoto, M. Arai, K. Kakurai, F. Esaka, A. Iyo, H. Kito, H. Eisaki and S.-i. Shamoto, J. Phys. Soc. Jpn., **79**, 074715 (2010).

[283] L. Shan, J. Gong, Y.-L. Wang, B. Shen, X. Hou, C. Ren, C. Li, H. Yang, H.-H. Wen, S. Li and P. Dai, Phys. Rev. Lett., **108**, 227002 (2012).

[284] Z.-H. Liu, P. Richard, K. Nakayama, G.-F. Chen, S. Dong, J.-B. He, D.-M. Wang, T.-L. Xia, K. Umezawa, T. Kawahara, S. Souma, T. Sato, T. Takahashi, T. Qian, Y. Huang, N. Xu, Y. Shi, H. Ding and S.-C. Wang, Phys. Rev. B, **84**, 064519 (2011).

[285] F. Ahn, I. Eremin, J. Knolle, V. B. Zabolotnyy, S. V. Borisenko, B. Büchner and A. V. Chubukov, Phys. Rev. B, **89**, 144513 (2014).

[286] R. Nourafkan, G. Kotliar and A.-M. S. Tremblay, Phys. Rev. Lett., **117**, 137001 (2016).

[287] T. Saito, S. Onari, Y. Yamakawa, H. Kontani, S. V. Borisenko and V. B. Zabolotnyy, Phys. Rev. B, **90**, 035104 (2014).

[288] K. Matan, S. Ibuka, R. Morinaga, S. Chi, J. W. Lynn, A. D. Christianson, M. D. Lumsden and T. J. Sato1, Phys. Rev. B, **82**, 054515 (2010).

[289] c.f. the report for experiment 4-02-478 performed at IN20 in ILL on Co-overdoped $Ba(Fe_{1-x}Co_x)_2As_2$.

[290] I. Morozov, A. Boltalin, O. Volkova, A. Vasiliev, O. Kataeva, U. Stockert, M. Abdel-Hafiez, D. Bombor, A. Bachmann, L. Harnagea, M. Fuchs, H.-J. Grafe, G. Behr, R. Klingeler, S. Borisenko, C. Hess, S. Wurmehl and B. Büchner, Crystal Growth & Design, **10**, 4428 (2010).

[291] B. I. Zimmer, W. Jeitschko, J. H. Albering, R. Glaum and M. Reehuis, Journal of Alloys and Compounds, **229**, 238 (1995).

[292] H. Luetkens, H.-H. Klauss, M. Kraken, F. J. Litterst, T. Dellmann, R. Klingeler, C. Hess, R. Khasanov, A. Amato, C. Baines, M. Kosmala, O. J. Schumann, M. Braden, J. Hamann-Borrero, N. Leps, A. Kondrat, G. Behr, J. Werner and B. Büchner, Nat. Mater., **8**, 305 (2009).

[293] Y. Chen, J. W. Lynn, J. Li, G. Li, G. F. Chen, J. L. Luo, N. L. Wang, P. Dai, C. dela Cruz and H. A. Mook, Phys. Rev. B, **78**, 064515 (2008).

[294] A. Martinelli, A. Palenzona, M. Tropeano, M. Putti, C. Ferdeghini, G. Profeta and E. Emerich, Phys. Rev. Lett., **106**, 227001 (2011).

[295] A. J. Drew, C. Niedermayer, P. J. Baker, F. L. Pratt, S. J. Blundell, T. Lancaster, R. H. Liu, G. Wu, X. H. Chen, I. Watanabe, V. K. Malik, A. Dubroka, M. Rossle, K. W. Kim, C. Baines and C. Bernhard, Nat. Mater., **8**, 310 (2009).

[296] S. Sanna, R. De Renzi, G. Lamura, C. Ferdeghini, A. Palenzona, M. Putti, M. Tropeano and T. Shiroka, Phys. Rev. B, **80**, 052503 (2009).

[297] R. Kappenberger, S. Aswartham, F. Scaravaggi, C. G. Blum, M. I. Sturza, A. U. Wolter, S. Wurmehl and B. Büchner, Journal of Crystal Growth, **483**, 9 (2018).

[298] A.-J. Dianoux and G. Lander (Editors), *ILL Neutron Data Booklet*, (Old City Publishing2003).

[299] E. A. Goremychkin, R. Osborn, C. H. Wang, M. D. Lumsden, M. A. McGuire, A. S. Sefat, B. C. Sales, D. Mandrus, H. M. Rønnow, Y. Su and A. D. Christianson, Phys. Rev. B, **83**, 212505 (2011).

[300] P. Cheng, W. Bao, S. Danilkin, T. Zhao, J. Sheng, J. Liu, W. Luo and J. Wang, Advances in Condensed Matter Physics, **2015**, 1 (2015).

[301] Y. Xiao, M. Zbiri, R. A. Downie, J.-W. G. Bos, T. Brückel and T. Chatterji, Phys. Rev. B, **88**, 214419 (2013).

[302] A. Kondrat, J. E. Hamann-Borrero, N. Leps, M. Kosmala, O. Schumann, A. Köhler, J. Werner, G. Behr, M. Braden, R. Klingeler, B. Büchner and C. Hess, The European Physical Journal B, **70**, 461 (2009).

[303] L. Malavasi, G. A. Artioli, C. Ritter, M. C. Mozzati, B. Maroni, B. Pahari and A. Caneschi, J. Am. Chem. Soc., **132**, 2417 (2010).

[304] P. M. Aswathy, J. B. Anooja and U. Syamaprasad, Journal of the American Ceramic Society, **96**, 1176 (2013).

[305] H. Ponce-Flores and A. Conde-Gallardo, Journal of Superconductivity and Novel Magnetism, **27**, 673 (2014).

[306] A. Furrer, J. M. Thierry and Strässle, *Neutron Scattering in Condensed Matter Physics*, (World Scientific 2010), isbn: 981-02-4830-X.

[307] B. T. M. Willis and C. J. Carlile, *Experimental Neutron Scattering*, (Oxford University Press 2009), isbn: 978-0-19-851970-6.

[308] G. Shirane, S. M. Shapiro and J. M. Tranquada, *Neutron Scattering with a Triple-Axis Spectrometer*, (Cambridge University Press 2004), isbn: 0-511-03732-5.

[309] W. Marshall and S. W. Lovesey, *Theory of Thermal Neutron Scattering*, (Oxford University Press 1971), isbn: 1114819115.

[310] T. Chatterji, *Neutron Scattering from Magnetic Materials*, (Elsvier 2006), isbn: 978-0-444-51050-1.

[311] G. L. Squires, *Introduction to the Theory of Thermal Neutron Scattering*, (Dover Publications, Inc., 1996), isbn: 0-486-69447-X.

[312] M. Nakamura, R. Kajimoto, Y. Inamura, F. Mizuno, M. Fujita, T. Yokoo and M. Arai, J. Phys. Soc. Jpn., **78**, 093002 (2009).

[313] M. Popovici, Acta Crystallographica, **A31**, 507 (1975).

[314] R. M. Moon, T. Riste and W. C. Koehler, Phys. Rev., **181**, 920 (1969).

Danksagung

Wann immer eine solche Arbeit wie die Promotion zu Ende geht und damit ein Lebensabschnitt abgeschlossen wird, ist es Zeit zurück zu schauen und sich bei allen Leuten zu bedanken, die einen auf diesem Weg begleitet haben.
Am Anfang des Weges stand natürlich die Wahl des Promotionsthemas, daher möchte ich mich herzlich bei Prof. Dr. Markus Braden für das in mich gesetzte Vertrauen, die Unterstützung bei der Bearbeitung und die Diskussionen über die Daten bedanken. Die Forschung an dem Zusammenspiel von Magnetismus und Supraleitung mittels Neutronenstreuung hat mit große Freude bereitet. Insbesondere der damit verbundene Austausch mit anderen Wissenschaftlern auf Konferenzen, oder beim Experiment selbst, habe ich sehr genossen. Des Weiteren möchte ich mich bei Prof. Dr. Thomas Lorenz dafür bedanken, dass er sich die Zeit genommen hat meine Arbeit zu begutachten. Außerdem danke ich ihm und Prof. Dr. Simon Trebst für das Stellen meiner Prüfungskommission. Ganz besonderer Dank gilt Rhea Kappenberger, Saicharan Aswartham, Sabine Wurmehl, Kunihiro Kihou und Chul-Ho Lee, denn ohne die von Ihnen synthetisierten und mir bereit gestellten Proben wäre keine Messung möglich gewesen.
Ferner möchte ich mich bei Chul-Ho Lee, Yvan Sidis, Paul Steffens, Karin Schmalzl, Navid Qureshi, Björn Fåk, Andrea Piovano, Astrid Schneidewind und Jitae Park für die tolle Unterstützung beim und die gemeinsame Zeit am Experiment bedanken.
Darüber hinaus möchte ich mich bei allen Mitarbeitern*innen des II. Physikalischen Instituts für die angenehme und produktive Atmosphäre bedanken, genau wie für die erkenntnisreichen Diskussionen. Dieser Dank gilt insbesondere denjenigen die mit mir das Büro 212 geteilt haben. Außerdem möchte ich mich bei Kevin Jenni, Sebastian Biesenkamp, Tobias Fröhlich und Christoph Grams für die Hilfe bei der Erstellung des LaTeX Dokuments, sowie für das Korrekturlesen bedanken. Abschließend möchte ich mich bei meiner Familie für die dauerhafte Unterstützung in allen Lebenslagen bedanken.

Abstract

Superconductivity is one of the most mesmerising phenomena in condensed matter physics research, and the most recent material class, where it was discovered in, are iron-based superconductors. These compounds display a prodigious interplay between their lattice/orbital degrees of freedom, magnetic order, superconductivity and electronic nematicity, which gives rise to a rich phase diagram. Today there is a broad consensus that superconductivity is driven by spin fluctuations (paramagnons), whose fingerprint in the excitation spectra (observable by inelastic neutron scattering) is the so-called spin resonance mode. It is directly related to the details of the superconducting pairing mechanism, and its connection to the lattice structure and magnetic order is studied by X-ray, elastic and inelastic neutron scattering experiments in this thesis.
The impact of antiferromagnetic order with large moments on the superconducting state is investigated by polarised inelastic neutron scattering in underdoped $Ba(Fe_{1-x}Co_x)_2As_2$, where both orders coexist on a microscopic scale. Since superconductivity emerges in the presence of broad magnetic anisotropy gaps, it is shown that the corresponding spin resonance mode appears only in the two transversal channels, at two distinct energies, and longitudinal contributions are gapped. This situation is in contrast to the one in optimally and overdoped $BaFe_2As_2$, where isotropic spin resonance modes are observed. Concluding, this anisotropy is attributed to a band- and orbital-selective pairing mechanism.
In $Ba_{1-x}Na_xFe_2As_2$ the interplay between structure, magnetic order and superconductivity is more intricate. The spins in the already orthorhombic and magnetically ordered phase undergo a second magnetic transition at a lower temperature, which rotates the moments from an alignment within the FeAs-layers to a perpendicular arrangement, by concomitantly suppressing the orthorhombic distortion. This spin reorientation transition highlights the importance of spin-orbit coupling in this material class. Moreover, in a naive picture, low-energy spin fluctuations, which promote superconductivity, rotate concomitantly with the associated static moments. However, polarised inelastic neutron scattering experiments revealed that this is not the case, and thus clearly demonstrate that the polarisation of low-energy spin excitations is uniform in iron-based superconductors.
Furthermore, the spin resonance mode in $Ba_{1-x}Na_xFe_2As_2$ consists of two contributions which display a remarkably different doping dependence. On the one hand, the intensity of the high-energy part traces the shape of the superconducting dome in the phase diagram. While, on the other hand, it is shown by absolute unit calculation, that the intensity of the low-energy part is the accumulated spec-

tral weight, which is removed from the magnetic Bragg peaks, as magnetic order and superconductivity compete for the same electronic states below T_c. For this reason, the low-energy part is most intense close to the magnetic end-point in the associated phase diagram and is strongly reduced in intensity beyond that point. In particular, the low-energy part in $Ba_{0.61}Na_{0.39}Fe_2As_2$ displays the strongest resonance mode ever observed in iron-based superconductors, while the high-energy contribution is similar intense as the one in optimally Co-doped $BaFe_2As_2$. Consequently, this observation provides a simple explanation on the origin of split spin resonance modes, observed in underdoped iron-based superconductors.

Kurzzusammenfassung

Supraleitung ist eines der faszinierendsten Phänomene in der Festkörperphysikforschung, wobei die jüngste Materialklasse in der es entdeckt wurde eisenbasierte Supraleiter sind. In diesen Verbindungen stehen die Freiheitsgrade des Kristallgitters/ der Orbitale, die magnetische Ordnung, Supraleitung und die elektronisch nematische Phase in einem erstaunlichen Wechselspiel. Darüber hinaus herrscht heutzutage ein breiter Konsens darüber, dass hier die Supraleitung durch Spinfluktuationen (Paramagnonen) getrieben wird. Das entsprechende experimentelle Kennzeichen im Anregungsspektrum (beobachtbar mittels inelastischer Neutronenstreuung) ist die sogenannte Spinresonanzmode, welche direkt mit den Details des supraleitenden Paarbildungsmechanismus verbunden ist. Um den Zusammenhang zwischen der Gitter-, Magnetstruktur und Supraleitung zu studieren, wurden in dieser Arbeit Röntgen- sowie elastische und inelastische Neutronenstreuexperimente durchgeführt.
Der Einfluss der antiferromagnetischen Ordnung auf den supraleitenden Zustand ist im unterdotierten $Ba(Fe_{1-x}Co_x)_2As_2$, das eine mikroskopische Phasenkoexistenz beider Phänomene aufweist, mittels polarisierter inelastischer Neutronenstreuung untersucht. Dabei wurde gezeigt, dass die Spinresonanzmode nur in den zwei transversalen Richtungen, bei zwei unterschiedlichen Energien, auftaucht, da die Supraleitung hier aus einem Zustand mit breiten magnetischen anisotropen Anregungslücken entsteht. Aus diesem Grund gibt es keine longitudinalen Beiträge zur Spinresonanzmode. Dies steht im Gegensatz zu optimal oder überdotierten $BaFe_2As_2$ Proben, bei denen eine isotrope Spinresonanzmode beobachtet wird. Schlussendlich wird die beobachtete Anisotropie einem band- und oribtalselektiven Paarbildungsmechanismus zugeordnet.
In $Ba_{1-x}Na_xFe_2As_2$ ist das Wechselspiel zwischen Kristallstruktur, magnetischer Ordnung und Supraleitung komplizierter als im obengenannten Fall. Die Spins durchlaufen, im bereits orthorhombisch und magnetisch geordneten Zustand, einen zweiten magnetischen Phasenübergang, dessen Übergangstemperatur kleiner ist als die des ersten. Bei diesem zweiten magnetischen Phasenübergang ändert sich die Ausrichtung der Spins bezüglich der FeAs-Ebenen von parallel zu senkrecht und die orthorhombische Verzerrung wird aufgehoben. Die Spinreorientierung zeigt die Wichtigkeit von Spin-Ortbit-Coupling in dieser Materialklasse auf. In einem einfachen Model müssten die niederenergetischen Spinfluktuationen, die unter anderem für die Entstehung der Supraleitung verantwortlich sind, der Neuausrichtung der statischen Momente folgen. Allerdings, konnte mit Hilfe polarisierter inelastischer Neutronenstreuung gezeigt werde, dass das nicht der Fall

ist. Folglich ist die Polarisation niederenergetischer Spinfluktuationen eine einheitliche Eigenschaft in eisenbasierten Supraleitern.
Außerdem besteht die Spinresonanzmode in $Ba_{1-x}Na_xFe_2As_2$ aus zwei Beiträgen, die beide eine bemerkenswerte und unterschiedliche Dotierungsabhängigkeit zeigen. Auf der einen Seite folgt die Intensität des höherenergetische Beitrags dem supraleitenden Dom in dazugehörigen Phasendiagram. Andererseits konnte mittels absoluter Einheitenbestimmung gezeigt werde, dass die Intensität der niederenergetischen Mode das akkumulierte spektrale Gewicht ist, welches aus der Intensitätsreduktion der magnetischen Braggpeaks resultiert, wenn magnetische und supraleidende Ordnung um die selben elektronischen Zustände konkurrieren. Aus diesem Grund ist in der Nähe des magnetischen Endpunkts des dazugehörigen Phasendiagram der niederenergetische Beitrag am größten und verliert massiv an Intensität, wenn dieser Punkt überschritten wird. Insbesondere ist die niederenergetische Spinresonanzmode in $Ba_{0.61}Na_{0.39}Fe_2As_2$ die intensivste, die je in eisenbasierten Supraleitern beobachtet wurde. Darüber hinaus ist die Intensität des höherenergetischen Beitrags fast identisch mit der in optimal dotierten $Ba(Fe_{1-x}Co_x)_2As_2$. Abschließend liefert diese Beobachtung eine einfache Erklärung über den Ursprung der Doppel-Spinresonanzmoden, die in unterdotierten eisenbasierten Supraleitern beobachtet werden.

Teilpublikationen

Die aufgelisteten Publikationen enthalten Teile dieser Dissertation, insbesondere Kapitel 2.1 und 3.2 beruhen darauf.

- **F. Waßer**, S. Wurmehl, S. Aswartham, Y. Sidis, J. T. Park, A. Schneidewind, B. Büchner and M. Braden, *Spin reorientation transition in Na-doped $BaFe_2As_2$ studied by single-crystal neutron diffraction*, Phys. Status Solidi B **254**, No. 1, 1600181 (2017)
- **F. Waßer**, C. H. Lee, K. Kihou, P. Steffens, K. Schmalzl, N. Qureshi and M. Braden, *Anisotropic resonance modes emerging in an antiferromagnetic superconducting state*, Scientific Reports, **7**, 10307 (2017)

Weitere Publikationen

Die aufgelistete Publikation resultierte aus Ergebnissen meiner Masterarbeit.

- **F. Waßer**, A. Schneidewind, Y. Sidis, S. Wurmehl, S. Aswartham, B. Büchner and M. Braden, *Spin reorientation in* $Ba_{0.65}Na_{0.35}Fe_2As_2$ *studied by single-crystal neutron diffraction*, Physical Review B, **91**, 060505(R) (2015)

Die aufgelistete Publikation ist nicht Bestandteil der Dissertation.

- C. H. Lee, K. Kihou, J. T. Park, K. Horigane, K. Fujita, **F. Waßer**, N. Qureshi, Y. Sidis, J. Akimitsu, and M. Braden, *Suppression of spin-exciton state in hole overdoped iron-based superconductors*, Scientific Reports, **6**, 23424 (2016)

Erklärung

Ich versichere, dass ich die von mir vorgelegte Dissertation selbständig angefertigt, die benutzten Quellen und Hilfsmittel vollständig angegeben und die Stellen der Arbeit − einschließlich Tabellen, Karten und Abbildungen −, die anderen Werken im Wortlaut oder dem Sinn nach entnommen sind, in jedem Einzelfall als Entlehnung kenntlich gemacht habe; dass diese Dissertation noch keiner anderen Fakultät oder Universität zur Prüfung vorgelegen hat; dass sie − abgesehen von unten angegebenen Teilpublikationen − noch nicht veröffentlicht worden ist sowie, dass ich eine solche Veröffentlichung vor Abschluss des Promotionsverfahrens nicht vornehmen werde. Die Bestimmungen der Promotionsordnung sind mir bekannt. Die von mir vorgelegte Dissertation ist von Prof. Dr. Markus Braden betreut worden.

Köln, den 10. Dezember, 2018 F. Waßer